Hydro-elastic analysis of flexible marine propellers

Maljaars, Pieter

DOI
10.4233/uuid:19c9610b-9a72-42a6-8340-2ba01ec78cc6

Publication date
2019

Document Version
Final published version

Citation (APA)
Maljaars, P. (2019). *Hydro-elastic analysis of flexible marine propellers*. [Dissertation (TU Delft), Delft University of Technology]. https://doi.org/10.4233/uuid:19c9610b-9a72-42a6-8340-2ba01ec78cc6

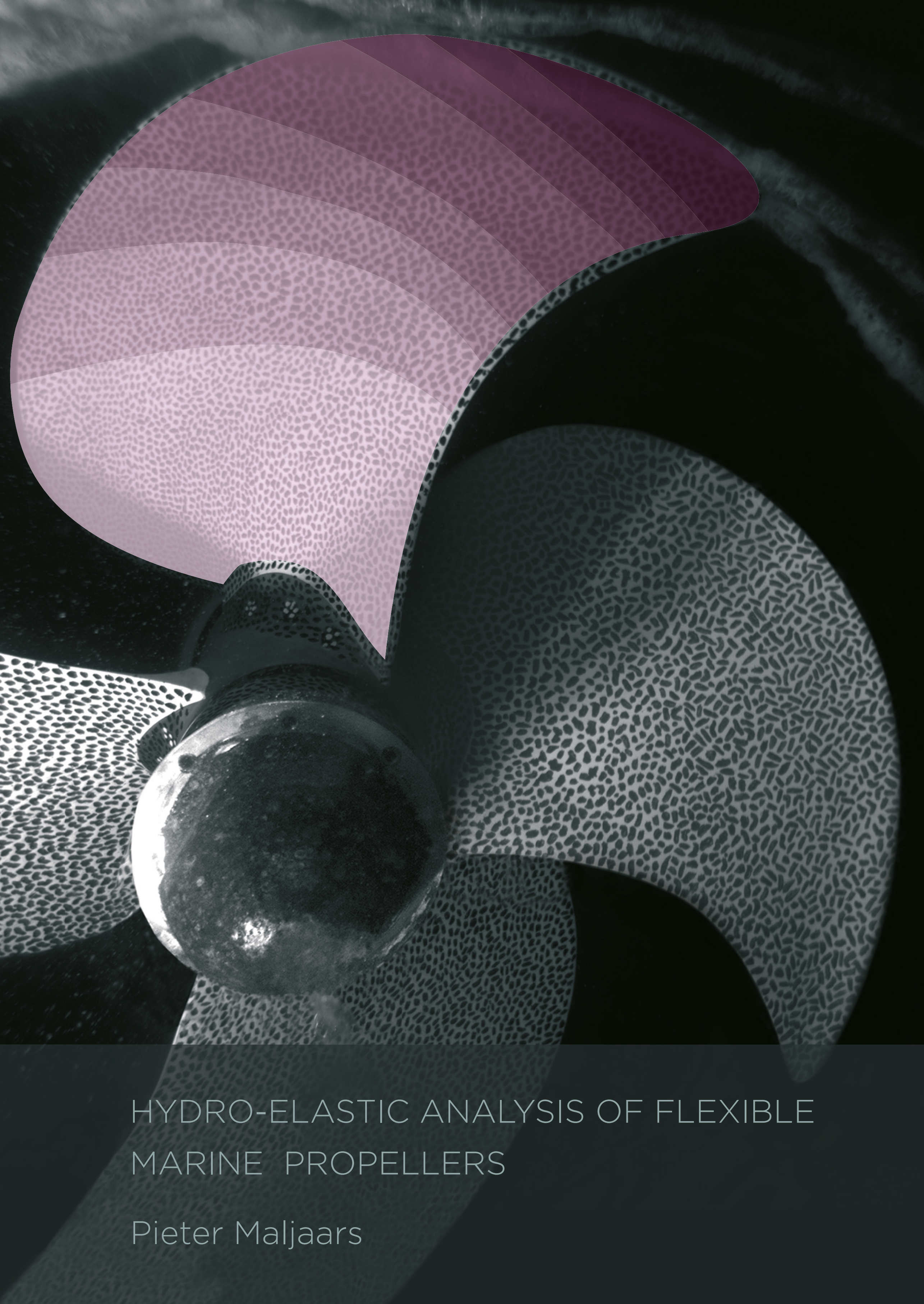

HYDRO-ELASTIC ANALYSIS OF FLEXIBLE MARINE PROPELLERS

Pieter Maljaars

HYDRO-ELASTIC ANALYSIS OF FLEXIBLE MARINE PROPELLERS

HYDRO-ELASTIC ANALYSIS OF FLEXIBLE MARINE PROPELLERS

Proefschrift

ter verkrijging van de graad van doctor
aan de Technische Universiteit Delft,
op gezag van de Rector Magnificus prof. dr. ir. T.H.J.J. van der Hagen,
voorzitter van het College voor Promoties,
in het openbaar te verdedigen op dinsdag 12 maart 2019 om 15:00 uur

door

Pieter Johannes MALJAARS

scheepsbouwkundig ingenieur,
Technische Universiteit Delft, Nederland
geboren te Vlissingen, Nederland.

Dit proefschrift is goedgekeurd door de

promotor: prof. dr. ir. M.L. Kaminski
promotor: prof. dr. ir. T.J.C van Terwisga

Samenstelling promotiecommissie:

Rector Magnificus,	voorzitter
Prof. dr. ir. M.L. Kaminski,	Technische Universiteit Delft
Prof. dr. ir. T.J.C van Terwisga,	Technische Universiteit Delft
Onafhankelijke leden:	
Prof. ir. J. Carlton,	City University London
Prof. dr. ir. C. Poelma,	Technische Universiteit Delft
Prof. dr. M. Veljkovic,	Technische Universiteit Delft
Prof. dr. ir. Y.L. Young,	University of Michigan
Prof. dr. ir. C. van Rhee,	Technische Universiteit Delft, reservelid
Overige leden:	
Dr. ir. J.H. den Besten,	Technische Universiteit Delft

The GreenProp research project leading to these results has received funding from the Netherlands Organisation for Scientific Research (NWO), project number 13278 and was also (financially) supported by the following organisations:
- Delft University of Technology
- Defense Materiel Organisation Netherlands
- Maritime Research Institute Netherlands
- Wärtsilä Netherlands B.V.
- Solico B.V.

Keywords: flexible propellers, composite propellers, hydro-elasticity, fluid-structure interaction

Printed by: Ridderprint

Cover: Persoonlijk Proefschrift (Photo courtesy of MARIN)

ISBN 978-94-6375-233-6

CONTENTS

SUMMARY

Higher efficiencies, higher cavitation inception speeds and reduced acoustic signature are claimed benefits of flexible composite propellers. Analysing the hydrodynamic performance of these flexible propellers, implies that a coupled fluid-structure interaction (FSI) computation has to be performed. An FSI coupling can be monolithic, which means the equations for the fluid and structural sub-problem are merged into one set of equations and solved simultaneously. Another approach is to apply a partitioned coupling, in which the existing fluid and structural sub-problem are sequentially solved. Then, coupling iterations are performed to converge to the monolithic solution. When coupling iterations are omitted, the approach becomes a so-called loose coupling. Due to the relatively high fluid added mass, flexible propeller computations require a strong coupling including coupling iterations. Coupling iterations make these kind of computations CPU intensive and therefore it is of importance to solve the structural and fluid problem efficiently.

In this thesis a methodology for solving the FSI of flexible marine propellers is presented, which is based on a strongly coupled partitioned approach. The structural problem has been solved with the finite element method (FEM). In the FEM calculations only one blade has been modelled without the hub. The blade has been fully clamped at the blade-hub interface. The FEM models have been discretised by solid quadratic elements to form a structured mesh. An approach was developed to establish the element dependent material orientations. FEM validation studies with static and dynamic test results show that the present way of composite propeller FEM modelling is reasonably accurate.

The hydrodynamic problem has been solved with the boundary element method (BEM). This is a time efficient, sufficiently accurate, way of solving the hydrodynamics of propellers. This method has been used already for decades in propeller design. BEM methods have their limitations, because they are based on potential flow assumptions meaning that phenomena like flow separation, flow transition, boundary layer build-up and vorticity dynamics are not captured. Therefore, a study was performed in which results obtained with the BEM-FEM coupling for uniform flow have been compared to experimental results and to results from an FSI coupling between a Reynolds-Averaged Navier-Stokes solver and a FEM. This comparison shows that the BEM-FEM method was able to provide reasonable results, even for cases in which significant flow separation and viscous effects were present. For many propeller geometries these effects will not dominate, therefore it is expected that the BEM-FEM coupling can correctly predict the hydro-elastic response for many cases.

For uniform flow conditions the coupling between the BEM and FEM solver was relatively straightforward to made, since dynamic effects do not need to be included and therefore fluid added mass instabilities will not arise, in contrast to non-uniform

flow conditions. To develop the BEM-FEM coupling for behind ship conditions (i.e. non-uniform flows), first of all it was relevant to characterise the typical blade flexibility and flow unsteadiness, because both govern the hydro-elastic response. A measure for the blade flexibility is the structural frequency ratio defined as the ratio between the lowest excitation frequency and the fundamental wet blade natural frequency. The unsteadiness of flows is characterised by the reduced frequency. For both, general expressions were derived, which show that the structural frequency ratio and the reduced frequency are both propeller scale invariant. From these expressions it can be concluded that the structural response is dominated by stiffness, although dynamic effects cannot be excluded. Further, it can be concluded that vibrating blade flows are highly unsteady.

Thereafter a study was performed in which different modelling choices for the development of the BEM-FEM coupling for non-uniform flow have been evaluated, which are: using a quasi-static or dynamic structural model, using closed form expressions for fluid added mass and hydrodynamic damping or not, recalculating the BEM hydrodynamic influence coefficients accordingly to the blade deformations or not. Considering a quasi-static FEM modelling of the structural response of flexible propellers, it can be concluded that this is not recommended since dynamic effects cannot be neglected, although the structural response of flexible propellers is dominated by stiffness. It has been demonstrated that the approximation of the hydro-elastic blade response by using closed form expressions for the fluid added mass and hydrodynamic damping terms provides reasonable results. Finally, it is shown that the significance of recalculating the BEM hydrodynamic influence coefficients is relatively small. This may be utilized, possibly in combination with the closed form expressions for fluid added mass and hydrodynamic damping contributions, to significantly reduce the computation time of flexible propeller FSI calculations.

Necessary for the realization of the BEM-FEM coupling for non-uniform flows was the development of a new FSI approach for periodic problems, called the time periodic coupling approach. This approach differs from a time step coupling with respect to the coupling iterations between fluid and structural solver. In a time periodic coupling the coupling iterations are not performed per time step but on period level. This was necessary for the present BEM-FEM coupling, since the BEM computation itself is iterative on period level rather than on time step level and therefore a time step coupling would not converge. In addition to this, for the case of a non-iterative fluid and structural solver, it has been shown that a time periodic coupling can significantly speed-up the convergence to the steady-state FSI solution of periodic problems. Because it allows to solve the structural problem in the frequency domain; therefore, transients, which slow down the convergence speed, are not computed. However, as shown, instabilities as appearing in time step couplings due to strong fluid added mass effects, arise in time periodic couplings as well. To combat stability problems, a matrix-free Krylov subspace iterative method, called the quasi-Newton inverse least squares method, was implemented in the time periodic framework. This resulted in fast convergence, also in the case of strong fluid added mass effects.

In the present BEM-FEM coupling the structural problem has been solved in the frequency domain and in modal space, which allows for a model reduction by including

only a limited number of mode shapes. The BEM-FEM coupling is not confined to this way of solving the structural equations. For instance, it would be also possible to include in the method a geometrically non-linear FEM calculation, because of the fully separated fluid and structural solver.

Finally, validation studies were performed for non-uniform inflow conditions. In the first experiment, blade deformations, as well as thrust and torque of model scale composite propellers were measured under laboratory conditions at and in cooperation with the Maritime Research Institute Netherlands (MARIN). In this experiment the dynamic blade response was measured for a full revolution and compared to numerical results as calculated with the BEM-FEM coupling for non-uniform flows. A comparison of the measured and computed dynamic response show that the trend in the results is similar. However, in magnitude significant differences between measurement and calculation results were found. For instance, at the propeller tip region the calculated deflections were significantly larger than measured. This difference is similar to what was found earlier for uniform flow conditions. Then, this was attributed to flow separation and viscous flow effects. The experiments have shown the feasibility of measuring the dynamic deformations of a propeller for a full revolution.

In a second experiment the blade deformations of a purposely designed glass-epoxy composite flexible propeller with a diameter of one meter were measured during full-scale trials. For this MARIN has developed a dedicated measurement set-up including customized hardware and software. In the experiment, the blade deformations were measured for two blades in the twelve o’clock, one o’clock and half past two position. The results show that the response of the two blades is almost identical, which gives confidence in the accuracy of the blade manufacturing process and measurement technique. A comparison of measured and computed blade response shows that the blade bending response is well predicted with the BEM-FEM coupling. The differences between measured and computed twist responses are larger and can be explained from uncertainties in the measured and calculated twist response, which are relatively large due to the small twist angles.

SAMENVATTING

De verwachte voordelen van flexibele composieten scheepschroeven zijn verbetering van het rendement, hogere cavitatie inceptie snelheden en gereduceerde akoestische signatuur. Het berekenen van de hydrodynamische prestaties van deze flexibele schroeven houdt in dat een vloeistof-structuur interactie (VSI) berekening moet worden gedaan. Een VSI-methode kan monolithisch zijn, hetgeen betekent dat de vergelijkingen voor de vloeistof en constructie tegelijkertijd worden opgelost met behulp van één set vergelijkingen. Een gepartitioneerde aanpak is ook mogelijk, dan worden het vloeistof- en constructieprobleem sequentieel opgelost. Koppelingsiteraties worden dan toegepast om te convergeren naar de monolithische oplossing. Wanneer er geen koppelingsiteraties worden toegepast, spreken we van een zogenaamde zwakke koppeling. Ten gevolge van de relatief grote bijdrage van de toegevoegde massa van het water is echter voor flexibele schroefberekeningen een sterke koppeling vereist. Koppelingsiteraties maken dit soort berekeningen rekenintensief, daarom is het van belang om VSI-problemen efficiënt op te lossen.

In dit proefschrift wordt een methode gepresenteerd om de VSI-respons van flexibele scheepschroeven uit te rekenen. De methode is gebaseerd op een sterk gekoppelde gepartitioneerde aanpak. Voor het oplossen van het structurele probleem is gebruikt gemaakt van de Eindige Elementen Methode (EEM). In de EEM-berekening is enkel het blad gemodelleerd, zonder de naaf. Het blad is volledig ingeklemd bij de bladvoet. Quadratische volume elementen zijn gebruikt in de discretisatie van de EEM-modellen. Een methode is ontwikkeld om per element de materiaal oriëntatie richtingen te definiëren. Validatie van de EEM-modellen met statische en dynamische testresultaten laat zien dat de gevolgde aanpak voor de EEM-modellering van composieten schroeven voldoende nauwkeurig is.

Voor het oplossen van het hydrodynamische probleem is gebruikt gemaakt van een panelenmethode (PM). Dit is een efficiënte en voldoende nauwkeurige methode om de hydrodynamica van scheepschroeven te berekenen. Deze methode wordt al enkele decennia gebruikt voor het ontwerpen van schroeven. Panelenmethoden hebben hun beperking omdat ze gebaseerd zijn op potentiaalstroming, dat betekent dat loslating, transitie van de stroming, opbouw van de grenslaag en werveldynamica niet meegenomen worden. Daarom is er onderzocht wat de invloed hiervan is op de resultaten. Resultaten berekend met de PM-EEM-koppeling zijn vergeleken met experimentele resultaten en met resultaten verkregen met een VSI-koppeling tussen een Reynolds-gemiddelde Navier-Stokes methode en een EEM. Deze vergelijkingsstudie laat zien dat de resultaten berekend met PM-EEM redelijk goed zijn, zelfs voor situaties waarin aanzienlijke loslating en viskeuze effecten aanwezig waren. In veel gevallen zullen deze effecten niet domineren, daarom is de verwachting dat de PM-EEM-koppeling het hydro-elastische gedrag in veel gevallen correct kan uitrekenen.

Voor uniforme aanstroomcondities is de koppeling tussen de PM en de EEM-berekening redelijk eenvoudig te realiseren, aangezien dynamische effecten geen rol spelen en daarom kan instabiliteit ten gevolge van toegevoegde massa niet optreden, in tegenstelling tot niet-uniforme aanstroomcondities. Om de PM-EEM-koppeling voor niet-uniforme aanstroomcondities te ontwikkelen is als eerste de karakteristieke bladflexibiliteit en instationairiteit van de stroming bepaald, omdat beide maatgevend zijn voor het hydro-elastische gedrag. Een maat voor de bladflexibiliteit is de constructiefrequentie ratio, gedefinieerd als de verhouding tussen de laagste excitatiefrequentie en de fundamentele eigenfrequentie van het blad in water. De instationairiteit van stromingen wordt gekarakteriseerd door de gereduceerde frequentie. Voor beide getallen is een formule afgeleid, waaruit volgt dat de constructiefrequentie ratio en de gereduceerde frequentie beide onafhankelijk zijn van de grootte van de schroef. Met deze formules kan ook aangetoond worden dat de constructierespons gedomineerd wordt door de stijfheid, hoewel dynamische effecten niet uitgesloten kunnen worden. Bovendien kan geconcludeerd worden dat de stroming ten gevolge van bladtrillingen erg instationair is.

Vervolgens is de invloed van verschillende modeleerkeuzes in het realiseren van de koppeling tussen de PM en EEM onderzocht, zoals: een quasi-statische of een dynamische modellering van de constructierespons, het wel of niet gebruiken van gesloten formules voor de toegevoegde massa en hydrodynamische demping en het wel of niet herberekenen van de PM hydrodynamische invloedscoëfficiënten aan de hand van de bladdeformaties. Met betrekking tot een quasi-statische EEM-modellering van de constructie respons van flexibele scheepschroeven kan geconcludeerd worden dat dit niet is aan te raden. Hoewel de constructierespons wordt gedomineerd door de stijfheid zijn echter dynamische effecten niet verwaarloosbaar. Er is ook aangetoond dat gesloten formules voor de toegevoegde massa en de hydrodynamische demping gebruikt kunnen worden om een redelijke benadering te krijgen van de hydro-elastische respons. Tot slot is aangetoond dat de invloed van het herberekenen van de PM hydrodynamische invloedscoëfficiënten relatief klein is. Dat kan gebruikt worden, mogelijk in combinatie met de gesloten formules voor toegevoegde massa en hydrodynamische demping, om de rekentijd van flexibele schroefberekeningen met een VSI-methode aanzienlijk te reduceren.

Een noodzakelijke stap voor het realiseren van de PM-EEM-koppeling voor niet-uniforme aanstroom condities was het ontwikkelen van een VSI-methode voor periodieke problemen, de tijdsperiodieke koppelingsmethode geheten. Deze methode verschilt van een tijdstapkoppeling met betrekking tot de koppelingsiteraties tussen de vloeistof en constructie. In een tijdsperiodieke koppeling worden de koppelingsiteraties niet per tijdstap uitgevoerd, maar op periodeniveau. Dit was een vereiste voor de ontwikkelde PM-EEM-koppeling, omdat de PM-berekening van zichzelf al iteratief is op periodeniveau in plaats van op tijdstapniveau en daarom zal een tijdstapkoppeling niet convergeren. Afgezien daarvan is ook aangetoond dat voor periodieke VSI-problemen een tijdsperiodieke koppeling de convergentie aanzienlijk kan versnellen in geval van niet-iteratieve methodes voor het berekenen van de omstroming en de constructierespons. De reden hiervoor is dat de constructievergelijkingen opgelost kunnen worden in het frequentiedomein, daardoor worden transiënten, die het convergentiegedrag nadelig beïnvloeden, niet uitgerekend.

Echter, zoals ook is aangetoond, instabiliteiten ten gevolge van sterke toegevoegde massa effecten van het water die optreden in geval van tijdstapkoppelingen, komen ook voor in een tijdsperiodieke koppeling. Om tot een stabiele tijdsperiodieke koppeling te komen is er gebruikt gemaakt van een matrix vrije Krylov deelruimte iteratieve methode en wel de zogeheten quasi-Newton inverse kleinste kwadraten methode. Ook in het geval van sterke toegevoegde massa effecten wordt met deze methode een snelle convergentie behaald.

In de PM-EEM-koppeling wordt het constructieprobleem opgelost in het frequentiedomein en in de modale ruimte, dat creëert de mogelijkheid om modelreductie toe te passen door een beperkt aantal trilvormen mee te nemen in de berekening. De PM-EEM-koppeling is niet beperkt tot het oplossen van het constructieprobleem op deze manier. Ten gevolge van de volledige scheiding tussen vloeistof- en constructieberekening zou het bijvoorbeeld ook mogelijk zijn om een geometrische niet-lineaire EEM-berekening in de methode te implementeren.

Tenslotte zijn validatiestudies uitgevoerd in niet-uniforme stromingen. In het eerste experiment zijn bladvervormingen en stuwkracht en koppel van composieten modelschroeven gemeten onder laboratoriumcondities bij en in samenwerking met Maritiem Onderzoek Instituut Nederland (MARIN). Voor een volledige omwenteling zijn dynamische bladvervormingen gemeten en vergeleken met numerieke resultaten berekend met de PM-EEM-koppeling voor niet-uniforme stromingen. Hieruit blijkt dat de trend in meet- en berekeningsresultaten vergelijkbaar is. Echter, in absolute zin zijn er aanzienlijke verschillen tussen meet- en berekeningsresultaten. Bij de schroeftip bijvoorbeeld zijn de berekende verbuigingen aanzienlijk groter dan gemeten. Een vergelijkbaar verschil was eerder al gevonden voor uniforme aanstroomcondities. Toen werd dit toegeschreven aan loslating en viskeuze effecten. De experimenten hebben aangetoond dat het mogelijk is om voor een volledige omwenteling de dynamische bladvervormingen van schroeven te meten.

In een tweede meting zijn de bladvervormingen van een speciaal daarvoor ontworpen glas-epoxy composieten flexibele schroef met een doorsnede van 1 m gemeten tijdens ware grootte metingen. Ten behoeve hiervoor is er door het MARIN een meetopstelling gemaakt inclusief hiervoor ontwikkelde hardware en software. Tijdens de metingen zijn de bladvervorming voor twee bladen gemeten in drie posities. De resultaten laten zien dat de respons van de twee bladen bijna identiek is, wat vertrouwen geeft in de nauwkeurigheid van het productieproces en de meetmethode. Het vergelijken van gemeten en berekenende bladrespons laat zien dat de buigrespons van het blad goed voorspeld wordt door de PM-EEM-koppeling. De verschillen tussen de gemeten en berekende hoekverdraaiing zijn groter. Dit kan verklaard worden vanuit de onzekerheden in gemeten en berekende hoekverdraaiingen, welke relatief groot zijn omdat de hoekverdraaiing zo klein zijn.

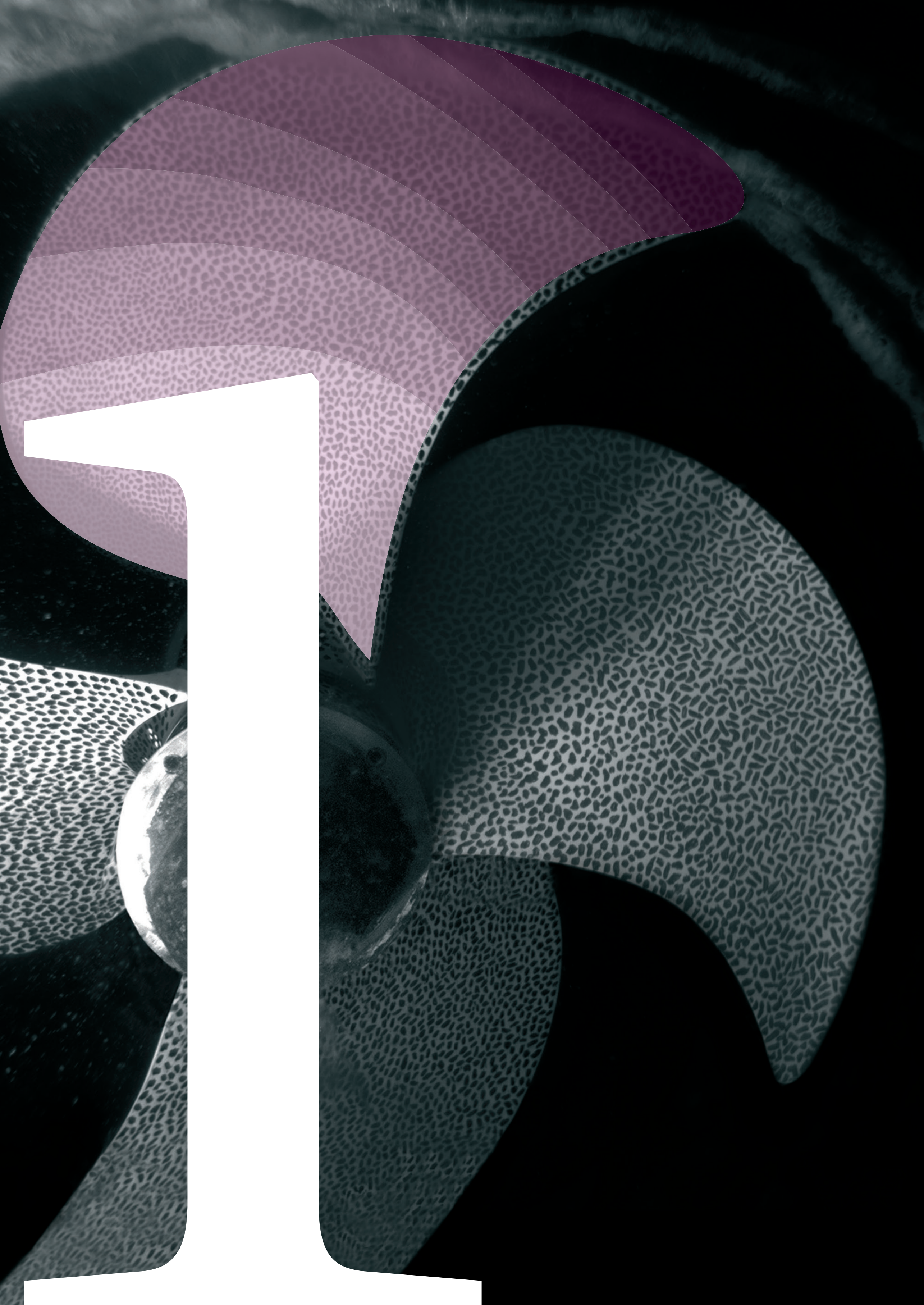

1

Chapter 1

Introduction

1.1. MOTIVATION

Since the introduction of the first marine propeller in the 19th century, revolutionary propeller designs have been developed throughout the years. One can think of super-cavitating and surface piercing propellers, but also counter rotating arrangements, etc. Already from the early days ship propellers have been made out of metals. The first use of fibre reinforced plastics, also called composites, for the propellers of Soviet fishing boats in the 1960s [1], can be certainly counted among the revolutionary developments in the field of marine propulsion as well. However, nickel-aluminium bronze (NAB) alloys have been remained the most common propeller material and composite propellers have been rarely applied. Although, over the last decades several examples of composite propellers have been reported [2-4], from which two are shown in Figure 1.1 and 1.2. It seems that composite propellers delight in a growing interest, given the increasing list of publications of last decade. This is not surprising given the clear benefits associated with the use of composite materials. Some benefits are inherent to composite material itself. Composites have a better corrosion resistance than metals [5]. Although the fatigue resistance of composite materials is difficult to quantify, it is generally acknowledged that the fatigue resistance of composites is better than that of metals [5]. An advantage, especially for navy applications, is the low magnetic signature of composites. Important drawbacks of composite materials are the lower cavitation erosion and impact damage resistance compared to NAB [6].

Figure 1.1: The composite propeller of the Triton (Photo: QinetiQ).

Figure 1.2: Composite propeller of the Alkmaar-class minehunter (Photo: Airborne Composites BV).

By fully exploiting the potential of composite materials, composite propellers may offer additional advantages on top of the aforementioned intrinsic benefits [2]. These advantages originate from the high strength to stiffness ratio of composite materials and the ability to optimize the laminate stiffness properties by tailoring ply orientations, fibre volume fraction and stacking sequence. In that way designs of flexible composite propellers have been made [7–9], which passively adapt to variations in fluid loading. Promising performance improvements have been asserted for hydro-elastic tailored flexible composite propellers. For instance, noise, cavitation or fuel reductions of up to 15% have been claimed [2]. Therefore, adaptive composite marine propellers have been indicated as a possible solution to the (foreseen) tightening of international legislation concerning emissions of CO_2, NO_x, particulate matters and underwater radiated noise [10].

The analysis of flexible composite propellers involve a fluid-structure interaction (FSI) calculation. Basically two approaches can be considered in FSI computations. The partitioned approach is based on separately solving fluid and structural sub-problem, where the interaction between the fluid and structural solution is maintained by performing coupling iterations between the two solvers. In a monolithic approach fluid and structural problem are simultaneously solved. For the hydro-elastic analysis of flexible propellers in uniform flows partitioned approaches have been presented, among others in [8, 11–19]. Since marine propellers usually operate in non-uniform wakefields, a method able to predict the unsteady hydro-elastic response would be more appropriate. Such unsteady methods have been developed as well, but are outnumbered by steady methods. A kind of monolithic unsteady approach has been presented in [20]. However, small blade deformations have been assumed, which seems to be a necessary assumption for the analysis of such a complicated problem in a monolithic framework. Furthermore, the method is limited to sub-cavitating conditions. Partitioned methods for the unsteady hydro-elastic analysis of flexible propellers have been presented as well [21–23]. An advantage of such a partitioned approach is that the structural problem may have been coupled to a black-box fluid solver able to model cavitating conditions as well, like in [23]. Important differences in fluid-structure coupling can be noticed between the different approaches, particularly, on how fluid stiffness, damping and added mass have been included in the analyses. Sometimes assumptions regarding those contributions have been adopted which may limit the generality of the methods. For instance fluid stiffness effects have been ignored and only fluid added mass and hydrodynamic damping contributions have been included [20]. In another method the hydrodynamic lift induced damping has been neglected by coupling the structure to an acoustic medium [21, 22]. Fluid stiffness effects have been accounted for by performing coupling iterations between a potential flow solver and the structural solver [21]. This is similar to [23], but in the latter work fluid velocity and acceleration effects have been included by deriving closed form expressions for fluid damping and added mass and adding those contributions to the structural damping and mass matrix. However, the derivation of the closed form expressions comprises several assumption including the assumption of small blade deformations [23].

In order to fully exploit the benefits that flexible composite propellers may offer, it is required to have a validated computational method for FSI, being able to accurately predict the hydro-elastic response of flexible propellers in uniform and non-uniform wakefields, for large blade deformations and cavitating and non-cavitating conditions. For that reason this study has been conducted.

1.2. RESEARCH OBJECTIVE

The objective of this study is to develop and validate a coupled BEM-FEM method for the hydro-elastic analysis of highly flexible composite propellers, showing large blade deformations, and operating in open-water and behind ship conditions. This work is limited to sub-cavitating conditions, but the method has to be easily expandable towards cavitating conditions as well.

APPROACH

It seems hardly possible to reach the goal of this study with a monolithic method. Such a method would comprise important simplifications and modelling of cavitation would be extremely difficult. Therefore, a partitioned approach has been adopted in which two existing black-box solvers have been coupled. The structural problem has been solved with the finite element method (FEM). The commercial FEM software Marc/Mentat has been used for this purpose. For flow modelling a boundary element method (BEM) was selected. BEM methods perform well for propeller calculations. They capture the most important flow details for many cases and are computationally cheap compared to viscous flow solvers, making them well suited for FSI calculations [5]. In this work the BEM method PROCAL has been used. PROCAL has been developed by the Maritime Research Institute Netherlands (MARIN) for the Cooperative Research Ships (CRS) for uniform and non-uniform propeller analysis in sub-cavitating and caviting conditions [24, 25] and has been adapted by the author for flexible propeller analyses. These adaptations to the BEM software have been based on a separate study because the BEM modelling of flexible propellers is not straightforward and involves several important modelling decisions.

In order to preserve all the PROCAL features for flexible propeller calculations and not to restrict the method to limited blade deformations, a fully partitioned approach has been adopted. Thus far, a full separation of fluid and structural problem for unsteady propeller calculations has not been applied. The most likely reason for this is the strong fluid-structure coupling in marine propeller FSI analyses. This requires a dedicated partitioned solution method to keep the process of alternately solving fluid and structural sub-problem stable. For the sake of stability a new approach for periodic FSI problems has been developed.

THESIS OUTLINE

The main body of this thesis (i.e. Chapter 2 to 6) is basically a collection of four scientific articles which have been published or submitted for publication. Chapter 2 to 4 have been based each on one article. Minor changes have been made to these articles in order to fit them into this thesis as separate chapters. Both Chapter 5 and 6 have been based on a fourth article. In Chapter 6 results have been included which were not included in that article.

In Chapter 2 the focus is on the structural modelling of composite propeller blades. The main contributions of this chapter are that it proposes a method to define the element dependent fibre orientations for the FEM modelling and that it shows a set-up how the stiffness properties of composite propeller blades could be verified.

Chapter 3 presents the BEM-FEM coupling for open-water conditions including a validation study. The fluid and structural sub-problems have been separately solved and coupling iterations have been accomplished to converge to the hydro-elastic solution. Since the BEM software PROCAL enables to model cavitation, the method can be used for cavitating conditions as well. In order to provide insights into the errors originating from the potential flow modelling, results obtained with the BEM-FEM coupling have been compared to results obtained from a higher fidelity FSI coupling between a Reynolds-Averaged Navier-Stokes solver and FEM. All the numerical results have been compared to experimental results obtained from blade deformation measurements in cavitation tunnel tests.

Thus far, there seems no clear consensus about the FSI modelling of flexible propellers in behind ship conditions, given the different assumptions which have been adopted in the methods as stated before. An important reason for this may be the lack of literature about the governing parameters in the fluid and structural modelling of flexible propeller blades. Chapter 4 aims to fill this gap. In that chapter it has been explained that fluid and structural response are characterized by reduced frequency and structural frequency ratio (i.e. the ratio between the fundamental blade natural frequency and excitation frequency). For both dimensionless quantities, general expressions have been derived. The second part of Chapter 4 contains a study in which different modelling options have been evaluated, like a quasi-static approach and the modelling of fluid acceleration and velocity effects with closed form expressions for fluid added mass and hydrodynamic damping.

Chapter 5 presents the BEM-FEM coupling method for behind ship conditions. In this method the fluid and structural sub-problems have been separately solved and a new approach as detailed in Appendix A has been used to perform coupling iterations on a periodic level, i.e. per revolution, rather than per time step. Chapter 6 presents a comparison of numerical results calculated with the BEM-FEM coupling for non-uniform flows with experimental results obtained from model scale laboratory experiments and full-scale measurements.

The last chapter reviews the main contributions and conclusions of this thesis and gives recommendations for future work.

REFERENCES

[1] A. Mouritz, E. Gellert, P. Burchill, and K. Challis, "Review of advanced composite structures for naval ships and submarines," *Composite Structures*, vol. 53, pp. 21–41, 2001.

[2] G. Marsh, "A new start for marine propellers?," *Reinforced Plastics*, vol. 48, no. 11, pp. 34–38, 2004.

[3] "Benefits of carbon composite marine propeller." `http://classnk-rd.com/pdf/katsudou201511_D.pdf`. Accessed on 13 July 2018.

[4] A. Brødsjø and P. Putting, "The design and manufacturing of a RTM composite propeller for a navy vessel," Tenth International Conference on Textile Composites, Lille, France, 2010.

[5] Y. Young, M. Motley, R. Barber, E. Chae, and N. Garg, "Adaptive composite marine propulsors and turbines: Progress and challenges," *Applied Mechanics Reviews*, vol. 68, no. 6, p. 060803, 2016.

[6] T. Yamatogi, H. Murayama, K. Uzawa, K. Kageyama, and N. Watanabe, "Study on cavitation erosion of composite material for marine propeller," 17th International Conference on Composite Materials, Edinburgh, Scotland, 2009.

[7] C. Lin, Y. Lee, and C. Hung, "Optimization and experiment of composite marine propellers," *Composite Structures*, vol. 89, no. 2, pp. 206–215, 2009.

[8] J. Blasques, C. Berggreen, and P. Andersen, "Hydro-elastic analysis and optimization of a composite marine propeller," *Marine Structures*, vol. 23, no. 1, pp. 22–38, 2010.

[9] Y. Lee and C. Lin, "Optimized design of composite propeller," *Mechanics of Advanced Materials and Structures*, vol. 11, no. 1, pp. 17–30, 2010.

[10] P. Maljaars, "Hydro-elastic analysis of flexible propellers: An overview," Fourth International Symposium on Marine Propulsors, Austin, TX, USA, 2015.

[11] N. Mulcahy, B. Prusty, and C. Gardiner, "Hydroelastic tailoring of flexible composite propellers," *Ship and Offshore Structures*, vol. 5, no. 4, pp. 359–370, 2010.

[12] T. Taketani, K. Kimura, S. Ando, and K. Yamamoto, "Study on performance of a ship propeller using a composite material," Third International Symposium on Marine Propulsors, Launceston, Australia, 2013.

[13] S. Solomon Raj and P. Ravinder Reddy, "Bend-twist coupling and its effect on cavitation inception of composite marine propeller," *International Journal of Mechanical Engineering and Technology*, vol. 5, no. 9, pp. 306–314, 2014.

[14] J. Kuo and W. Vorus, "Propeller blade dynamic stress," pp. 39–69, Tenth Ship Technology and Research (STAR) Symposium, Norfolk, VA, USA, 1985.

[15] D. Georgiev and M. Ikehata, "Hydro-elastic effects on propeller blades in steady flow," *Journal of the Society of Naval Architects of Japan*, vol. 184, pp. 1–14, 1998.

[16] H. Ghassemi, M. Ghassabzadeh, and M. Saryazdi, "Influence of the skew angle on the hydro-elastic behaviour of a composite marine propeller," *Journal of Engineering for the Maritime Environment*, vol. 226, no. 4, pp. 346–359, 2012.

[17] P. Maljaars and J. Dekker, "Hydro-elastic analysis of flexible marine propellers," in *Maritime Technology and Engineering* (C. Guedes Soares and T. Santos, eds.), pp. 705–715, CRC Press-Taylor & Francis Group: London, UK, 2014.

[18] P. Atkinson and E. Glover, "Propeller hydro-elastic effects," Propellers '88 symposium, SNAME, Virginia Beach, VA, USA, 1988.

[19] H. Lin and J. Lin, "Nonlinear hydroelastic behavior of propellers using a finite element method and lifting surface theory," *Journal of Marine Science and Technology*, vol. 1, no. 2, pp. 114–124, 1996.

[20] L. Jiasheng, Q. Yegao, and H. Hongxing, "Hydroelastic analysis of underwater rotating elastic marine propellers by using a coupled BEM-FEM algorithm," *Ocean Engineering*, vol. 146, no. 1, pp. 178–191, 2017.

[21] H. Lee, M. Song, J. Suh, and B. Chang, "Hydro-elastic analysis of marine propellers based on a BEM-FEM coupled FSI algorithm," *International Journal of Naval Architecture and Ocean Engineering*, vol. 6, no. 3, pp. 562–577, 2014.

[22] X. He, Y. Hong, and R. Wang, "Hydroelastic optimisation of a composite marine propeller in a non-uniform wake," *Ocean Engineering*, vol. 39, pp. 14–23, 2012.

[23] Y. Young, "Fluid–structure interaction analysis of flexible composite marine propellers," *Journal of Fluids and Structures*, vol. 24, no. 6, pp. 799–818, 2008.

[24] G. Vaz, *Modelling of sheet cavitation on hydrofoils and marine propellers using boundary element methods*. PhD thesis, Instituto Superior Técnico, Lisbon, Portugal, 2005.

[25] G. Vaz and J. Bosschers, "Modelling of three dimensional sheet cavitation on marine propellers using a boundary element method," Sixth International Symposium on Cavitation, Wageningen, The Netherlands, 2006.

2

Chapter 2

Finite element modelling and model updating of composite propellers

It is beyond all doubt that for an accurate finite element method (FEM) model of a composite propeller a correct modelling of the fibre orientations and material properties are required. Both subjects have been addressed in this chapter. An approach will be presented in order to accurately define the element dependent fibre orientations in doubly curved geometries like marine propeller blades. In order to improve the structural response prediction this chapter presents an inverse method based on experimental and numerical results which can be used for structural identification and FEM model updating. In the developed approach the residual between measurement results obtained with static experiments and results obtained with a FEM model is minimized by adapting the stiffness properties in the FEM calculation. This method has been successfully applied to two small-scale composite propellers. The obtained material properties have been determined with a relatively high confidence level. A verification by means of measured and calculated natural frequencies show also that accurate results were obtained with the inverse method.

This chapter is based on the journal paper: P. Maljaars, M. Kaminski and J. den Besten, "Finite element modelling and model updating of composite propellers," *Composite Structures,* vol. 176, pp. 154–163, 2017.

2.1. INTRODUCTION

The strength and stiffness of polymer composite structures depend on the orientation and distribution of fibres in the material. For that reason composite forming simulations have been developed in order to establish the orientation, distribution and wrinkling of fibres after draping into moulds, see for instance [1–3]. For an accurate response estimate of a composite structure the actual fibre orientation and distribution have to be correctly represented in a structural model. Correct modelling of the fibre orientations has been addressed in [4]. It has been proposed to develop a solid element model by extruding a shell element model with correct orientations. This method has been applied for the calculation of stresses in a gas turbine engine vane. The results show the significant effects of an accurate definition of fibre orientations in the finite element method (FEM) analysis of (doubly) curved geometries. The necessity of a FEM solver with functionality to extrude shell elements and an existing shell element model with correct orientations seems to be limitations of this method.

This chapter aims to present an accurate method without the aforementioned limitations, applicable to determine the material orientations in doubly curved solid FEM models, like marine propeller- and wind turbine blades.

Another important factor for accurate FEM modelling is the use of correct model input parameters. When destructive measurements are undesirable the input parameters could be deduced by solving an inverse problem. In the inverse problem model input parameters are obtained by combining experimental and model results. This special application of inverse methods is known as a mixed numerical-experimental technique (MNET). Since the nineties many papers have been published on the application of MNETs for mechanical problems, but these methods can be used for any other field if an accurate and sensitive experimental method is available and a good theoretical model exists [5]. Many different approaches are presented in literature for model updating by using MNETs, see for instance the references made in [6–9]. According to [10] all the different approaches for model updating can be divided into two main categories: deterministic methods and probabilistic model updating methods, where the first one is the most common approach [6]. An important drawback of the deterministic approach is the non-uniqueness of the solution which might occur especially when having a large number of updating parameters and an insufficiently large data set. A drawback of probabilistic methods is the mathematical complexity, but these methods can handle the non-uniqueness of the solution [6]. Examples of applications of model updating by means of deterministic and probabilistic approaches can be found in [11–16].

Another overview of MNET approaches can be based on the type of the experiments, either static or dynamic. Dynamic experiments seem to be preferred in literature. This could be attributed to the fact that with dynamic experiments natural frequencies can be efficiently obtained which are much more sensitive parameters than output parameters obtained from static experiments, according to [5]. However, with dynamic testing one is restricted to a global structural response, while static tests can be used to determine parameters that influences both global and local structural behaviour [17].

In [11] modal analysis measurements have been performed on a composite blade of a small sized wind turbine. An optimisation algorithm has been used to minimize the residual between measured and calculated natural frequencies and modes by adjusting the material properties. A similar approach, but on a much larger scale has been presented in [14]. In comparison to [11, 14], the blades considered in this work are of much smaller size and static measurements instead of dynamic experiments have been conducted.

2.2. PROPELLERS

The two considered propellers, (Figure 2.1), have a diameter of 0.34 m and the same geometry and glass-epoxy laminate lay-up, but differ with respect to the laminate orientation of the composite blades. For identification the propellers and the blades have been numbered as follows:

- Propeller 45: [+45°/-45°] laminate lay-up.
- Propeller 90: [0°/90°] laminate lay-up.
- Blade number 1 and 2 are designated to the upper and bottom blade, respectively, (Figure 2.2).

The 0°-direction of the laminae is parallel to the *z*-axis of the propeller blade coordinate system of Figure 2.2, where positive *x*-, *y*- and *z*-axis are pointing forward, portside and upwards, respectively. All the results are presented according to this coordinate system.

The design values for Young's moduli, *E*, Poisson ratios, *v*, and the shear moduli, *G*, of the composite laminates are given in Table 2.1.

	E_{11} **[GPa]**	E_{22} **[GPa]**	υ_{12} **[-]**	G_{12} **[GPa]**
[+45°/−45°]	8.92	8.92	0.589	8.31
[0°/90°]	18.8	18.8	0.132	2.81

Table 2.1: Design values for the [+45°/-45°] and [0°/90°] laminate in-plane elastic properties.

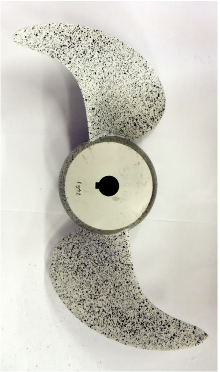

Figure 2.1: Image of one of the two-bladed propellers.

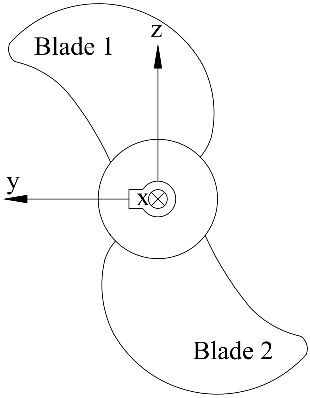

Figure 2.2: Propeller blade coordinate system; *x*-, *y*-, *z*-axis positive to upstream, portside and top, respectively.

2.3. EXPERIMENTS

This section describes the experiments which have been executed to obtain a dataset to be used in the mixed numerical experimental technique as presented in Section 2.5. The measurements were carried out at and cooperation with Maritime Research Institute Netherlands (MARIN).

2.3.1. SELECTED TYPE OF EXPERIMENTS

For this work static experiments have been selected for the following reasons:

- Results of the sensitivity study presented in Section 2.4.4 show that output parameters obtained from static experiments could be very sensitive.
- There were uncertainties on the practicability to obtain sufficient and accurate data with dynamic tests.
- Local information of the tip region can be more easily obtained with static experiments. It can be expected that the stiffness of the tip region will dominate the blade structural response since the propeller tips are very flexible compared to the stiffness of the remaining blade body part.

2.3.2. MEASUREMENT SET-UP

For the static experiments a turning lathe was used as measurement set-up, (Figure 2.3). The propellers were mounted on a shaft clamped in the fixed chuck jaws. On the carriage of the turning lathe a load cell with a PVC ball was mounted, such that by moving the carriage a force was applied on the propeller blades by the PVC ball. With Hertzian contact theory a design for the PVC ball has been made such that the contact stresses of the propeller blades would not exceed the maximum allowable compressive stress. For a radius of 20 mm this criterion was satisfied.

Figure 2.3: Measurement set-up for the static tests.

2.3.3. MEASUREMENT TECHNIQUE

In the static tests the applied force and the structural response of the blades have been measured. The force was measured with a 1 kN force transducer with an accuracy of 0.4 N. The spatial distribution of the suction side propeller blade structural response was measured with a digital image correlation (DIC) technique. With a DIC technique a very accurate recording of the blade displacement field could be achieved. A general value for the 95% confidence interval of the measured deformations is 25 μm. DIC is a full-field image analysis method, based on grey value digital images that finds the displacements and deformations of an object in three dimensional space [18, 19]. The method tracks the grey value pattern from which the deformations of the blades were calculated using the Vic3D software. In the post-processing of the image data a procedure was implemented to correct for blade displacements induced by deformations and displacements of the shaft. In order to use the DIC technique, the object surface needs to contain a random speckle pattern with no preferred orientation and sufficiently high contrast. In Figure 2.1 one of the speckled propellers is shown.

2.3.4. SELECTED LOADING CONDITIONS

As shown in Section 2.4.4 only the in-plane material properties are sensitive parameters and could be determined with an MNET. To identify the four in-plane material properties at least four responses with their variation directly attributing to the variation of these parameters are necessary. To be on the safe side two additional loading conditions have been selected. The tip region is the most interesting blade part to investigate since the stiffness of the tip will dominate the blade structural response. The six loading conditions have been selected such that on average the tip structural response dominates, being sensitive to all the in-plane material properties, according to the results presented in Section 2.4.4. The selected points are depicted and denoted in Figure 2.4. The maximum loads have been determined such that the propeller blade stresses are below the maximum allowable stress and that the responses obtained for different loading conditions have similar magnitude in order to avoid biasing of one of the loading conditions.

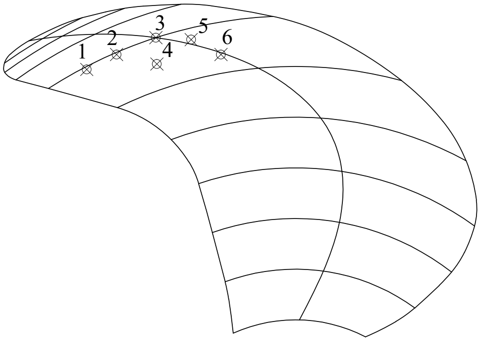

Figure 2.4: Selected points for the six loading conditions.

2.4. FEM MODELLING OF THE PROPELLERS

This section describes how the propellers have been modelled in FEM. Special attention has been paid to define the material orientations. A new approach is presented to model the material orientations in the propeller blades.

2.4.1. GEOMETRY REPRESENTATION OF THE PROPELLER

For FEM modelling and calculations Marc/Mentat has been used. The FEM models consist of one propeller blade without the hub part. The stiffness contribution of the hub has been modelled by a full clamping of the propeller blade at the blade-hub interface. The underlying assumption is that the stiffness of the hub is much higher than the stiffness of the blades, [20–22].

The propeller blades could be discretised using solid or shell elements. A disadvantage of a shell element model is that interlaminar stresses cannot be obtained, in contrast to solid elements. Another advantage of solid elements is that a better description of the actual geometry can be obtained.

In this work solid elements have been applied. Quadratic solid elements were preferred over linear elements since linear elements require many elements in through-thickness direction in order to accurately model the bending dominated blade response.

For the computations a 58 × 60 × 4 element distribution was used. This means that 58 elements are placed along the chord of the propeller, 60 panels in radial direction and 4 elements in through-thickness direction. From convergence perspective a 29 × 30 × 4 mesh would be sufficient. However, the finer mesh with four times more contact nodes was used in order to obtain a smoother representation of the structural response in the FEM contact analyses.

2.4.2. MATERIAL ORIENTATIONS

In Section 2.1 the importance of a proper material orientation for doubly curved structures has been described. Standard commercial FEM software packages are usually not able to define unambiguously the material orientations in complex geometries [4]. Local element coordinate systems are usually available in FEM software packages. With this feature the through-thickness material orientation can be directed perpendicular to the outside surface of the elements. However, the alignment of the two other material axes will depend on the orientation of the element itself (Figure 2.6a). This can result in an erroneous material orientation and a misprediction of the structural stiffness. To determine for each element the material orientation a new approach has been developed in which the following steps have been taken.

A known direction is the through-thickness material orientation which is the normal to the element surface, (direction three of Figure 2.5). The first and second direction are in plane of the element surface. For a propeller in the blade coordinate system (Figure 2.2), it can be assumed that one of the principal material directions will be in the x-y plane (Figure 2.5), since the blade is slightly curved in radial direction. Then, the second material direction is the intersection between the plane of the element surface and the x-y plane. This is in essence the projection of the 90°-direction unto the element. Then, the first direction of Figure 2.5 can be found by taking the outer product between the trough-thickness material direction and the second material direction. In case of a single curved geometry this approach results in the correct orientations. In case of doubly curved geometries it depends on the assumption of the second plane. The developed element dependent material orientation has been, if not explicitly stated, used for all the FEM calculations.

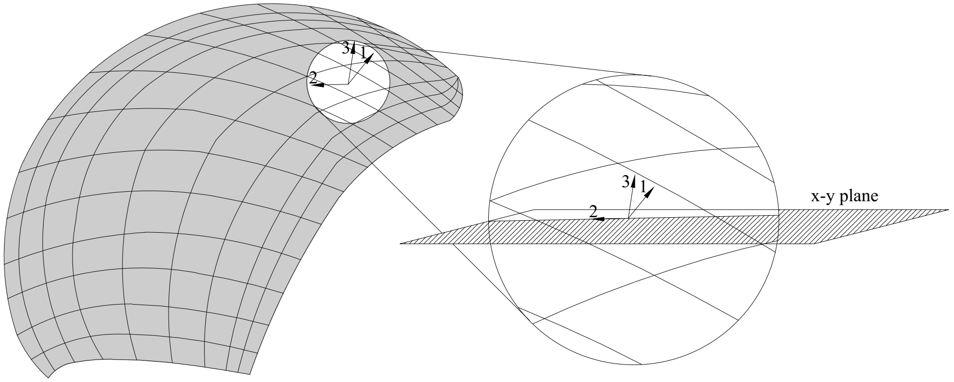

Figure 2.5: Determination of the material orientations.

A small comparative study has been performed between a FEM model with the material orientations based on the local element coordinate system and the developed element dependent material orientations. The typical difference between these two material orientations has been sketched in Figure 2.6.

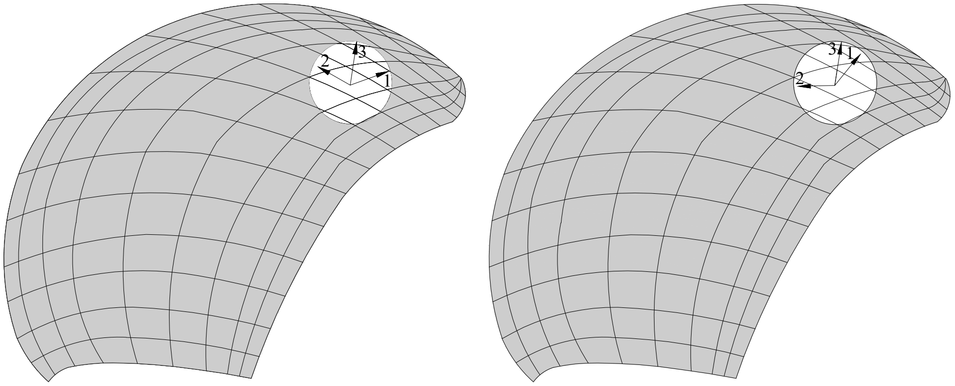

(a) Material orientations based on local element coordinate system.

(b) Developed element dependent material orientations.

Figure 2.6: Differences between the two material orientations.

Results of calculated natural frequencies of the FEM models with the two different material orientations are presented in Table 2.2. Relatively large differences in natural frequencies have been obtained for the first two modes. Depending on the meshing procedure, larger differences could be expected when the propeller geometry contains more skew or when the material is more anisotropic.

Mode	**Local Material Orientation**	**Developed Material Orientation**	**Difference %**
1	495	474	4.4
2	704	654	7.6
3	1283	1267	1.3

Table 2.2: Natural frequencies [Hz] for propeller 45 calculated with the two different FEM models.

2.4.3. LOAD CASES AND BOUNDARY CONDITIONS

Contact analyses have been selected to model the experiments in FEM. The PVC ball which was used to apply static loads on the blades has been modelled as an undeformable body. Analyses have been performed with and without friction. A friction coefficient of 0.3, as a common value for friction between two polymers, has been adopted for the analyses with friction included.

Displacement constraints in y- and z-direction were applied on the PVC ball, because the static load was only applied in x-direction. On the blade itself, displacement constraints have been imposed on the intersection area between blade and hub in order to model the blade-hub connection.

2.4.4. SENSITIVITY STUDY

Sensitivity studies have been performed with the FEM models in order to select different loading conditions which show high sensitivity for at least one stiffness parameter, such that all the stiffness parameters are sensitive in at least one loading condition. The sensitivity study has been conducted to investigate the differences in sensitivities between natural frequency results and static test data as well.

In this sensitivity study the different stiffness parameters have been systematically changed in order to investigate their dependency on the response of the FEM model. The sensitivities were approximated using a forward finite difference technique. This has been performed by using the results of two FEM analyses for two states of a stiffness parameter P_j,

$$S_j = \frac{R_j\left(P_j + \Delta P_j\right) - R_j\left(P_j\right)}{\Delta P_j} / \frac{R_j\left(P_j\right)}{P_j} \tag{2.1}$$

In this equation S_j denotes the relative variation of the output (deformations or natural frequencies) due to a relative difference of an input parameter P_j. Relative sensitivities have been used instead of the actual sensitivities $\frac{\Delta R_j}{\Delta P_j}$ since the sensitivities of different calculations (natural frequency analysis and contact analysis) with different output parameters have to be compared. The output parameters for the natural frequency analyses are the first six natural frequencies. The output parameters for the contact analyses are the norm of the structural blade response, $\|\mathbf{u}_i\|$ for the six loading conditions, i defined in Section 2.3.4.

The sensitivities of the natural frequencies and the static output parameters of propeller 45 and 90 are presented in Figure 2.7 and 2.8 respectively, from which the following conclusions can be drawn:

- The through-thickness properties (E_{33}, G_{23}, G_{13}, μ_{23}, μ_{13}) of the laminate are hardly sensitive. Therefore, the sensitivities of these material properties are not shown in Figure 2.7 and 2.8, because it can be expected that these properties cannot be accurately deduced with an MNET using the selected loading conditions.

- The in-plane Poisson ratio (μ_{12}) of propeller 90 is hardly sensitive, it is expected that this stiffness property cannot be accurately determined with an MNET using the selected loading conditions.

- The average sensitivities of the in-plane stiffness properties for the contact analyses are larger than for the natural frequency analyses, especially for propeller 90. In contrast to what is stated in [5] this advocates the use of static data in the MNET.

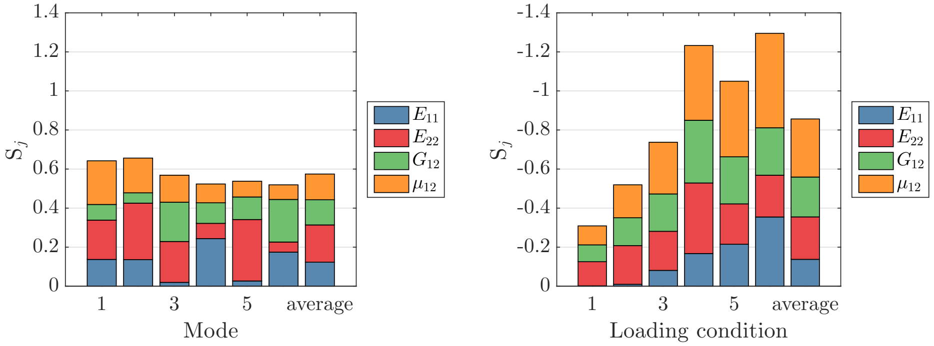

(a) Natural frequency analysis.

(b) Contact analysis.

Figure 2.7: Relative sensitivities of the in-plane material properties for propeller 45, an increase of stiffness results in an increase of natural frequeny and a decrease of deformations, indicated by respectively the positive and negative sign.

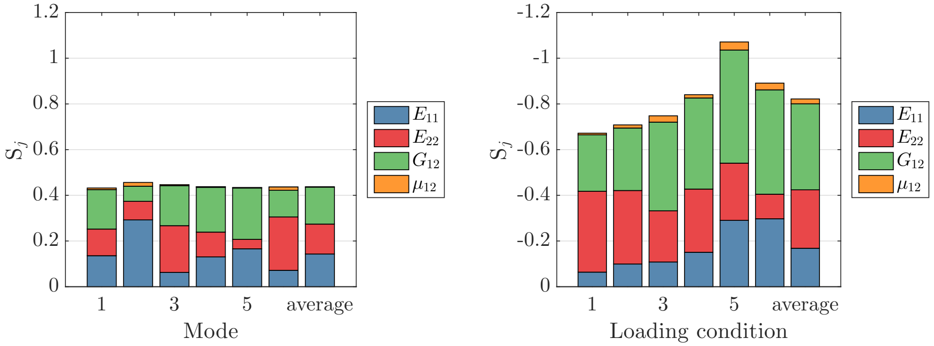

(a) Natural frequency analysis.

(b) Contact analysis.

Figure 2.8: Relative sensitivities of the in-plane material properties for propeller 90, an increase of stiffness results in an increase of natural frequeny and a decrease of deformations, indicated by respectively the positive and negative sign.

2.5. THE MIXED NUMERICAL EXPERIMENTAL TECHNIQUE

A deterministic model updating method has been developed in order to identify the stiffness parameters of the propeller blades. Figure 2.9 shows a flow chart of the developed approach. In the MNET the experimental data obtained from the static tests have been combined with the FEM model as presented in Section 2.4. After measuring of the structural response the results have to be transformed to the blade coordinate system. Before calculating the residual between measured and calculated displacement field the calculated displacement field has been interpolated. Subsequently, an optimisation algorithm of Matlab is used to minimize the residual by varying the stiffness parameters until a converged result is obtained. The interpolation of the FEM results, the transformation of the measured deformations and the optimisation algorithm will be explained in more detail in the next subsections.

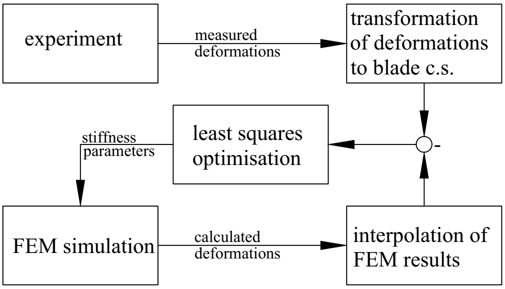

Figure 2.9: Flow chart of the applied mixed numerical experimental approach.

2.5.1. INTERPOLATION OF THE FEM RESULTS

Considering the contact non-linearity in the structural response, a cubic spline interpolation has been applied in order to obtain the calculated deformations at the same load sampling points as the measurements. In the order of 10^3 points describe the calculated displacement field, compared to $10^5 - 10^6$ points for the measurements. In order to exploit the resolution of the measured displacement field, a second interpolation has been applied to increase the resolution of the calculated displacement field with one order of magnitude. This increase of the resolution show an improvement of the results obtained with the MNET (i.e. the 95% confidence interval became smaller).

2.5.2. TRANSFORMATION OF THE MEASURED DEFORMATIONS

By post-processing the DIC images the measured deformations have been defined in the image correlation coordinate system. However, the relative position and orientation of this coordinate system to the blade coordinate system was not exactly known. Therefore, the measured undeformed blade geometry has been mapped on the design geometry as drawn in the blade coordinate system. The mapping problem has been formulated as an optimization problem in which the transformation between the two coordinate systems is determined by minimizing the objective function $f(\mathbf{x})$,

$$\min_{\mathbf{x}} f(\mathbf{x}) = \sum_i F_i^2(\mathbf{x}) \tag{2.2}$$

In this case the objective function is the sum of squares of the differences between the coordinates of the sampling points in the undeformed measured geometry and design geometry as drawn in the blade coordinate system, $\sum F_i^2(\mathbf{x})$.

2.5.3. OPTIMISATION ALGORITHM

For the mapping problem and in the MNET the same optimisation algorithm of Matlab has been used. Both problems are very similar; either a residual between two geometries or a residual between two displacement fields has to be minimized. In case of the MNET the term $\sum F_i^2(\mathbf{x})$ in Eq. (2.2) is the sum of squares of the residuals between measured and calculated deformations at the sampling points. The 'lsqnonlin' algorithm available in the optimization toolbox of Matlab has been used to solve the minimization problems. This algorithm is dedicated to solve non-linear least-squares problems with a vector of residuals to be minimized rather than the sum of squares.

2.6. RESULTS

Results of three different analyses performed with the MNET as specified in Table 2.3, will be presented in this section. The results of the analyses will be compared to each other with respect to the final l^2 norm of the residual. Furthermore the l^2 norms of the results will be compared to the l^2 norms obtained with the design stiffness properties. Finally, the model updating with the MNET will be verified by comparing measured and calculated natural frequencies of the blades.

Analysis	**No. of Optim. Variables**	**Friction**
A	4	Yes
B	3	Yes
C	3	No
D	NA	No
E	NA	Yes

Table 2.3: Analysis A to C specifies the different MNET analyses, analysis D and E are calculations with the design material properties.

2.6.1. RESULTS OF THE MNET ANALYSES

Based on the results of the sensitivity study it has been decided to perform MNET analyses with the in-plane Young's and shear moduli as optimisation variables and also analyses with the in-plane Poisson ratio as additional variable, both analyses with friction included. For the stiffness parameters not used as optimisation variables the design values have been adopted. In order to check the influence of friction on the estimated stiffness properties, an analysis without friction has been conducted as well. The results of the different analyses are presented in Figure 2.10 and 2.11. The results show that:

- The 95% confidence bounds are generally between the 5% and 10% of the estimated mean values, except for the Poisson ratio. Especially for propeller 90 the confidence bounds for the Poisson ratio are relatively high. This was already expected from the results of the sensitivity study.

- The estimated parameters for the different blades of propeller 90 are very similar, generally the difference is smaller than 10%. The differences between the results obtained for the blades of propeller 45 are larger.

- Friction results in a totally different estimate for the mean values, the results obtained with and without friction included, differ approximately 20%.

- The estimated parameters obtained from the analyses with 3 and 4 optimisation variables and friction included are very similar.

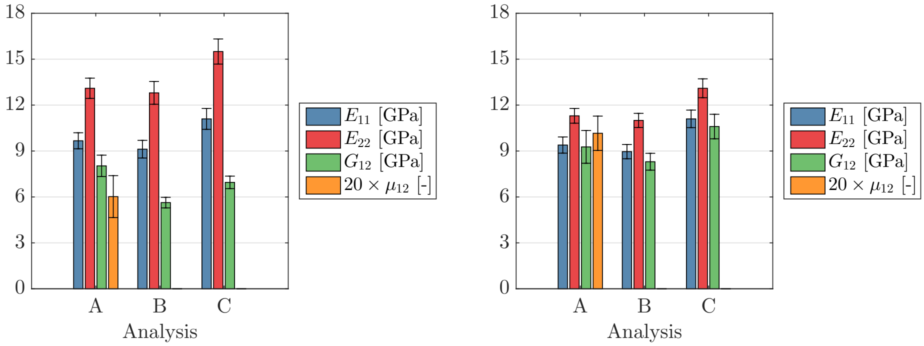

(a) Blade 1.

(b) Blade 2.

Figure 2.10: Mean values and 95% confidence bounds obtained for the in-plane stiffness properties of propeller 45 for three different MNET analyses.

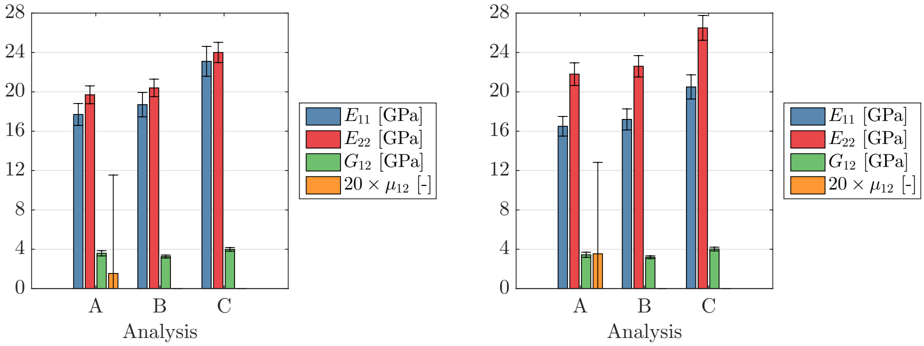

(a) Blade 1.

(b) Blade 2.

Figure 2.11: Mean values and 95% confidence bounds obtained for the in-plane stiffness properties of propeller 90 for three different MNET analyses.

In order to show the improvement of the resemblance between measured and calculated response the bending and pitch/twist deformations of propeller 90, blade 2 are depicted for the maximum load at each loading condition in Figure 2.12. This figure shows that the response calculated from the design material properties is already close to the measured response, but a further improvement is obtained with the MNET results.

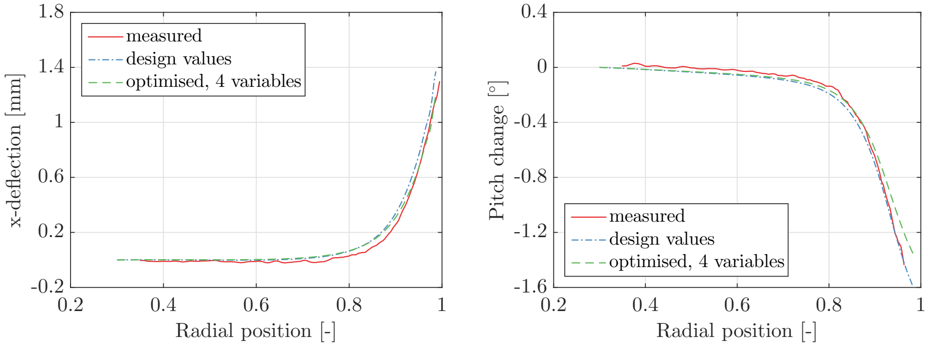

(a) Bend deformation, loading condition 1. (b) Twist deformation, loading condition 1.

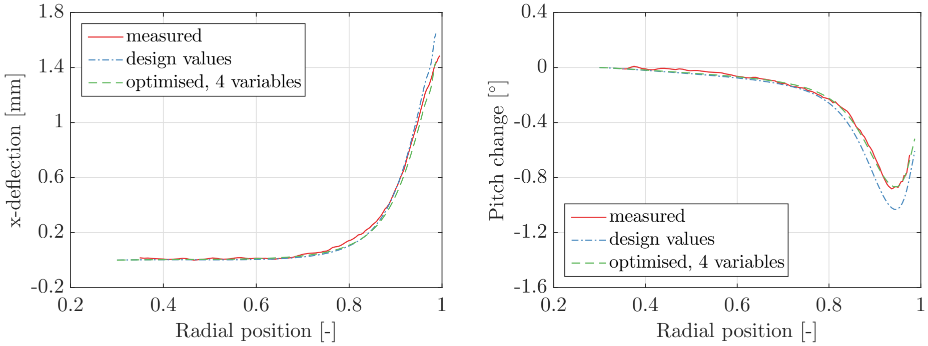

(c) Bend deformation, loading condition 2. (d) Twist deformation, loading condition 2.

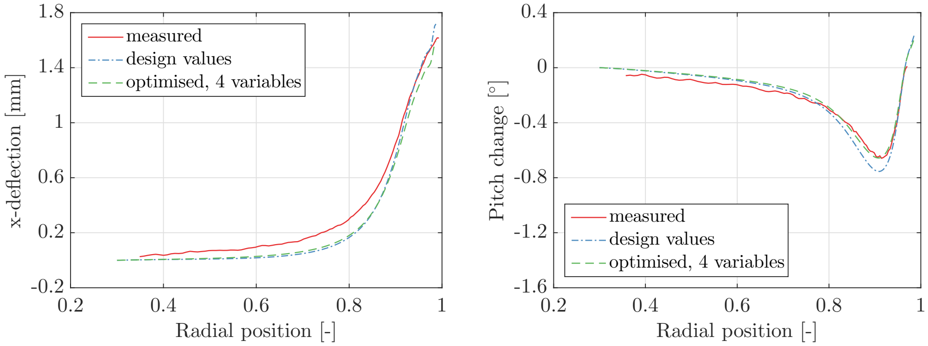

(e) Bend deformation, loading condition 3. (f) Twist deformation, loading condition 3.

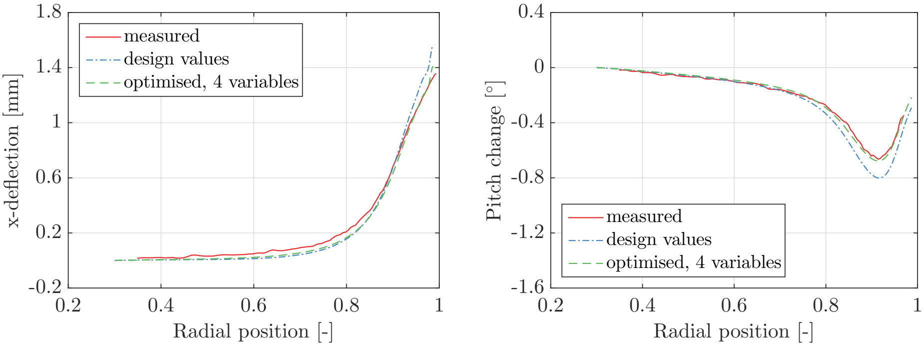

(g) Bend deformation, loading condition 4. (h) Twist deformation, loading condition 4.

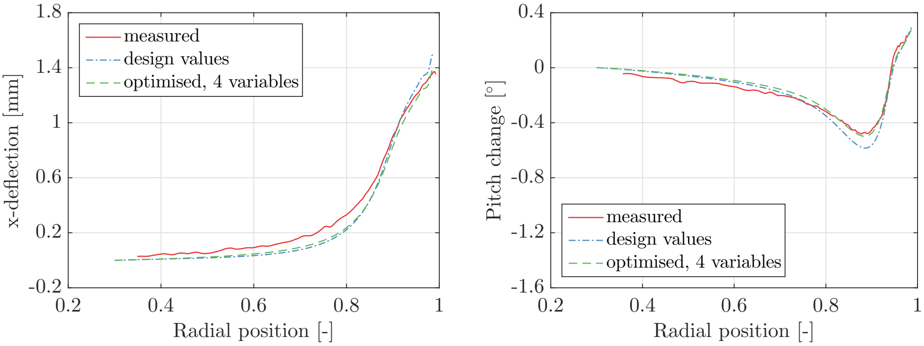

(i) Bend deformation, loading condition 5. (j) Twist deformation, loading condition 5.

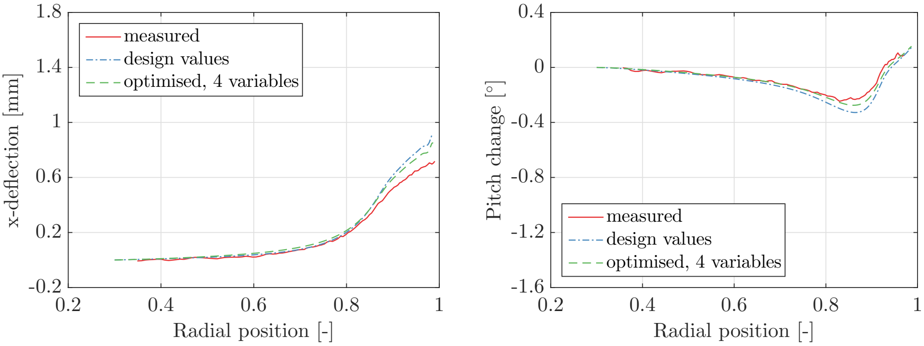

(k) Bend deformation, loading condition 6. (l) Twist deformation, loading condition 6.

Figure 2.12: Measured and computed bend and twist deformations of propeller 90, blade 2. Simulations have been conducted with the design material properties and the material properties obtained from analysis A.

2.6.2. COMPARISON OF THE RESULTS

The l^2 norms of the residuals between calculated and measured responses for different analyses have been presented in Figure 2.13. The results show that the l^2 norm of the residuals for the calculations based on the design parameters with friction included, are significantly smaller than without friction, meaning that the neglection of friction seems to be unreasonable. The l^2 norms of the residuals obtained with the different MNET analyses are very similar. The improvement of the resemblance between measurements and calculations is the highest for blade 2 of propeller 90. In order to explain this, the difference in the l^2 norm of the residual between analysis B and E has been presented for each loading condition in Figure 2.14. Overall, a reduction in the l^2 norm is obtained by applying the MNET. However, for all the four blades one or two loading conditions show individually an increase in the l^2 norm, while this increase in the l^2 norm is the smallest for propeller 90, blade 2. Larger inaccuracies in the static experiments of the other blades is a possible explanation for the highest reduction in the l^2 norm of the residual of propeller 90, blade 2.

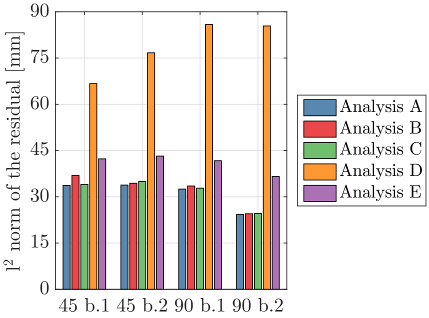

Figure 2.13: l^2 norms of the residuals between calculated and measured responses for analysis A to E.

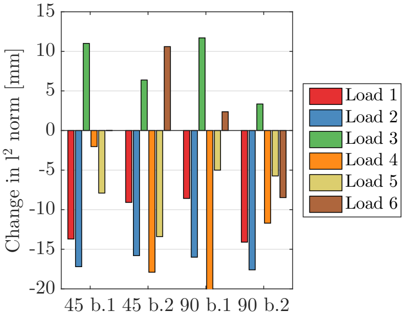

Figure 2.14: Difference in the l^2 norm per loading condition between analysis B and E.

2.6.3. VERIFICATION OF THE RESULTS

In order to verify the results obtained with the MNET, measured blade frequencies have been compared to calculated natural frequencies from FEM models with the design material properties and the material properties obtained from analysis A. For propeller 90 only the first natural frequency was experimentally determined. For propeller 45 two natural frequencies were measured. The results in table 2.4 show that the calculated frequencies are close to the measured frequencies. This confirms what is stated above that the actual material properties are close to the design material properties. More importantly, the small differences between measured natural frequencies and natural frequencies calculated from the material properties as computed with the MNET, show that good results have been obtained with the MNET.

Propeller	**45**				**90**	
Blade	1		2		1	2
Frequency of mode	1	2	1	2	1	1
Experiment	473	686	473	686	460	487
Design material properties	100%	95%	100%	95%	108%	102%
4 optim. variables	100%	102%	104%	102%	112%	105%

Table 2.4: Calculated blade natural frequencies as a percentage of the measured blade frequencies in [Hz].

2.7. CONCLUSIONS

This chapter presents the FEM modelling, a model updating method by means of an MNET and a comparison of experimental and numerical obtained structural response results for two small-scale composite propellers. For the FEM modelling of the blades an approach to determine the element dependent material orientations in doubly curved geometries has been developed. The advantage of the presented approach is that the in-plane material directions are independent of the orientation of the element itself, in contrast to material orientations aligned to the local element coordinate system. Natural frequency calculations show a significant difference between results obtained with the material orientations aligned to the local element coordinate system and the presented element dependent material orientations.

The FEM calculations have been combined in an MNET approach with an experimental static dataset in order to deduce non-destructively the blade (in-plane) material properties by minimizing the residual between measured and computed structural response. A sensitivity study has been performed to identify the differences between dynamic and static output parameters and to be able to select the loading conditions for the MNET analyses.

This chapter shows that it is possible to determine the stiffness properties of small-scale composite marine propeller blades by making use of an MNET based on static experiments and a deterministic approach. More specifically the following conclusions can be drawn. First of all, the MNET analyses result in reliable estimates for the in-plane material properties of the blades. This is also confirmed by the verification study in which calculated and measured natural frequencies have been compared. Secondly, by using the material properties obtained with the MNET, an improvement of the resemblance between measured and calculated structural response is obtained. This improvement is relatively small because the design material properties are already close to the actual material properties. Thirdly, the results show that friction has an important influence on the estimated results and cannot be neglected. Finally, the results of the sensitivity study show that static output parameters could be more sensitive parameters than natural frequency results.

REFERENCES

[1] B. Chen and M. Govindaraj, “A physically based model of fabric drape using flexible shell theory,” *Textile Research Journal*, vol. 65, pp. 324–330, 1995.

[2] R. ten Thije, *Finite element simulations of laminated composite forming processes.* PhD thesis, University of Twente, Enschede, The Netherlands, 2007.

[3] A. Willems, *Forming simulation of textile reinforced composite shell structures.* PhD thesis, University of Leuven, Leuven, Belgium, 2008.

[4] J. Chen, S. Hallet, and M. Wisnom, “Modelling complex geometry using solid finite element meshes with correct composite material orientations,” *Computers and Structures*, vol. 88, pp. 602–609, 2010.

[5] A. Cardon, H. Sol, W. De Wilde, J. De Visscher, K. Hoes, and D. Dinescu, “Mixed

numerical-experimental techniques: past, present and future," in *Recent Advances in Experimental Mechanics* (E. Gdoutos, ed.), pp. 551–560, Springer: Dordrecht, The Netherlands, 2004.

[6] M. Aghagholizadeh and N. Catbas, "A review of model updating methods for civil infrastructure systems," in *Computational Techniques for Civil and Structural Engineering* (J. Kruis, Y. Tsompanakis, and B. Topping, eds.), pp. 83–99, Saxe-Coburg Publications: Stirlingshire, UK, 2015.

[7] J. Mottershead and M. Friswell, "Model updating in structural dynamics: a survey," *Journal of Sound and Vibration*, vol. 167, no. 2, pp. 347–375, 1993.

[8] S. Rad, *Methods for updating numerical models in structural dynamics.* PhD thesis, University of London, London, UK, 1997.

[9] W. Visser, *Updating structural dynamics models using frequency response data.* PhD thesis, University of London, London, UK, 1992.

[10] I. Behmanesha, B. Moavenia, G. Lombaertb, and C. Papadimitriouc, "Hierarchical Bayesian model updating for structural identification," *Mechanical Systems and Signal Processing*, vol. 64-65, pp. 360–376, 2015.

[11] J. Gross, T. Oberhardt, P. Reuss, and L. Gaul, "Model updating of the Ampair wind turbine substructures," 32nd International Modal analysis conference, Orlando, FL, USA, 2014.

[12] S. Hwang and C. Chang, "Determination of elastic constants of materials by vibration testing," *Composite Structures*, vol. 49, no. 2, pp. 183–190, 2000.

[13] D. Lecompte, A. Smits, H. Sol, J. Vantomme, and D. Van Hemelrijck, "Mixed numerical-experimental technique for orthotropic parameter identification using biaxial tensile tests on cruciform specimens," *International Journal of Solids and Structures*, vol. 44, no. 5, pp. 1643–1656, 2007.

[14] M. Luczak, S. Manzato, B. Peeters, K. Branner, P. Berring, and M. Kahsin, "Updating finite element model of a wind turbine blade section using experimental modal analysis results," *Shock and Vibration*, vol. 2014, pp. 71–82, 2014.

[15] H. Sol, H. Hua, J. De Visscher, J. Vantomme, and W. De Wilde, "A mixed numerical-experimental technique for the non-destructive identification of the stiffness properties of fibre reinforced composite materials," *NDT & E International*, vol. 30, pp. 85–91, 1997.

[16] J. Beck, "Updating models and their uncertainties 1: Bayesian statistical framework," *Journal of Engineering Mechanics*, vol. 124, no. 4, pp. 455–461, 1998.

[17] H. Schlune and M. Plos, "Bridge assessment and maintenance based on finite element structural models and field measurements, state-of-the-art review," tech. rep., Department of Civil and Environmental Engineering Division of Structural Engineering, Chalmers University of Technology, Goẗeborg, Sweden, 2008.

[18] M. Sutton, J. Orteu, and H. Schreier, *Image Correlation for Shape, Motion and Deformation Measurements: Basic Concepts,Theory and Applications.* Springer: New York, NY, USA, 1st ed., 2009.

[19] E. van den Bunt and W. Lafeber, “Optical measurement techniques in model testing,” 2nd International conference on advanced model measurement technology for EU maritime industry, Newcastle upon Tyne, UK, 2011.

[20] J. Blasques, C. Berggreen, and P. Andersen, “Hydro-elastic analysis and optimization of a composite marine propeller,” *Marine Structures*, vol. 23, pp. 22–38, 2010.

[21] P. Maljaars and J. Dekker, “Hydro-elastic analysis of flexible marine propellers,” in *Maritime Technology and Engineering* (C. Guedes Soares and T. Santos, eds.), pp. 705–715, CRC Press-Taylor & Francis Group: London, UK, 2014.

[22] Y. Young, “Time-dependent hydro-elastic analysis of cavitating propulsors,” *Journal of fluids and structures*, vol. 23, pp. 269–295, 2007.

3

Chapter 3

Propeller hydro-elastic analysis in uniform flows

In the past several decades, many papers have been published on fluid-structure coupled calculations to analyse the hydro-elastic response of flexible (composite) propellers. The flow is usually modelled either by the Navier-Stokes equations or as a potential flow, by assuming an irrotational flow. Phenomena as separation of the flow, flow transition, boundary layer build-up and vorticity dynamics are not captured in a non-viscous potential flow. Nevertheless, potential flow based methods have been shown to be powerful methods to resolve the hydrodynamics of propellers. With the upcoming interest in flexible (composite) propellers, a valid question is what the consequences of the potential flow simplifications are with regard to the coupled fluid-structure analyses of these types of propellers. This question has been addressed in the following way: calculations and experiments were conducted for uniform flows only, with a propeller geometry that challenges the potential flow model due to its sensitivity to leading edge vortex separation. Calculations were performed on the undeformed propeller geometry with a Reynolds-averaged Navier-Stokes (RANS) solver and a boundary element method (BEM). These calculations show some typical differences between the RANS and BEM results. The flexible propeller responses were predicted by coupled calculations between BEM and a finite element method (FEM) and RANS and FEM. The applied methodologies are briefly described. Results obtained from both calculation methods have been compared to experimental results obtained from blade deformation measurements in a cavitation tunnel. The results show that, even for the extreme cases, promising results have been obtained with the BEM-FEM coupling. The BEM-FEM calculated responses are consistent with the RANS-FEM results.

This chapter is based on the journal paper: P. Maljaars, L. Bronswijk, J. Windt, N. Grasso and M. Kaminski, “Experimental validation of fluid-structure interaction computations of flexible composite propellers in open water conditions using BEM-FEM and RANS-FEM methods,” *Journal of Marine Science and Engineering*, vol. 6, no. 4, 51, 2018.

3.1. INTRODUCTION

In the last several decades, many papers have been published on the hydro-elastic analysis of flexible (composite) propellers. The majority of the studies were limited to steady inflow conditions. In these studies, mainly three different approaches were used for the hydrodynamic calculations of flexible propellers viz. Reynolds-averaged Navier-Stokes methods (RANS), boundary element methods (BEM) and vortex lattice methods (VLM). In BEM and VLM computations, the flow is assumed to be a potential flow.

RANS solvers were used in the flexible propeller fluid-structure interaction (FSI) computations presented in [1–4]. BEM solvers were applied in the hydro-elastic propeller analysis as presented in [5–12]. In the hydro-elastic coupling, procedures presented in [13, 14] VLM solvers were applied.

The fundamental difference between RANS computations and potential flow based calculations is that phenomena as separation of the flow, flow transition, boundary layer build-up and vorticity dynamics are not modelled in the latter one. For rigid propellers, the consequences of these flow simplifications have been studied in the past. Results of such studies were presented in the proceedings of the first and fourth Symposium on Marine Propulsors, for instance. These proceedings include papers with results of comparative studies with different RANS and BEM calculations together with experimental results for rigid propellers [15, 16]. Around the optimum efficiency, a good agreement between BEM, RANS and experimental results is obtained. An increasing inaccuracy of the BEM results can be expected for larger skew angles and smaller advance coefficients [12]. This is explained by the increased leading edge vortex strength for decreasing advance ratios and increasing skew angles. This indicates that, for blade integrated values like thrust and torque, vorticity phenomena may not be negligible for high loading conditions and propellers with considerable skew. However, comparative studies between RANS and potential flow based hydro-elastic calculations for flexible propellers are still lacking.

Recently, the influence of viscous effects on the hydro-elastic response of hydrofoils has been investigated [17, 18]. It has been shown that the flow-induced bend-twist coupling effects of a flexible hydrofoil in fully turbulent and attached flow conditions are well predicted with an inviscid FSI method [17]. However, when the stability boundaries are reached (i.e., static/dynamic divergence or flutter velocity boundaries), viscous FSI methods were recommended to predict the dynamic response, especially for solid-to-fluid added mass ratios smaller than four [18]. Therefore, it is expected that, for uniform flow conditions, in which dynamic instabilities are irrelevant, an accurate prediction of the FSI response of marine propellers can be obtained with an inviscid method when the flow is fully turbulent and attached.

However, both conditions are not met for the small-scale propellers considered in this chapter. Measurements and calculations have been performed at a transitional flow regime, partly laminar and partly turbulent. Secondly, experiments have been conducted at relatively high angles of attack resulting in a leading edge vortex and flow separation at the trailing edge. Finally, due to the finite blade size, a vortex is generated at the blade tips. The influence of these viscous effects and vorticity phenomena on the hydro-elastic response prediction is not known. Therefore, experimental and RANS-FEM results have been used to validate a BEM-FEM coupled calculation for uniform flows.

The main purpose of this work is to validate the RANS-FEM and BEM-FEM coupled calculations with experimental results and to show what the consequences of the potential flow simplifications are with regard to the coupled fluid-structure response. This chapter is structured as follows: first, the different propellers are described in Section 3.2. Section 3.3 provides information about the structural modelling. In Section 3.4, the fluid models are explained. The BEM-FEM and RANS-FEM coupling are described in Section 3.5. Section 3.6 presents a comparison of open water measurements and BEM and RANS calculations for a rigid propeller. In Section 3.7, the cavitation tunnel experiments are explained. Section 3.8 presents an uncertainty estimation for measurements and RANS-FEM and BEM-FEM calculations. In Section 3.9, the experimental results obtained for the flexible propellers are compared to results obtained with the BEM-FEM and RANS-FEM coupling. Conclusions are given in Section 3.10.

3.2. PROPELLERS AND FLOW CONDITIONS

PROPELLERS

Four propellers are considered. The propellers have a diameter, D, of 0.34 m and are similar in size and geometry, but differ with respect to blade material. Two propellers are made out of glass fibre reinforced epoxy with different laminate orientations, these propellers have been studied in previous chapter. The other two propellers are made of isotropic material: one bronze propeller and one made of epoxy. The propellers have been labelled as follows:

- Propeller bronze: this propeller is assumed completely rigid.
- Propeller epoxy: this propeller is the most flexible one.
- Propeller 45: $[+45°/-45°]$ laminate lay-up.
- Propeller 90: $[0°/90°]$ laminate lay-up.

The 0°-direction of the laminae is parallel to the z-axis of the propeller blade coordinate system, where positive x-, y- and z-axis are pointing forward, portside and upwards, respectively, see Figure 2.2 of previous chapter. All the results are presented according to this coordinate system.

The Young's moduli E, Poisson ratios v and the shear moduli G of the composite laminates are given in Table 2.1 of previous chapter. The elastic properties for the epoxy material are presented in Table 3.1.

E [GPa]	v [-]	G [GPa]
3.60	0.300	1.39

Table 3.1: Elastic properties of epoxy.

FLOW CONDITIONS

For the open water calculations, computations have been performed for a constant rotational speed, n, of 1170 rpm and varying advance speed, keeping the Reynolds number as constant as possible for different flow conditions.

The flexible propeller calculations have been performed for the measured conditions with advance ratios around 0.37, 0.64 and 0.85 as given in Table 3.2. All calculations have been performed for uniform inflow conditions. The last column of Table 3.2 presents the Reynolds number, Re, based on the chord length, C, and flow velocity at 0.7 of the propeller radius, r,

$$Re_{0.7r} = \frac{\rho C_{0.7r}\sqrt{v^2 + (0.7\pi nD)^2}}{\mu} \tag{3.1}$$

with ρ the density of water taken as 1000 kg/m^3 and μ the dynamic viscosity equal to $1.01 \cdot 10^{-3}$ Pa·s.

	$\boldsymbol{J = \frac{60v}{nD}}$	$\boldsymbol{v}$ **[m/s]**	$\boldsymbol{n}$ **[rpm]**	$\boldsymbol{Re_{0.7r} \times 10^6}$
Prop. Epoxy, blade 1	0.37	1.88	900	1.28
Prop. Epoxy, blade 1	0.64	3.97	1098	1.60
Prop. Epoxy, blade 1	0.85	6.73	1392	2.10
Prop. 45, blade 1	0.38	1.92	900	1.28
Prop. 45, blade 1	0.64	3.99	1098	1.60
Prop. 45, blade 1	0.85	6.75	1398	2.10
Prop. 90, blade 2	0.38	1.98	900	1.28
Prop. 90, blade 2	0.66	4.09	1098	1.60
Prop. 90, blade 2	0.85	6.74	1398	2.10

Table 3.2: Flow conditions for the flexible propeller calculations and measurements.

3.3. STRUCTURE MODEL

For FEM modelling and computations, Marc/Mentat has been used. The FEM models consist of one propeller blade without the hub part. The hub has not been modelled. The blade has been fully clamped at the blade-hub interface. The models were discretised by quadratic solid elements. A mesh convergence study has been conducted in order to ensure a mesh independent solution for the calculated deformations. Structured FEM meshes have been used, identified with the following three discretisation parameters: N_c the number of elements in chordwise direction, N_r the number of elements in radial direction and N_n the number of elements in through-thickness direction. Table 3.3 presents the deformations of the tip for a static load case obtained with FEM models for different meshes. These results show that, for the $29 \times 30 \times 4$ element distribution, the tip displacement differs approximately 0.1% from the grid independent solution. Therefore, the $29 \times 30 \times 4$ element distribution has been used for all the FEM calculations.

In the FEM modelling, special attention has been given to the establishment of the material orientations in composite blades as discussed in Chapter 2. Standard commercial FEM software packages are usually not able to define unambiguously the material orientations in complex geometries [19]. In Chapter 2 an approach has been presented to determine the element dependent material orientations in doubly curved structures. In this method, the through-thickness direction and the projection of the transverse laminate (90°)-direction on the element surface are used to establish the material orientation per element.

N_c	N_r	N_n	**Tip Deflection [mm]**
116	120	4	16.76
58	60	4	16.76
58	60	8	16.76
29	30	4	16.74

Table 3.3: Results of the finite element method mesh convergence study.

3.4. FLUID MODELS

This section provides information about the fluid models which have been used. First, the BEM modelling has been discussed. Secondly, the RANS modelling, including a presentation of the RANS discretisation uncertainties.

3.4.1. BEM MODEL

For this work, the BEM PROCAL, developed by the Maritime Research Institute Netherlands (MARIN) [20, 21] was used. In BEM, only the surfaces of the object have to be discretized. From a grid sensitivity study, it was concluded that a 29 × 30 element distribution is sufficient to obtain a grid independent solution. In the previous section, it was revealed that, in the FEM model, 29 and 30 elements are distributed along the blade chord and radius, respectively. This means that the BEM and FEM solvers require a similar distribution of panels or elements on the propeller surface. This property has been used by applying identical mesh distributions in the FEM and the BEM model in order to avoid the need for an interpolation of pressure and structural response between the two grids.

Two corrections are applied on the PROCAL pressures before they are imposed on the FEM model. The first correction is to rectify for an overestimation of the pressures at the propeller tip. In general, with a potential flow solver, a pressure difference between blade face and back at the tip will be computed, while, in reality, this pressure difference will be zero. To correct for this, the calculated pressures from a certain propeller radius are smoothed to a zero pressure coefficient at the tip. The default from where this tip pressure correction is applied is 95% of the propeller radius. This value has been used throughout this work. The pressure smoothing radius has an important influence on the propeller blade deformations at the tip, since the tip is relatively flexible and therefore the tip deformations are sensitive to small changes in pressure distribution [22].

The second correction is a viscous correction to include frictional losses. The viscous shear stresses have been computed using the maximum skin friction coefficient calculated from the Blasius formulation for laminar flow, ITTC formulation for transition to turbulent flow [23] and the Prandtl-Schlichting formulation. The skin friction coefficients have been used to calculate the blade tangential forces from the total velocities and element areas per element. These forces have been imposed on the FEM model.

The correction for the minimum allowable pressure coefficient as explained in Section 3.6.1 has not been used in the BEM-FEM calculations because this correction applies only for the lowest advance ratios of 0.37 and 0.38, but hardly affects the hydro-elastic response for these conditions.

3.4.2. RANS MODEL

RANS calculations have been conducted with the CFD software ReFRESCO developed at MARIN. ReFRESCO [24] is a community based open-usage/open-source CFD code for the maritime world. It solves multiphase (unsteady) incompressible viscous flows using the Navier-Stokes equations, complemented with turbulence models, cavitation models and volume-fraction transport equations for different phases. The equations are discretised using a finite-volume approach with cell-centered collocated variables, in strong-conservation form and a pressure-correction equation based on the SIMPLE algorithm is used to ensure mass conservation [25, 26].

Since open water conditions are considered, the computations can be conducted using a body fitted, rotating reference system. For this, the propeller has been modelled in a rotating circular domain with diameter and length three and five times the propeller diameter, respectively. The propeller is located in the middle of this domain. The computational domain consists of a structured multi-block grid built with GridPro, using a standard block topology developed at MARIN. The topology is applied quite often and gives good quality grids, most of the time. However, for the propeller considered here, grid generation was cumbersome due to the relatively high skew of the propeller blades, the relatively thin leading edge and propeller section thicknesss. The quality of the grid was not very high, which leads to convergence problems of the solver when using higher order discretisations of the convective fluxes (QUICK scheme). Therefore, for all calculations, a blending between central and upwind discretisation was used. Figures of the domain, grid and propeller are depicted in Figure 3.1. For all the calculations, the $k-\sqrt{k}L$ turbulence model has been used as described in [27]. The $k-\sqrt{k}L$ turbulence model gives very similar results as the $k-\omega$ SST model, but shows in general an improved iterative convergence. This has been shown explicitly for propeller flows [28].

The boundary conditions applied on the domain and propeller are given in Table 3.4. At the inlet, the velocity is imposed. At the outlet, a combination of an outflow and pressure condition is imposed. Behind the propeller, the velocity derivatives are imposed to be zero; at the remainder of the outlet, the pressure is imposed. The propeller, hub and shaft have a no-slip boundary condition. In the calculations, no wall functions have been used, i.e., in all calculations, the non-dimensional wall distance y+ was below 1. At the outer surface of the circular domain, a free-slip boundary condition is applied, i.e., the velocities normal to the surface are zero and the tangential velocities are free.

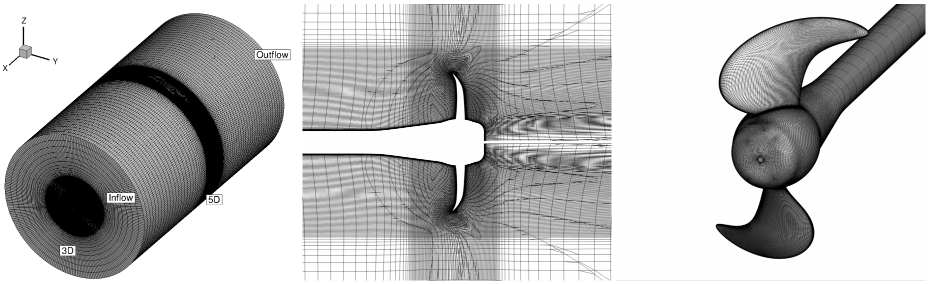

Figure 3.1: Domain and grid for the Reynolds-averaged Navier-Stokes computations.

	Boundary Condition
Inlet	Prescribed inflow velocity.
Inner outlet	Neumann boundary condition on velocity and pressure.
Outer outlet	Dirichlet boundary condition on pressure, Neumann on velocity.
Propeller, hub and shaft	Velocity is zero, no wall functions applied (y+ should be <1).
Outer surface flow domain	Normal and tangential velocity are zero and free, respectively.

Table 3.4: Boundary conditions for the Reynolds-averaged Navier-Stokes calculations.

THRUST AND TORQUE RANS DISCRETISATION UNCERTAINTIES

The discretisation errors in the thrust and torque values obtained with the RANS calculations have been estimated with the method described in [29]. In this approach, the numerical uncertainty is obtained using solutions on systematically refined grids. The error is estimated with power series expansions as a function of the typical cell size. The expansions are fitted to the data in the least-squares sense. For the present uncertainty estimation, four grids with cell densities described in Table 3.5 have been used. The third row gives the relative step size. This parameter identifies the representative grid cell size and is the cubic root of the ratio between the amount of grids cells for finest grid and the considered grid.

Grid	Amount of Cells	Relative Step Size
A	917,000	2.18
B	2,390,000	1.58
C	3,790,000	1.36
D	9,460,000	1.00

Table 3.5: Amount of cells and relative step size for the different grids.

Figure 3.2 shows the results of the discretisation uncertainty quantification for the thrust and torque values computed for the three advance coefficients. The graphs show that the order of accuracy, p, is in the range 0.5 to 1.7. $p = *1,2$ means that a fit was made using first and second order exponents. The order of accuracy is smaller than the typical value of two that would have been obtained when a quadratic upwind differencing (QUICK) scheme was used for the convective flux discretisation. However, with a QUICK scheme, the computations did not converge.

The results show that the discretisation uncertainties are small (<3%) for the advance ratios 0.37 and 0.64. The uncertainties are the highest for the largest advance coefficient, 7.7% and 11.2% for the thrust and torque, respectively. These values are higher than generally accepted. Therefore, for the advance ratio of 0.85, a computation has been performed with a further refined grid. Unfortunately, this calculation required a smaller blending factor to converge and therefore it was decided to stay with grid D.

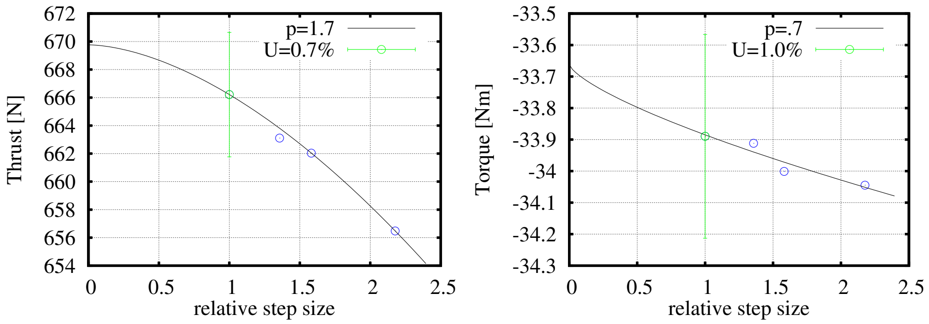

(a) Thrust, $J = 0.37$.

(b) Torque, $J = 0.37$.

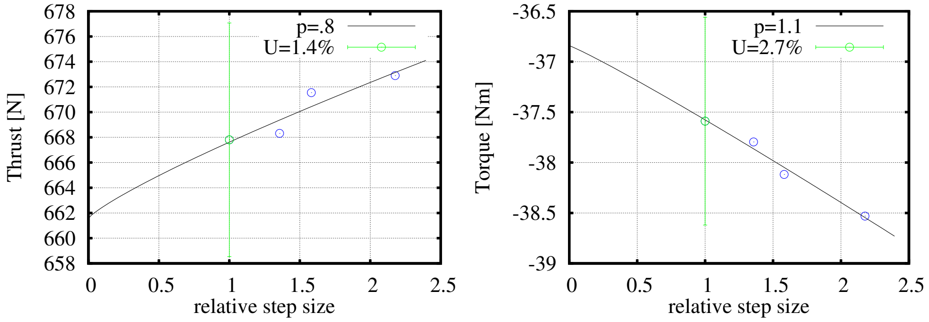

(c) Thrust, $J = 0.64$.

(d) Torque, $J = 0.64$.

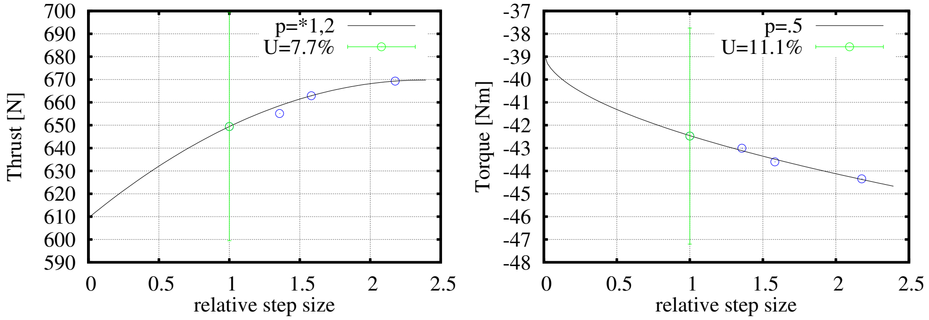

(e) Thrust, $J = 0.85$.

(f) Torque, $J = 0.85$.

Figure 3.2: Numerical uncertainty of the thrust and torque, U and order of accuracy, p, for various advance ratios.

3.5. FLUID-STRUCTURE COUPLING

The BEM-FEM and RANS-FEM coupling procedure are explained in this section, starting with the BEM-FEM coupling.

3.5.1. BEM-FEM COUPLING

Figure 3.3 shows the coupling procedure between the BEM solver PROCAL and the FEM software Marc/Mentat. In this coupling, the following non-linear equation is solved,

$$\mathbf{Ku} = \mathbf{f}_{BEM}(\mathbf{u}) + \mathbf{f}_{viscous}(\mathbf{u}) + \mathbf{f}_{centrifugal} \tag{3.2}$$

where $\mathbf{f}_{BEM}$, $\mathbf{f}_{viscous}$ and $\mathbf{f}_{centrifugal}$ denote potential flow force, viscous forces and centrifugal forces, respectively. $\mathbf{K}$ is the stiffness matrix. Essentially, all the variables in Eq. (3.2) are a function of the deformations $\mathbf{u}$. Since the blade deformations are relatively small, geometric linear elastic analyses are performed with the FEM solver and therefore the stiffness matrix and centrifugal force vector are assumed to be independent of $\mathbf{u}$.

The first step in the coupled BEM-FEM calculation is a PROCAL calculation on the undeformed geometry. The tip pressure correction is applied on the pressures obtained with PROCAL as explained in Section 3.4.1. Next, the viscous forces are calculated to account for frictional losses. Subsequently, the calculated pressures and viscous forces are used to calculate the structural response of the propeller blade. The structural deformations are used to construct a new propeller geometry from which new fluid pressures are calculated. When not converged, the iteration loop starts again.

3.5.2. RANS-FEM COUPLING

Recently, MARIN has developed an FSI module in ReFRESCO, the implementation and a verification study have been presented in [30]. The method is a partitioned strong coupling approach, meaning that the fluid and structural problem are solved separately and coupling iterations are performed each time step to obtain the coupled solution. To stabilize this procedure under-relaxation is applied by means of the Aitken adaptive under-relaxation method. For transfer of information across the fluid-structure interface, a radial basis-function (RBF) interpolation is used.

In [30], a verification study was presented for the unsteady problem of the flow around a rigid cylinder with a flexible flap (the Turek benchmark [31]). Results obtained with the FSI module of ReFRESCO were in good agreement with results presented in literature.

The FSI module has been developed for unsteady FSI problems. For steady FSI problems, like the flow around a flexible propeller in open water conditions, the FSI module can be used by performing unsteady simulations until equilibrium is obtained. This was applied in this work, since only open water conditions have been considered. For steady FSI problems the equilibrium solution should be irrespective of the time step in the RANS and FEM calculation, which was the case for all the computations. The most convenient was to apply the same time step in RANS and FEM calculation.

Figure 3.4 shows the flow chart for one time step with the RANS-FEM coupling. Each time step starts with a RANS computation. Then, the pressures are transferred to the FEM calculation by using an RBF interpolation. With FEM, the structural response is computed. Subsequently, the structural response is transferred to the RANS calculation by again using an RBF interpolation. Based on the blade deformations, the RANS grid is adapted and the pressures are recomputed until convergence is obtained. Then, the following time step is resolved in the same way. For the steady problems considered in this chapter, the RANS-FEM calculation runs through a number of time steps until the steady state solution is obtained.

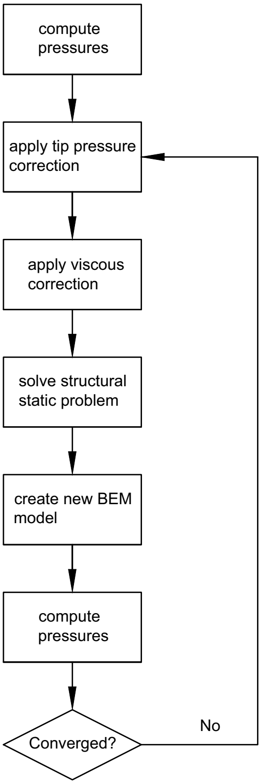

Figure 3.3: Flow chart of the BEM-FEM coupling.

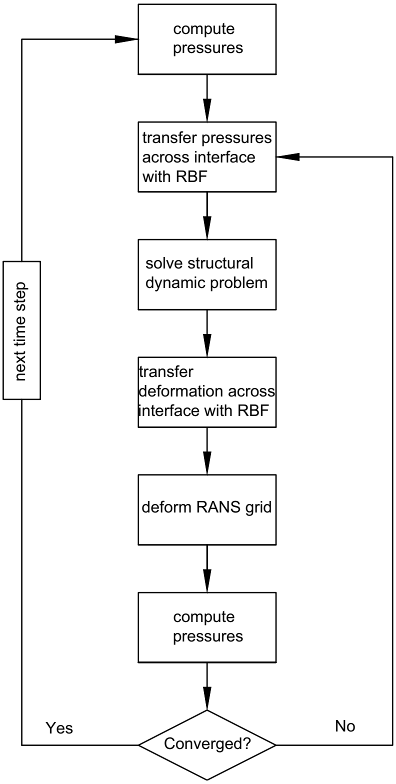

Figure 3.4: Flow chart of one time step with the RANS-FEM coupling.

3.6. COMPARISON OF EXPERIMENTAL, BEM AND RANS RESULTS FOR THE BRONZE PROPELLER

In this section experimental results obtained for the bronze propeller have been compared to results obtained from BEM and RANS calculations. First of all, calculated and measured open-water diagrams have been compared. Then, there will be focussed on the pressure distributions obtained from the BEM and RANS calculations for a better understanding of the differences between the BEM and RANS results.

3.6.1. OPEN WATER DIAGRAM BRONZE PROPELLER

The open water diagram of the bronze propeller has been measured and compared to calculated open water diagrams with PROCAL and ReFRESCO. Open water measurements have been performed in the deepwater towing tank of MARIN at a constant rotational speed of 1170 rpm and varying advance speed. The Reynolds number based on velocity and chord length at 0.7 of the propeller radius then varies between 1.64×10^6 and 1.90×10^6. A total measurement uncertainty (precision and bias) of 3% on thrust and torque can be adopted for these measurements.

COMPARISON OF EXPERIMENTAL AND BEM RESULTS

For the BEM calculations, a discretisation error of 0.5% in thrust and torque is estimated by taking the percentage difference between the mesh independent thrust and torque values and the values obtained for the considered panel distribution. The measured and calculated open water curves are depicted in Figure 3.5 with their uncertainty bands. Particularly for $J < 0.4$ and $J > 1$, a relatively large discrepancy between measured and calculated curves is seen, especially for the torque coefficient. For $J > 1$, viscous effects play an increasingly important role and therefore the results of the PROCAL calculations diverge from the measured results. The discrepancy for low advance coefficients is attributed to the relatively sharp leading edge. This results, for heavy loading conditions, in unrealistic high flow velocities and consequently low pressures at the leading edge, since the flow does not separate in the BEM calculation. In reality, the flow will separate, which will limit the suction pressure. The torque is mainly affected by the unrealistic low pressures at the leading edge because the surface normals at the leading edge point mainly in the direction of the blade nose-tail line and therefore the low leading edge pressures reduce the drag rather than the lift. A correction on the suction pressures can be applied by restricting the minimum pressure coefficient, C_p, obtained with the BEM calculation by replacing lower pressures with that value. By properly selecting the minimum allowable pressure coefficient for the different advance ratios, the dotted KQ curve of Figure 3.5 is obtained. For $J > 0.4$, no minimum pressure correction has been applied.

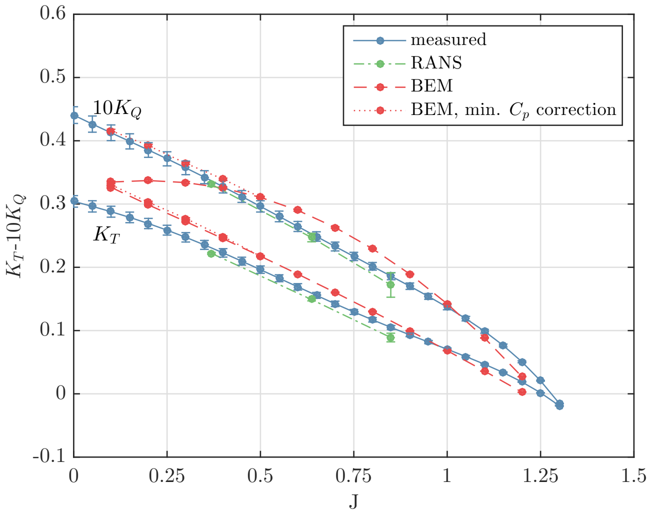

Figure 3.5: Measured and calculated open water diagrams of the bronze (rigid) propeller.

COMPARISON OF EXPERIMENTAL AND RANS RESULTS

The calculated open water coefficients with ReFRESCO together with the discretisation uncertainty bandwidths are depicted in Figure 3.5 as well. The RANS computed thrust and torque coefficients are smaller than the measured values. The uncertainty bars show that the differences can be explained from uncertainties in the RANS computations and the measurements, except for the highest advance coefficient. That means that, with the present RANS calculation, the thrust and therefore the pressure distribution cannot be correctly resolved for this propeller at $J = 0.85$. A plausible explanation for this is the modelling error originating from the turbulence model, while a transition model might be more appropriate. This modelling uncertainty might be significant for this condition, since, for an increasing advance ratio, the lift force decrease and viscous forces become more important.

3.6.2. COMPARISON OF BEM AND RANS PRESSURE DISTRIBUTIONS

Figure 3.5 shows significant differences between BEM and RANS results. Not surprisingly, the RANS results seem more accurate than the BEM results, since the RANS calculation includes viscous flow modelling and vorticity phenomena. To investigate the differences between BEM and RANS results in more detail, pressure distributions obtained with both methods for the first three flow conditions of Table 3.2 have been compared. For these flow conditions, the limiting streamlines on the propeller suction side are depicted in Figure 3.6. As indicated by the contraction of the streamlines, three flow separation areas can be distinguished: separation at the leading edge resulting in a leading edge vortex, a separation area at the trailing edge and flow separation at the propeller tip. The least flow separation is obtained for the highest advance coefficient.

The pressure distributions for the three BEM and RANS computations are presented in Figures 3.7–3.12. In these figures, the pressure is made dimensionless with the fluid density, propeller rotation rate and diameter. These results show that the suction side pressure is generally lower for the BEM computations. Overall, the BEM computed pressures on the pressure side are higher than those obtained from the RANS computations. These results correspond with the differences in thrust and torque between the RANS and BEM computations as presented in Table 3.6.

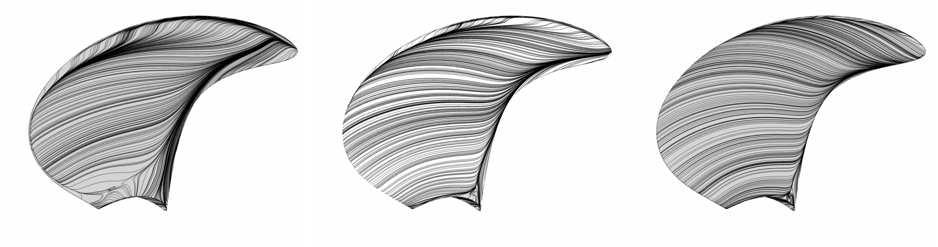

Figure 3.6: Limiting streamlines on the propeller suction side for $J = 0.37$, $J = 0.64$ and $J = 0.85$.

	K_T(BEM)	K_T(RANS)	%	$10K_Q$(BEM)	$10K_Q$(RANS)	%
$J = 0.37$	0.255	0.222	−13%	0.344	0.331	−4%
$J = 0.64$	0.177	0.149	−16%	0.278	0.247	−11%
$J = 0.85$	0.114	0.089	−22%	0.208	0.172	−17%

Table 3.6: K_T and $10K_Q$ for the rigid propeller Reynolds-averaged Navier-Stokes and boundary element method calculations.

For the conditions $J = 0.37$ and $J = 0.64$, the angle of attack on the blades is high, leading to a strong suction peak in the pressure distribution. In the RANS computations, the flow separates as shown in Figure 3.6. At the blade tip, the differences in pressure distribution obtained from RANS and BEM computations are evident: the BEM calculations show unrealistic pressures due to a non-physical modelling of the flow. In the BEM-FEM coupled calculations, the tip pressure correction is applied to correct for that.

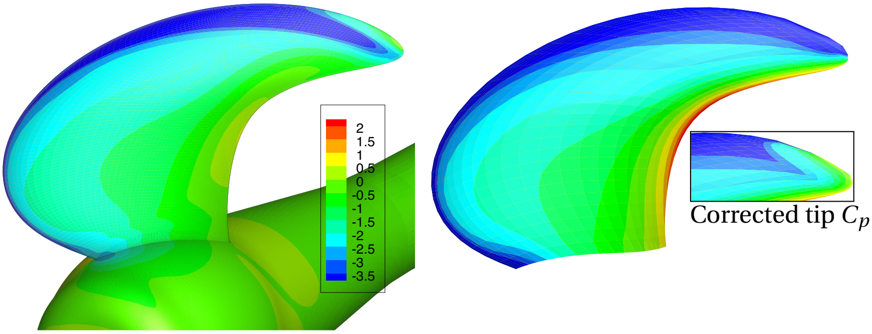

Figure 3.7: Pressure coefficient, C_p, on the suction side for $J = 0.37$, RANS (left) BEM (right). The insert figure shows the BEM pressure distribution after the tip pressure correction.

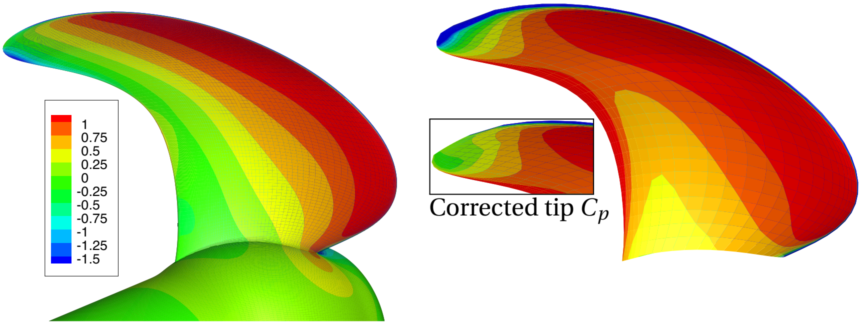

Figure 3.8: Pressure coefficient, C_p, on the pressure side for $J = 0.37$, RANS (left) BEM (right). The insert figure shows the BEM pressure distribution after the tip pressure correction.

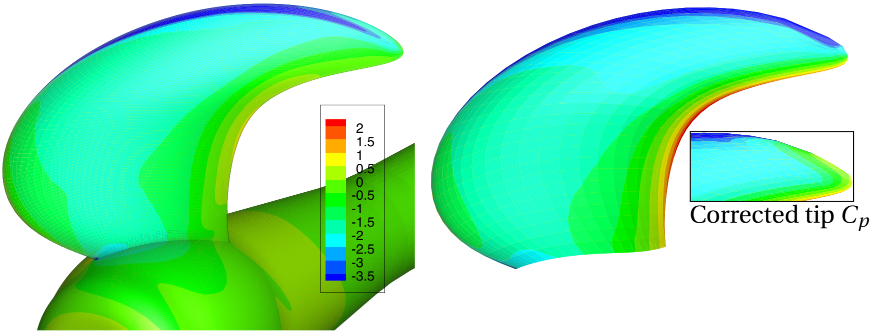

Figure 3.9: Pressure coefficient, C_p, on the suction side for $J = 0.64$, RANS (left) BEM (right). The insert figure shows the BEM pressure distribution after the tip pressure correction.

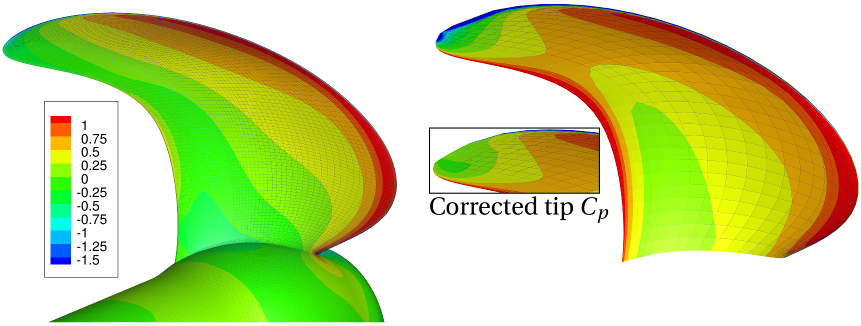

Figure 3.10: Pressure coefficient, C_p, on the pressure side for $J = 0.64$, RANS (left) BEM (right). The insert figure shows the BEM pressure distribution after the tip pressure correction.

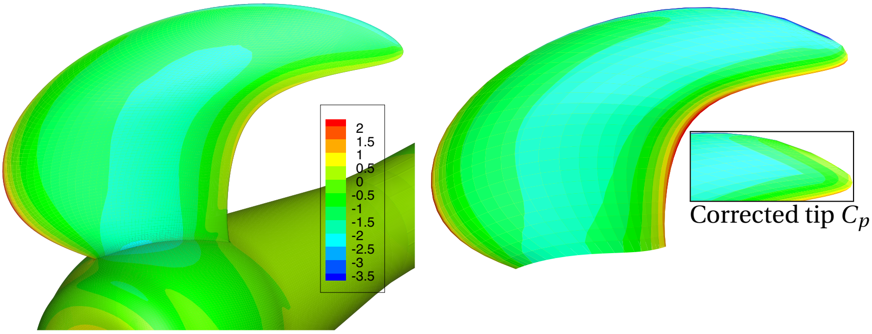

Figure 3.11: Pressure coefficient, C_p, on the suction side for $J = 0.85$, RANS (left) BEM (right). The insert figure shows the BEM pressure distribution after the tip pressure correction.

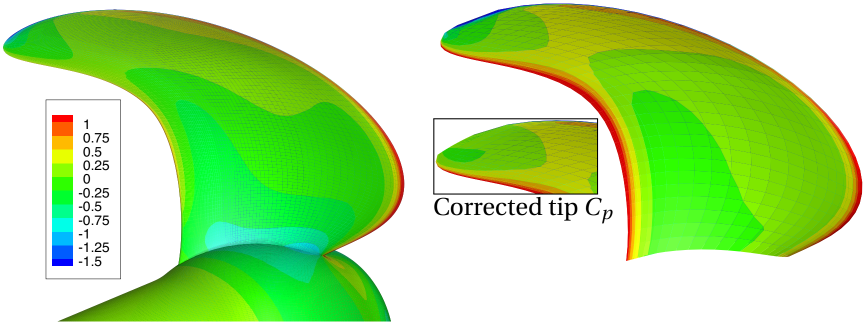

Figure 3.12: Pressure coefficient, C_p, on the pressure side for $J = 0.85$, RANS (left) BEM (right). The insert figure shows the BEM pressure distribution after the tip pressure correction.

3.7. FLEXIBLE PROPELLER CAVITATION TUNNEL EXPERIMENTS

Usually, thrust, torque and blade deformations are measured and used for validation of the hydro-elastic propeller calculations. In this work, the focus is on the blade deformations rather than thrust and torque values for several reasons: first of all, the deformation field provides spatially distributed information about the propeller response in contrast to the blade integrated values like thrust and torque. Secondly, the uncertainties in the measured blade deformations are smaller than the uncertainties in thrust and torque changes due to blade flexibility. The reason is that thrust and torque changes can be easily affected by unintended small deviations in propeller geometry introduced in the complicated manufacturing of flexible propellers. Stereo-photography with a Digital Image Correlation (DIC) technique was selected to measure the propeller blade deformations. With this system, a very accurate recording of the complete 3D blade deformation field was achieved.

3.7.1. MEASUREMENT SET-UP

The measurements were conducted by MARIN using their cavitation tunnel test facility. The propeller is mounted on the tunnel shaft, which is connected to an encoder. This encoder sends impulse signals used for the triggering of the strobe lights and the cameras. The test set-up used in the cavitation tunnel is explained in Figure 3.13. It consists of the following elements:

- Two synchronized and calibrated cameras with FireWire interface; resolution: 1388 × 1038 pixels; maximum frame rate 16 fps at full resolution.
- Stroboscopic lights with flash duration in the micro second range. Flash duration is kept as short as possible to avoid motion blur at the blade tip.
- The shaft encoder mounted on the shaft, provides 360 pulses per revolution.
- A pulse selector is able to select one of these 360 pulses as a trigger, which is sent to the stroboscopes and the cameras. Therefore, a trigger can be supplied, with a

resolution of one degree for every blade position. The cameras and the strobe are synchronized such that the strobe flash falls within the time frame that the camera shutter is open.

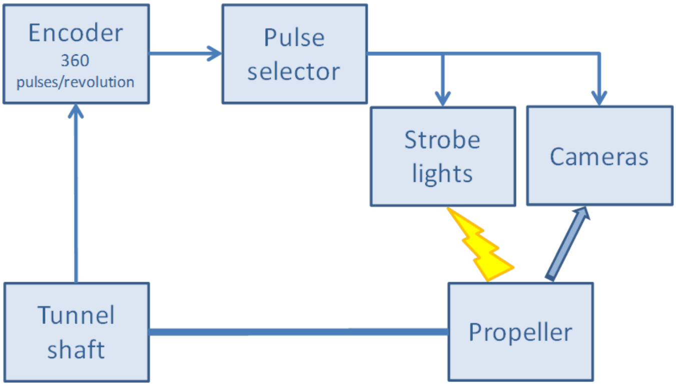

Figure 3.13: Cavitation tunnel set-up diagram.

Figure 3.14 shows the initially proposed camera set-up. Two purpose-built windows were mounted in place of the cavitation tunnel lateral windows to have an optimal camera view. Figure 3.15 shows a picture of the realized test set-up. During the experiments, one of the windows was moved to the bottom of the tunnel to further improve the view on the blade surfaces. In addition, the cameras were mounted on a vibration damping structure to ensure their isolation from vibrations.

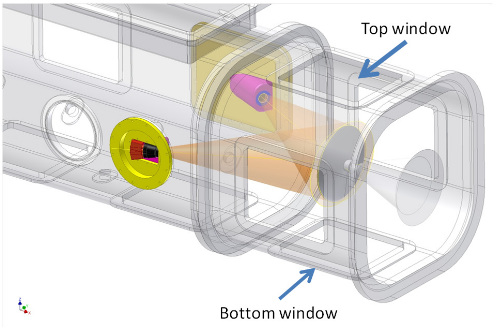

Figure 3.14: Proposed camera set-up.

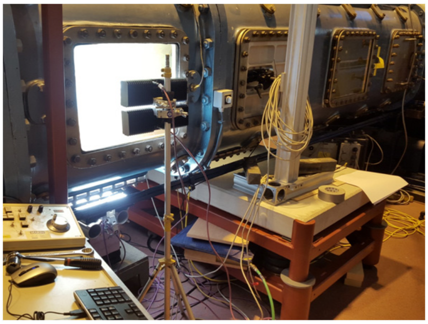

Figure 3.15: Picture of the cavitation tunnel test set-up.

3.7.2. MEASUREMENT TECHNIQUE

The image data acquired with the calibrated stereo camera system have been used to compute the blade deformations by means of DIC. DIC is a full-field image analysis method, based on grey value digital images, that finds the displacements and deformations of an object in three-dimensional space [32]. During the blade deformation, the method tracks the grey value pattern from which the deformations of the object are calculated. This method can be used in several applications. In particular, it has been successfully applied for blade deformation measurements both in uniform flow in the cavitation tunnel and in behind ship model condition in the towing tank [33].

In order to use the DIC technique, the surface of the measured object must have a random speckle pattern with no preferred orientation and sufficiently high contrast. The size of the features in the pattern should be large enough to be distinguished. If the material does not naturally show a usable speckle pattern, this must be applied through printing or painting. With this technique, very accurate measurements of the blade response were achieved. Several images for each blade position were acquired and image averaging was applied to filter out deformations resulting from high frequency vibrations of the propeller blade, and to remove possible bubbles or particles in the water. The results were further post-processed and a procedure was applied to correct for rigid body motions induced by vibrations and movements of the shaft.

3.8. EXPERIMENTAL, MODELLING AND DISCRETISATION UNCERTAINTIES FLEXIBLE PROPELLER CASES

This section provides the results of the uncertainty analyses, subdivided in experimental, modelling and discretisation uncertainties.

3.8.1. EXPERIMENTAL UNCERTAINTIES

Regarding the experimental uncertainties, two types of errors can be distinguished: precision errors and systematic errors. Precision errors are due to the statistical variability in the measured data set and can be reduced by repeating the test a number of times until the true average value of the measurement distribution is obtained. To reduce the precision errors in the measurements, averaging of the results was applied. Thrust, torque, flow speed and rotation rate are time averaged values. To obtain the true average deformations, image averaging with 30 images was applied. Therefore, it is expected that the precision errors are small compared to the systematic errors. Only for the DIC measurements was a precision error determined because this precision error is not reduced with the image averaging, since the results are averaged before the cross-correlation. In order to estimate this precision error, a test was performed. A rigid flat plate, with a speckle pattern, was mounted on the cavitation tunnel shaft. The displacements of the plate in the axial direction due to different tunnel speeds (from 0 to 6 m/s) were measured. Given the stiffness of the plate, bend and shear deformations of the plate can be neglected. Therefore, the measured displacements are due to the compression of the tunnel shaft and are assumed constant over the plate area. The distribution of the rigid displacement is an indicator of the precision error. A 95% confidence interval of around 20 μm was obtained. From the results, it was also concluded that this precision error is independent of the displacement magnitude or tunnel flow speed (see also [22]).

A DIC systematic error of 30 μm has been assumed. This value is based on the measured blade response adjacent to the hub where zero blade deformations can be expected, but which is generally not the case. The total uncertainty for the DIC measurements becomes 50 μm by taking the sum of the precision and systematic error.

3.8.2. MODELLING UNCERTAINTIES

Modelling uncertainties originate from different sources. There are modelling uncertainties due to simplifications in the mathematical models. For instance, in the BEM calculations, by assuming a potential flow and in the RANS calculations by adopting the $k-\sqrt{k}L$ turbulence model instead of a transition model, which would be able to predict the transition from laminar to turbulent flow.

There are also modelling uncertainties in the RANS-FEM and BEM-FEM calculations due to not exactly modelling the properties and conditions as appearing in the cavitation tunnel experiments. For this class of modelling errors, uncertainty levels have been estimated. The following modelling errors have been judged to be the most important, modelling errors due to:

1. using the design propeller geometry instead of the as-built geometry,
2. using the design propeller stiffness instead of the actual propeller stiffness,
3. neglecting of the cavitation tunnel walls.

The first modelling error is due to using the design propeller stiffness instead of the actual propeller stiffness. Based on measured and computed blade natural frequencies, a stiffness systematic error of ±5% and ± 10% has been assumed for epoxy propeller and composite propellers, respectively.

An important modelling error is introduced by performing the calculations with the design geometry instead of the as-built geometry. The influence of the difference between as-built and design geometry on the blade forces was investigated by comparing results of BEM calculations obtained for the different geometries. This investigation indicated that, depending on the propeller blade and flow condition, a significant difference in thrust force due to inaccuracies in the blade geometry can be assumed (see also [22]).

The modelling error due to neglecting the tunnel walls is only relevant for the BEM-FEM calculations, since the RANS-FEM calculations were performed in a bounded circular domain. This error has been estimated with Glauert's correction for tunnel wall effects [34]. With Glauert's correction, the unbounded flow velocity is replaced by an equivalent mean tunnel flow speed resulting in the same thrust.

3.8.3. DISCRETISATION UNCERTAINTIES

The discretisation uncertainties in the BEM-FEM calculations are smaller than 0.5% and assumed negligible compared to the modelling errors as described above. The RANS grid discretisation uncertainties in bend and twist deformations have been estimated with the same method and grids as used for the thrust and torque uncertainty estimation in Section 3.4.2. This means that, in total, twelve RANS-FEM calculations have been performed; for every flow condition, four calculations with the four RANS grids. Then, for each radial station, the uncertainties in mid-chord bend deformation and twist deformation were calculated from the solutions of the four systematically refined grids.

3.8.4. TOTAL UNCERTAINTIES

Tables 3.7 and 3.8 present the uncertainties at the propeller tip for the RANS-FEM calculations. The separate uncertainty contributions are are added in quadrature, resulting in the total uncertainties as given in the last columns. From these results, it can be concluded that the discretisation uncertainty dominates in the total bend and twist deformation uncertainty of the lowest and highest advance ratio. From this, it can be concluded that convergence of thrust and torque (as shown in Section 3.4.2) does not automatically mean that the blade structural response is converged as well.

The separate contributions of the modelling uncertainties for the composite propellers are not shown here. However, for propeller 90, the stiffness uncertainty has the largest contribution. For propeller 45, the blade geometry uncertainty has more or less the same magnitude as the stiffness uncertainty. The contribution in uncertainty due to the presence of the tunnel walls for the epoxy propeller BEM-FEM calculation was relatively large, since the stiffness uncertainty is smaller than for the composite propellers.

	RANS-FEM Result	**Modelling Uncertainty 1**	**Modelling Uncertainty 2**	**Discretisation Uncertainty**	**Total Uncertainty**
$J = 0.37$	4.34	−0.157; 0.0	−0.212; 0.211	−0.386; 0.386	−0.468; 0.440
$J = 0.64$	4.11	−0.184; 0.0	−0.200; 0.201	−0.025; 0.025	−0.273; 0.202
$J = 0.85$	4.20	−0.233; 0.0	−0.185; 0.183	−0.290; 0.290	−0.415; 0.343

Table 3.7: Uncertainties (lower and upper levels) in mid-chord bend deformation at the tip in [mm].

	RANS-FEM Result	**Modelling Uncertainty 1**	**Modelling Uncertainty 2**	**Discretisation Uncertainty**	**Total Uncertainty**
$J = 0.37$	−2.29	0.0; 0.066	−0.089; 0.090	−0.508; 0.508	−0.515; 0.520
$J = 0.64$	−1.95	0.0; 0.083	−0.093; 0.091	−0.092; 0.092	−0.131; 0.154
$J = 0.85$	−2.58	0.0;0.128	−0.101; 0.102	−0.335; 0.335	−0.350; 0.373

Table 3.8: Uncertainties (lower and upper levels) in twist deformation at the tip in [°].

3.9. COMPARISON OF EXPERIMENTAL, BEM-FEM AND RANS-FEM RESULTS

Figures 3.16–3.18 show the uncertainty intervals for measured and calculated bend and twist deformations against the radial position on the blades. By investigating the results obtained for the epoxy propeller, in general, the measured bending responses are well predicted with RANS-FEM calculations. The uncertainties bandwidths for the RANS-FEM calculated twist deformations of the lowest and highest advance ratio are relatively large, mainly caused by the discretisation uncertainty, but do not partially overlap with the measurements. The differences between the twist deformations obtained from the RANS-FEM calculation and measurements for $J = 0.85$ is explainable given the deviation between RANS computed thrust and the rigid propeller open water measurement as presented in Section 3.6.1 for this condition. It was pointed out that these differences might originate from modelling errors in the turbulence modelling. A plausible explanation for the differences at $J = 0.37$ is the severe flow separation that might be incorrectly resolved with a RANS model and the turbulence model. It can be concluded that the best agreement between measurements and the RANS-FEM calculations is obtained for the advance ratio of $J = 0.64$, in which leading edge vortex separation is present but limited compared to the lowest advance ratio, and viscous forces might be less dominating than for the highest advance coefficient.

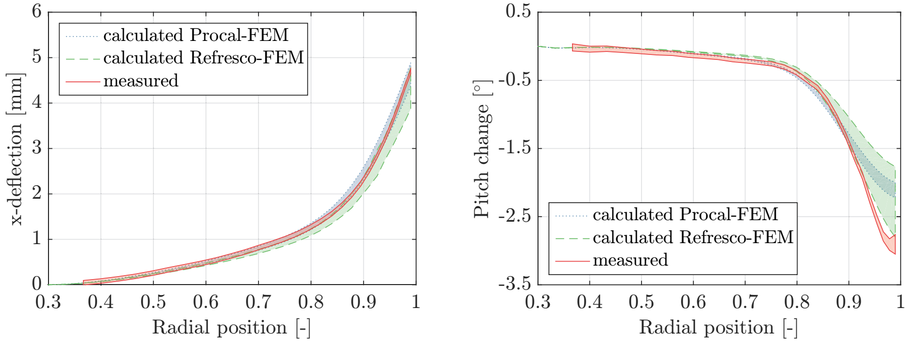

(a) Bend deformation, $J = 0.37$.

(b) Twist deformation, $J = 0.37$.

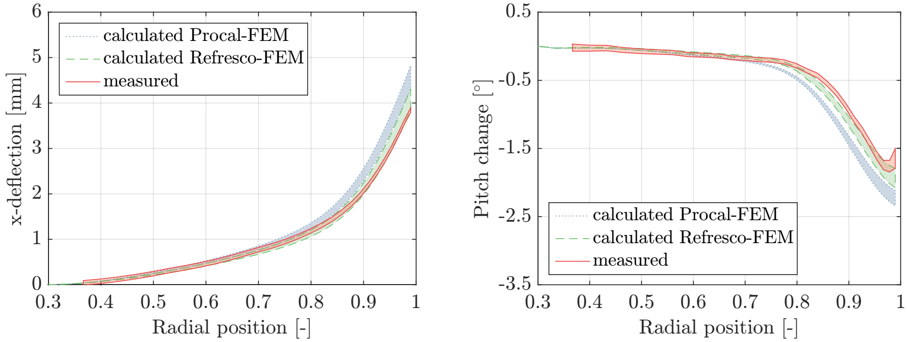

(c) Bend deformation, $J = 0.64$.

(d) Twist deformation, $J = 0.64$.

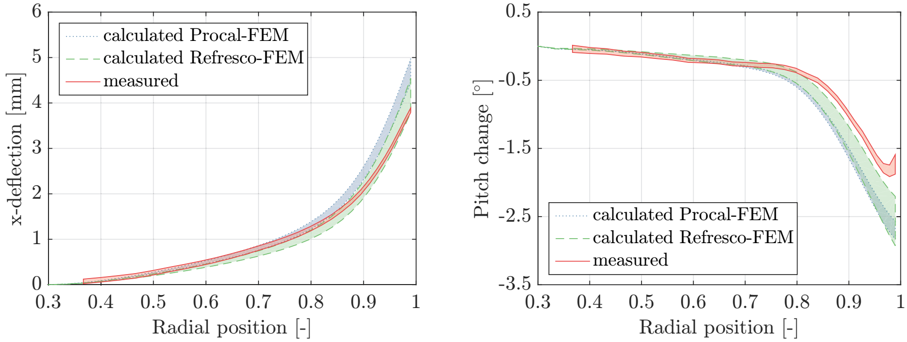

(e) Bend deformation, $J = 0.85$.

(f) Twist deformation, $J = 0.85$.

Figure 3.16: Uncertainty intervals for bend (left) and twist (right) deformations of mid-chord points of epoxy propeller blade 1 against the radial position on the blade, for the measured and calculated responses.

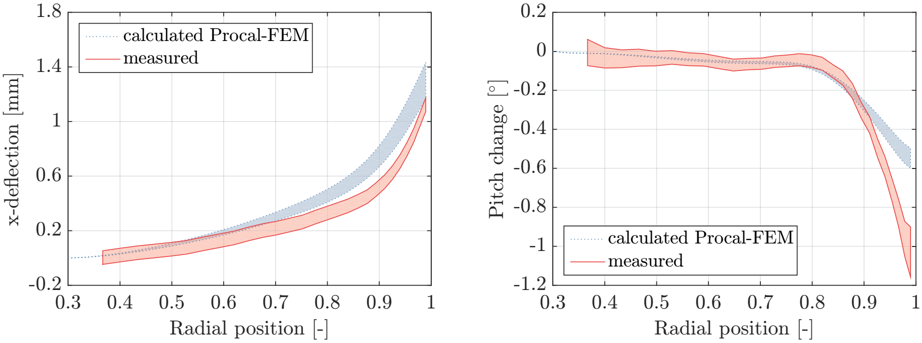

(a) Bend deformation, $J = 0.38$.

(b) Twist deformation, $J = 0.38$.

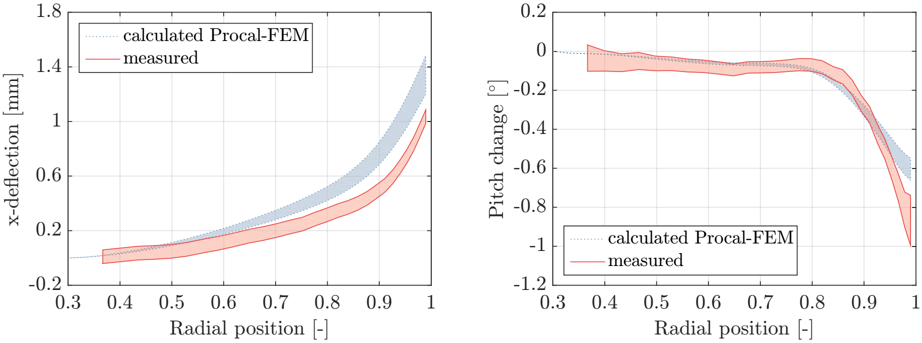

(c) Bend deformation, $J = 0.64$.

(d) Twist deformation, $J = 0.64$.

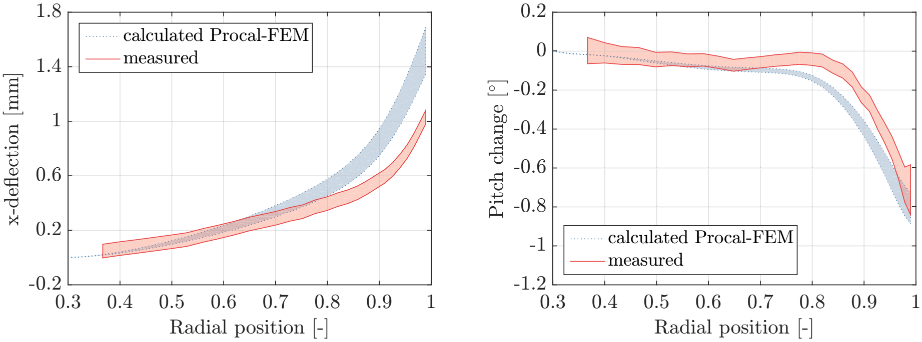

(e) Bend deformation, $J = 0.85$.

(f) Twist deformation, $J = 0.85$.

Figure 3.17: Uncertainty intervals for bend (left) and twist (right) deformations of mid-chord points of propeller 45 blade 1 against the radial position on the blade, for the measured and calculated responses.

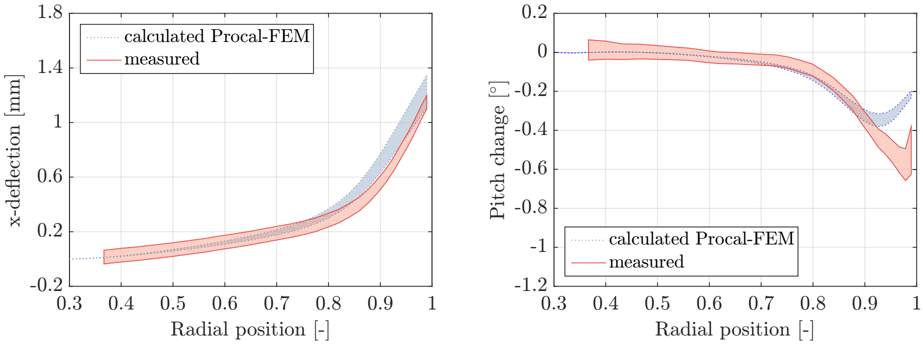

(a) Bend deformation, $J = 0.38$. (b) Twist deformation, $J = 0.38$.

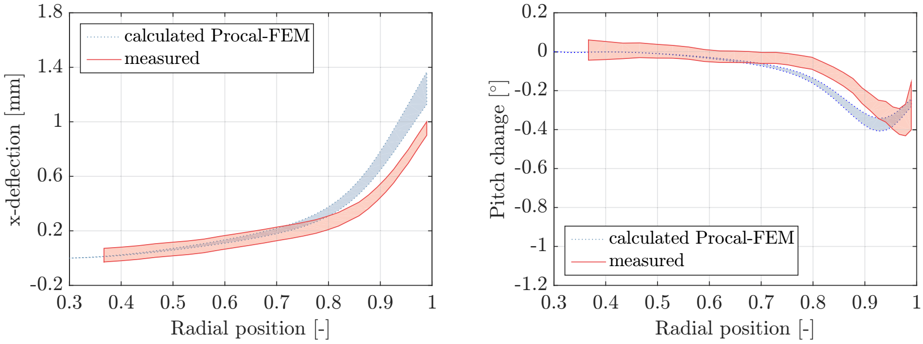

(c) Bend deformation, $J = 0.66$. (d) Twist deformation, $J = 0.66$.

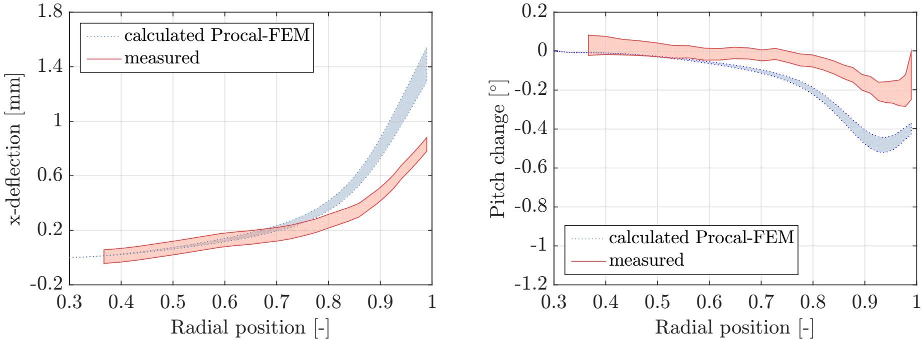

(e) Bend deformation, $J = 0.85$. (f) Twist deformation, $J = 0.85$.

Figure 3.18: Uncertainty intervals for bend (left) and twist (right) deformations of mid-chord points of propeller 90 blade 2 against the radial position on the blade, for the measured and calculated responses.

In general, the responses calculated with the BEM-FEM coupling are larger and differ more from the measured deformations than those obtained with RANS-FEM calculations. This is in line with the differences in thrust and torque computed with BEM and RANS compared to the measured open water diagram as presented in Figure 3.5. By looking at the BEM-FEM calculated response of the composite blades, it can be concluded that, for all the blades and loading conditions, the uncertainty intervals for measured and BEM-FEM calculated responses overlap up to 0.7 of the propeller radius. Overall, the best resemblance between measured and BEM-FEM calculated responses is obtained for the epoxy propeller. This is explained by the less complicated modelling of the epoxy material than that of composite material.

In general, the results obtained for epoxy and composite propellers are consistent: bend deformations are always over-predicted with the BEM-FEM coupling. For the twist deformations, it depends on the loading condition: for the lowest and the highest advance coefficient, the twist deformations are under-predicted and over-predicted, respectively. For the intermediate advance coefficient, the best agreement between measured and calculated twist deformations is obtained.

Since no RANS-FEM computations are performed for the composite propellers, it is difficult to examine whether the differences between calculated and measured responses for these propellers can be explained from the BEM modelling uncertainty. For propeller 45, it is assumed that this is the case, since qualitatively the predicted and measured response for this propeller is very similar to the response of the epoxy propeller. For propeller 90, the differences between measured and calculated response are larger, especially for the advance ratio of 0.85. Furthermore, the twist deformation of this propeller is completely different from the other two propellers, but qualitatively well-predicted with the BEM-FEM coupling.

3.10. CONCLUSIONS

In this chapter, a BEM-FEM coupling is presented for analysing the hydro-elastic behaviour of flexible propellers in uniform flows. This method has been validated with small-scale experiments and compared to the results of RANS-FEM calculations.

From the comparison between the measured open water diagram and the open water curves calculated with BEM and RANS, it can be concluded that, for the two lowest advance ratios considered in this work, the resemblance between RANS predicted and measured K_T and K_Q values is acceptable. The differences that were found for the highest advance ratio might originate from the turbulence modelling. A transition model might be more appropriate, especially for the highest advance coefficient, but was considered out of the current scope. It can be concluded that the open water curves calculated with PROCAL clearly show the limitations of BEM. For high advance coefficients ($J > 1$), the viscous effects play an increasing role and therefore the PROCAL results become inaccurate. For $J < 0.4$, a strong leading edge vortex is generated in the RANS results, and it is hypothesized that this is the reason that the results of the PROCAL calculations diverge from measured results for low advance ratios.

Interesting results are obtained from the uncertainty analysis with the RANS grids. It has been shown that convergence of the thrust and torque values does not automatically mean that the blade structural response is converged as well. Therefore, it is recommended to include a criteria on the convergence of blade bending and twisting in grid refinement studies for these types of calculations.

From the comparison of RANS-FEM and BEM-FEM results to the results of the blade deformation measurements on the epoxy propeller, it can be concluded that the bending response is well predicted with the RANS-FEM and BEM-FEM simulations. For the BEM-FEM coupling, this is despite the limitations of BEM and the complicated flow characteristics. Therefore, it is expected that, for many other propeller geometries, the BEM-FEM coupling can correctly predict the bending response. Depending on the advance ratio, a fair to poor prediction of the twist deformations of the epoxy propeller is obtained with the RANS-FEM and BEM-FEM coupling. The best agreement between measured and calculated twist deformations is obtained for the RANS-FEM results for an advance ratio of 0.64, in which leading edge vortex separation is present but limited compared to the lowest advance ratio and viscous forces might be less dominating than for the highest advance coefficient.

The results of this chapter show that the differences between measured and predicted responses of the composite propellers are larger than for the epoxy propeller. This is attributed to the more complicated FEM modelling of the composite material and most likely there is a bigger spread between design and actual material properties than for the epoxy material. Therefore, it is recommended to validate these types of fluid–structure analyses with propellers made out of isotropic and flexible material. When composite materials are used, it is recommended to do the experiments on a larger scale or with very flexible composite blades so that the measurement uncertainty becomes less dominant.

Regarding the consequences of the potential flow simplifications on the FSI response of flexible propeller, it can be concluded that, for the lowest and the highest advance coefficient, the uncertainty bandwidths of the twist deformation curves obtained with BEM-FEM and RANS-FEM overlap. This is due to the large RANS-FEM discretisation uncertainty in these calculations, rather than a correct prediction of the twist deformations with the BEM-FEM coupling, since, for these conditions, the BEM-FEM predicted twist responses deviate significantly from the measurements. The differences between measured and BEM-FEM calculated twist deformations are, for the low advance ratio, explained by the strong leading edge vortex separation, which is not computed in the BEM. For the highest advance ratio, viscous effects play an increasingly important role. It is obvious that the best resemblance between measurements, RANS-FEM and BEM-FEM results, is obtained for the intermediate advance ratio for which flow separation and viscous effects play a less dominant role. Hence, it can be concluded that, with a BEM-FEM approach, the bending response can be well predicted; however, in case of extreme flow separation and viscous effects, a BEM-FEM approach for computing the twist deformations is not recommended.

REFERENCES

[1] N. Mulcahy, B. Prusty, and C. Gardiner, "Hydroelastic tailoring of flexible composite propellers," *Ship and Offshore Structures*, vol. 5, no. 4, pp. 359–370, 2010.

[2] X. He, Y. Hong, and R. Wang, "Hydroelastic optimisation of a composite marine propeller in a non-uniform wake," *Ocean Engineering*, vol. 39, pp. 14–23, 2012.

[3] T. Taketani, K. Kimura, S. Ando, and K. Yamamoto, "Study on performance of a ship propeller using a composite material," Third International Symposium on Marine Propulsors, Launceston, Australia, 2013.

[4] S. Solomon Raj and P. Ravinder Reddy, “Bend-twist coupling and its effect on cavitation inception of composite marine propeller,” *International Journal of Mechanical Engineering and Technology*, vol. 5, no. 9, pp. 306–314, 2014.

[5] J. Kuo and W. Vorus, “Propeller blade dynamic stress,” pp. 39–69, Tenth Ship Technology and Research (STAR) Symposium, Norfolk, VA, USA, 1985.

[6] D. Georgiev and M. Ikehata, “Hydro-elastic effects on propeller blades in steady flow,” *Journal of the Society of Naval Architects of Japan*, vol. 184, pp. 1–14, 1998.

[7] Y. Young, “Time-dependent hydro-elastic analysis of cavitating propulsors,” *Journal of Fluids and Structures*, vol. 23, pp. 269–295, 2007.

[8] J. Blasques, C. Berggreen, and P. Andersen, “Hydro-elastic analysis and optimization of a composite marine propeller,” *Marine Structures*, vol. 23, pp. 22–38, 2010.

[9] H. Ghassemi, M. Ghassabzadeh, and M. Saryazdi, “Influence of the skew angle on the hydro-elastic behaviour of a composite marine propeller,” *Journal of Engineering for the Maritime Environment*, vol. 226, no. 4, pp. 346–359, 2012.

[10] H. Sun and Y. Xiong, “Fluid-structure interaction analysis of flexible marine propellers,” *Applied Mechanics and Materials*, vol. 226-228, pp. 479–482, 2012.

[11] H. Lee, M. Song, J. Suh, and B. Chang, “Hydro-elastic analysis of marine propellers based on a BEM-FEM coupled FSI algorithm,” *International Journal of Naval Architecture and Ocean Engineering*, vol. 6, no. 3, pp. 562–577, 2014.

[12] P. Maljaars and J. Dekker, “Hydro-elastic analysis of flexible marine propellers,” in *Maritime Technology and Engineering* (C. Guedes Soares and T. Santos, eds.), pp. 705–715, CRC Press-Taylor & Francis Group: London, UK, 2014.

[13] P. Atkinson and E. Glover, “Propeller hydro-elastic effects,” Propellers ’88 symposium, SNAME, Virginia Beach, VA, USA, 1988.

[14] H. Lin and J. Lin, “Nonlinear hydroelastic behavior of propellers using a finite element method and lifting surface theory,” *Journal of Marine Science and Technology*, vol. 1, no. 2, pp. 114–124, 1996.

[15] F. Salvatore, H. Streckwall, and T. van Terwisga, “Propeller cavitation modelling by CFD - Results from the VIRTUE 2008 Rome workshop,” First International Symposium on Marine Propulsors, Trondheim, Norway, 2009.

[16] G. Vaz, D. Hally, T. Huuva, N. Bulten, P. Muller, P. Becchi, J. Herrer, S. Whitworth, R. Macé, and A. Korsström, “Cavitating flow calculations for the E779A propeller in open water and behind conditions: code comparison and solution validation,” Fourth International Symposium on Marine Propulsors, Austin, TX, USA, 2015.

[17] E. Chae, D. Akcabay, and Y. Young, “Influence of flow-induced bend-twist coupling on the natural vibration responses of flexible hydrofoils,” *Journal of Fluids and Structures*, vol. 69, pp. 323–340, 2017.

[18] E. Chae, D. Akcabay, A. Lelong, J. Astolfi, and Y. Young, “Numerical and experimental investigation of natural flow-induced vibrations of flexible hydrofoils,” *Physics of Fluids*, vol. 28, p. 075102, 07 2016.

[19] J. Chen, S. Hallet, and M. Wisnom, “Modelling complex geometry using solid finite element meshes with correct composite material orientations,” *Computers and Structures*, vol. 88, pp. 602–609, 2010.

[20] G. Vaz, *Modelling of sheet cavitation on hydrofoils and marine propellers using boundary element methods.* PhD thesis, Instituto Superior Técnico, Lisbon, Portugal, 2005.

[21] G. Vaz and J. Bosschers, “Modelling of three dimensional sheet cavitation on marine propellers using a boundary element method,” Sixth International Symposium on Cavitation, Wageningen, The Netherlands, 2006.

[22] P. Maljaars, N. Grasso, M. Kaminski, and W. Lafeber, “Validation of a steady BEM-FEM coupled simulation with experiments on flexible small scale propellers,” Fifth International Symposium on Marine Propulsors, Espoo, Finland, 2017.

[23] ITTC 1978, “Report of performance committee,” 15th International Towing Tank Conference, The Hague, The Netherlands, 1978.

[24] “ReFRESCO community site.” `http://www.refresco.org`. Accessed on 12 March 2018.

[25] G. Vaz, F. Jaouen, and M. Hoekstra, “Free-surface viscous flow computations. Validation of URANS code FRESCO,” 28th International Conference on Ocean, Offshore and Arctic Engineering, Honolulu, HI USA, 2009.

[26] C. Klaij and C. Vuik, “Simple-type preconditioners for cell-centered, colocated finite volume discretization of incompressible Reynolds-averaged Navier-Stokes equations,” *International Journal for Numerical Methods in Fluids*, vol. 71(7), pp. 830–849, 2013.

[27] F. Menter, Y. Egorov, and D. Rusch, “Steady and unsteady flow modelling using the k-skl model,” Turbulence Heat and Mass Transfer, Dubrovnik, Croatia, 2006.

[28] D. Rijpkema, J. Baltazar, and J. Falcao de Campos, “Viscous flow simulations of propellers in different Reynolds number regimes,” Fourth International Symposium on Marine Propulsors, Austin, TX, USA, 2015.

[29] L. Eça and M. Hoekstra, “A procedure for the estimation of the numerical uncertainty of cfd calculations based on grid refinement studies,” *Journal of Computational Physics*, vol. 262, pp. 104–130, 2014.

[30] S. Jongsma, E. van der Weide, and J. Windt, “Implementation and verification of a partitioned strong coupled fluid-structure interaction approach in a finite volume method,” International Conference in Hydrodynamics, Egmond aan Zee, The Netherlands, 2016.

[31] S. Turek and J. Hron, “Proposal for numerical benchmarking of fluid-structure interaction between an elastic object and laminar incompressible flow,” in *Fluid-Structure Interaction - Modelling, Simulation, Optimization* (H. Bungartz and M. Schäfer, eds.), p. 371–385, Springer: Berlin/Heidelberg, Germany, 2006.

[32] J. Sutton, J. Ortue, and H. Schreier, *Image Correlation for Shape, Motion and Deformation Measurements: Basic Concepts, Theory and Applications.* Springer: New York, NY, USA, 1st ed., 2009.

[33] G. Zondervan, N. Grasso, and W. Lafeber, “Hydrodynamic design and model testing techniques for composite ship propellers,” Fifth international symposium on marine propulsion, Espoo, Finland, 2017.

[34] H. Glauert, *The elements of aerofoil and airscrew theory.* Cambridge University Press: New York, NY, USA, 2nd ed., 1947.

4

Chapter 4

Flexible propeller boundary element modelling aspects

Boundary element methods (BEMs) have been used for propeller hydrodynamic calculations since the 1990s. More recently, these methods are being used in combination with finite element methods (FEMs) in order to calculate flexible propeller fluid-structure interaction (FSI) response. The main advantage of using BEM for flexible propeller FSI calculations is the relatively low computational demand in comparison with higher fidelity methods. However, the BEM modelling of flexible propellers is not straightforward and requires several important modelling decisions. The consequences of such modelling choices depend significantly on propeller structural behaviour and flow condition. The two dimensionless quantities that characterise structural behaviour and flow condition are the structural frequency ratio and the reduced frequency. For both, general expressions have been derived for (flexible) marine propellers. Regarding the BEM-FEM coupled analyses, it is shown that a quasi-static FEM modelling does not suffice, particularly due to the fluid-added mass and hydrodynamic damping contributions that are not negligible. It is demonstrated that approximating the hydro-elastic blade response by using closed form expressions for the fluid added mass and hydrodynamic damping terms provides reasonable results, since the structural response of flexible propellers is stiffness dominated. Finally, it is shown that the significance of recalculating the hydrodynamic influence coefficients is relatively small. This might be utilized, possibly in combination with the closed form expressions for fluid added mass and hydrodynamic damping contributions, to significantly reduce the computation time of flexible propeller FSI calculations.

This chapter is based on the journal paper: P. Maljaars, M. Kaminski and H. den Besten, "Boundary element modelling aspects for the hydro-elastic analysis of flexible marine propellers," *Journal of Marine Science and Engineering,* vol. 6, no. 2, 67, 2018.

4.1. INTRODUCTION

Over the last two decades, an increased interest in flexible propellers can be noticed given the growing list of publications on the hydro-elastic analysis of flexible marine propellers. Several publications present a methodology for the numerical analysis of these types of propellers in steady and unsteady inflow conditions. These methods typically involve partitioned fluid-structure interaction (FSI) computations, meaning that the fluid and structural problem are separately solved and coupling iterations are required to converge to the fully coupled solution. For steady propeller FSI computations mainly Reynolds-averaged Navier-Stokes (RANS) methods [1–4] and boundary element methods (BEM) [5–12] have been used for solving the fluid part of the coupled problem.

The fundamental difference between RANS and BEM is that, in the latter, a potential flow is assumed, meaning that phenomena as flow separation, flow transition, boundary layers and vorticity dynamics are not captured. Results of validation studies on flexible propellers in open water conditions with BEM-FEM (finite element method) and RANS-FEM methods have been presented in Chapter 3. Despite the limitations of a BEM and the complicated flow characteristics considered in that work, a fairly good estimate of the propeller hydro-elastic response was obtained with the BEM-FEM approach. Given the relatively low computational demand of BEM in comparison to a RANS method, BEM is an attractive method for the FSI analysis of flexible propellers.

The BEM modelling of flexible propellers in steady and unsteady flow requires several modelling choices, for instance, how to include propeller deformations in the BEM analysis. Is a full geometry update necessary at every time step or can an accurate solution be obtained more efficiently by partly updating the propeller geometry every time step? How can fluid added mass and hydrodynamic damping be included: explicitly with closed form expressions [7] or implicitly in the BEM calculation? Answers to these questions do not seem to be available in literature. The main purpose of this work is to fill this knowledge gap and therefore several modelling choices have been evaluated.

The BEM models for steady and unsteady flexible propeller analyses as proposed in this chapter look similar to the model as presented in [7]. However, on the following aspects, these models are different. In [7], the BEM modelling relies on the assumption of negligibly small blade deformations. The most extensive model presented in this chapter is applicable for large elastic blade deformations, since blade deformation and vibration effects are implicitly included in the BEM calculation by updating the blade geometry and the body boundary impermeability condition at each computation step. Another difference is that the BEM modelling approach as presented in [7] is based on an explicit treatment of fluid added mass and hydrodynamic damping forces, while, in this work, both an implicit and explicit modelling of fluid added mass and hydrodynamic damping effects have been considered.

The consequences of BEM modelling choices depend significantly on flow condition and structural behaviour. The two dimensionless quantities that characterise propeller structural behaviour and flow condition are the structural frequency ratio (the ratio between the lowest excitation frequency and the fundamental wet blade natural frequency) and the reduced frequency. For both, general expressions have been derived for (flexible) marine propellers.

This chapter is structured as follows. In Section 4.2, general expressions for reduced frequencies and structural frequency ratios of flexible composite propellers are derived. Section 4.3 describes the BEM modelling of flexible propellers. Section 4.4 presents the derivation of closed form expressions for fluid added mass and hydrodynamic damping. In Section 4.5, the hydrodynamic loads on a plunging hydrofoil are investigated and important conclusions are drawn with respect to the frequency dependence of fluid added mass and hydrodynamic damping. Section 4.6 presents different BEM models for steady and unsteady flexible propeller calculations and include the results of a comparative study. Section 4.7 contains the conclusions.

4.2. FLOW AND STRUCTURAL RESPONSE CHARACTERISATION

In this section, expressions are derived to estimate the characteristics of fluid and structural response for flexible marine propellers. Section 4.2.1 provides expressions for the fundamental blade natural frequency in air and water and the structural frequency ratio. Section 4.2.2 shows a typical value for the propeller flow reduced frequency. In Section 4.2.3, estimated natural frequencies in air and water obtained for flexible versions of the highly skewed Seiun-Maru propeller have been compared to FEM calculation results.

4.2.1. STRUCTURAL FREQUENCY RATIO

The structural response of a one degree-of-freedom (1-DoF) linear mass-spring-damper system with oscillatory excitation can be assigned to one of the following regimes, depending on the ratio between excitation frequency ω and natural frequency ω_0:

- $\omega << \omega_0$; quasi-static regime, structural response dominated by stiffness.
- $\omega = \omega_0$; resonance regime, structural response dominated by damping.
- $\omega >> \omega_0$; dynamic regime, structural response dominated by mass.

In general, the fundamental natural frequency of a propeller blade is the frequency of the first bending mode. The blade natural frequencies depend on the stiffness and mass and can be computed using solution techniques available in FEM software. For a quick approximation of the first two natural frequencies in air and water, formulas are provided in [13, 14]. The fundamental dry natural frequency, ω_0^{dry}, in rad/s can be estimated for moderately skewed propellers with,

$$\omega_0^{dry} = \frac{2\pi}{3.28\,(R - r_h)^2}\sqrt{\left(\frac{E}{\rho}\right)\left(\frac{t_m}{c_m}\right)c_r\,t_r} \tag{4.1}$$

where R is the propeller radius, r_h is the hub radius, E the Young's modulus ρ the blade material density, t_m the mean blade thickness, t_r the root blade thickness, c_m the mean chord length and c_r the root chord length. The fundamental wet natural frequency of nickel aluminium bronze (NAB) propellers is generally 62–64% of the value in air [15], meaning that, for the first mode, the modal fluid added mass is approximately 2.5 times the NAB blade modal mass. Thus, the fundamental wet natural frequency, ω_0^{wet}, for any propeller material is given by,

$$\omega_0^{wet} = \frac{2\pi}{3.28\,(R-r_h)^2}\sqrt{\left(\frac{E}{\rho+2.5\rho_{NAB}}\right)\left(\frac{t_m}{c_m}\right)c_r\,t_r} \tag{4.2}$$

where ρ_{NAB} is the density of the NAB material.

From Eqs. (4.1) and (4.2), it can be concluded that, when NAB blade material with a typical Young's modulus and density of 110 GPa and 7600 kg/m^3 is replaced by a glass-epoxy composite material with a typical Young's modulus and density of 20 GPa and 1700 kg/m^3, the dry natural frequencies will slightly decrease. When a carbon-epoxy material is considered with a typical Young's modulus and density of 75 GPa and 1600 kg/m^3, the dry natural frequencies will be significantly higher than for the NAB equivalent. The fundamental wet natural frequency of a glass-epoxy blade will be considerably lower than its NAB equivalent, while for a carbon-epoxy blade, it is approximately the same. Due to the lower material density of fibre reinforced plastics, the fluid added mass has a more pronounced effect on the wet natural frequencies than in the case of a NAB propeller. From Eqs. (4.1) and (4.2), it can be concluded that the dry and wet blade frequencies scale inversely proportional with the geometrical blade scale.

Analogous to the structural frequency ratio of a 1-DoF linear mass-spring-damper system, the structural response behaviour of propeller blades can be characterised by the ratio of the frequency corresponding to the dominant blade mode and the excitation frequency. As will be shown latter, if the response of flexible propellers is stiffness dominated, then, the first blade mode will dominate the structural response. Hence, the wet fundamental blade frequency is the typical frequency used for the structural frequency ratio. The lowest excitation frequency is the shaft rotation frequency. Since the shaft rotation speed, n, is related to the blade radius by the tip speed, $v_{tip} = 2\pi nR$, the following expression for the ratio between excitation frequency $\omega = 2\pi n$ and wet fundamental blade frequency, i.e., the structural frequency ratio, $\frac{\omega}{\omega_0^{wet}}$, can be derived,

$$\frac{\omega}{\omega_0^{wet}} = \frac{3.28\,v_{tip}\,(R-r_h)^2}{2\pi R\sqrt{\left(\frac{E}{\rho+2.5\rho_{NAB}}\right)\left(\frac{t_m}{c_m}\right)c_r\,t_r}} \tag{4.3}$$

In order to avoid cavitation, a typical value for the maximum allowable tip speed is around 35 m/s. Therefore, the maximum tip speed in ship propeller design is a constant rather than a variable. By proportionally scaling the propeller dimensions R, r_h, t_m, c_m, c_r and t_r, the structural frequency ratio does not change. Hence, the structural frequency ratio is independent of the geometrical propeller scale.

4.2.2. PROPELLER FLOW REDUCED FREQUENCY

For fluids around lifting bodies, a dimensionless number exists that describes the unsteadiness of the flow and is called the reduced frequency. In the expression for the reduced frequency, k, an oscillation frequency is related to the flow speed,

$$k = \frac{\omega c}{2v_0} \tag{4.4}$$

where c is the chord length and v_0 the undisturbed flow velocity. For small reduced frequencies, the unsteadiness of the flow is negligible and a quasi-steady approach can be justified. For higher reduced frequencies, the circulatory lift reduces, which is called the lift deficiency and a phase lag between the circulatory part of the lift and the body motion exists due to the wake vorticity. Lift deficiency and phase lag functions for a flat plate foil in small amplitude unsteady motion were derived by Theodorsen [16], see Figure 4.1.

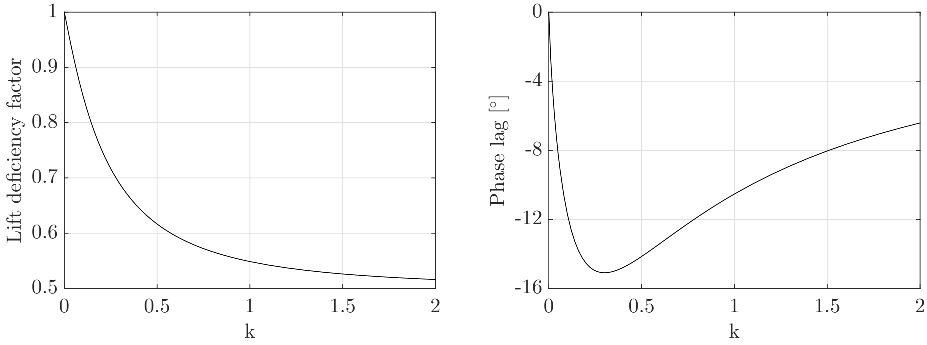

Figure 4.1: Graphical description of the Theodorsen's lift deficiency (left) and phase lag (right) functions for small amplitude unsteady motions of a flat plate foil.

The propeller flow reduced frequency at 70% of the blade radius is obtained from the shaft rotation speed and is given by,

$$k_{0.7} = \frac{2\pi n c_{0.7}}{2v_{0,0.7}} \tag{4.5}$$

where $c_{0.7}$ is the chord length at $0.7R$ and is typically 40% of the blade diameter, D. $v_{0,0.7}$ is the undisturbed flow speed at $0.7R$. $v_{0,0.7}$ is approximately $0.7\pi nD$. Hence, for conventional propellers, a typical value for the reduced frequency at $0.7R$ is 0.57. This value can be considered as highly unsteady according to Figure 4.1 and appears to be independent of the geometrical propeller scale.

4.2.3. SEIUN-MARU PROPELLER FREQUENCIES

The expressions for the fundamental natural frequencies have been verified by comparing estimated dry and wet fundamental blade frequencies to FEM calculated frequencies for the highly skewed Seiun-Maru propeller. The Seiun-Maru is a Japanese training vessel. The geometry of the propeller is available in the public domain [17] and its main particulars are summarized in Table 4.1.

Diameter	3600 mm	Boss Ratio	0.1972
Pitch Ratio (mean)	0.92	Total Skew Angle	45°
Expanded Area Ratio	0.7	Rake Angle	−3.03°
Number of Blades	5	Blade Section	Modified SRI-B

Table 4.1: Main particulars of the highly skewed Seiun-Maru propeller.

Figure 4.2 shows the dry and wet fundamental blade frequencies calculated with the FEM and estimated with Eqs. (4.1) and (4.2). For the various materials, the properties as mentioned before have been used. For the FEM calculations, a Poisson ratio of 0.3 has been adopted and the fluid added mass has been calculated with the approach described in Section 4.4. The differences between the frequencies obtained with FEM and the estimation formulas are smaller than 20% for all the cases. It is expected that, for propellers with less skew, the differences will be smaller, since Eq. (4.1) was proposed for moderately skewed propellers [13, 14]. Nevertheless, the estimated natural frequencies are accurate enough to identify the structural response regime and Eq. (4.3) is proposed to attribute the structural behaviour to stiffness, damping or mass dominated response. For a maximum allowable tip speed of 35 m/s, the structural frequency ratios as given in Figure 4.3 have been obtained for the various Seiun-Maru propellers. It can be concluded that the structural response of composite propeller blades is expected to be predominantly quasi-static and probably a quasi-static structural approach might give a good approximation of the blade response. This will be further evaluated in Section 4.6.

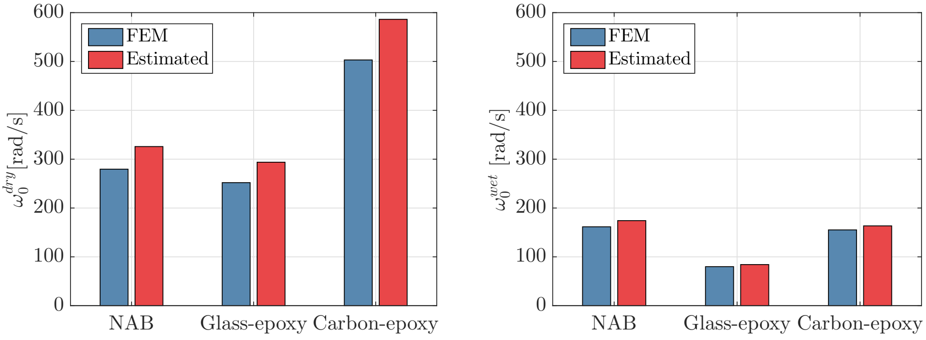

Figure 4.2: Dry (left) and wet (right) fundamental blade frequencies of the Seiun-Maru propeller for different blade materials obtained with FEM and estimated with Eqs. (4.1) and (4.2).

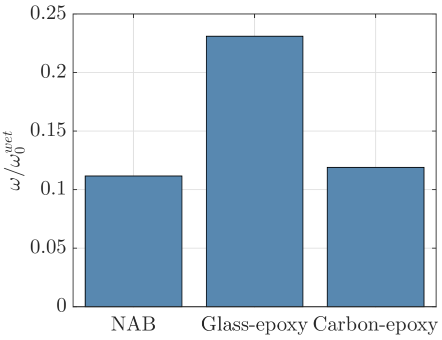

Figure 4.3: Structural frequency ratios for the various Seiun-Maru propellers.

4.3. HYDRODYNAMIC METHOD FOR PROPELLER FORCES

In the present study, the BEM PROCAL has been used for the hydrodynamic calculations. PROCAL is a panel method developed by the Maritime Research Institute Netherlands (MARIN) for the Cooperative Research Ships [18, 19]. PROCAL solves the integral equation for the velocity potential in a fluid domain based on the Morino formulation [20]. In this integral formulation, the propeller induced velocity disturbances are considered irrotational. Then, by defining the scalar variable ϕ as the disturbance velocity potential, the total velocity, $\mathbf{v}$, relative to the operating propeller becomes,

$$\mathbf{v}(\mathbf{x},t) = \mathbf{v}_0(\mathbf{x},t) + \nabla\phi(\mathbf{x},t) \tag{4.6}$$

where t is the time and $\mathbf{x}$ is the position vector in a Cartesian coordinate system. The undisturbed velocity, $\mathbf{v}_0$, can be written as the sum of the ship's effective wake field velocity and the effect of the propeller angular velocity, with the wake field velocity, $\mathbf{v}_w$, and with the propeller angular velocity, $\boldsymbol{\theta}$,

$$\mathbf{v}_0(\mathbf{x},t) = \mathbf{v}_w(\mathbf{x},t) - \boldsymbol{\theta} \times \mathbf{x} \tag{4.7}$$

The flow is assumed to be incompressible and has a constant density. Therefore, Laplace's equation applies to the disturbance velocity potential,

$$\nabla^2\phi(\mathbf{x},t) = 0 \tag{4.8}$$

Then, the fluid pressures p are related to the total velocity and the disturbance velocity potential according to Bernoulli's law,

$$\frac{\partial\phi}{\partial t} + \frac{1}{2}|\mathbf{v}|^2 + \frac{p}{\rho} + gz = \frac{p_{ref}}{\rho} + \frac{1}{2}|\mathbf{v}_0|^2 \tag{4.9}$$

For a propeller, p_{ref} is the pressure far upstream (along the shaft axis) and it obeys the hydrostatic law, $p_{ref} = p_{atm} + \rho g z_{shaft}$, with p_{atm} being the atmospheric pressure at the free surface, and submergence, z, at the shaft as, z_{shaft}. In order to solve Eq. (4.8), boundary conditions have to be imposed on the propeller surface, S_B, and wake sheet, S_W, which contains the shed vorticity. On the propeller surface, an impermeability condition is imposed,

$$\nabla\phi \cdot \mathbf{n} = -\mathbf{v}_0 \cdot \mathbf{n} \tag{4.10}$$

where $\mathbf{n}$ is the surface normal. For the wake sheet, a kinematic and dynamic boundary condition can be formulated. The kinematic boundary condition prescribes that the wake sheet is a stream-surface of the flow,

$$\mathbf{v} \cdot \mathbf{n} = 0 \tag{4.11}$$

The wake sheet itself is an imaginary surface in the flow with zero thickness. The wake sheet cannot support a pressure difference between its upper and lower side. This dynamic boundary condition can be written as,

$$\Delta p = p^+ - p^- = 0 \tag{4.12}$$

where $^+$ and $^-$ denote the upper and lower side of the wake sheet. At the blade trailing edge, this is the so-called Kutta condition.

4.3.1. INTEGRAL FORMULATION FOR DISTURBANCE POTENTIAL

A relation between the potential at any point in the fluid domain and the source strengths (normal component of the disturbance velocity at the body boundary) exists and is given by the integral equation following from the third Green's identity. Using Morino's formulation [20], this can be written as,

$$\begin{aligned}\epsilon(\mathbf{a})\phi(\mathbf{a},t) &= \int_{S_B}\left[\phi(\mathbf{b},t)\frac{\partial G(\mathbf{a},\mathbf{b})}{\partial \mathbf{n}_b} - G(\mathbf{a},\mathbf{b})\frac{\partial \phi(\mathbf{b},t)}{\partial \mathbf{n}_b}\right] dS \\ &+ \int_{S_W}\left[\Delta\phi(\mathbf{b},t)\frac{\partial G(\mathbf{a},\mathbf{b})}{\partial \mathbf{n}_b} - G(\mathbf{a},\mathbf{b})\Delta\left(\frac{\partial \phi(\mathbf{b},t)}{\partial \mathbf{n}_b}\right)\right] dS \qquad (4.13)\end{aligned}$$

where **a** is a point in the fluid domain, and **b** is a point on the fluid domain boundary surface. G is the Green's function for the Laplace equation defined as,

$$G(\mathbf{a},\mathbf{b}) = \frac{1}{r(\mathbf{a},\mathbf{b})} \qquad r(\mathbf{a},\mathbf{b}) = |\mathbf{r}| = |\mathbf{a}-\mathbf{b}| \qquad (4.14)$$

$\mathbf{n_b}$ is the outward normal at **b**. ϵ is a constant that depends on the field point **a** and is 2π if **a** is on the fluid boundary surface. With the dynamic boundary condition for the wake sheet, the following integral equation is obtained,

$$\begin{aligned}2\pi\phi(\mathbf{a},t) &= \int_{S_B}\left[\phi(\mathbf{b},t)\frac{\partial G(\mathbf{a},\mathbf{b})}{\partial \mathbf{n}_b} - \frac{\partial \phi(\mathbf{b},t)}{\partial \mathbf{n}_b}G(\mathbf{a},\mathbf{b})\right] dS \\ &+ \int_{S_W}\Delta\phi(\mathbf{b},t)\frac{\partial G(\mathbf{a},\mathbf{b})}{\partial \mathbf{n}_b} dS \qquad (4.15)\end{aligned}$$

In this integral equation, the geometry of the body and wake sheet are constant. This means that the points **b** on the fluid domain boundary surfaces and the surface areas are time invariant, which is obviously not the case for a deformable body. In that case, the integral formulation of Eq. (4.15) transforms to the unsteady flow and time-variant body integral equation,

$$\begin{aligned}2\pi\phi(\mathbf{a}(t),t) &= \int_{S_{B(t)}}\left[\phi(\mathbf{b}(t),t)\frac{\partial G(\mathbf{a}(t),\mathbf{b}(t))}{\partial \mathbf{n}_b(t)} - \frac{\partial \phi(\mathbf{b}(t),t)}{\partial \mathbf{n}_b(t)}G(\mathbf{a}(t),\mathbf{b}(t))\right] dS \\ &+ \int_{S_{W(t)}}\Delta\phi(\mathbf{b}(t),t)\frac{\partial G(\mathbf{a}(t),\mathbf{b}(t))}{\partial \mathbf{n}_b(t)} dS \qquad (4.16)\end{aligned}$$

4.3.2. NUMERICAL FORMULATION

The integral equations Eqs. (4.15) and (4.16) are solved in PROCAL by approximating the surfaces S_B and S_W by N_{total} panels. On each panel, a collocation point is defined where the integral equation is applied. Finally, a system of equations is obtained, unknown in the strengths of the source and dipole elements. With the imposed boundary conditions, the system of equations can be solved and the potential at the boundaries is obtained. This subsection briefly describes the system of equations for the non-cavitating propeller calculations considered in this work. For the formulation of the discretised problems, the discretisation parameters and equations as presented in [18] have been used. For a more thorough derivation, one is referred to that publication.

GEOMETRY DISCRETISATION

In PROCAL, the entire fluid domain boundary surface, consisting of body surface, S_B, and wake surface, S_W, is decomposed in a key part containing one blade with corresponding hub section and wake sheet and a symmetry part including the other blades, hub sections and wake sheets. The motivation for this subdivision in key- and symmetry surfaces is to obtain a smaller system of equations by utilizing the symmetry properties of ship propellers. The symmetry of flexible propellers in an unsteady flow can be questioned due to time varying deformations and will be discussed further in Section 4.6.

Figure 4.4 shows the discretised geometry of a propeller and wake. The discretisation parameters displayed in this figure have the following meaning:

- N_{surfs}: Number of surfaces, N_{surfs} is 2; the blade surfaces and the hub surfaces.
- N_{sym}: Number of symmetries for each surface. In general, N_{sym} is equal to the number of propeller blades.
- N_i: Number of panels in the streamwise direction.
- N_j: Number of panels in the radial direction.
- N_{wi}: Number of panels on the wake sheet in the streamwise direction.
- N_{wj}: Number of panels on the wake sheet in the radial direction.

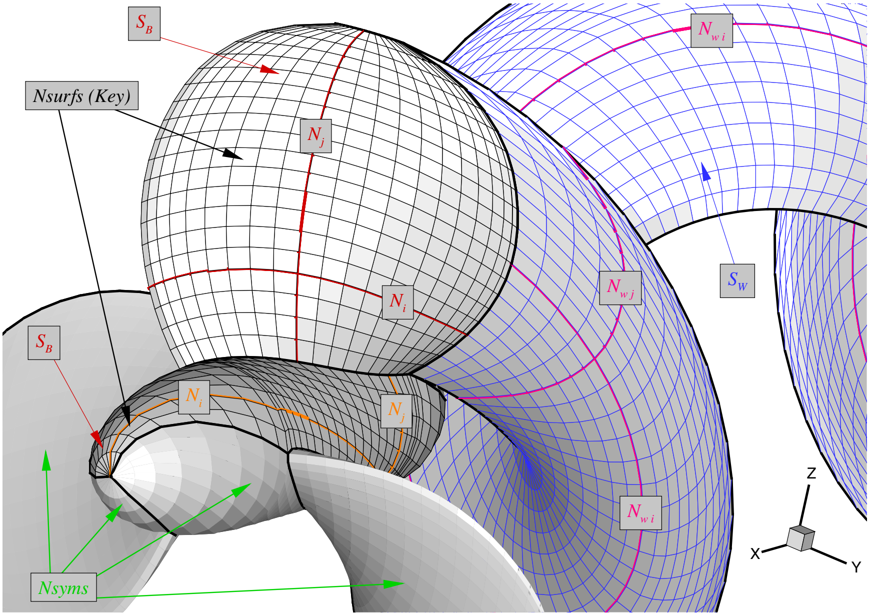

Figure 4.4: Geometry discretisation parameters for an unsteady propeller calculation. (Image taken from [18] with permission of the author.)

STEADY FLOW AND RIGID PROPELLER FORMULATION

For a rigid propeller in a steady flow, Eq. (4.15) can be discretized as follows,

$$\sum_{isurf=1}^{N_{surfs}} \sum_{isym=1}^{N_{syms}} \left[\sum_{j=1}^{N_j} \sum_{i=1}^{N_i} \left(D_{nij}\phi_{ij} - S_{nij}\sigma_{ij} \right) + \sum_{j=1}^{N_{wj}} \sum_{i=1}^{N_{wi}} W_{nij}\Delta\phi_{ij} \right] = 0 \qquad n = 1, \ldots, N_{total} \tag{4.17}$$

where D_{nij}, S_{nij} and W_{nij} are the hydrodynamic influence coeficients for the body dipoles, body sources and wake dipoles, respectively. They are defined as,

$$D_{nij} = \begin{cases} -\dfrac{1}{2\pi} \displaystyle\int_{S_{B_{ij}}} \dfrac{\mathbf{n}_{ij} \cdot \mathbf{r}_{nij}}{r_{nij}^3} dS_{B_{ij}}, & \text{if } n \text{ does not refer to element } i, j \\ 1 - \dfrac{1}{2\pi} \displaystyle\int_{S_{B_{ij}}} \dfrac{\mathbf{n}_{ij} \cdot \mathbf{r}_{nij}}{r_{nij}^3} dS_{B_{ij}}, & \text{if } n \text{ refers to element } i, j \end{cases} \tag{4.18}$$

and

$$S_{nij} = \frac{1}{2\pi} \int_{S_{B_{ij}}} \frac{1}{r_{nij}} dS_{B_{ij}} \qquad W_{nij} = -\frac{1}{2\pi} \int_{S_{W_{ij}}} \frac{\mathbf{n}_{ij} \cdot \mathbf{r}_{nij}}{r_{nij}^3} dS_{W_{ij}} \tag{4.19}$$

σ_{ij} and ϕ_{ij} are the source and dipole strengths respectively at collocation point i, j on the body surface. $\Delta\phi_{ij}$ is the dipole strength at collocation point i, j on the wake surface. N_{total} is the total number of panels for which the flow quantities have to be solved: $N_{total} = \sum_{isurf=1}^{N_{surfs}} N_i N_j$.

In case of a steady flow calculation, the symmetry surfaces can be taken into account by adding the influence coefficients of key- and symmetry surfaces together; for instance, for the dipole influence coefficients,

$$D_{nij}^{*} = D_{nij} + \sum_{isym=2}^{N_{syms}} D_{nij} \tag{4.20}$$

In general, the strength of a vortex shed by a lifting body is time invariant. This follows from the dynamic and kinematic boundary condition on the wake surface (Eqs. (4.11) and (4.12)). By using Bernoulli's theorem, this yields that the dipole strengths are time invariant following a wake particle. Furthermore, for steady flow conditions the dipole strengths $\Delta\phi_{ij}$ on the wake sheet are the same at fixed j but different i. Accordingly, the dipole influence coefficients of each j strip can be added,

$$W_{nj}^{*} = \sum_{i=1}^{N_{wi}} W_{nij}^{*} \tag{4.21}$$

Making use of the symmetry properties of the problem and the summation of the wake dipole influence coefficients, Eq. (4.17) can be written as,

$$\sum_{isurf=1}^{N_{surfs}} \left[\sum_{j=1}^{N_j} \sum_{i=1}^{N_i} D_{nij}^{*}\phi_{ij} + \sum_{j=1}^{N_{wj}} W_{nj}^{*}\Delta\phi_j \right] = \sum_{isurf=1}^{N_{surfs}} S_{nij}^{*}\sigma_{nij} \qquad n = 1, \ldots, N_{total} \tag{4.22}$$

The body source strengths are known from the impermeability boundary condition (Eq. (4.10)) and moved to the right-hand-side of the equation. The matrix defined at the left-hand-side of Eq. (4.22) is a full square matrix with dimension $\left(N_{total} + \sum_{isurf=1}^{Nsurfs} N_{wj}\right)^2$. However, the number of known source strengths is equal to N_{total}, meaning that an additional set of $\sum_{isurf=1}^{Nsurfs} N_{wj}$ equations have to be defined in order to close the system of equations. These additional equations can be deduced from the Kutta condition imposing that the tangential velocities at the blade trailing edge, computed on the upper and lower side of the body surface, are equal. The discretised translation of the Kutta condition is the Morino Kutta condition [20] expressing that the difference of the potential values between the upper and lower side of the body trailing edge is equal to the wake dipole strength,

$$\Delta\phi_j = \phi_{N_i j} - \phi_{1j} \tag{4.23}$$

This equation holds for every strip j of the propeller, resulting in a number of N_{wj} additional equations per surface. Then, the system of equations becomes,

$$\begin{bmatrix} \mathbf{D}^* & \mathbf{W}^* \\ -\mathbf{I}_u + \mathbf{I}_l & \mathbf{I} \end{bmatrix} \begin{bmatrix} \phi \\ \Delta\phi \end{bmatrix} = \begin{bmatrix} \mathbf{S}^* & \mathbf{0} \\ \mathbf{0} & \mathbf{0} \end{bmatrix} \begin{bmatrix} \sigma \\ 0 \end{bmatrix} \tag{4.24}$$

where $\mathbf{D}^*$, $\mathbf{W}^*$ and $\mathbf{S}^*$ are the body dipole, wake dipole and body source influence coefficients matrices, respectively. The matrices $\mathbf{I}_u$, $\mathbf{I}_l$ and $\mathbf{I}$ contain only ones and zeros to account for the Morino Kutta condition. Eq. (4.24) can be written as,

$$\left[\mathbf{B}^*\right]\{\phi\} = \left[\mathbf{S}^*\right]\{\sigma\} \tag{4.25}$$

where $[\mathbf{B}^*] = [\mathbf{D}^*] + [\mathbf{W}^*]\,[\mathbf{I}_u - \mathbf{I}_l]$ is the total dipole influence coefficients matrix.

UNSTEADY FLOW AND RIGID PROPELLER FORMULATION

For an unsteady flow and rigid propeller, the inflow conditions and, consequently, the source strengths depend on the blade position. In PROCAL, an unsteady problem is solved by performing k steady flow like calculations, where k is the number of revolutions, N_{revs}, required for convergence times the number of time steps during one revolution, N_t, i.e., $k = N_{revs} N_t$.

There is an important difference between a steady computation and the k-th calculation of an unsteady computation. For steady calculations, the symmetry properties of the propeller inflow and geometry are exploited to obtain a smaller system of equations. In case of an unsteady flow, the inflow is generally non-symmetric. To avoid simultaneously solving the system of equations for all key and symmetry surfaces, an iterative procedure is applied.

In this iterative procedure, the distinction between the key and symmetry surfaces is maintained. The system of equations is solved for the key surfaces only, while, for the symmetry surfaces, a previous solution of the key surfaces is taken from the time step k_{isym} when the key surfaces were at the same spatial position as the symmetry surfaces at the current time step. This means that the contribution of the symmetry surfaces can be moved to the right-hand-side of the equation. Then, the solution is obtained by solving the systems of equations every time step and a multiple number of revolutions until convergence. In this way, the discretised system of equations is given by,

$$\begin{aligned}
\sum_{isurf=1}^{N_{surfs}} \Bigg[\sum_{j=1}^{N_j}\sum_{i=1}^{N_i} D_{nij}\phi_{ij}^{k} + \sum_{j=1}^{N_{wj}} W_{n1j}\Delta\phi_{1j}^{k} \Bigg] = & \sum_{isurf=1}^{N_{surfs}} \Bigg[\sum_{j=1}^{N_j}\sum_{i=1}^{N_i} S_{nij}\sigma_{ij}^{k} + \sum_{j=1}^{N_{wj}}\sum_{i=2}^{N_{wi}} W_{nij}\Delta\phi_{ij}^{k} \Bigg] \\
& - \sum_{isurf=1}^{N_{surfs}}\sum_{isym=2}^{N_{syms}} \Bigg[\sum_{j=1}^{N_j}\sum_{i=1}^{N_i} D_{nij}\phi_{ij}^{k_{isym}} \\
& + \sum_{j=1}^{N_j}\sum_{i=1}^{N_i} S_{nij}\sigma_{ij}^{k_{isym}} - \sum_{j=1}^{N_{wj}}\sum_{i=1}^{N_{wi}} W_{nij}\Delta\phi_{ij}^{k_{isym}} \Bigg] \\
& n = 1,\ldots,N_{total} \\
& k = 1,\ldots,N_{revs}N_t
\end{aligned} \tag{4.26}$$

UNSTEADY FLOW AND FLEXIBLE PROPELLER FORMULATION

In case of an unsteady flow and flexible propeller, all the influence coefficients are time dependent, which results in,

$$\begin{aligned}
\sum_{isurf=1}^{N_{surfs}} \Bigg[\sum_{j=1}^{N_j}\sum_{i=1}^{N_i} D_{nij}^{k}\phi_{ij}^{k} + \sum_{j=1}^{N_{wj}} W_{n1j}^{k}\Delta\phi_{1j}^{k} \Bigg] = & \sum_{isurf=1}^{N_{surfs}} \Bigg[\sum_{j=1}^{N_j}\sum_{i=1}^{N_i} S_{nij}^{k}\sigma_{ij}^{k} + \sum_{j=1}^{N_{wj}}\sum_{i=2}^{N_{wi}} W_{nij}^{k}\Delta\phi_{ij}^{k} \Bigg] \\
& - \sum_{isurf=1}^{N_{surfs}}\sum_{isym=2}^{N_{syms}} \Bigg[\sum_{j=1}^{N_j}\sum_{i=1}^{N_i} D_{nij}^{k_{isym}}\phi_{ij}^{k_{isym}} \\
& + \sum_{j=1}^{N_j}\sum_{i=1}^{N_i} S_{nij}^{k_{isym}}\sigma_{ij}^{k_{isym}} - \sum_{j=1}^{N_{wj}}\sum_{i=1}^{N_{wi}} W_{nij}^{k_{isym}}\Delta\phi_{ij}^{k_{isym}} \Bigg] \\
& n = 1,\ldots,N_{total} \\
& k = 1,\ldots,N_{revs}N_t
\end{aligned} \tag{4.27}$$

Eq. (4.27) shows that the symmetry influence coefficients are time dependent as well and are equal to the influence coefficients of the symmetry surfaces on the key surfaces at time step k_{isym} when the key surfaces were at the same spatial position as the symmetry surfaces at the current time step. This means that the symmetry surface influence coefficients have to be stored in memory N_t times increasing the required computer memory significantly. Therefore, in the BEM model for unsteady flexible propeller calculations, it has been decided to use the symmetry surface influence coefficients at time step k for the symmetry surface influence coefficients of time step k_{isym} (i.e. $k_{isym} = k$ for D, S, W in the right-hand-side of Eq. 4.27). This modelling choice, together with the importance of the recalculation of the key blade influence coefficients, will be discussed further in Section 4.6.

THE KUTTA CONDITION FOR FLEXIBLE PROPELLERS

It has to be discussed whether the Kutta condition can be applied in the unsteady flexible propeller BEM model because the Kutta condition was proposed solely for steady flows [21]. Later, the Kutta condition has been modified for unsteady models, which had been questioned [22]. Some guidelines for the applicability of the Kutta condition for unsteady flows have been given in [23]. Given the relatively small deformations of flexible propellers and that the unsteady blade forces mainly originate from the non-uniform wakefield rather than from the blade vibrations, it has been assumed that the Kutta condition is still valid for flexible propeller calculations.

THE WAKE GEOMETRY OF FLEXIBLE PROPELLERS

In case of a vibrating blade, the wake geometry will follow the blade movements and therefore it has to be explained how the wake geometry has been modelled in the unsteady flexible propeller BEM model.

The effect of the wake geometry of a plunging airfoil for reduced frequencies up to 8 has been studied in the past [24]. Two different wake models were investigated. A free wake model in which the vortices shed from the trailing edge move in accordance with the induced velocities of all other vortices, in addition to the free-stream velocity and a prescribed wake model in which case the vortices are convected downstream with the free-stream velocity. The results show that the wake model has little effect on the forces generated by the airfoil. Therefore, in the unsteady flexible propeller BEM model a prescribed wake geometry is used. The wake geometry depends on the blade geometry, which means that, for every calculation step in which the blade influence coefficients are recalculated, the prescribed wake geometry is redefined and the wake influence coefficients are recomputed as well.

4.4. PROPELLER FLUID ADDED MASS AND HYDRODYNAMIC DAMPING

For the derivation of the fluid added mass and hydrodynamic damping matrices, the total disturbance potential, Φ, is decomposed in two parts. Without any assumption, Φ can be decomposed into a disturbance potential φ due to only the vibration velocities of the blade in the non-uniform wakefield and a disturbance potential ϕ for the flexible propeller in the non-uniform wakefield excluding the blade vibration velocity contribution,

$$\Phi = \phi + \varphi \tag{4.28}$$

Note that this decomposition of the total disturbance potential looks similar to what has been presented in [7], but differs on the following aspects. In [7], φ is the disturbance potential of the flexible blade in a uniform wakefield, here φ is the disturbance potential due to only the vibration velocities of the blade in the non-uniform wakefield. Here, ϕ denotes the remaining part of the disturbance potential, including the disturbance potential due to the rigid blades in a non-uniform wakefield and the disturbance potential due to the blade deformations in that wakefield. In [7], formally, the later part is included in φ, but has been neglected by assuming small blade deformations, which is expressed in the kinematic boundary condition for φ.

With $\mathbf{v}_0$ as inflow velocity, the total velocity $\mathbf{v}$ is equal to,

$$\mathbf{v} = \mathbf{v}_0 + \nabla\phi + \nabla\varphi \tag{4.29}$$

ϕ and φ can both be solved with the hydrodynamic method described before. The kinematic boundary condition for ϕ is the impermeability condition as given in Eq. (4.10), but for a deforming blade,

$$\nabla\phi \cdot \mathbf{n}(\mathbf{x},\delta) = -\mathbf{v}_0 \cdot \mathbf{n}(\mathbf{x},\delta) \tag{4.30}$$

where the surface normal vector is also a function of blade deformation, δ, not only of $\mathbf{x}$. The kinematic boundary condition for φ is

$$\frac{\partial\varphi}{\partial n} = \frac{\partial\boldsymbol{\delta}}{\partial t} \cdot \mathbf{n}(\mathbf{x},\delta) \tag{4.31}$$

This boundary condition means that the flow on the deforming blade should have the same velocity as the vibration velocity of the deformed blade itself. The term $\frac{\partial\boldsymbol{\delta}}{\partial t} \cdot \mathbf{n}(\mathbf{x},\delta)$ denotes the normal component of the blade vibration velocity. The pressures on the blade follow from the unsteady Bernoulli equation,

$$p = p_{ref} - \rho\left(\frac{\partial\phi}{\partial t} + \frac{\partial\varphi}{\partial t} + \frac{1}{2}|\mathbf{v}|^2 - \frac{1}{2}|\mathbf{v}_0|^2\right) \tag{4.32}$$

A pressure contribution due to vibration velocities only can be obtained by decomposing p in p_ϕ and p_φ, where p_φ denotes the pressure contribution due to blade vibrations and p_ϕ is the remaining force contribution,

$$\begin{aligned}
p &= p_\phi + p_\varphi \\
p_\phi &= p_{ref} - \rho\left(\frac{\partial\phi}{\partial t} + \mathbf{v}_0 \cdot \nabla\phi + \nabla\phi \cdot \nabla\varphi + \frac{1}{2}\left|\nabla\phi\right|^2\right) \\
p_\varphi &= \rho\left(-\frac{\partial\varphi}{\partial t} - \mathbf{v}_0 \cdot \nabla\varphi + \frac{1}{2}\left|\nabla\varphi\right|^2\right)
\end{aligned} \tag{4.33}$$

For a total decomposition of the pressure contribution due to ϕ and φ, the term $\nabla\phi \cdot \nabla\varphi$ in Eq. (4.33) has been neglected [7]. In addition, the second order term $\frac{1}{2}\left|\nabla\varphi\right|^2$ is excluded by assuming that φ is small compared to ϕ [7].

4.4.1. FLUID ADDED MASS AND HYDRODYNAMIC DAMPING MATRICES

To obtain closed form expressions for added mass and hydrodynamic damping, the assumptions regarding the pressure contributions of $\nabla\phi \cdot \nabla\varphi$ and $\frac{1}{2}\left|\nabla\varphi\right|^2$ are adopted, which results in,

$$p_\phi = p_{ref} - \rho\left(\frac{\partial\phi}{\partial t} + \mathbf{v}_0 \cdot \nabla\phi + \frac{1}{2}\left|\nabla\phi\right|^2\right) \tag{4.34}$$

$$p_\varphi = \rho\left(-\frac{\partial\varphi}{\partial t} - \mathbf{v}_0 \cdot \nabla\varphi\right) \tag{4.35}$$

The pressure p_ϕ can be obtained by solving ϕ with the hydrodynamic method described in Section 4.3.2. The pressure contribution p_φ can be related to blade vibration velocities and accelerations. Similar to a rigid blade problem, the vibration velocity induced potential φ

can be obtained by applying Green's identities. Hence, in discrete form,

$$\{\varphi\} = \begin{cases} \left[\mathbf{B}^*\right]^{-1}\left[\mathbf{S}^*\right]\left\{\dfrac{\partial\varphi}{\partial n}\right\}, & \text{with a constant strength vortex wake sheet} \\ \left[\mathbf{D}^*\right]^{-1}\left[\mathbf{S}^*\right]\left\{\dfrac{\partial\varphi}{\partial n}\right\}, & \text{without a vortex wake sheet} \end{cases} \tag{4.36}$$

The dipole and source influence coefficient matrices $[\mathbf{B}^*]$, $[\mathbf{D}^*]$ and $[\mathbf{S}^*]$ are taken time-invariant, assuming that the change in influence coefficients with time is negligible, which is assumed valid for small blade deformations [7]. By using the matrices with summed key- and symmetry influence coefficients, the implicit assumption is that the blade vibration problem is symmetric. The two cases of a constant strength vortex wake sheet and without a vortex wake sheet (i.e., not satisfying the Kutta condition) are introduced here because it will be shown in Section 4.5.1 that these two cases provide the upper and lower limit of the frequency dependent fluid added mass and hydrodynamic damping.

According to Eq. (4.31), $\frac{\partial\varphi}{\partial n}$ is related to the blade vibration velocities. When $\dot{\mathbf{u}}$ are the blade nodal velocities obtained from the structural calculation, the kinematic boundary condition for φ can be written as,

$$\left\{\frac{\partial\varphi}{\partial n}\right\} = [\mathbf{T}]\,[\mathbf{N}]\,\{\dot{\mathbf{u}}\} \tag{4.37}$$

where $[\mathbf{T}]$ is the transformation matrix that relates the normal velocities at the nodes to the collocation points in the BEM analysis. $[\mathbf{N}]$ is the transformation matrix to obtain the surface normal velocities from the 3D nodal velocities. According to Eq. (4.31), this transformation matrix is a function of the blade deformation. To obtain closed form expressions for added mass and hydrodynamic damping, this has to be neglected, which is assumed valid for the case of small blade deformations [7]. This means that, for the closed form expressions, the kinematic boundary condition as given in [7] is applied,

$$\frac{\partial\varphi}{\partial n} = \frac{\partial\boldsymbol{\delta}}{\partial t}\cdot\mathbf{n}(\mathbf{x}) \tag{4.38}$$

where $\mathbf{n}$ is for the undeformed blade geometry. In case of a constant strength vortex wake sheet, the pressures, $p_{\mathbf{v}_0\nabla\varphi}$, due to $\mathbf{v}_0\nabla\varphi$ at the BEM collocation points are given by,

$$\left\{p_{\mathbf{v}_0\nabla\varphi}\right\} = -\rho\,[\mathbf{V}_0]\,[\nabla]\left[\mathbf{B}^*\right]^{-1}\left[\mathbf{S}^*\right][\mathbf{T}]\,[\mathbf{N}]\,\{\dot{\mathbf{u}}\} \tag{4.39}$$

where $[\mathbf{V}_0]$ is the matrix with inflow velocities and $[\nabla]$ the discrete form of the gradient operator. Then, the forces at the BEM collocation points, $f_{\mathbf{v}_0\nabla\varphi}$, are obtained after multiplying the pressures by the BEM panel areas,

$$\left\{f_{\mathbf{v}_0\nabla\varphi}\right\} = -\rho\,[\mathbf{A}]\,[\mathbf{V}_0]\,[\nabla]\left[\mathbf{B}^*\right]^{-1}\left[\mathbf{S}^*\right][\mathbf{T}]\,[\mathbf{N}]\,\{\dot{\mathbf{u}}\} \tag{4.40}$$

where $[\mathbf{A}]$ is the diagonal matrix with the BEM panel areas. The 3D force components at the FEM nodes are equal to,

$$\left\{\mathbf{f}_{\mathbf{v}_0\nabla\varphi}\right\} = -\rho\,[\mathbf{N}]^T\,[\mathbf{T}]^T\,[\mathbf{A}]\,[\mathbf{V}_0]\,[\nabla]\left[\mathbf{B}^*\right]^{-1}\left[\mathbf{S}^*\right][\mathbf{T}]\,[\mathbf{N}]\,\{\dot{\mathbf{u}}\} \tag{4.41}$$

from which it can be concluded that the hydrodynamic damping matrix, $[\mathbf{C}_h]$, is equal to,

$$[\mathbf{C}_h] = -\rho\,[\mathbf{N}]^T\,[\mathbf{T}]^T\,[\mathbf{A}]\,[\mathbf{V}_0]\,[\nabla]\,\left[\mathbf{B}^*\right]^{-1}\left[\mathbf{S}^*\right][\mathbf{T}]\,[\mathbf{N}] \tag{4.42}$$

Due to $\mathbf{v}_0$, the hydrodynamic damping matrix depends on the inflow velocity. Hence, in case of a propeller operating in a non-uniform flow, the hydrodynamic damping matrix will change in accordance with the blade rotation angle. To arrive at a constant hydrodynamic damping matrix, the author proposes to decompose the non-uniform propeller inflow velocity into a circumferentially averaged constant velocity field in which the free-stream velocity only depends on the radial position and a disturbing flow field, denoted with $\bar{\mathbf{v}}_0$ and $\tilde{\mathbf{v}}_0$, respectively. Then, the total inflow velocity is,

$$\mathbf{v}_0\,(\mathbf{x}, t) = \bar{\mathbf{v}}_0\,(\mathbf{x}) + \tilde{\mathbf{v}}_0\,(\mathbf{x}, t) \tag{4.43}$$

The constant hydrodynamic damping matrix is then equal to,

$$[\mathbf{C}_h] = -\rho\,[\mathbf{N}]^T\,[\mathbf{T}]^T\,[\mathbf{A}]\left[\bar{\mathbf{V}}_0\right][\nabla]\left[\mathbf{B}^*\right]^{-1}\left[\mathbf{S}^*\right][\mathbf{T}]\,[\mathbf{N}] \tag{4.44}$$

in case of a constant strength vortex wake sheet. Without a vortex wake sheet, the constant hydrodynamic damping matrix is,

$$[\mathbf{C}_h] = -\rho\,[\mathbf{N}]^T\,[\mathbf{T}]^T\,[\mathbf{A}]\left[\bar{\mathbf{V}}_0\right][\nabla]\left[\mathbf{D}^*\right]^{-1}\left[\mathbf{S}^*\right][\mathbf{T}]\,[\mathbf{N}] \tag{4.45}$$

In a similar way, the fluid added mass matrix can be derived. Analogous to Eq. (4.37), it can be written,

$$\left\{\frac{\partial^2\varphi}{\partial t\partial n}\right\} = [\mathbf{T}]\,[\mathbf{N}]\,\{\ddot{\mathbf{u}}\} \tag{4.46}$$

In case of a constant strength vortex wake sheet, the pressures due to $\frac{\partial\varphi}{\partial t}$, $p_{\frac{\partial\varphi}{\partial t}}$, are given by,

$$\left\{p_{\frac{\partial\varphi}{\partial t}}\right\} = -\rho\left[\mathbf{B}^*\right]^{-1}\left[\mathbf{S}^*\right][\mathbf{T}]\,[\mathbf{N}]\,\{\ddot{\mathbf{u}}\} \tag{4.47}$$

Then, the forces at the BEM collocation points, $f_{\frac{\partial\varphi}{\partial t}}$, are

$$\left\{f_{\frac{\partial\varphi}{\partial t}}\right\} = -\rho\,[\mathbf{A}]\left[\mathbf{B}^*\right]^{-1}\left[\mathbf{S}^*\right][\mathbf{T}]\,[\mathbf{N}]\,\{\ddot{\mathbf{u}}\} \tag{4.48}$$

The 3D force components at the nodes are equal to,

$$\left\{\mathbf{f}_{\frac{\partial\varphi}{\partial t}}\right\} = -\rho\,[\mathbf{N}]^T\,[\mathbf{T}]^T\,[\mathbf{A}]\left[\mathbf{B}^*\right]^{-1}\left[\mathbf{S}^*\right][\mathbf{T}]\,[\mathbf{N}]\,\{\ddot{\mathbf{u}}\} \tag{4.49}$$

from which it can be concluded that the fluid added mass matrix, $[\mathbf{M}_h]$, is equal to,

$$[\mathbf{M}_h] = -\rho\,[\mathbf{N}]^T\,[\mathbf{T}]^T\,[\mathbf{A}]\left[\mathbf{B}^*\right]^{-1}\left[\mathbf{S}^*\right][\mathbf{T}]\,[\mathbf{N}] \tag{4.50}$$

in case of a constant strength vortex wake sheet. Without a vortex wake sheet, the fluid added mass matrix is,

$$[\mathbf{M}_h] = -\rho\,[\mathbf{N}]^T\,[\mathbf{T}]^T\,[\mathbf{A}]\left[\mathbf{D}^*\right]^{-1}\left[\mathbf{S}^*\right][\mathbf{T}]\,[\mathbf{N}] \tag{4.51}$$

In the derivation of the closed form expressions for added mass and hydrodynamic damping, the following assumptions have been made:

(1) $\frac{1}{2}\left|\nabla\varphi\right|^2$ and $\nabla\phi\cdot\nabla\varphi$ are negligible.

(2) The influence coefficient matrices can be taken time-invariant.

(3) The summed key- and symmetry influence coefficients matrices can be used.

(4) The blade deformation can be neglected in the kinematic boundary condition.

(5) The fluctuating part of the hydrodynamic damping in case of an non-uniform wakefield is negligible.

It will be shown in the next section that the first assumption is only valid for high reduced frequencies for which conditions the hydrodynamic damping force is small anyway and the added mass force dominates. Assumptions 2 and 5 will be evaluated in Section 4.6 by comparing results of fully coupled FSI analyses of the Seiun-Maru propeller obtained from different BEM modelling approaches.

4.4.2. FLUID ADDED MASS VALIDATION

In order to validate the fluid added mass matrix calculation, the natural frequencies of the four Boswell propellers [25] have been calculated and compared to results as presented in [7]. The four propellers were designed to study the influence of the skew angle on propeller performance and cavitation behaviour and have skew angles of 0°, 36°, 72° and 108°, identified by number 4381, 4382, 4383 and 4384, respectively. The natural frequencies of the propellers have been calculated with the commercial FEM package Marc/Mentat using the following material properties: fluid density 1000 kg/m^3, blade material density 2800 kg/m^3, Young's modulus 75 GPa and Poisson ratio 0.33. The FEM models consist of one propeller blade without the hub part. The hub has not been modelled. The blade has been fully clamped at the blade-hub interface. The models were discretised by quadratic solid elements using a 29 × 30 × 4 element distribution, meaning that 29, 30 and 4 elements are distributed in chord-wise, radial and through-thickness direction, respectively [26, 27]. The added mass matrices have been computed from Eq. (4.51) and diagonalised with a Hinton-Rock-Zienkiewicz lumping technique, which means that the diagonal entries of the full added mass matrix are scaled with the ratio of the sum of the entries that contribute to the motion in the same direction over the sum of the diagonal entries that contribute to the motion in that direction [7].

Figure 4.5 shows the dry and wet natural frequencies for the four propeller blades from Young [7] and present work. By comparing the results, it can be concluded that natural frequencies from present work are consistent with the results as presented by Young [7]. The dry natural frequencies of [7] and present work are close together. The biggest differences are in the wet natural frequencies, probably due to a slightly different added mass calculation, for instance, by calculating the added mass from the influence coefficients of one blade only instead of including the influence coefficients of the symmetry blades in the added mass calculation.

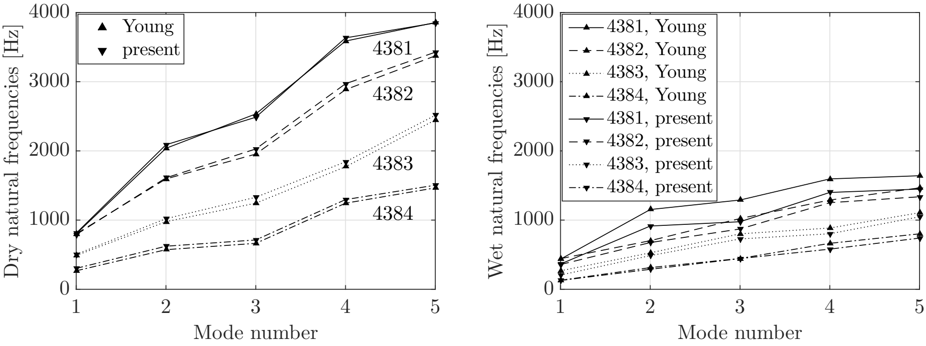

Figure 4.5: Comparison of the dry (left) and wet (right) natural frequencies of the Boswell propeller blades from Young [7] and present work.

4.5. HYDRODYNAMIC LOADS ON A PLUNGING HYDROFOIL

In this section, the hydrodynamic loads on a plunging hydrofoil are investigated in order to evaluate the modelling of fluid added mass and hydrodynamic damping with the closed form expressions. The problem considered here concerns the hydrodynamic loads on a prismatic hydrofoil with a span of 20 m, chord of 1 m, a NACA 0012 cross section profile and a zero angle of attack for a prescribed sinusoidal plunge motion in water (density ρ is 1000 kg/m^3). The flow velocities, $\mathbf{v}_0$, in (m/s) are characterized by the following three velocity components,

$$\mathbf{v}_0 = \begin{bmatrix} v_x & v_y & v_z \end{bmatrix}^T = \begin{bmatrix} 1 & 0.1 \cdot sin(\omega t) & 0 \end{bmatrix}^T \tag{4.52}$$

where v_x and v_z are the chord- and spanwise velocity components, respectively. The plunge velocity is denoted by v_y and ω is the plunge frequency.

4.5.1. FLUID ADDED MASS AND HYDRODYNAMIC DAMPING OF A PLUNGING HYDROFOIL

The fluid added mass and hydrodynamic damping of the plunging hydrofoil have been obtained in two different ways. The first approach is from the closed form expressions for fluid added mass and hydrodynamic damping (Eqs. (4.44), (4.45) and (4.50), (4.51)) and taking the sum of matrix elements that contribute to the plunge motion. The second approach is by obtaining the hydrodynamic loads on a plunging hydrofoil from an unsteady PROCAL calculation.

The values obtained from the closed form expressions for the fluid added mass and hydrodynamic damping depend on the wake model. The two limit cases are a constant strength vortex wake sheet like in steady flow calculations and without a vortex wake sheet. Without a vortex wake sheet, the fluid added mass of the hydrofoil in water as obtained from Eq. (4.51) is approximately 16×10^3 kg, (note that this corresponds to the added mass of flat plate with length 20 m and width 1 m). For that case, the hydrodynamic damping obtained with Eq. (4.45) is zero, since without a vortex wake sheet the circulation is zero.

By satisfying the Kutta condition and assuming a constant strength vortex wake sheet, the added mass of the hydrofoil calculated from Eq. (4.50) is much bigger: 46 × 10^3 kg. A hydrodynamic damping of 52 × 10^3 kg/s has been obtained from Eq. (4.44) in that case. As a sanity check, this value has been compared to the lift force of a NACA 0012 profile, for instance presented in [28]. For the maximum plunge velocity of 0.1 m/s, the angle of attack is approximately 0.1 rad. For this small angle, the lift force is approximately equal to the force in plunge direction, which is $0.1 \times 52 \times 10^3 = 52 \times 10^2$ N; then, the lift coefficient is equal to 0.52, which corresponds to [28].

In the second approach, the prescribed plunge velocity is imposed on a BEM model of the hydrofoil and the forces are calculated with an unsteady PROCAL calculation. The hydrodynamic forces in plunge direction are subdivided in a circulatory and non-circulatory part. The non-circulatory part is the force contribution from the acceleration potential in the Bernoulli equation and is due to the body acceleration. The circulatory part is the remaining force contribution and contains the hydrodynamic damping part.

The non-circulatory plunge force is subdivided into two force contributions, one 90° out of phase with the body acceleration and the other in antiphase with the body accelerations. The added mass is obtained by dividing the latter part by the body acceleration. In the same way, the hydrodynamic damping is determined: the hydrodynamic damping is the circulatory plunge force in antiphase with the body velocity, divided by the body velocity.

Figure 4.6 shows the results obtained for the fluid added mass and hydrodynamic damping. The results show that fluid added mass and damping depend on the reduced frequency of the plunging motion. The low frequency limits are obtained for a constant strength vortex wake sheet (Eqs. (4.44) and (4.50)). The high frequency limits are obtained from the closed form expressions without taking into account the vortex wake sheet (Eqs. (4.45) and(4.51)). This shows that the assumption of a constant added mass [29] and hydrodynamic damping is only valid for sufficiently low or high reduced frequencies.

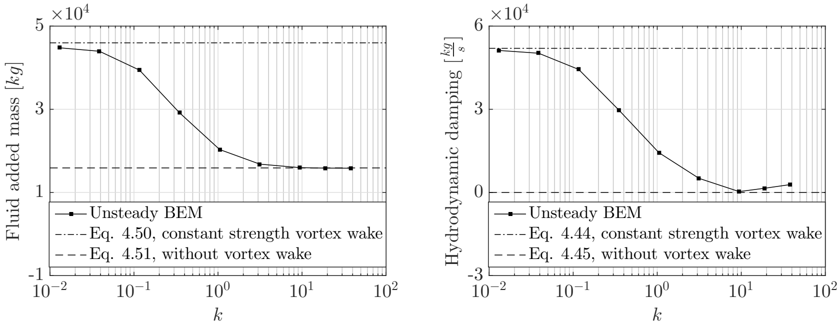

Figure 4.6: Added mass (left) and hydrodynamic damping (right) of the hydrofoil for different plunge frequencies.

4.5.2. CIRCULATORY AND NON-CIRCULATORY FORCES ON A PLUNGING HYDROFOIL

Figure 4.7 shows for which reduced frequencies the circulatory and non-circulatory forces in plunge direction can be correctly predicted with the closed form expressions for fluid added mass and hydrodynamic damping. The left graph of Figure 4.7 presents the amplitude of the non-circulatory force in plunge direction obtained with the unsteady BEM as a function of the reduced frequency, together with the force amplitudes which are obtained from the high and low frequency limit of the fluid added mass force. The right graph shows something similar but then for the circulatory force in plunge direction. Figure 4.8 presents the phase shift between the circulatory plunge force and the body velocity, and non-circulatory plunge force and body acceleration. The most important results of Figures 4.7 and 4.8 can be summarized as follows:

- For small reduced frequency, the amplitude of the circulatory plunge force is underestimated with the low frequency limit of the hydrodynamic damping force as obtained from Eq. (4.44). This is a result of neglecting the pressure term due to $\frac{1}{2}\nabla\varphi^2$ in the derivation of the closed form expressions. However, the circulatory plunge force is well in antiphase with the body velocity.

- For small reduced frequency, the amplitude of the non-circulatory plunge force agrees well with the low frequency limit of the added mass force as obtained from Eq. (4.50). However, the non-circulatory plunge force is not perfectly in antiphase with the body acceleration. This phase lag is due to unsteady wake effects.

- For high reduced frequency, the amplitude of the non-circulatory plunge force agrees well with the high frequency limit of the added mass force as obtained from Eq. (4.51). Furthermore, the non-circulatory plunge force is well in antiphase with the body acceleration.

- For high reduced frequency, the amplitude of the circulatory plunge force approaches the high frequency limit of the hydrodynamic damping force as obtained from Eqs. (4.45).

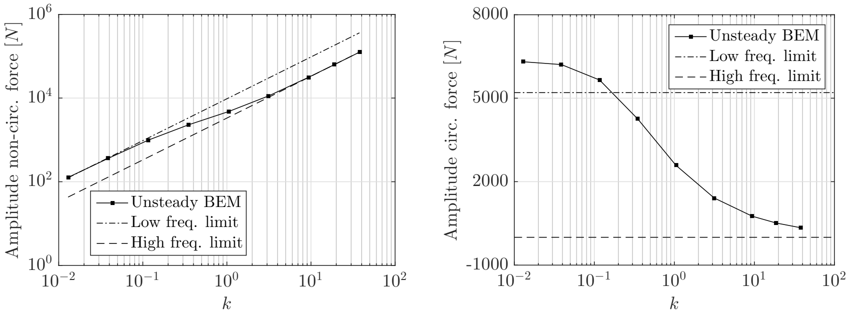

Figure 4.7: Amplitude of the non-circulatory (left) and circulatory forces (right) in plunge direction for different plunge frequencies.

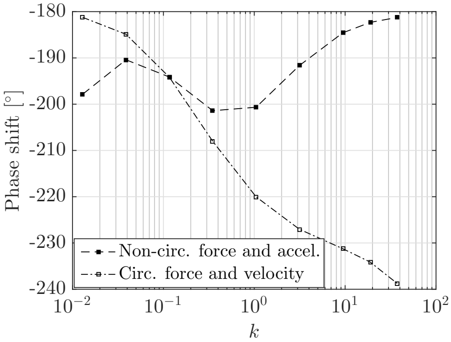

Figure 4.8: Phase shift between the non-circulatory plunge force relative to the acceleration and the circulatory plunge force relative to the velocity for different plunge frequencies.

This means that, only for high reduced frequencies ($k > 4$), the plunge forces can be correctly estimated with the closed form expressions. As revealed in Section 4.2.2, the reduced frequency for propeller blade vibrations excited by the first shaft harmonic is around 0.5. Hence, the question that remains is how accurately the hydro-elastic response of flexible propellers is predicted by modelling the fluid added mass and hydrodynamic damping effects with the closed form expressions. This will be discussed further in Section 4.6.

4.6. STEADY AND UNSTEADY FLEXIBLE PROPELLER CALCULATIONS WITH DIFFERENT BEM-FEM COUPLED APPROACHES

The following questions regarding the FSI modelling of flexible propellers with a BEM-FEM coupled approach could be raised based on what has been discussed:

(1) How important is the re-calculation of key and symmetry body and wake influence coefficients in the BEM modelling?

(2) Is it valid to use for the symmetry surface influence coefficients at time step k_{isym} the symmetry influence coefficients of time step k, in order to reduce computer memory?

(3) Can the hydro-elastic response of flexible propellers be accurately predicted by modelling the fluid added mass and hydrodynamic damping effects with the closed form expressions and what has been taken for the the fluid added mass and hydrodynamic damping matrix, i.e., the low frequency limit, high frequency limit or something in between?

(4) As the structural response is stiffness dominated, would a quasi-static FEM calculation be sufficient?

In order to give answers to these modelling questions, different BEM-FEM coupling approaches were implemented and the hydro-elastic responses of quasi-isotropic glass-epoxy and carbon-epoxy Seiun-Maru propellers in uniform and non-uniform flows have been compared. In order to judge from these results which modelling approach is acceptable and which is not, criteria on accuracy levels have to be given. The purpose of the BEM-FEM coupled calculations is to predict correctly the hydro-elastic behaviour of flexible propellers. A measure for the hydro-elastic behaviour from a propeller performance perspective is the blade thrust change due to flexibility. An accuracy level of 10% on the blade thrust change is considered as acceptable. This seems significant but means that an accuracy of 1% in blade thrust is required in case the blade thrust change is 10% of the blade thrust itself. Additionally, in order to assess the structural response results, an accuracy level of 5% is considered as acceptable.

4.6.1. BEM MODELS FOR STEADY AND UNSTEADY FLEXIBLE PROPELLER CALCULATIONS

In contrast to standard PROCAL applications, for flexible propellers, the blades deform and for unsteady cases induce fluid velocities and accelerations due to blade vibrations as well. As a result of blade deformations:

- panel normal vectors become time-dependent, which is reflected in the panel source strengths.
- pressures have to be evaluated from the computed velocity potentials on a modified grid.
- influence coefficients of key- and symmetry blades and wake surfaces become time-dependent.

The blade vibration velocity and acceleration hydrodynamic effects can be included in the FSI calculations in two ways: either implicitly by imposing the kinematic boundary condition of Eq. (4.31) in the PROCAL calculations or explicitly by including the fluid added mass and hydrodynamic damping effects in the FSI calculations with the closed form expressions of Eqs. (4.44), (4.45) and (4.50), (4.51).

Based on this, the following three BEM models have been proposed:

- Fully geometry dependent BEM model with fluid added mass and hydrodynamic damping effects implicitly included, denoted by FGDI-BEM.
- Fully geometry dependent BEM model with fluid added mass and hydrodynamic damping effects explicitly included, denoted by FGDE-BEM.
- Partially geometry dependent BEM model with fluid added mass and hydrodynamic damping effects implicitly included, denoted by PGDI-BEM.

Uniform flow calculations can be considered as a special case of an unsteady calculation without time effects, blade velocities and accelerations, which means the implicit or explicit modelling of fluid added mass and hydrodynamic damping is irrelevant and the different BEM models are denoted by FGD-BEM and PGD-BEM.

FGDI-BEM MODEL

In the FGDI-BEM model, all the geometry dependent items in a PROCAL calculation, including source strengths, blade and wake influence coefficients, are recalculated based on the deformed blade geometry and the pressures are evaluated on the modified BEM model. Note that, for the symmetry surface influence coefficients of time step k_{isym}, the symmetry influence coefficients of time step k have been used in order to save computer memory. The blade vibration velocity and acceleration effects are implicitly included in the BEM calculation by imposing Eq. (4.31) as an additional boundary condition supplementary to the boundary condition of Eq. (4.30).

FGDE-BEM MODEL

The FGDE-BEM model is the same as the FGDI-BEM model except that PROCAL solves only the disturbance velocity potential without the contribution of blade vibration velocities, ϕ, from the kinematic boundary condition of Eq. (4.30). The blade vibration velocity and acceleration effects are included in the FSI analyses by means of the closed form expressions for fluid added mass and hydrodynamic damping. The main advantage of this approach is that the fluid added mass and hydrodynamic damping can be explicitly included in the structural computation, which stabilizes the FSI solution and reduces CPU time [30].

The question that remains is which fluid added mass and hydrodynamic damping matrix have to be taken. The reduced frequency for propeller blade vibration flows is around 0.5 for an oscillation frequency equal to the shaft rotation rate. For higher harmonics, the reduced frequency is obviously a multiple of the fundamental reduced frequency. From the left graph of Figure 4.6, it can be concluded that, for such high reduced frequencies, the fluid added mass is approaching the high frequency limit. Therefore, the added mass matrix has been computed without taking the vortex wake sheet into account, i.e., Eq. (4.51).

Based on the right graph of Figure 4.6, 50% of the low frequency limit of the hydrodynamic damping term, i.e., Eq. (4.44), has been taken for the hydrodynamic damping matrix.

PGDI-BEM MODEL

In the PGDI-BEM model, blade vibration and velocity effects have been incorporated in the same way as in the FGDI-BEM model. The difference is to which level the blade geometry update is included in the BEM calculations. In the PGDI-BEM model for each time step, source strengths are recalculated from the deformed blade geometry and pressures and forces are evaluated on the modified BEM model. However, the blade and wake influence coefficients are kept constant throughout the analyses. This can reduce the CPU time significantly. The blade and wake influence coefficients used in the unsteady calculations with the PGDI-BEM model are obtained for the averaged deformed blade geometry. The average deformed blade geometry is calculated from a steady BEM-FEM computation with the circumferentially averaged wakefield, $\bar{\mathbf{v}}_0$, for the inflow velocities. The steady calculations with the PGD-BEM model are conducted with the hydrodynamic influence coefficients of the undeformed propeller blade geometry.

4.6.2. STEADY AND UNSTEADY BEM-FEM COUPLING

In Chapter 3, the BEM-FEM coupling for the steady analyses has been presented, including a validation study. The coupling is based on a partitioned approach in which fluid and structure problem are solved with separate codes. For the fluid part, any of the PROCAL BEM models as described above has been used. For the structural modelling, the FEM package Marc/Mentat has been used. The blade FEM modelling has been described in previous chapters. In summary, the FEM models consist of one propeller blade without the hub part. The hub has not been modelled. The blade has been fully clamped at the blade-hub interface. The models are discretised by quadratic solid elements using a 29 × 30 × 4 element distribution, meaning that 29, 30 and 4 elements are distributed in chord-wise, radial and through-thickness direction, respectively. The unsteady FEM calculations have been conducted in modal space and a model reduction is applied by using only the first 40 mode shapes.

Since a partitioned FSI approach has been adopted, coupling iterations between BEM and FEM solver are required to converge to the monolithic solution. For steady analyses, these coupling iterations converge in any case. However, without a dedicated coupling algorithm instabilities occur in unsteady analyses due to strong fluid added mass effects. Special attention has been paid to the coupling algorithm for the unsteady BEM-FEM analyses. A detailed description of this BEM-FEM coupling is out of the scope of this chapter and has been be revealed in Chapter 5 and Appendix A. In short, in the unsteady BEM-FEM coupling, the periodicity of the problems is utilized by coupling the BEM and FEM solver on period level instead per time step. This time periodic coupling [31] is the most obvious approach to couple PROCAL with the structural problem because PROCAL is completely periodical in nature. Think of the vortex wake shedding and the use of symmetry blades and therefore a non-periodic solution could not be treated in PROCAL. Furthermore, the time periodic approach allows for first letting PROCAL converge before new disturbances enter the equations. After all, the PROCAL computations itself are already iterative and, in strongly coupled FSI problems, it is advantageous to have the inner loop converge first. In order to stabilize the coupling iterations on period level, a Quasi-Newton inverse least squares partitioned solution method has been implemented [32].

The unsteady BEM-FEM coupling procedure has been verified with the FSI solutions of a pitching hydrofoil in water with a span of 1 m, chord of 0.1 m, a NACA 0009 cross section profile and a zero initial angle of attack subjected to a controlled external moment, M_0, equal to $34.9 \cdot sin(\omega t)$ Nm [33]. The inflow velocity, v_0, is equal to 5 m/s. For this problem, the equation for the pitch motion, θ, reads,

$$I_\theta \ddot{\theta} + C_\theta \dot{\theta} + K_\theta \theta = M_0 + M_{fluid} \tag{4.53}$$

where I_θ is the structural moment of inertia equal to 1.429×10^{-3} kg·m^2, C_θ is the structural damping parameter equal to 0.096 kg·m^2/s, K_θ is the structural torsional stiffness equal to 1000 Nm. M_{fluid} is the moment exerted by fluid forces. M_{fluid} has been subdivided in fluid added mass, fluid damping and fluid stiffness forces defined by the following approximation formulas [29],

$$M_{fluid} = -M_f \ddot{\theta} - C_f \dot{\theta} - K_f \theta \tag{4.54}$$

$$
\begin{aligned}
M_f &= \frac{\pi}{128}\rho c^4 \\
C_f &= \begin{cases} 0.105k^{-0.4}\rho v_0 c^3, & \text{for k}\leq 4 \\ 0.010k^{0.6}\rho v_0 c^3, & \text{for k}\geq 12 \end{cases} \\
K_f &= \begin{cases} (0.090k-0.80)\,\rho v_0^2 c^2, & \text{for k}\leq 4 \\ (0.065k-0.90)\,\rho v_0^2 c^2, & \text{for k}\geq 12 \end{cases}
\end{aligned}
\tag{4.55}
$$

The monolithic solution is obtained by moving the fluid forces from the right-hand-side of the equation of motion to the left-hand-side and then the exact solution for θ can be computed. The coupling procedure solution is obtained by keeping the fluid forces on the right-hand-side as unknowns and iterations are required to converge to the monolithic solution. Figure 4.9 shows the monolithic solution and the time periodic coupling solution for two of the cases with fluid added mass to structural mass ratio of 1.72 as also presented in [33]. For both cases, the time period coupling procedure converges to the monolithic solution, for the $\omega = 4.83$ rad/s case in four coupling iterations and for the case with $\omega = 483$ rad/s in seven coupling iterations. This shows that the coupling procedure is appropriate for periodic FSI problems with strong fluid added mass effects, like in flexible propeller FSI analyses.

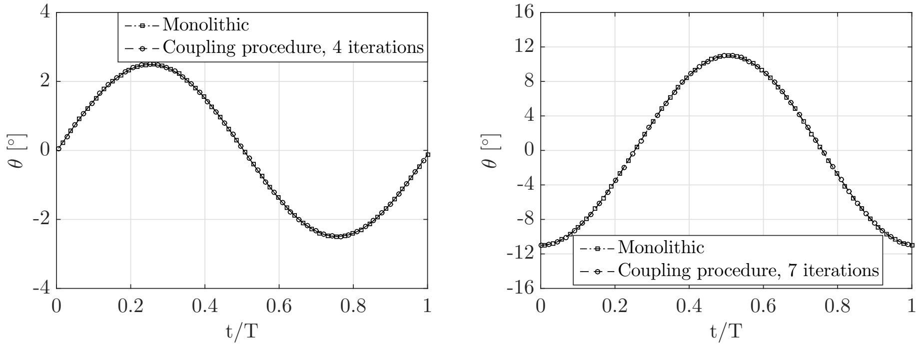

Figure 4.9: Comparison of the monolithic and coupling procedure solution of the predicted pitch motion, θ, as a function of the normalized time, t/T, for $\omega = 4.83$ rad/s (left) and $\omega = 483$ rad/s (right) graph.

4.6.3. STEADY ANALYSES WITH FGD-BEM MODEL AND PGD-BEM MODEL

In order to obtain an answer to the first modelling question raised in the beginning of this section, calculations were performed with the FGD-BEM and PGD-BEM model on the Seiun-Maru propeller for various uniform flow conditions. All steady BEM-FEM coupled calculations are performed for a quasi-isotropic glass-epoxy material, with material properties as presented before. The advance ratio J, free stream velocity V, propeller rotation rate and blade thrust T_0 in undeformed configuration are given in Table 4.2. The rotation rate and advance speeds were selected in such a way that the undeformed propeller thrust is more or less the same for all the flow conditions and the power required for the advance ratio of 0.7 corresponds roughly to the maximum continuous rating power of the Seiun-Maru vessel [34].

J	V [m/s]	[rpm]	T_0 [kN]
0.3	2.98	165	96.6
0.5	5.72	191	96.0
0.7	9.97	237	96.2
0.9	19.6	364	97.3

Table 4.2: Flow conditions for the steady flexible propeller calculations.

Figure 4.10 shows the results that are obtained with the FGD-BEM and PGD-BEM model. In the left graph, the reduction in blade thrust due to blade flexibility calculated with the two models is given as a percentage of T_0, together with the percentage difference between the blade thrust reductions obtained with both models. It can be seen that with the PGD-BEM model the blade thrust reduction is smaller for all advance ratios. The relative difference between the blade thrust reductions obtained with both models reduces with increasing advance ratio. The explanation for this is that, for increasing advance ratio, the relative contribution of the disturbance velocity potential, calculated with the PGD-BEM model in a simplified way, reduces.

The right graph shows the tip deformations obtained with both models. Since the blade thrust calculated with both models is close, the differences in tip deformations are relatively small as well. From the results, it can be concluded that without recalculation of the blade and wake influence coefficients, the inaccuracy in thrust change for the two lowest advance ratios is slightly larger than the 10%, but satisfies the 5% deformation inaccuracy. The PGD-BEM results for the two highest advance coefficients satisfy the accuracy criteria, which means that updating of the influence coefficients is not necessary for these conditions.

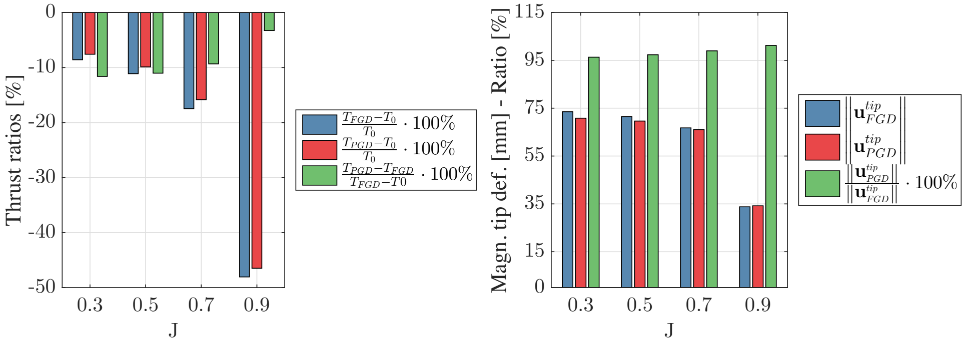

Figure 4.10: Blade thrust (left) and tip deformation (right) results obtained with the FGD-BEM and PGD-BEM model for various advance ratios. The subscripts $_{FGD}$ and $_{PGD}$ indicate with which BEM model the results were obtained.

4.6.4. UNSTEADY ANALYSES

This section presents results obtained for various non-uniform flows, fully BEM-FEM coupled calculations on the Seiun-Maru propeller and its ship effective wakefield [35] as shown in Figure 4.11. All the calculations are performed for quasi-isotropic glass-epoxy or carbon-epoxy material, with material properties as presented before. All the calculations are performed for a ship speed of 21 knots and a rotation rate of 240 rpm, which is roughly the rotation rate resulting in the maximum continuous engine power of 7723 kW [34], according to the graph showing the power against propeller revolution rate as presented in [17].

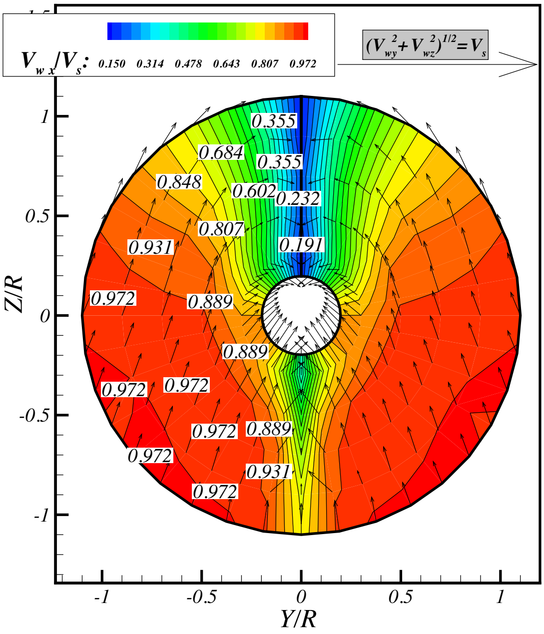

Figure 4.11: Seiun-Maru ship effective wakefield. (Image taken from [18] with permission of the author.)

First, several results obtained with the FGDE-BEM model are presented together with a result, which is obtained from a static calculation of the blade structural response. In addition, the contributions of fluid added mass and hydrodynamic damping forces are revealed. Secondly, results obtained with the FGDI-BEM, FGDE-BEM and PGDI-BEM model are compared, results obtained from a static blade structural response calculation are included in this comparison. Finally, the results of two different PGDI-BEM model calculations are compared.

UNSTEADY ANALYSES WITH FGDI-BEM, PGDI-BEM AND FGDE-BEM MODEL

In this subsection, results obtained with the FGDI-BEM, PGDI-BEM and FGDE-BEM models have been compared in order to find answers to modelling question 2 and 3 and to answer modelling question 1 from an unsteady problem perspective.

Figures 4.12 and 4.13 show the blade thrust for one revolution calculated for the glass-epoxy and carbon-epoxy propeller with the three methods, together with the blade thrust obtained for an unsteady PROCAL analysis with a completely rigid propeller.

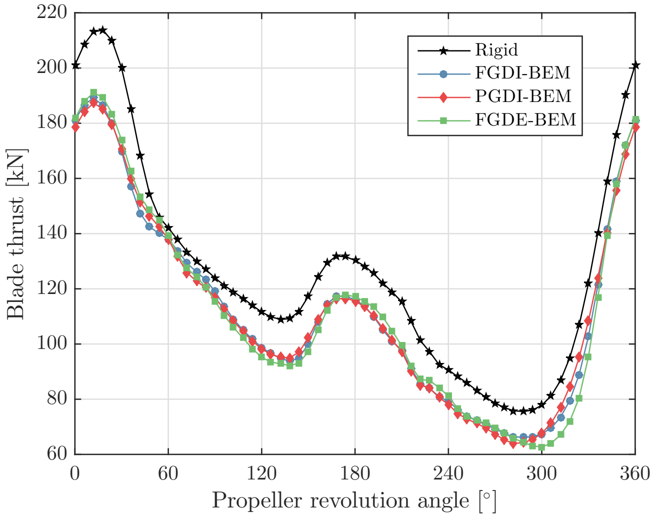

Figure 4.12: Blade thrust computed with different BEM-FEM couplings for the glass-epoxy Seiun-Maru propeller.

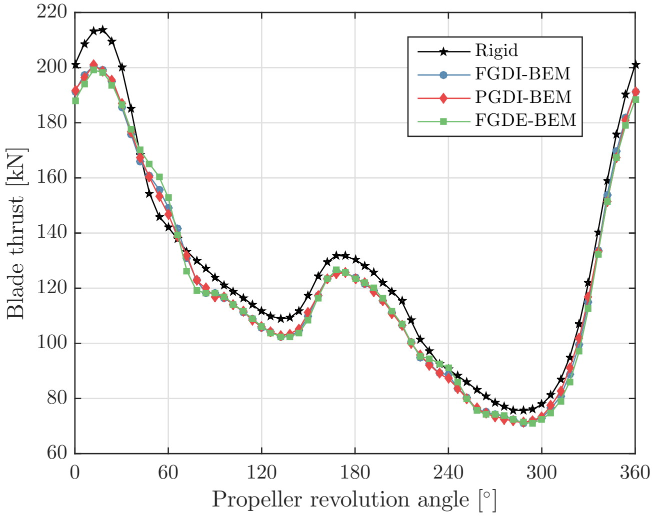

Figure 4.13: Blade thrust computed with different BEM-FEM couplings for the carbon-epoxy Seiun-Maru propeller.

Figures 4.14 and 4.15 show the modal participation factors for the first three dry blade modes as obtained from these analyses. Figure 4.16 summarizes the reduction of minimum, maximum and average blade thrust due to blade flexibility as obtained from these calculations. An interesting outcome of these calculations is that the reduction of the peak thrust due to blade flexibility is significantly larger than the reduction of the average thrust. This demonstrates the potential advantage of flexible propellers to improve cavitation inception speeds and cavitation noise.

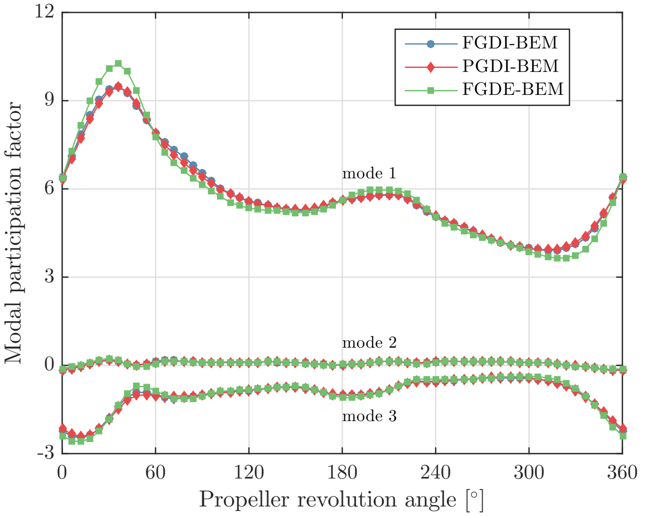

Figure 4.14: Modal participation factors for the first three modes computed with different BEM-FEM couplings for the glass-epoxy Seiun-Maru propeller.

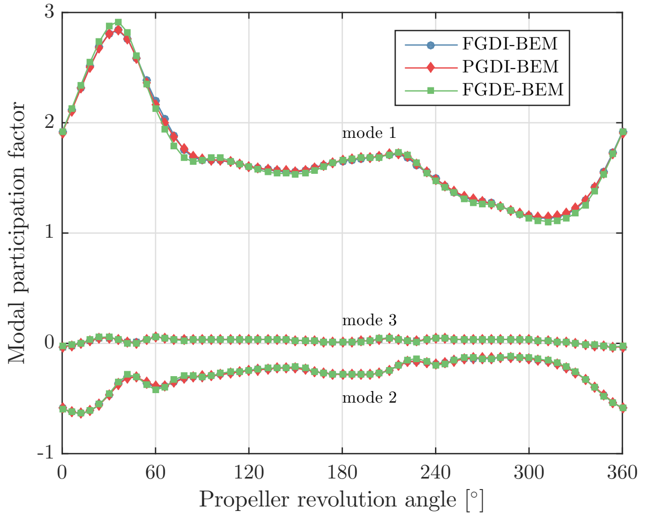

Figure 4.15: Modal participation factors for the first three modes computed with different BEM-FEM couplings for the carbon-epoxy Seiun-Maru propeller.

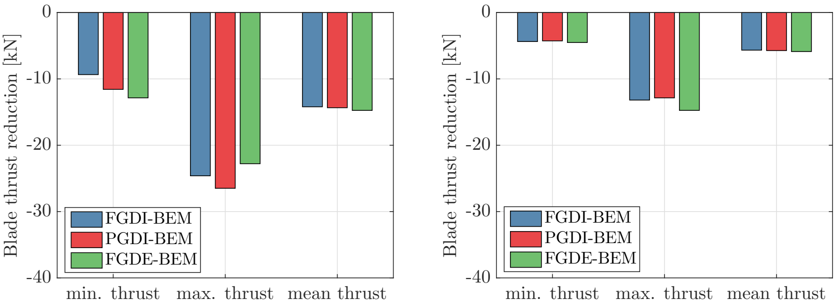

Figure 4.16: Thrust reduction for minimum, maximum and average blade thrust calculated for the glass-epoxy (left) and the carbon-epoxy (right) propeller as obtained from the BEM-FEM coupled calculations.

The FGDI-BEM model is the most extensive and complete BEM modelling of the flexible blades; therefore, all the other results will be compared to results obtained with this model. First, it can be seen that the differences between the results obtained with the FGDI-BEM and the PGDI-BEM model are small, meaning that the computationally intensive process of recalculating all the influence coefficients at every time step is relatively unimportant. This is in line with the results obtained with the FGD-BEM and PGD-BEM model for the steady cases. In answer to modelling question 1, it can be concluded that updating of the influence coefficients can be omitted for these unsteady flexible propeller calculations. Based on this conclusion, an answer can be given to the second modelling question as well. Since updating of the influence coefficients makes such a small contribution to the final results, it can be concluded that the symmetry surface influence coefficients of time step k instead of k_{isym} can be safely used for the symmetry surfaces because the symmetry surfaces are in the far-field with respect to the key blade and therefore the error in thrust reduction from this modelling choice will be much smaller than the modelling error introduced by not updating the key surface influence coefficients.

An answer to the third modelling question can be based on a comparison of the results obtained with the FGDE-BEM model to the results obtained with the FGDI-BEM calculations. It can be concluded that the hydro-elastic response prediction of the glass-epoxy flexible Seiun-Maru propeller with the FGDE-BEM model does not satisfy the accuracy criterion regarding the change in blade thrust. However, it can be seen that the structural responses are fairly well predicted by modelling the fluid added mass and hydrodynamic damping effects with the closed form expressions, more specifically by using the high frequency limit for the fluid added mass matrix and for the hydrodynamic damping matrix by taking 50% of the low frequency limit. The main reason that the results obtained with the FGDE-BEM model are fairly close to results obtained with the FGDI-BEM model is that the structural response of flexible propellers is dominated by stiffness and therefore the consequences of modelling errors in the fluid added mass and hydrodynamic damping contributions are relatively small.

UNSTEADY ANALYSES WITH FGDE-BEM MODEL

The purpose of this subsection is to give an answer to the fourth modelling question. It will be shown whether a quasi-static approach for the blade structural response calculation gives acceptable results (i.e., inaccuracy in thrust change <10% and inaccuracy in structural response <5%) and what the contribution is of the fluid added mass and hydrodynamic damping forces. Therefore, several computations with the unsteady FGDE-BEM-FEM coupling were conducted. The FGDE-BEM model has been taken, since the fluid added mass and hydrodynamic damping forces are explicitly calculated and their contribution to the total force can be easily presented.

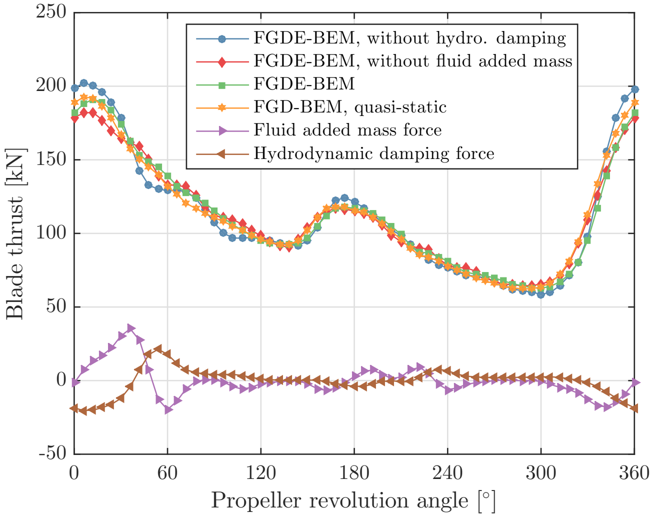

Figure 4.17: Blade thrust, fluid added mass and hydrodynamic damping force computed with the FGDE-BEM-FEM coupling with and without including the fluid added mass and hydrodynamic damping in the calculations, for the glass-epoxy Seiun-Maru propeller.

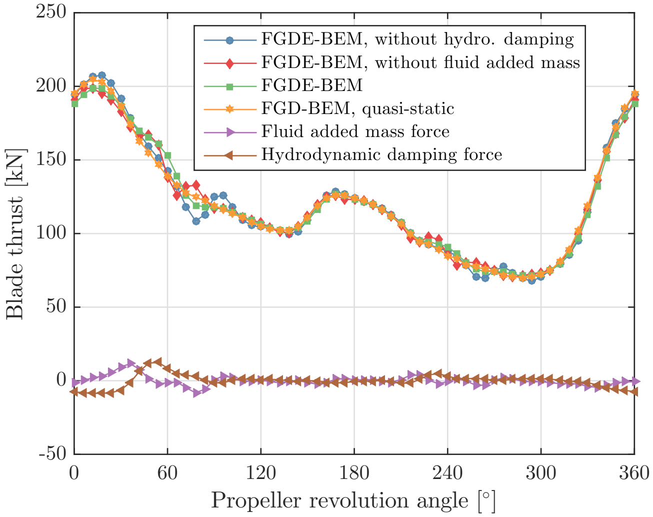

Figure 4.18: Blade thrust, fluid added mass and hydrodynamic damping force computed with the FGDE-BEM-FEM coupling with and without including the fluid added mass and hydrodynamic damping in the calculations, for the carbon-epoxy Seiun-Maru propeller.

Figures 4.17 and 4.18 show the blade thrust for one revolution computed with four different FGDE-BEM-FEM coupled calculations for the glass-epoxy and carbon-epoxy propeller, including fluid added mass and hydrodynamic damping, without hydrodynamic damping, without fluid added mass and a quasi-static analysis of the structural response. In these figures, the force contributions due to fluid added mass and hydrodynamic damping are included as well.

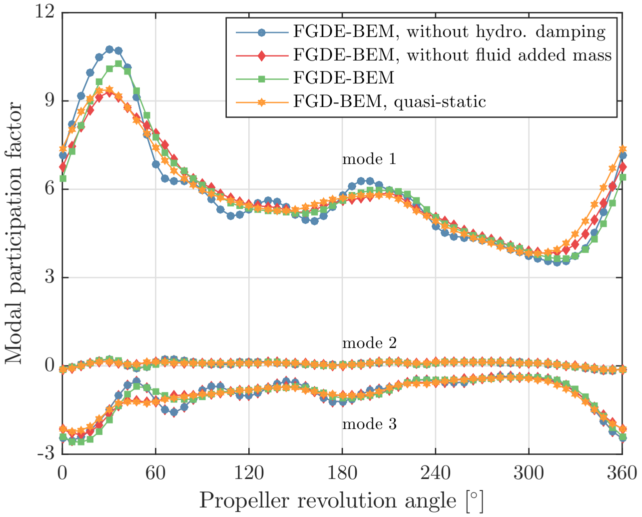

Figure 4.19: Modal participation for the first three modes computed with the FGDE-BEM-FEM coupling with and without including the fluid added mass and hydrodynamic damping in the calculations, for the glass-epoxy Seiun-Maru propeller.

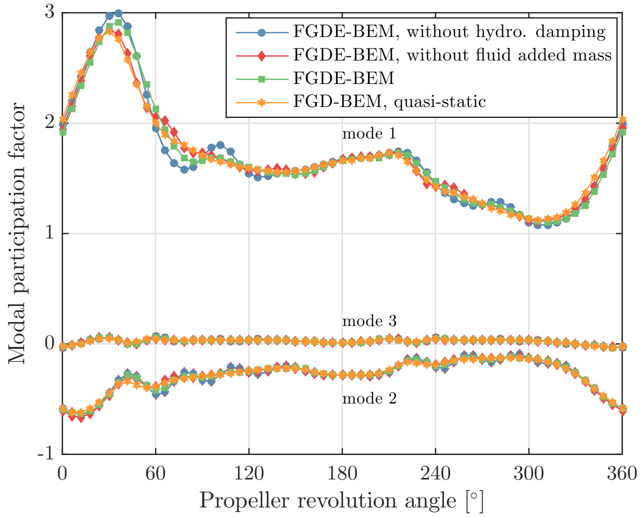

Figure 4.20: Modal participation for the first three modes computed with the FGDE-BEM-FEM coupling with and without including the fluid added mass and hydrodynamic damping in the calculations, for the carbon-epoxy Seiun-Maru propeller.

Figures 4.19 and 4.20 show the modal participation factors for the first three dry blade modes as obtained from the three different analyses. Figure 4.21 summarizes the reduction of minimum, maximum and average blade thrust due to blade flexibility.

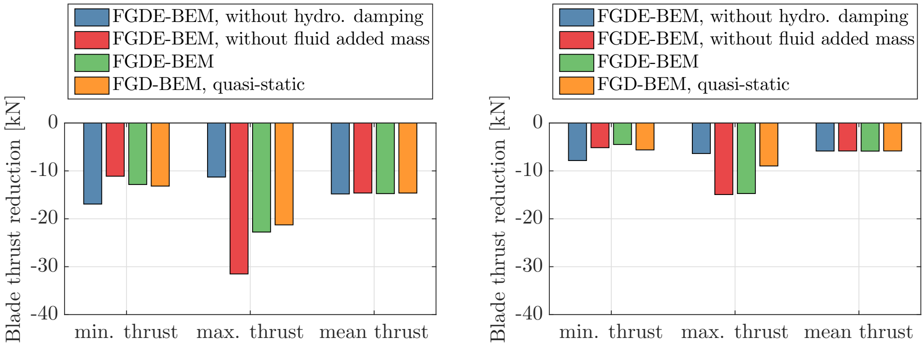

Figure 4.21: Thrust reduction for minimum, maximum and average blade thrust calculated for glass-epoxy (left) and carbon-epoxy (right) propeller as obtained from the various FGDE-BEM calculations.

These results show that a quasi-static FEM modelling cannot be used for an accurate prediction of the hydro-elastic response for these cases. This can be illustrated for instance with the blade thrust reduction results for the carbon-epoxy calculation. It can be expected that a quasi-static FEM approach will work the best for this case, since the structural frequency ratio for the carbon-epoxy propeller is significantly smaller than for the glass-epoxy propeller. However, a significant difference between reduction of the maximum thrust value calculated with the FGDE-BEM and the quasi-static approach is obtained for this case. Therefore, it is concluded that a quasi-static FEM modelling of flexible propellers should be applied with great care.

The importance of including fluid added mass and hydrodynamic damping in the calculations has been illustrated with two other calculations: one, BEM-FEM coupled calculation with the FGDE-BEM model without hydrodynamic damping included and one without fluid added mass included. These results show that, by neglecting fluid added mass or hydrodynamic damping, the average thrust corresponds very well with the average thrust obtained from a calculation in which both terms are included. However, significant differences can be seen in the calculated maximum blade thrust values and the shape of the blade thrust curves during a full revolution. The same conclusion can be drawn from the structural responses, as the differences in results obtained from the different calculations are too big to justify neglecting fluid added mass and/or hydrodynamic damping.

4.7. CONCLUSIONS

This work presents expressions to characterize the flow and structural response of flexible marine propellers. From these formulas, the conclusion can be drawn that the structural frequency ratio of flexible blades and the reduced frequency of vibrating blade flows is independent of the geometrical propeller scale.

The formulas were used to estimate the dry and wet fundamental blade frequencies of the highly skewed Seiun-Maru propeller for different blade materials. These frequencies were compared to results obtained from FEM calculations, from which can be concluded that reasonable results are obtained by using the estimation formulas. From the prediction of the structural frequency ratio for a quasi-isotropic glass-epoxy and carbon-epoxy Seiun-Maru propeller, it can be expected that the structural response is stiffness dominated. It can be discussed what the structural behaviour of flexible propellers is in general. It can be argued that the structural response of flexible propellers is dominated by the stiffness in general because the structural frequency ratio is independent of the geometrical propeller scale. Secondly, the Seiun-Maru propeller has relatively low blade frequencies due to the heavily skewed blade, and, therefore, in the case of other blade geometries, the structural frequency ratio is probably smaller.

A large part of this publication is used to explain possible BEM modelling approaches of flexible propellers. A derivation is presented on how fluid added mass and hydrodynamic damping matrices can be obtained from the hydrodynamic influence coefficients. To obtain closed form expressions for the added mass and hydrodynamic damping, several assumptions were made. The validity of using the closed form expressions for added mass and hydrodynamic damping forces has been studied by investigating the hydrodynamic loads on a plunging hydrofoil. The results of this study show that fluid added mass and hydrodynamic damping forces are frequency dependent due to flow memory effects as a consequence of the vortex wake sheet. The high frequency limit of the added mass and hydrodynamic damping forces is obtained without considering a vortex wake sheet. The low frequency limit is obtained for a constant strength vortex wake sheet. For sufficiently high reduced frequencies ($k > 4$), the added mass force converges to the high frequency limit and the hydrodynamic damping approaches the high frequency limit for the damping force, which is zero. From the results obtained for the hydrofoil only, it cannot be concluded that the closed form expressions can be used for correctly modelling fluid added mass and hydrodynamic damping effects in case of flexible propellers. Three other modelling questions regarding the hydro-elastic response modelling were raised and answers to these questions have been obtained by comparing results of different BEM-FEM coupled analyses of the Seiun-Maru propeller in steady and unsteady flows. In order to assess the different results, criteria on accuracy levels has been adopted. As acceptable accuracy level for the blade thrust change 10% has been used. That seems significant but means, in the case of 10% blade thrust change due to flexibility, an accuracy of 1% on the blade thrust itself. For the structural response, an accuracy level of 5% in blade deformation response has been considered.

From the study with the different BEM-FEM calculations, the following conclusions can be drawn: Firstly, the recalculation of influence coefficients seems to be of minor importance and can be omitted to reduce CPU time.

Secondly, by modelling explicitly the blade vibration and acceleration hydrodynamic effects by using the high frequency limit for the fluid added mass term and by taking 50% of the low frequency limit for the hydrodynamic damping term, the hydro-elastic response was reasonably well predicted, although the glass-epoxy propeller case did not satisfy the accuracy criteria. The main reason for these reasonable results is that the structural response of flexible propellers is dominated by the stiffness and therefore the consequences of modelling errors in the fluid added mass and hydrodynamic damping contributions are relatively small. For cases with structural frequencies around 0.2, the application of this modelling approach needs to be considered carefully and is not recommended for cases with higher structural frequency ratios as considered in this work.

Regarding a quasi-static FEM modelling of the structural response of flexible propellers, it can be concluded that this is not recommended for two reasons. First of all, the fluid added mass and hydrodynamic damping contributions are relatively small but not negligible. Secondly, the structural response of flexible propellers is dominated by stiffness, but already the results for the carbon-epoxy propeller with a structural frequency ratio of around 0.15 show that dynamic effects have to be included. This would be even more important for cases were the structural frequency ratio is higher or the higher harmonics of the blade force are more significant.

REFERENCES

[1] N. Mulcahy, B. Prusty, and C. Gardiner, “Hydroelastic tailoring of flexible composite propellers,” *Ship and Offshore Structures*, vol. 5, no. 4, pp. 359–370, 2010.

[2] X. He, Y. Hong, and R. Wang, “Hydroelastic optimisation of a composite marine propeller in a non-uniform wake,” *Ocean Engineering*, vol. 39, pp. 14–23, 2012.

[3] T. Taketani, K. Kimura, S. Ando, and K. Yamamoto, “Study on performance of a ship propeller using a composite material,” Third International Symposium on Marine Propulsors, Launceston, Australia, 2013.

[4] S. Solomon Raj and P. Ravinder Reddy, “Bend-twist coupling and its effect on cavitation inception of composite marine propeller,” *International Journal of Mechanical Engineering and Technology*, vol. 5, no. 9, pp. 306–314, 2014.

[5] J. Kuo and W. Vorus, “Propeller blade dynamic stress,” pp. 39–69, Tenth Ship Technology and Research (STAR) Symposium, Norfolk, VA, USA, 1985.

[6] D. Georgiev and M. Ikehata, “Hydro-elastic effects on propeller blades in steady flow,” *Journal of the Society of Naval Architects of Japan*, vol. 184, pp. 1–14, 1998.

[7] Y. Young, “Time-dependent hydro-elastic analysis of cavitating propulsors,” *Journal of Fluids and Structures*, vol. 23, pp. 269–295, 2007.

[8] J. Blasques, C. Berggreen, and P. Andersen, “Hydro-elastic analysis and optimization of a composite marine propeller,” *Marine Structures*, vol. 23, pp. 22–38, 2010.

[9] H. Ghassemi, M. Ghassabzadeh, and M. Saryazdi, “Influence of the skew angle on the hydro-elastic behaviour of a composite marine propeller,” *Journal of Engineering for the Maritime Environment*, vol. 226, no. 4, pp. 346–359, 2012.

[10] H. Sun and Y. Xiong, “Fluid-structure interaction analysis of flexible marine propellers,” *Applied Mechanics and Materials*, vol. 226-228, pp. 479–482, 2012.

[11] H. Lee, M. Song, J. Suh, and B. Chang, “Hydro-elastic analysis of marine propellers based on a BEM-FEM coupled FSI algorithm,” *International Journal of Naval Architecture and Ocean Engineering*, vol. 6, no. 3, pp. 562–577, 2014.

[12] P. Maljaars and J. Dekker, “Hydro-elastic analysis of flexible marine propellers,” in *Maritime Technology and Engineering* (C. Guedes Soares and T. Santos, eds.), pp. 705–715, CRC Press-Taylor & Francis Group: London, UK, 2014.

[13] G. Baker, “Vibration patterns of propeller blades,” *Transaction NECIES*, vol. 57, pp. 1040–1041, 1940.

[14] R. Fischer, “Singing propellers - Solution and case histories,” *Marine Technology*, vol. 45, no. 4, pp. 221–227, 2008.

[15] J. Carlton, *Marine propellers and propulsion.* Butterworth Heinemann: Oxford, UK, 1994.

[16] T. Theodorsen, “General theory of aerodynamic instability and the mechanism of flutter,” Tech. Rep. 496, National Advisory Committee for Aeronautics, 1935.

[17] Y. Ukon and H. Yuasa, “Pressure distribution and blade stress on a higly skewed propeller,” *Proceedings of 19th symposium of Naval Hydrodynamics*, pp. 793–814, 1992.

[18] G. Vaz, *Modelling of sheet cavitation on hydrofoils and marine propellers using boundary element methods.* PhD thesis, Instituto Superior Técnico, Lisbon, Portugal, 2005.

[19] G. Vaz and J. Bosschers, “Modelling of three dimensional sheet cavitation on marine propellers using a boundary element method,” Sixth International Symposium on Cavitation, Wageningen, The Netherlands, 2006.

[20] L. Morino and C. Kuo, “Subsonic potential aerodynamics for complex configurations: a general theory,” *AIAA Journal*, vol. 12, no. 2, p. 191–197, 1974.

[21] M. La Mantia and P. Dabnichki, “Influence of the wake model on the thrust of oscillating foil,” *Engineering Analysis with Boundary Elements*, vol. 35, pp. 404–414, 2011.

[22] M. La Mantia and P. Dabnichki, “Unsteady panel method for flapping foil,” *Engineering Analysis with Boundary Elements*, vol. 33, pp. 572–580, 2009.

[23] J. Katz and A. Plotkin, *Low-speed aerodynamics.* Camebridge University Press: New York, NY, USA, 2001.

[24] J. Young, *Numerical Simulation of the Unsteady Aerodynamics of Flapping Airfoils.* PhD thesis, The University of New South Wales, Sydney, Australia, 2005.

[25] R. Boswell, “Design, cavitation performance and open-water performance of a series of research skewed propellers,” Tech. Rep. 3339, David W. Taylor Naval Ship Research Development Center, West Bethesda, MD, USA, 1971.

[26] P. Maljaars, L. Bronswijk, J. Windt, N. Grasso, and M. Kaminski, "Experimental validation of fluid-structure interaction computations of flexible composite propellers in open water conditions using BEM-FEM and RANS-FEM methods," *Journal of Marine Science and Engineering*, vol. 6, no. 4, p. 51, 2018.

[27] P. Maljaars, M. Kaminski, and J. den Besten, "Finite element modelling and model updating of small scale composite propellers," *Composite Structures*, vol. 176, pp. 154–163, 2017.

[28] I. Abbott and A. von Doenhoff, *Theory of wing sections.* Dover Publications: Mineola, NY, USA, 1959.

[29] C. Muňch, P. Ausoni, O. Braun, M. Farhat, and F. Avellan, "Fluid–structure coupling for an oscillating hydrofoil," *Journal of Fluids and Structures*, vol. 26, pp. 1018–1033, 2010.

[30] P. Maljaars, M. Kaminski, and J. den Besten, "A new approach for computing the steady state fluid-structure interaction response of periodic problems," *Journal of Fluids and Structures*, vol. 84, pp. 140–152, 2018.

[31] B. Beulen, M. Rutten, and F. van de Vosse, "A time-periodic approach for fluid-structure interaction in distensible vessels," *Journal of Fluids and Structures*, vol. 25, no. 5, pp. 954–966, 2009.

[32] J. Degroote, R. Haelterman, S. Annerel, P. Bruggeman, and J. Vierendeels, "Performance of partitioned procedures in fluid–structure interaction," *Computers and Structures*, vol. 88, no. 7–8, pp. 446–457, 2010.

[33] Y. Young, E. Chae, and D. Akcabay, "Hybrid algorithm for modeling of fluid-structure interaction in incompressible, viscous flows," *Acta Mechanica Sinica*, vol. 28, no. 4, p. 1030–1041, 2012.

[34] H. Kato and Y. Kodama, "Microbubbles as a skin friction reduction device—a midterm review of the research," pp. 793–814, 4th Symposium on Smart Control of Turbulence, Tokyo, Japan, 2003.

[35] B. Gindroz, T. Hoshino, and J. Pylkkanen, "22nd ITTC Propulsion Committee Propeller RANS/Panel Method Workshop," Proceedings of the 22nd ITTC, Grenoble, France, 1998.

5

Chapter 5

BEM-FEM coupling for non-uniform flows

This chapter presents a partitioned fluid-structure interaction (FSI) coupling for the non-uniform flow hydro-elastic analysis of highly flexible propellers in cavitating and non-cavitating conditions. The chosen fluid model is a potential flow solved with a boundary element method (BEM). The structural sub-problem has been modelled with a finite element method (FEM). In the present method, the fully partitioned framework allows one to use another flow or structural solver. An important feature of the present method is the time periodic way of solving the FSI problem. In a time periodic coupling, the coupling iterations are not performed per time step but on a periodic level, which is necessary for the present BEM-FEM coupling, but can also offer an improved convergence rate compared to a time step coupled method. Thus, it allows to solve the structural problem in the frequency domain, meaning that any transients, which slow down the convergence process, are not computed. As proposed in the method, the structural equations of motion can be solved in modal space, which allows for a model reduction by involving only a limited number of mode shapes.

This chapter is based on the journal paper: P. Maljaars, N. Grasso, J. den Besten and M. Kaminski, “BEM-FEM coupling for the analysis of flexible propellers in non-uniform flows and validation with full-scale measurements,” submitted to *Journal of Fluids and Structures*.

5.1. INTRODUCTION

Over the last decades many papers have been published on the hydro-elastic analysis of flexible (composite) propellers. The majority of studies have been limited to steady inflow conditions. Fewer papers have been published about the hydro-elastic analysis in behind ship conditions, i.e. involving non-uniform flows, for instance [1–4]. The most probable reason for this is that the non-uniform flow conditions complicate the analyses significantly. First of all, the hydro-elastic analysis needs to be performed with the structural dynamic equations, a quasi-static analysis does not suffice, as shown in the previous chapter. This means that hydrodynamic damping and fluid added mass effects have to be incorporated in the analysis. For composite propellers the ratio between fluid added mass and structural mass will be much higher than one, as elucidated in Chapter 4. Computations with such high fluid added mass ratios are prone to instabilities [5, 6] and therefore either a monolithic method has to be adopted, in which the fluid and structural problem are solved simultaneously, or a dedicated partitioning between fluid and structural solver is required to stabilize the coupling iterations between the two sub-domains.

A second complicating factor due to the non-negligible hydrodynamic damping and fluid added mass effects is that structural blade vibration velocities and accelerations have to be coupled to the fluid as well, whereas for uniform flow calculations only the blade deformations matter. Two different approaches have been presented in literature to cope with this. In [1–4] the vibration-induced pressures have been written in terms of closed form expressions for added mass and hydrodynamic damping and moved to the left-hand side of the structural equations. The advantage of this approach is that the vibration induced pressures are directly included in the structural analysis, resulting in a faster convergence. However, the derivation of the closed form expressions has been based on several assumptions (see Chapter 4), with the small blade deformation assumption as the most important one. A more precise approach would be to include the vibration velocities and accelerations of the propeller blade by additional boundary conditions in the flow calculation. In the previous chapter both approaches have been compared. It was concluded that the first approach provides reasonable results, because the structural response was dominated by stiffness and therefore the consequences of modelling errors in the fluid added mass and hydrodynamic damping contributions were relatively small. The second approach is recommended for problems involving significant blade deformations, i.e. highly flexible blades.

The purpose of this chapter is to present a fluid structure interaction (FSI) method for the hydro-elastic analysis of highly flexible blades in behind ship conditions. Since the kind of monolithic method as presented in [4] is limited to small deformations and extension of this method to large blade deformations seems hardly possible, a partitioned method has been adopted. An advantage of a partitioned method is that for the structural and fluid sub-problem existing black-box solvers can be used. In this thesis, for the fluid simulations a boundary element method (BEM) has been used, but the present method may be suitable for other flow solvers as well. A BEM was chosen because this method is particularly effective in capturing the flow details but requires only 1% of the effort needed for fully viscous flow simulations [7]. In this work, the BEM PROCAL, developed by the Maritime Research Institute Netherlands (MARIN) [8, 9], has been used. In PROCAL cavitation models have been implemented. Hence, the present method can be applied for the (non-)uniform flow FSI analysis of highly flexible blades, showing large blade deformations, in cavitating and non-cavitating conditions.

5.2. BEM-FEM COUPLING PROCEDURE FOR NON-UNIFORM FLOWS

The unsteady coupling procedure to compute the steady-state FSI response of flexible propellers in behind ship conditions (i.e. in non-uniform flows) will be discussed in the following, starting with some background knowledge on FSI, a brief description of fluid and structural modelling and finally an explanation of the coupling scheme.

5.2.1. FLUID-STRUCTURE INTERACTION

MONOLITHIC AND PARTITIONED FSI

Monolithic or partitioned methods can be used to solve FSI problems. In a monolithic method the fluid and structure problem are simultaneously solved using a single code. This might be difficult to realize because fluid and structural solvers are usually completely different each using its own optimized tools specific for the field of application. Furthermore, a monolithic solver might be very inefficient since structural and fluid problems are often solved differently (linearly and non-linearly) and with different temporal resolutions. However, in a monolithic scheme both fields have to be integrated with the highest of the two temporal resolutions. Another option is a partitioned method in which the fluid and structure problem are solved in separate codes. In case of strong interaction between fluid and structure, a partitioned method requires coupling iterations to converge to the monolithic solution, which can be computationally expensive. An important advantage of such a partitioning for the present method is that the structural problem may be coupled to a black-box fluid solver able to model cavitation as well. That was also an important reason to adopt a partitioned method for this work.

TIME STEP AND TIME PERIODIC PARTITIONED FSI

In a time step FSI coupling, fluid and structural calculations are alternately performed for each time step. In case of one fluid and structural evaluation for each time step, a time step difference exists between fluid and structural solution. Then, for strongly coupled FSI problems, sub-iterations between fluid and structural solver are required to reach dynamic equilibrium for each time instant. A necessary step in the development of the non-uniform flow BEM-FEM coupling was the development of the time periodic coupling method as detailed in Appendix A. This method differs from a time step coupling with respect to the coupling iterations between the fluid and structural solver. In a time periodic coupling, the coupling iterations are not performed per time step but on a periodic level, which is necessary for the present BEM-FEM coupling, since the BEM method PROCAL is completely periodical in nature. Think of the vortex wake shedding and the use of symmetry blades [8] and therefore a non-periodic solution could not be treated in PROCAL and a time step coupling would not converge. Apart from this, it has been shown in Appendix A that a time periodic coupling can significantly speed-up the convergence to the steady-state FSI solution of periodic problems, because it allows to solve the structural problem in the frequency domain, meaning that any transients, which slow down the convergence, are not computed. However, as shown, convergence problems as appearing in time step couplings due to strong fluid added mass effects, arise in time periodic couplings as well. This requires a dedicated partitioned solution method.

PARTITIONED SOLUTION METHODS

In a partitioned FSI method fluid and structural problems are separately solved and the coupling between the two sub-domains is accomplished by imposing boundary interface conditions. In that case a partitioned solution method has to be provided in which it is defined how the body boundary interface information has to be exchanged between the two solvers. Especially in case of a high ratio between fluid added mass and structural mass and an incompressible fluid, the solution process may not converge without a dedicated partitioned solution method [5]. Two of these partitioned solution methods have been investigated in a time step and time periodic framework in Appendix A. It has been shown that the Quasi-Newton inverse least squares (QN-ILS) method outperforms the Aitken under-relaxation method in any case. Furthermore, the QN-ILS method in a time periodic framework converges for any fluid added mass ratio. Therefore, in this thesis the QN-ILS method is applied in the unsteady coupling procedure for flexible propellers. For more results obtained with the QN-ILS partitioned solution method and the implementation of this in a time-periodic framework one is referred to Appendix A . Details on the mathematical background of the QN-ILS method can be found in [10].

5.2.2. FLUID MODEL DESCRIPTION

In order to determine the fluid forces for flexible propellers in behind-ship conditions several modifications to PROCAL have been made by the author in order to include deformation induced fluid velocities and accelerations. Due to blade deformations panel normal vectors become time-dependent, which is reflected in the panel source strengths. The hydrodynamic influence coefficients of the blade also become time-dependent. Finally, the pressures and fluid forces have to be evaluated from the computed velocity potentials on a modified grid. PROCAL has been modified to make it suitable for shape adaptive propeller modelling.

In Chapter 4 two different approaches to include blade deformation effects in BEM have been proposed. Both were implemented in PROCAL. In the partially geometry dependent (PGD) BEM modelling the source strengths are calculated from the blade deformation dependent panel normal vectors and the pressures and forces are evaluated on the modified BEM geometry, while keeping blade and wake influence coefficients constant. In the fully geometry dependent (FGD) BEM modelling, blade and wake influence coefficients are blade deformation dependent as well. This requires a significant amount of additional calculation time since the system of equations has to be recalculated for every time step. The results obtained with the PGD-BEM model are close to results obtained with FGD-BEM model. Although, it has been shown in the previous chapter that some results obtained for the most flexible case with the PGD-BEM model do not comply with the accuracy criteria. Therefore, applying this modelling approach for very flexible cases needs to be considered carefully.

In the FGD-BEM modelling the total disturbance velocity potential Φ is solved with PROCAL. The total velocity, $\mathbf{v}$, relative to the operating propeller becomes,

$$\mathbf{v}(\mathbf{x}, t) = \mathbf{v}_0(\mathbf{x}, t) + \nabla\Phi(\mathbf{x}, t) \tag{5.1}$$

with $\mathbf{v}_0$ the inflow velocity, t the time and $\mathbf{x}$ the position vector in a Cartesian coordinate system. The velocity, $\mathbf{v}_0$, can be written as the sum of the ship's effective wake field velocity, $\mathbf{v}_w$, and the effect of the propeller angular velocity, $\boldsymbol{\theta}$,

$$\mathbf{v}_0(\mathbf{x},t) = \mathbf{v}_w(\mathbf{x},t) - \boldsymbol{\theta} \times \mathbf{x} \tag{5.2}$$

The flow is assumed to be incompressible and have a constant density. Therefore, Laplace's equation applies to the disturbance velocity potential,

$$\nabla^2 \Phi(\mathbf{x},t) = 0 \tag{5.3}$$

Then, the fluid pressures, p, are related to the total velocity and the disturbance velocity potential according to Bernoulli's law,

$$\frac{\partial \Phi}{\partial t} + \frac{1}{2}|\mathbf{v}|^2 + \frac{p}{\rho} + gz = \frac{p_{ref}}{\rho} + \frac{1}{2}|\mathbf{v}_0|^2 \tag{5.4}$$

For a propeller, p_{ref} is the pressure far upstream (along the shaft axis) and it obeys the hydrostatic law, $p_{ref} = p_{atm} + \rho g z_{shaft}$, with p_{atm} the atmospheric pressure at the free surface, and the submergence z at the shaft being z_{shaft}. In order to solve Eq. 5.3 boundary conditions have to be imposed on the propeller surface, S_B and wake sheet, S_W, which contains the shed vorticity. On the propeller surface the impermeability condition is imposed for a deforming and vibrating blade,

$$\nabla \Phi \cdot \mathbf{n}(\mathbf{x},\boldsymbol{\delta}) = -\mathbf{v}_0 \cdot \mathbf{n}(\mathbf{x},\boldsymbol{\delta}) + \frac{\partial \boldsymbol{\delta}}{\partial t} \cdot \mathbf{n}(\mathbf{x},\boldsymbol{\delta}) \tag{5.5}$$

The right hand side of this boundary condition consists of two parts, the surface normal velocity due to the inflow velocity, $\mathbf{v}_0 \cdot \mathbf{n}(\mathbf{x},\delta)$, where the surface normal vector is also a function of blade deformation, $\boldsymbol{\delta}$. The second part, $\frac{\partial \boldsymbol{\delta}}{\partial t} \cdot \mathbf{n}(\mathbf{x},\boldsymbol{\delta})$, is the vibration velocity of the deformed blade itself.

A relation between the disturbance potential on the fluid boundary surface and the source strengths (normal component of the disturbance velocity at the body boundary) for an unsteady flow and deformable body is given by the following integral equation (see also Chapter 4),

$$\begin{aligned} 2\pi\Phi(\mathbf{a}(\boldsymbol{\delta}),t) = & \int_{S_{B(\boldsymbol{\delta})}} \left[\Phi(\mathbf{b}(\boldsymbol{\delta}),t) \frac{\partial G(\mathbf{a}(\boldsymbol{\delta}),\mathbf{b}(\boldsymbol{\delta}))}{\partial \mathbf{n}_b(\boldsymbol{\delta})} - \frac{\partial \Phi(\mathbf{b}(\boldsymbol{\delta}),t)}{\partial \mathbf{n}_b(\boldsymbol{\delta})} G(\mathbf{a}(\boldsymbol{\delta}),\mathbf{b}(\boldsymbol{\delta})) \right] dS \\ & + \int_{S_{W(\boldsymbol{\delta})}} \Delta\Phi(\mathbf{b}(\boldsymbol{\delta}),t) \frac{\partial G(\mathbf{a}(\boldsymbol{\delta}),\mathbf{b}(\boldsymbol{\delta}))}{\partial \mathbf{n}_b(\boldsymbol{\delta})} dS \end{aligned} \tag{5.6}$$

This integral equation follows from Morino's formulation of Green's third identity [11] and the dynamic boundary condition on the wake sheet. In this equation $\mathbf{a}$ and $\mathbf{b}$ are points on the fluid domain boundary surface and $\mathbf{n_b}$ is the outward normal at $\mathbf{b}$. The Green's function, G, for the Laplace equation is defined as,

$$G(\mathbf{a},\mathbf{b}) = \frac{1}{r(\mathbf{a},\mathbf{b})}, \qquad r(\mathbf{a},\mathbf{b}) = |\mathbf{r}| = |\mathbf{a}-\mathbf{b}| \tag{5.7}$$

The integral equation Eq. 5.6 is solved in PROCAL by approximating the surfaces S_B and S_W by N_{total} panels. On each panel a collocation point is defined where the integral equation is applied. Finally, a system of equations is obtained, unknown in the strengths of the source and dipole elements. The system of equations is updated every time step according to the deformations in blade geometry and blade vibration velocities. For more details about the FGD-BEM modelling approach one is referred to the previous chapter.

5.2.3. STRUCTURE MODEL DESCRIPTION

Details about geometry and material aspects in the FEM modelling of composite ship propellers have been given in Chapter 2. This subsection reveals the structural dynamic equations for a propeller blade and the analyses of dry and wet blade natural frequencies and mode shapes required for the structural analyses with a reduced model in modal space.

PROPELLER BLADE STRUCTURAL EQUATIONS

For the case of a propeller in behind ship condition the structural dynamic equations for a propeller blade in a blade fixed (i.e. rotating) reference system is given by,

$$[\mathbf{M}_s]\{\ddot{\mathbf{u}}\} + [\mathbf{C}_s]\{\dot{\mathbf{u}}\} + [\mathbf{K}_s]\{\mathbf{u}\} = \{\mathbf{f}_h\} + \left\{\mathbf{f}_{fict}\right\} \tag{5.8}$$

where $[\mathbf{M}_s]$, $[\mathbf{C}_s]$ and $[\mathbf{K}_s]$ denote structural mass, damping and stiffness matrices. $\{\mathbf{f}_h\}$ is the hydrodynamic force vector, which implicitly includes fluid added mass, hydrodynamic damping and fluid stiffness contributions. The vector $\left\{\mathbf{f}_{fict}\right\}$ represents the fictitious forces as a result of solving a rotating problem in a body fixed reference system.

LOADS

The hydrodynamic pressures are computed with the FGD-BEM model as explained in Section 5.2.2. Analyses are performed only for constant angular speeds which means that Euler forces are zero but centrifugal forces and Coriolis forces are present. The centrifugal force on a mass m rotating with angular velocity $\dot{\boldsymbol{\theta}}$ at position $\mathbf{p}$ is,

$$\mathbf{f}_{centrifugal} = m\left(\dot{\boldsymbol{\theta}} \times \left(\dot{\boldsymbol{\theta}} \times \mathbf{p}\right)\right) \tag{5.9}$$

The Coriolis force is equal to,

$$\mathbf{f}_{Coriolis} = 2m\left(\dot{\boldsymbol{\theta}} \times \frac{d\mathbf{p}}{dt}\right) \tag{5.10}$$

The Coriolis force contributes to the total damping but is assumed to be negligible in comparison to the hydrodynamic damping and therefore neglected in the analyses [3]. Hence, only the centrifugal forces contribute to the fictitious force vector in Eq. 5.8.

DRY NATURAL FREQUENCIES AND EIGENMODES

For an N degree of freedom structural system with mass matrix, $[\mathbf{M}]$, and stiffness matrix, $[\mathbf{K}]$, the structural dynamic equation for forced vibration is,

$$[\mathbf{M}]\{\ddot{\mathbf{u}}\} + [\mathbf{K}]\{\mathbf{u}\} = \{\mathbf{f}\} \tag{5.11}$$

where $\{\ddot{\mathbf{u}}\}$ and $\{\mathbf{u}\}$ are the structural acceleration and deformation vectors and $\{\mathbf{f}\}$ is the force vector. The natural frequencies $\omega_{i=1...N}$ and corresponding modes $\boldsymbol{\psi}_{i=1...N}$ follow from the solution of the eigenvalue problem,

$$\left[-\omega^2\mathbf{M}+\mathbf{K}\right]\{\mathbf{u}\} = \{\mathbf{0}\} \tag{5.12}$$

The eigenmodes are orthogonal with respect to the system mass and stiffness matrix. This property can be utilized to transform the system of equations to the modal space. An uncoupled system of equations is obtained and the degrees of freedom are the modal participation factors, q_i, rather than the nodal structural response vectors. The first step in this transformation is to write the structural deformation vector as a linear combination of all the eigenmodes, $\boldsymbol{\psi}_{i=1...N}$,

$$\{\mathbf{u}\} = \sum_{i=1}^{N} \boldsymbol{\psi}_i q_i = [\boldsymbol{\Psi}]\left\{\mathbf{q}\right\} \tag{5.13}$$

$$[\boldsymbol{\Psi}] = \left[\boldsymbol{\psi}_1, \boldsymbol{\psi}_2, \ldots, \boldsymbol{\psi}_N\right] \tag{5.14}$$

$$\left\{\mathbf{q}\right\} = \begin{bmatrix} q_1 \\ q_2 \\ \vdots \\ q_N \end{bmatrix} \tag{5.15}$$

Substituting these expressions in the structural dynamic equations and multiplying by $[\boldsymbol{\Psi}]^T$ gives,

$$[\boldsymbol{\Psi}]^T[\mathbf{M}][\boldsymbol{\Psi}]\left\{\ddot{\mathbf{q}}\right\} + [\boldsymbol{\Psi}]^T[\mathbf{K}][\boldsymbol{\Psi}]\left\{\mathbf{q}\right\} = [\boldsymbol{\Psi}]^T\{\mathbf{f}\} \tag{5.16}$$

When the modes are normalized with respect to the mass matrix, i.e. $[\boldsymbol{\Psi}]^T[\mathbf{M}][\boldsymbol{\Psi}] = [\mathbf{I}]$, the following uncoupled system of equations is obtained,

$$[\mathbf{I}]\left\{\ddot{\mathbf{q}}\right\} + [\boldsymbol{\Omega}]\left\{\mathbf{q}\right\} = [\boldsymbol{\Psi}]^T\{\mathbf{f}\} \tag{5.17}$$

where $[\mathbf{I}]$ is the identity matrix and $[\boldsymbol{\Omega}]$ is a diagonal matrix with the square of the natural frequencies ω_i on its main diagonal.

WET NATURAL FREQUENCIES AND EIGENMODES

From the closed form expression for the fluid added mass matrix as presented in Chapter 4 a full non-symmetrical added mass matrix can be obtained. To calculate the wet natural frequencies and mode shapes the added mass matrix has to be added to the structural mass matrix. A possible approach is to lump the off-diagonal terms of the added mass matrix on its main diagonal and add it to the structural mass matrix in order to compute wet natural frequencies and mode shapes by solving the corresponding eigenvalue problem [3]. An important reason for this lumping is that many of the commercial FEM software packages cannot handle non-symmetric and non-sparse matrices.

To avoid lumping of the fluid added mass matrix and adding of the fluid added mass contribution by discrete masses in a black-box FEM solver, the wet natural frequencies and mode shapes can be computed directly from dry frequencies and mode shapes and the fluid added mass matrix by the following approach. First of all, the modal added mass matrix, $[\mathbf{\Gamma}]$, has to be computed from the full and non-symmetrical added mass matrix $[\mathbf{M}_h]$. In order to obtain a fully uncoupled system of equations, the modal added mass matrix needs to be symmetric. A symmetric modal added matrix, $[\mathbf{\Gamma}]$, is obtained in the following way,

$$[\mathbf{\Gamma}] = [\mathbf{\Psi}]^T \left[\mathbf{M}_h^*\right] [\mathbf{\Psi}] \tag{5.18}$$

where $\left[\mathbf{M}_h^*\right] = \frac{1}{2}\left([\mathbf{M}_h] + [\mathbf{M}_h]^T\right)$. The symmetric modal added mass matrix is added to the structural modal mass matrix $[\mathbf{I}]$. In order to obtain the wet natural frequencies and mode shapes a second eigenvalue problem has to be solved in analogy with Eq. 5.12,

$$\left[-\bar{\omega}^2 [\mathbf{I} + \mathbf{\Gamma}] + \mathbf{\Omega}\right] \left\{\mathbf{q}\right\} = \{\mathbf{0}\} \tag{5.19}$$

From this eigenvalue problem the wet natural frequencies $\bar{\omega}_{i=1...N}$ and eigenvectors $\boldsymbol{\theta}_{i=1...N}$ are obtained. The eigenvectors $\boldsymbol{\theta}_i$ are eigenmodes in modal space. These eigenmodes are mass normalized with the total modal mass matrix $[\mathbf{I} + \mathbf{\Gamma}]$. The wet mode shapes are obtained by multiplying the matrix with the dry mode shapes by the eigenvector matrix $[\mathbf{\Theta}]$,

$$\left[\bar{\mathbf{\Psi}}\right] = [\mathbf{\Psi}] [\mathbf{\Theta}] \tag{5.20}$$

where $[\mathbf{\Theta}] = [\boldsymbol{\theta}_1, \boldsymbol{\theta}_2, \ldots, \boldsymbol{\theta}_N]$. The wet modal stiffness matrix, $\left[\bar{\mathbf{\Omega}}\right]$, is a diagonal matrix with the squared wet natural frequencies $\bar{\omega}_i$ on its main diagonal and is equal to $[\mathbf{\Theta}]^T [\mathbf{\Omega}] [\mathbf{\Theta}]$.

5.3. COUPLING SCHEME

Figure 5.1 presents schematically the FSI coupling procedure. In this scheme index r is the counter of the number of PROCAL revolutions and index k is the counter of the number of FSI cycles. Generally, r will be larger than k since PROCAL requires an iterative procedure over a number of propeller revolutions in order to converge to a steady state flow solution. A propeller revolution is subdivided in M time steps. At the beginning of the first PROCAL calculation the indices k and r are one. The coupling scheme will be explained step by step in the following subsections.

PRESSURE CALCULATION

The coupling scheme starts by computing with PROCAL the steady state solution for the loads on the undeformed propeller in the non-uniform wakefield. As mentioned before, PROCAL solves this problem iteratively and therefore after every propeller revolution, r, the convergence to the steady state solution is checked. The converged hydrodynamic pressures for the full revolution at an FSI cycle, k, are denoted with superscript $k-1$ since in the PROCAL calculation the structural response of the previous FSI cycle has been used. After the PROCAL analysis the convergence of the FSI solution is monitored by comparing the hydrodynamic loads of the present and previous FSI cycle. When the load difference between these two cycles is smaller than a specified tolerance, the FSI solution is said to have converged, otherwise the calculation continues with two pressure corrections. The first correction is for the overestimation of the pressures at the propeller tip obtained. The second one is a viscous correction for frictional losses. Both have been explained in more detail in Chapter 3.

LOADS

Once the pressures have been computed, they are imposed on the FEM model and the corresponding equivalent nodal forces are calculated together with the equivalent nodal forces of the centrifugal load. With the wet mode shapes the loads for a full revolution are converted to wet modal space. Important to note is that identical meshes have been used in the BEM and FEM model. The main advantage is that no interpolation of pressures and structural response is required in the exchange of boundary interface information between the fluid and structural domain.

STRUCTURAL EQUATIONS IN WET MODAL SPACE

For a better convergence, estimates for fluid added mass and hydrodynamic damping have been added to the hydrodynamic force vector, $\mathbf{f}_h$, and added to the left-hand side of the structural dynamic equation. Then, Eq. 5.8 for FSI cycle k reads,

$$\begin{aligned}\left([\mathbf{M}_s]+\left[\mathbf{M}_h^*\right]\right)\{\ddot{\mathbf{u}}\}^k+([\mathbf{C}_s]+[\mathbf{C}_h])\{\dot{\mathbf{u}}\}^k+[\mathbf{K}_s]\{\mathbf{u}\}^k=&\\ \{\mathbf{f}_h\}^{k-1}+\left\{\mathbf{f}_{fict}\right\}^{k-1}+\left[\mathbf{M}_h^*\right]\{\ddot{\mathbf{u}}\}^{k-1}+[\mathbf{C}_h]\{\dot{\mathbf{u}}\}^{k-1}&\end{aligned} \tag{5.21}$$

where $[\mathbf{C}_h]$ denotes the hydrodynamic damping matrix. The derivation of added mass and hydrodynamic damping matrices has been elaborated in Chapter 4. Eq. 5.21 shows clearly the main drawback of a partitioned method; the structural response for FSI cycle k is computed from the loads based on the previous FSI cycle $k-1$.

The structural problem is solved in wet modal space. Accordingly, Eq. 5.21 transforms to,

$$\begin{aligned}&\left[\bar{\boldsymbol{\Psi}}\right]^T\left([\mathbf{M}_s]+\left[\mathbf{M}_h^*\right]\right)\left[\bar{\boldsymbol{\Psi}}\right]\{\ddot{\mathbf{r}}\}^k+\left[\bar{\boldsymbol{\Psi}}\right]^T([\mathbf{C}_s]+[\mathbf{C}_h])\left[\bar{\boldsymbol{\Psi}}\right]\{\dot{\mathbf{r}}\}^k+\left[\bar{\boldsymbol{\Psi}}\right]^T[\mathbf{K}_s]\left[\bar{\boldsymbol{\Psi}}\right]\{\mathbf{r}\}^k=\\ &\left[\bar{\boldsymbol{\Psi}}\right]^T\left[\mathbf{M}_h^*\right]\left[\bar{\boldsymbol{\Psi}}\right]\{\ddot{\mathbf{r}}\}^{k-1}+\left[\bar{\boldsymbol{\Psi}}\right]^T[\mathbf{C}_h]\left[\bar{\boldsymbol{\Psi}}\right]\{\dot{\mathbf{r}}\}^{k-1}+\left[\bar{\boldsymbol{\Psi}}\right]^T\left(\{\mathbf{f}_h\}+\left\{\mathbf{f}_{fict}\right\}\right)^{k-1}\end{aligned} \tag{5.22}$$

which can be written as,

$$[\boldsymbol{I}]\{\ddot{\mathbf{r}}\}^k+\left[\bar{\boldsymbol{Z}}\right]\{\dot{\mathbf{r}}\}^k+\left[\bar{\boldsymbol{\Omega}}\right]\{\mathbf{r}\}^k=\left[\bar{\boldsymbol{\Psi}}\right]^T\{\mathbf{f}\}^{k-1} \tag{5.23}$$

where $\left[\bar{\boldsymbol{Z}}\right]$ is the total damping matrix in wet modal space. After this transformation a weak coupling in the system of equations still exists as a result of the full hydrodynamic damping matrix, $[\mathbf{C}_h]$. This coupling in the system of equations has been neglected and model reduction has been applied by computing the modal participation factors only for a limited number of mode shapes.

The flow chart of Figure 5.1 shows that the added mass and hydrodynamic damping forces are approximated based on the response of the previous FSI cycle and are added to the other excitation forces, resulting in M modal force vectors for a full revolution $\left[\bar{\boldsymbol{\Psi}}^T\mathbf{f}_0,\bar{\boldsymbol{\Psi}}^T\mathbf{f}_1,\ldots,\bar{\boldsymbol{\Psi}}^T\mathbf{f}_{M-1}\right]$.

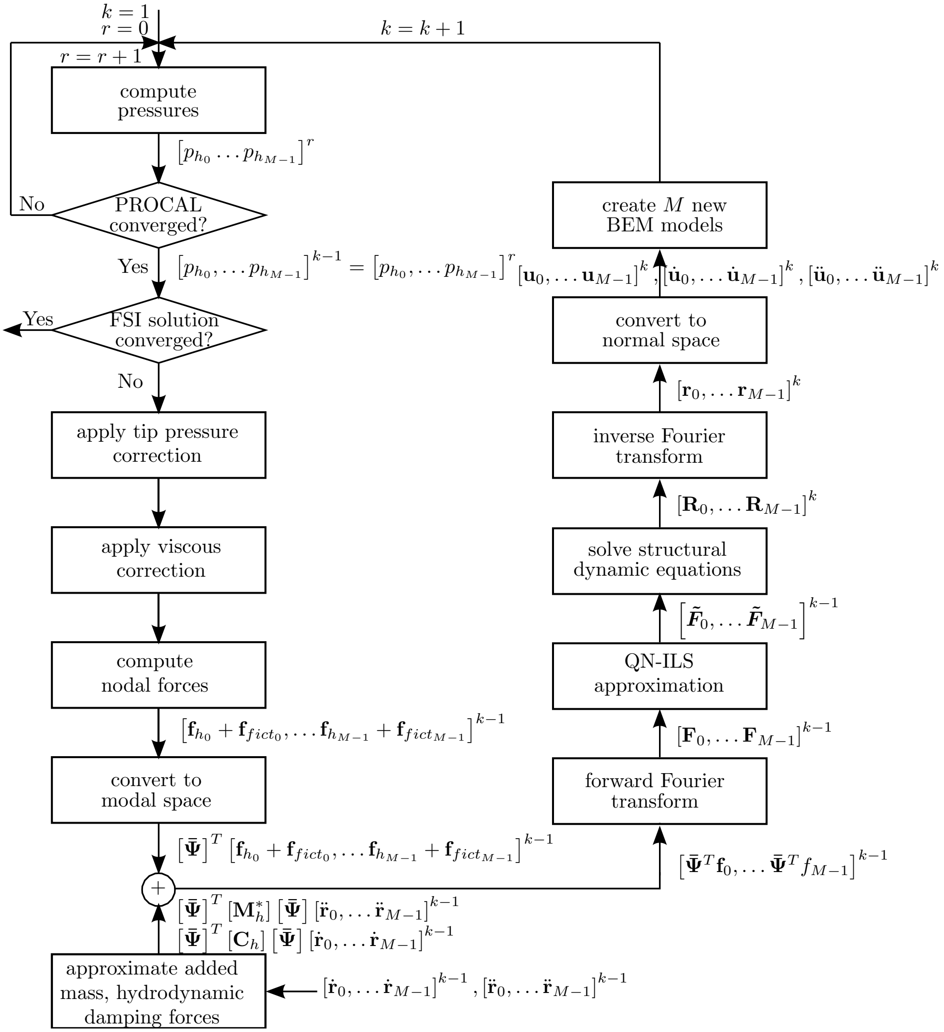

Figure 5.1: Flow chart of the coupling scheme.

FOURIER TRANSFORM

The time periodic coupling allows one to solve the structural problem in the frequency domain by taking advantage of the periodicity in the problem, resulting in a faster convergence to the steady state solution than in case of solving the problem in the time-domain as shown in Appendix A. With the forward Fourier transform the sequence of modal force vectors for a full revolution $\left[\bar{\boldsymbol{\Psi}}^T\mathbf{f}_0,\bar{\boldsymbol{\Psi}}^T\mathbf{f}_1,\dots,\bar{\boldsymbol{\Psi}}^T\mathbf{f}_{M-1}\right]$ transform into M modal force vectors in the frequency domain, $[\mathbf{F}_0,\mathbf{F}_1\dots\mathbf{F}_{M-1}]$, which are defined by,

$$\{\mathbf{F}_m\}=\sum_{l=0}^{M-1}\left[\bar{\boldsymbol{\Psi}}\right]^T\{\mathbf{f}_l\}\,e^{-im\hat{\omega}t_l},\qquad m=0,1,\dots,M-1 \tag{5.24}$$

where $\hat{\omega}$ is the fundamental frequency equal to $2\pi n$ in rad/s with n the propeller revolution rate in Hz. The inverse transform is then,

$$\left\{\bar{\boldsymbol{\Psi}}^T \mathbf{f}_l\right\} = \sum_{m=0}^{M-1} \{\mathbf{F}_m\} e^{im\hat{\omega}t_l}, \qquad l = 0, 1, \ldots, M-1 \tag{5.25}$$

QN-ILS APPROXIMATION

By computing the structural response for each FSI cycle straight from Eq. 5.23 the FSI solution will most likely diverge because of the strong coupling between fluid and structure. Therefore, a dedicated partitioned solution method is required to keep the iterative solution process stable and to converge to the steady state FSI solution in an efficient way. The method which has been implemented in this work is the Quasi-Newton inverse least squares (QN-ILS) method which belongs to the class of matrix-free Krylov subspace methods. Within the coupling method the frequency domain wet modal forces $\{\mathbf{F}\}^{k-1}$ might be used as an approximation for $\{\mathbf{F}\}^k$. Repeating this for subsequent FSI cycles is basically a Gauss-Seidel iterative way of solving the FSI problem, which does not necessarily (efficiently) converge. With the QN-ILS method a better approximation for $\{\mathbf{F}\}^k$ is made based on all previous iterates of $\{\mathbf{F}\}$ instead of simply using the last one, i.e. $\{\mathbf{F}\}^{k-1}$. The basic idea behind the QN-ILS approximation is that the best approximation for $\{\mathbf{F}\}^k = \left\{\tilde{\boldsymbol{F}}\right\}^{k-1}$, where $\left\{\tilde{\boldsymbol{F}}\right\}^{k-1}$ is that linear combination of $\{\mathbf{F}\}$ from previous iterates $\{k-1, k-2, \ldots 0,\}$ that will minimise the residual of the FSI solution [12]. For more information one is referred to Appendix A.

FREQUENCY DOMAIN SOLUTION IN WET MODAL SPACE

Similar to the modal forces the time domain discretised wet modal participation factors $\mathbf{r}_l$ are related to the wet modal participation factors in the frequency domain $\mathbf{R}_m$ by,

$$\{\mathbf{r}_l\} = \sum_{m=0}^{M-1} \{\mathbf{R}_m\} e^{im\hat{\omega}t_l}, \qquad l = 0, 1, \ldots M-1 \tag{5.26}$$

Eq. 5.23 can be written with the Fourier transformed QN-ILS approximated modal forces, $\left\{\tilde{\boldsymbol{F}}_m\right\}$, and wet modal participation factors, $\{\mathbf{R}_m\}$ as,

$$\left(-[\boldsymbol{I}]\, m^2\hat{\omega}^2 + i\left[\bar{\boldsymbol{Z}}\right] m\hat{\omega} + \left[\bar{\boldsymbol{\Omega}}\right]\right)\{\mathbf{R}_m\}^k e^{im\hat{\omega}t} = \left\{\tilde{\boldsymbol{F}}_m\right\}^{k-1} e^{im\hat{\omega}t} \tag{5.27}$$

The wet modal participation factors can be solved for $m = 0, \ldots, M-1$ using,

$$\{\mathbf{R}_m\}^k = \left(-[\boldsymbol{I}]\, m^2\hat{\omega}^2 + i\left[\bar{\boldsymbol{Z}}\right] m\hat{\omega} + \left[\bar{\boldsymbol{\Omega}}\right]\right)^{-1} \left\{\tilde{\boldsymbol{F}}_m\right\}^{k-1}, \qquad m = 0, 1, \ldots, M-1 \tag{5.28}$$

TIME DOMAIN SOLUTION IN NORMAL SPACE

Having computed the sequence of M wet modal participation factors in the frequency domain, the next step is to convert the solution to the time domain. The time domain wet modal participation factors $\{\mathbf{r}_l\}$ can be obtained from the inverse Fourier transform of Eq. 5.26. In analogy with Eq. 5.13 the time domain nodal deformations can be obtained from the wet mode shapes and the wet modal participation factors,

$$\{\mathbf{u}_l\} = \left[\bar{\boldsymbol{\Psi}}\right]\{\mathbf{r}_l\}, \qquad l = 0, 1, \ldots M-1. \tag{5.29}$$

BEM MODEL UPDATING

Based on the structural response calculated for FSI cycle k, M new BEM models are constructed for the next FSI cycle. The new BEM models include the deformed geometry and the adapted hydrodynamic influence coefficients based on the calculated structural deformations at each time step. This has been accomplished by constructing new panel files which include the geometry of the deformed blade with the PROPART toolbox [13]. From these new panel files the corresponding hydrodynamic influence coefficients are calculated in PROCAL. Secondly, the source strengths are redefined for each time step with Eq. 5.5 which includes the blade vibration velocities. Then, a new FSI cycle starts by first computing the steady state solution for the loads from the updated BEM models. When the loads from the present and previous FSI cycle differ less than a certain tolerance the fully coupled FSI solution is obtained, otherwise the iterative procedure continues until convergence.

5.4. SUMMARY

A partitioned FSI coupling for the non-uniform flow hydro-elastic analysis of highly flexible propellers in cavitating and non-cavitating conditions has been presented. The method is a partitioned FSI method in which coupling iterations between fluid and structural solver are performed on a periodic level rather than per time step in order to accomplish the strong coupling between the fluid and structural sub-domain. A time periodic coupling was necessary for the present BEM-FEM coupling, since the BEM method is completely periodical in nature and therefore a time step coupling would not converge. In addition, a time periodic coupling allows to solve the structural problem in the frequency domain, which is advantageous for the convergence speed. In the BEM-FEM coupling procedure the structural sub-problem has been solved in the frequency domain, in wet modal space, which allows for a model reduction by involving only a limited number of mode shapes. The present FSI framework is not confined to this way of solving the structural equations. For instance, it would be also possible to include a geometrically non-linear FEM, because of the full separation of fluid and structural solver. In the next chapter the BEM-FEM coupling for non-uniform flows is validated with experimental data obtained from model- and full-scale measurements.

REFERENCES

[1] H. Lee, M. Song, J. Suh, and B. Chang, “Hydro-elastic analysis of marine propellers based on a BEM-FEM coupled FSI algorithm,” *International Journal of Naval Architecture and Ocean Engineering*, vol. 6, pp. 562–577, 2014.

[2] X. He, Y. Hong, and R. Wang, “Hydro-elastic optimisation of a composite marine propeller in a non-uniform wake,” *Ocean Engineering*, vol. 39, p. 14–23, 2012.

[3] Y. Young, “Time-dependent hydro-elastic analysis of cavitating propulsors,” *Journal of Fluids and Structures*, vol. 23, pp. 269–295, 2007.

[4] L. Jiasheng, Q. Yegao, and H. Hongxing, “Hydroelastic analysis of underwater ro-

tating elastic marine propellers by using a coupled BEM-FEM algorithm," *Ocean Engineering*, vol. 146, no. 1, pp. 178–191, 2017.

[5] E. van Brummelen, "Partitioned iterative solution methods for fluid-structure interaction," *International Journal for Numerical Methods in Fluids*, vol. 65, no. 1-3, pp. 3–27, 2011.

[6] E. van Brummelen, "Added mass effects of compressible and incompressible flows in fluid-structure interaction," *Journal of Applied Mechanics*, vol. 76, no. 2, p. 021206, 2009.

[7] Y. Young, M. Motley, R. Barber, E. Chae, and N. Garg, "Adaptive composite marine propulsors and turbines: Progress and challenges," *Applied Mechanics Reviews*, vol. 68, no. 6, p. 060803, 2016.

[8] G. Vaz, *Modelling of sheet cavitation on hydrofoils and marine propellers using boundary element methods.* PhD thesis, Instituto Superior Técnico, Lisbon, Portugal, 2005.

[9] G. Vaz and J. Bosschers, "Modelling of three dimensional sheet cavitation on marine propellers using a boundary element method," Sixth International Symposium on Cavitation, Wageningen, The Netherlands, 2006.

[10] J. Degroote, R. Haelterman, S. Annerel, P. Bruggeman, and J. Vierendeels, "Performance of partitioned procedures in fluid-structure interaction," *Computers Structures*, vol. 88, no. 7–8, pp. 446–457, 2010.

[11] L. Morino and C. Kuo, "Subsonic potential aerodynamics for complex configurations: a general theory," *AIAA Journal*, vol. 12, no. 2, p. 191–197, 1974.

[12] T. Scholcz, *Multi-fidelity methods for fluid-structure interaction and uncertainty quantification.* PhD thesis, Delft University of Technology, Delft, The Netherlands, 2015.

[13] J. Huisman and E. Foeth, "Automated multi-objective optimization of ship propellers," Fifth International Symposium on Marine Propulsors, Espoo, Finland, 2017.

6

Chapter 6

Validation of the BEM-FEM coupling for non-uniform flows

This chapter includes validation studies on model- and full-scale of the fluid-structure interaction (FSI) method as presented in previous chapter. In this method a boundary element method (BEM) and a finite element method (FEM) are coupled. The coupling applies to the condition of non-uniform flows. For the validation study on model-scale the blade deformations of two 0.34 m diameter composite propellers were measured with a stereo camera measurement set-up in combination with a digital image correlation (DIC) technique for a full revolution. A comparison between measurement and calculation results shows that qualitatively the blade deflections have been correctly predicted with the non-uniform flow BEM-FEM coupling, although, quantitatively significant differences were found. These differences are attributed to differences between the actual wakefield and the wakefield as used in the calculations.

For the full-scale validation study a purposely designed composite propeller with a diameter of 1 m was manufactured. Also an underwater measurement set-up including a stereo camera system, remote control of the optics and illumination system was developed. During sea trials the blade deflections were measured in three different positions. A comparison between measured and calculated torque shows that the measured torque is much larger than computed. This is attributed to the differences between effective and nominal wakefields, where the latter one has been used for the calculations. To correct for the differences between measured and computed torque the calculated pressures have been amplified accordingly. In that way the deformations which have been computed with the BEM-FEM coupling for non-uniform flows became very similar to the measured results.

This chapter is partly based on the journal paper: P. Maljaars, N. Grasso, J. den Besten and M. Kaminski, “BEM-FEM coupling for the analysis of flexible propellers in non-uniform flows and validation with full-scale measurements,” submitted to *Journal of Fluids and Structures.*

6.1. INTRODUCTION

Several experimental studies with flexible propellers have been presented in literature. Some of these studies have been used for the validation of uniform flow fluid-structure interaction (FSI) computations, but rarely for the validation of FSI computations in non-uniform flows. For instance in [1], the tip deformations of propellers with a diameter of 0.61 m have been measured in uniform flow by using a laser tracking technique and the results have been compared to numerical results obtained with a BEM-FEM coupling. It was concluded that the numerical predictions compared well with the experimental results. More details about the propellers, tests and results as presented in [1] can be found in [2]. The latter paper presents results of measurements and computations in a non-uniform four-cycle wakefield. Compared to numerical results the magnitude of the measured pitch change was larger than predicted, however the trends were predicted well. In [3] the experimental results presented in [1, 2] have been used for validation of their unsteady BEM-FEM coupling and similar results were found. Experimental results for propellers with a diameter of 0.25 m in a uniform flow have been obtained in [4] by manually measuring from image data the propeller tip displacements and comparing these results with numerical results obtained from FSI computations.

A stereo camera system in combination with a digital image correlation (DIC) technique is an optical technique that can provide the full-field blade deformations. This is a promising technique and has many advantages, including high resolution results, non-intrusive measuring and good accuracy over a range of scales [5]. The application of a DIC technique for measuring propeller blade deformations in a uniform flow has been described in [6]. An improved version of that measurement set-up has been used to obtain the uniform flow experimental data presented in Chapter 3. These measurements are used for the validation of the steady BEM-FEM coupling method, showing that reasonable results can be obtained with the method. A slightly different optical technique was applied to measure the blade deformations of a small propeller with a diameter of 0.25 m in a uniform flow with the blade surface covered with markers instead of the random speckle pattern applied for DIC [7].

Hence, it can be concluded that in so far as literature presents results on the validation of flexible propeller calculations, those studies are for model-scale propellers (maximum diameter of 0.61 m), where the measurement results have been obtained from laboratory tests. Except in [2] results for non-uniform flow conditions have been shown.

This chapter shows experimental results obtained from model-scale laboratory experiments and full-scale tests, both for in-behind ship conditions. In the model-scale experiments the propeller blade deformations have been measured for a full revolution with a stereo camera set-up. The experimental results have been compared to the numerical results computed with the non-uniform flow BEM-FEM coupling presented in the previous chapter.

The full-scale tests have been performed with a purposely designed 1 m diameter glass-epoxy propeller and an underwater measurement set-up. The full blade displacement field has been measured for three different blade positions and compared to calculation results obtained with the non-uniform flow BEM-FEM coupling.

This chapter is structured as follows. In Section 6.2 the validation study with the model-scale composite propellers is presented. Section 6.3 explains the full-scale propeller design and measurement set-up and provides a comparison between numerical and experimental results. Conclusions are given in Section 6.4.

6.2. VALIDATION ON MODEL-SCALE

In this section the experiments with the model-scale propellers will be described and finally a comparison between experimental and calculation results is given.

6.2.1. PROPELLERS AND FLOW CONDITIONS

The measurements have been conducted with the two-bladed, 0.34 m in diameter, right turning composite propellers as shown and defined in Section 2.2. The FEM modelling of these propellers have been described in Section 2.4. With these FEM models the natural frequencies and mode shapes have been computed which have been used in the non-uniform flow BEM-FEM coupling calculations to compute the structural response with modal analyses, see Chapter 5.

6.2.2. CAVITATION TUNNEL MEASUREMENTS

In Chapter 3 a validation study with the same propellers have been presented for uniform flow. In that chapter it has been shown that these propeller are challenging to solve with a BEM solver due to flow separation. On the other hand it has been shown that, depending on the flow condition, the hydro-elastic response has been well predicted with the uniform flow BEM-FEM coupling. A next step was to perform the same kind of experiments but then in non-uniform flow. Again the measurements have been conducted at and in cooperation with the Maritime Research Institute Netherlands (MARIN). MARIN's cavitation tunnel was used as the testing facility. This section first describes the wakefield for the non-uniform flow experiments. Then the measurement technique is explained and finally the measurement set-up is described.

WAKEFIELD

The first preparations regarding the non-uniform flow measurements started with defining a target wakefield for the experiments. The wakefield in Figure 6.1 was chosen as a target and has been mainly based on the following considerations: first of all, the non-uniform wakefield has to result in a significant difference between maximum and minimum blade deformation during a revolution. The target was a maximum deformation of approximately twice the minimum deformation. Secondly, the hydro-elastic response of flexible propellers is mainly quasi-static as discussed in Chapter 4 and therefore harmonics in the wakefield which would excitate dynamic blade vibrations have to be small. The next step was to design the geometry and position of a flow obstructing body which would result in the target wakefield at the propeller plane. This has been performed by MARIN by solving an optimization problem. In the optimization problem the difference between the target wakefield and a wakefield calculated with a Reynolds-averaged Navier-Stokes (RANS) solver has been minimised by using a genetic algorithm. After less than 20 generations the algorithm converged and the wakefield of Figure 6.2 was obtained. Figure 6.2 is the wakefield without propeller-body interaction, i.e. the nominal wakefield. As input for BEM calculations the effective wakefield, i.e. the nominal wakefield plus propeller-body interaction is required. The effective wakefield has been computed by MARIN from a RANS-BEM calculation [8]. Figure 6.3 shows the calculated effective wakefield for a flow velocity of 6.75 m/s and a propeller revolution rate of 1300 rpm. The following step was to confirm by measurements that the wakefield behind the body is as expected from the RANS calculation.

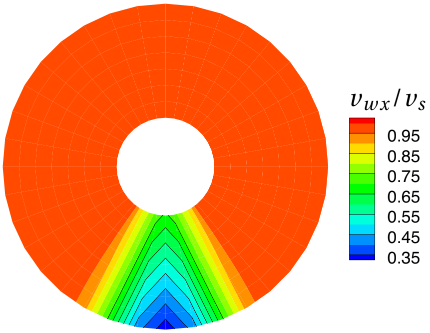

Figure 6.1: Target wakefield (only axial).

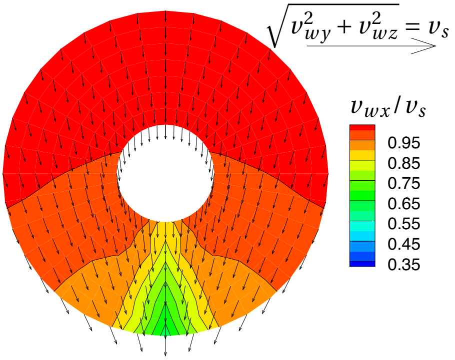

Figure 6.2: RANS nominal wakefield.

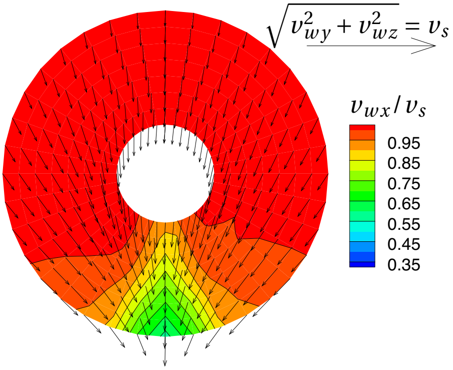

Figure 6.3: RANS effective wakefield.

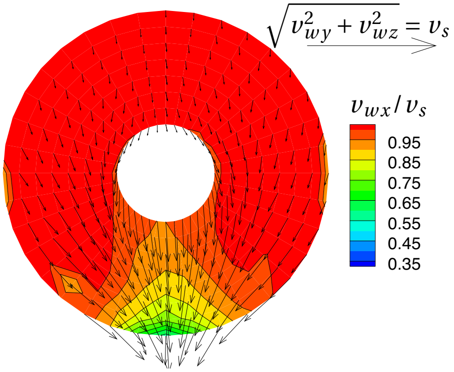

Figure 6.4: Measured nominal wakefield.

Two possible measurement techniques were considered for measuring the nominal wakefield in the cavitation tunnel, using Pitot tubes or using Particle Image Velocimetry (PIV). The later one was chosen because with PIV the wakefield can be fully captured and PIV is a non-intrusive method. PIV works by taking images of particles in a flow illuminated by a laser sheet. These particles act as tracers of the flow. The flow velocity can be obtained from the displacement of the captured particles in subsequent images by using cross-correlation and the time difference between the images. Figure 6.5 shows drawings of the PIV measurement set-up.

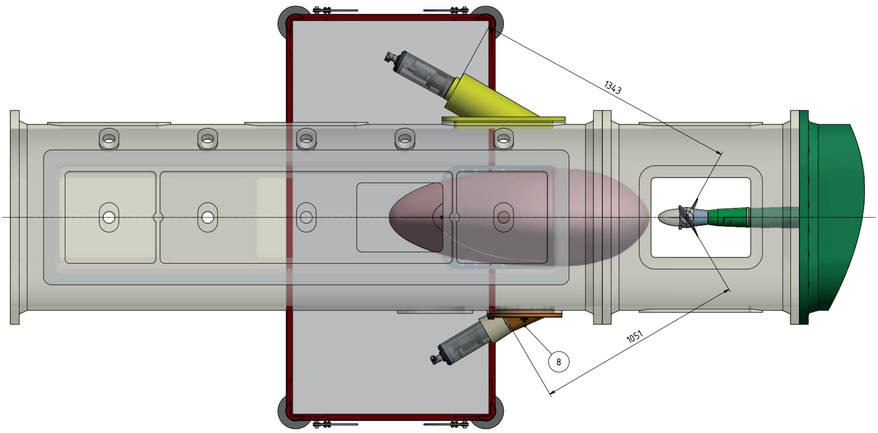

(a) Top-view with PIV cameras.

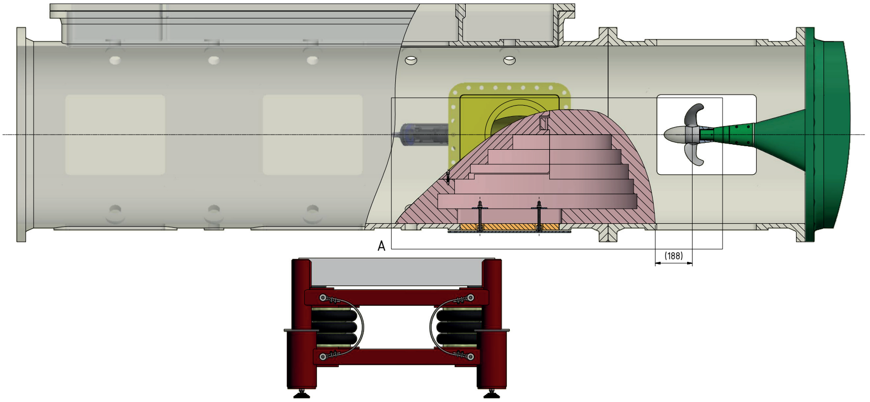

(b) Side-view.

Figure 6.5: Cavitation tunnel PIV measurement set-up, flow is from left to right (Courtesy of MARIN).

MEASUREMENT TECHNIQUE

Similarly to the non-uniform flow experiments as presented in Chapter 3 a digital image correlation technique (DIC) has been used for measuring the blade deformations. DIC is a full-field image analysis method, based on grey value digital images that finds the displacements and deformations of an object in three dimensional space [9]. The method tracks the grey value pattern from which the deformations of the object are calculated. In order to use the DIC technique, the surface of the measured object must have a random speckle pattern with no preferred orientation and sufficiently high contrast. The size of the features in the pattern should be large enough to be distinguished. For that reason on the suction side of the propeller blades a hand-painted speckle pattern was applied (Figure 2.1).

On average 35 image pairs for each blade position were acquired. The image data was acquired with a temporal resolution of one degree. In the post-processing bad images due to cavitation were discarded. The remaining images have been post-processed individually and from each image pair the blade deformation field has been obtained after a correction for rigid body motions induced by vibrations and movements of the shaft. This means approximately 35 deformation fields have been obtained for each blade position. These deformation fields have been averaged to reduce the precision error, which turned out to be large in these experiments, especially due to transient dynamics in the blade response. An image averaging, (i.e. averaging of the results before post-processing as applied in the post-processing of the uniform flow experiments) was not possible due to the transient dynamics.

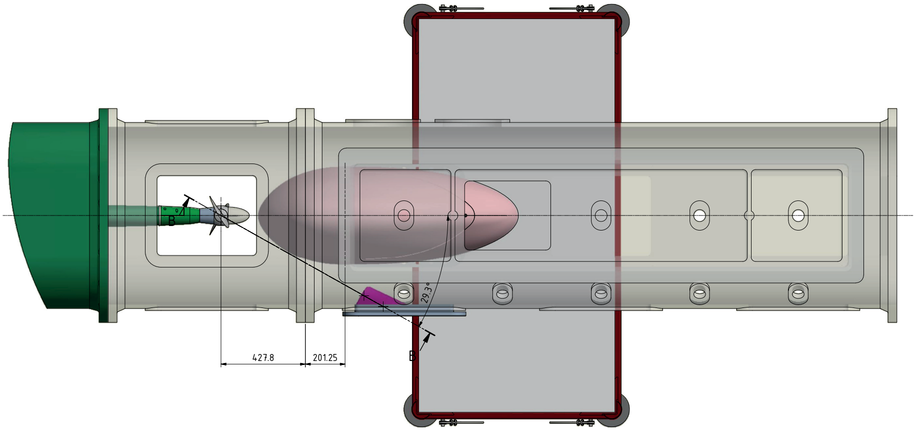

(a) Top-view.

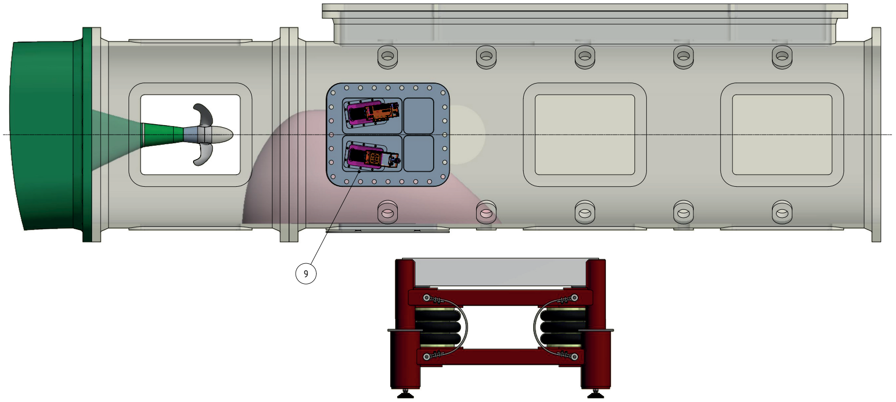

(b) Side-view with window for DIC cameras.

Figure 6.6: Cavitation tunnel DIC measurement set-up, flow is from right to left (Courtesy of MARIN).

MEASUREMENT SET-UP

The measurement set-up is similar to the one explained in Chapter 3 but differs in several aspects to make it dedicated for non-uniform flow experiments. First of all, the body for the wakefield generation has been placed inside the tunnel. This made the bottom window, which was used in the uniform flow experiments for one of the DIC cameras, unusable for observations. For that reason a new observation window was made for the side of the tunnel in which both cameras were placed. Hence, both cameras were positioned much closer together, which lowers the measurement accuracy, but on the other hand it is advantageous for capturing the propeller for a full revolution. Drawings of the cavitation tunnel measurement set-up have been shown in Figure 6.6.

UNCERTAINTIES

The accuracy of the present DIC measurements can be expected to be lower compared to the uniform flow DIC measurements as presented in Chapter 3 for the following three reasons. First of all, the cameras were placed closer together. Secondly, in the present images the full propeller is in view, while for the non-uniform flow experiments only one blade was visible. Thirdly, the camera view angle in the non-uniform flow measurements was optimized to achieve best results. In these experiments the full blade revolution has been captured and therefore the camera view angle is not optimal for most of the blade positions. Also a lot of transient dynamic behaviour was observed during the measurements and is present in the data as well. These dynamics originate from three main sources. These sources are: flow separation behind the body, flow separation due to the observation window which partly sticks into the tunnel (Figure 6.6) and unsteady cavitation.

In Chapter 3 $\pm 20\ \mu m$ has been reported as precision uncertainty for the DIC measurements. Since the results have been averaged after post-processing, this precision uncertainty has been reduced to zero. In Chapter 3 the systematic DIC uncertainty has been based on the measured blade response adjacent to the hub which should be nearly zero, but which is generally not the case. From this a minimum systematic uncertainty of $\pm 60\ \mu$m has been assumed for these measurements. This uncertainty has been increased along the radius, by $\pm 10\ \mu$m for every 10% increase in propeller radius starting from 60% of the propeller radius and onwards. Hence the maximum systematic uncertainty is ±0.1 mm at the propeller tip.

The uncertainties in the calculated blade deflections have been derived from the uncertainties shown in Figures 3.17 and 3.18. From these figures a relation between deflections and uncertainties can be deduced, which have been used to establish the uncertainties in the calculated blade responses.

COMPARISON OF DEFLECTIONS

Measurements and analyses have been conducted with propeller 45 and propeller 90. For propeller 45 a measurement has been performed for a tunnel flow speed of 6.75 m/s and a rotation rate of 1450 rpm. The measurement with propeller 90 has been performed at the same flow speed but for the lower rotation rate of 1350 rpm. The structural response for both blades have been simultaneously measured, since the whole propeller was in view, however only results for blade 1 will be shown, because both measurements provide the best data for blade 1.

Figure 6.7 and 6.8 show the measured and calculated blade deflections for both conditions, with the 95% uncertainty intervals (U_{95}) as defined above. The deflections at points on 0.75 of the blade chord length have been shown, since for these points the measurements did provide results up to 90% of the blade radius, R, ($r = 0.9R$), while for the mid-chord points this was less. The calculation results have been obtained with the BEM-FEM coupling for non-uniform flows. These calculations should be performed with an effective wakefield. However, it is not possible to measure the effective wakefield, therefore from the measured nominal wakefield an effective wakefield has been derived by subtracting the difference between calculated nominal and effective wakefield (Figures 6.2 and 6.3) from to the measured nominal wakefield, (Figure 6.4). Calculations have been also performed with the measured nominal wakefield, only the deflections for $r = 0.9R$ have been shown for that case. From the differences between the calculation results obtained with the nominal and the effective wakefield it can be concluded that propeller-body interaction effects cannot be neglected for these cases. Regarding the experimental results, the raw signals and the filtered signals have been shown in Figures 6.7 and 6.8.

From Figures 6.7 and 6.8 it can be concluded that up to $r = 0.8R$ the uncertainty bandwidths for measurements and calculations overlap. This could be attributed to the relatively large uncertainties for the small deflections found for $r \leq 0.8R$. On the other hand the predicted and measured curves for a full revolution are qualitatively very similar, especially for the results presented for propeller 90 in Figure 6.8. This propeller has been tested at the condition which is most similar to the condition for which the nominal and effective wakefields have been computed. Hence, the effective wakefield which has been used in the calculation of propeller 90 is more correct for this condition than for the analysis of propeller 45. This also indicates that it might be important for these analyses to use effective wakefields specific for each particular loading condition.

The measured and calculated responses for $r = 0.9R$ differ significantly and measurement and calculation uncertainties do not overlap. The calculated deflections are much larger than measured, especially at the wakepeak for the results obtained for propeller 45 and for the whole revolution in case of propeller 45. This corresponds to the results presented in Figures 3.17 and 3.18 for uniform flow where also the predicted deflections at the tip are significantly larger than measured. In Chapter 3 these differences have been attributed to leading edge vortex separation and viscous effects which have not been modelled in BEM.

Also the twist deformations have been analysed, however the uncertainty in the measurement results was too large and the twist deformations were too small to make a comparison with the calculated twist deformations.

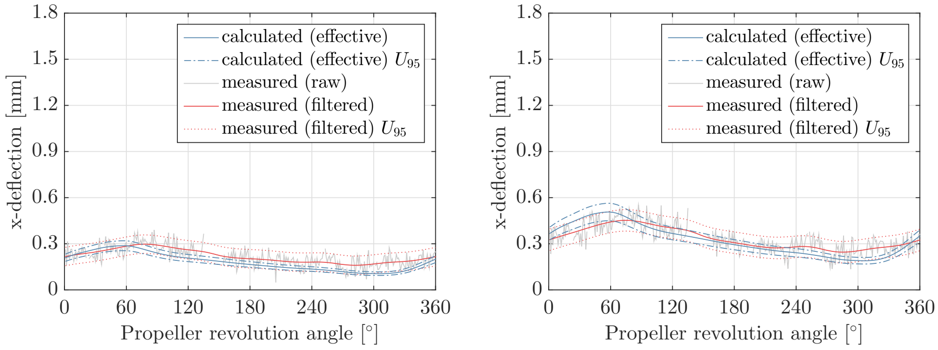

(a) $r = 0.6R$.

(b) $r = 0.7R$.

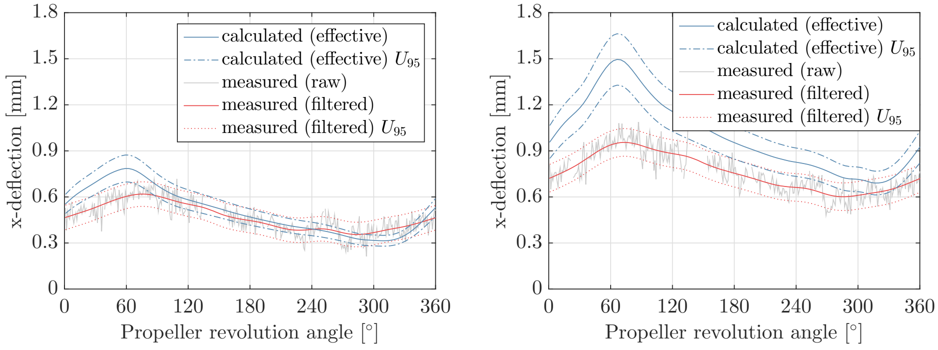

(c) $r = 0.8R$.

(d) $r = 0.9R$.

Figure 6.7: Propeller 45, blade 1, (1450 rpm), measured and calculated deflections of points on 0.75 of the chord length for a full revolution, at four radial stations, with 0°corresponding to the six o'clock position.

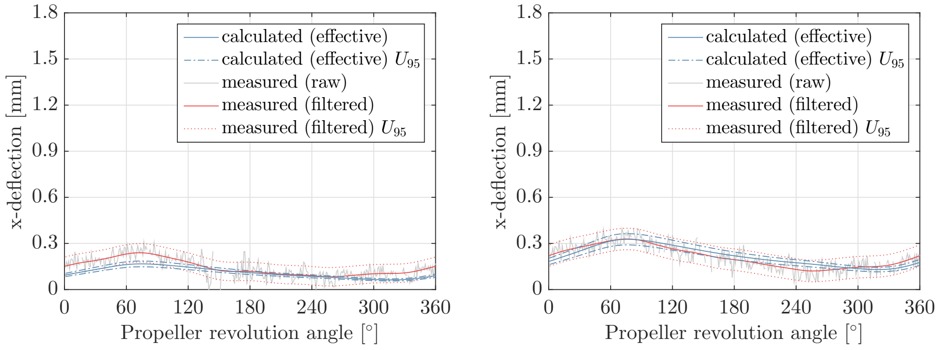

(a) $r = 0.6R$.

(b) $r = 0.7R$.

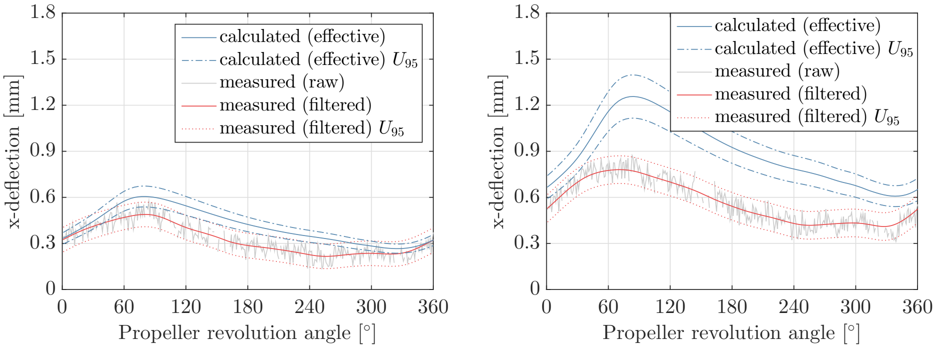

(c) $r = 0.8R$.

(d) $r = 0.9R$.

Figure 6.8: Propeller 90, blade 1, (1350 rpm), measured and calculated deflections of points on 0.75 of the chord length for a full revolution, at four radial stations, with 0°corresponding to the six o'clock position.

COMPARISON OF THRUST

During the measurement also the total thrust and torque have been measured, these signals show a lot of variation, indicating unsteadiness in the flow due to unsteady flow separation behind the body. From the measured thrust time signals spectra have been obtained and compared to the harmonics in the calculation results. Figure 6.9 show the thrust harmonics for the calculations and the measurements. For both cases the mean thrust is over-predicted in the calculations. The calculation results show perfect peaks at multiples of the blade passing frequency, which are also much larger than in the measurements. Another difference between measurement and calculation results are the rotation rate harmonics which are not present in the calculation results, but clearly visible in the spectra of the measurements. Rotation rate harmonics were not expected because the propeller should have two blades which respond similarly. The measurement results show that this is not the case. A probable reason might be the difference between the blade geometries and the positioning of the blades in the hub as pointed out in [10].

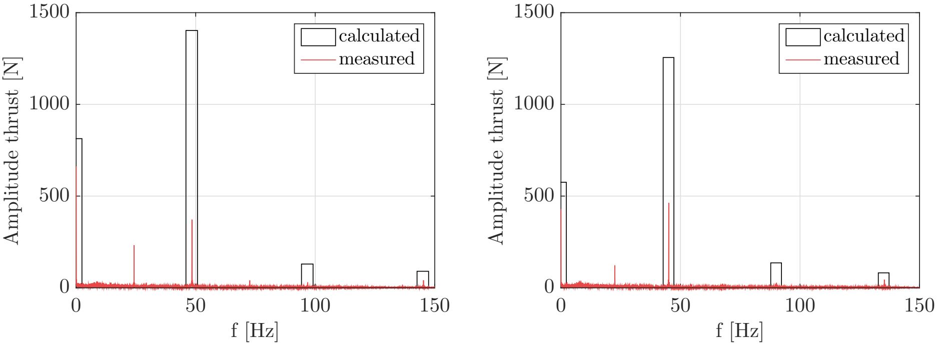

Figure 6.9: Comparison of measured and calculated propeller thrust harmonics for propeller 45, 1450 rpm (left) and propeller 90, 1350 rpm (right), the amplitude of the harmonics have been amplified with a factor 10, except for the 0$^{\text{th}}$ harmonic, i.e. the mean thrust.

6.3. VALIDATION ON FULL-SCALE

This section describes the most important details of the full-scale propeller and its design. Also, the full-scale measurements are described. Finally, a comparison between the experimental and numerical results is made.

6.3.1. VESSEL AND WAKEFIELD

The full-scale measurements have been performed on the Nautilus, a diving support vessel of the Royal Dutch Navy, see Figure 6.10. The main particulars of the the vessel are summarized in Table 6.1. The Nautilus is a twin-screw vessel of which the port-side propeller has been replaced by a composite one. The non-uniform nominal wakefield at the port-side propeller plane has been calculated with a RANS solver for a ship speed of 10 kn. Figure 6.11 shows the computed wakefield.

Figure 6.10: The Nautilus (Photo: H. Huppel).

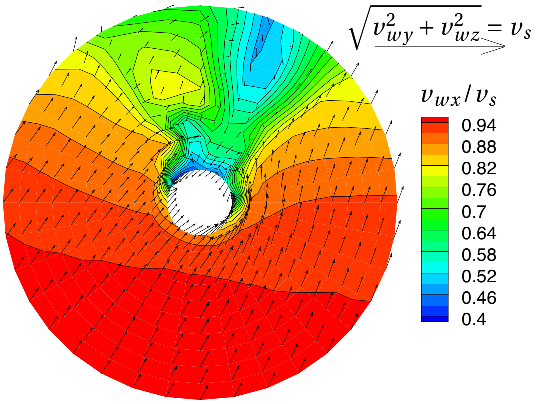

Figure 6.11: Nominal wakefield at the portside propeller plane of the Nautilus.

Length	37.8 m	Maximum speed	10.5 kn
Beam	8.7 m	Propulsion	Twin-screw
Depth	3.1 m	Engine	2×Volvo Penta Diesel 280 kW
Draught	1.5 m		

Table 6.1: Main particulars of the Nautilus.

6.3.2. PROPELLER GEOMETRY

In an early design stage it was assessed that the existing blade geometry, Figure 6.12a, would result in an unacceptable amount of suction side sheet cavitation at higher speeds. Furthermore, to enhance blade flexibility, a propeller geometry with more skew was desired. Therefore, a new propeller geometry, Figure 6.12b, with a similar open-water performance as the existing blade geometry was designed. The main particulars of the new and old propeller geometry are summarized in Table 6.2. The main differences between the old and new propeller geometry are in the skew and camber of the propeller section profiles. The change in skew for increasing blade flexibility the change in camber to get rid of the cavitation. Initially, the thicknesses of the composite section profiles were taken similarly to what would have been used in the design of a nickel-aluminium bronze propeller (NAB) propeller, but in a later stage the blade thickness at the root section has been significantly increased to allow for the realisation of the blade-hub connection.

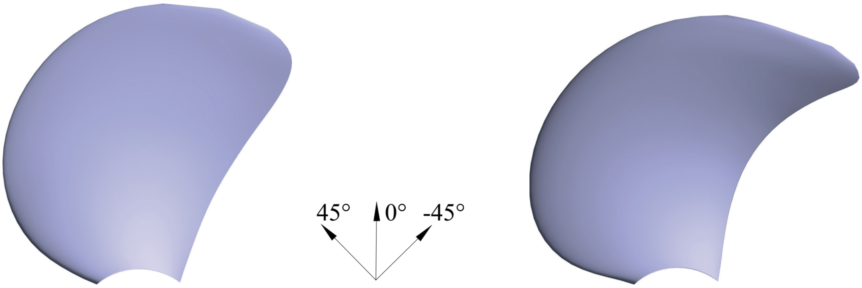

(a) NAB blade.

(b) Composite blade.

Figure 6.12: Geometry of NAB and composite blade and ply angle definition.

	NAB propeller	**Composite propeller**
Diameter	1000 mm	1000 mm
Pitch Ratio (mean)	0.94	0.85
Expanded Area Ratio	0.73	0.75
Number of Blades	4	4
Thickness Ratio (mean)	0.0620	0.0817
Camber Ratio (mean)	0.0137	0.0299
Boss Ratio	0.1825	0.1825
Total Skew Angle	29.5°	40.4°
Direction of rotation	outward-turning	outward-turning

Table 6.2: Main particulars of the original NAB and composite propeller.

6.3.3. PROPELLER STRUCTURAL DESIGN

Following the propeller geometry design the propeller structural design was made. The structural design has been based on several considerations, itemized below.

- Since the composite propeller is a retrofit on an existing drive train system, it was most obvious to manufacture separate composite blades and connect the blades to a NAB hub.
- For validation purposes a propeller as flexible as possible was desirable. For that reason glass fibre reinforced epoxy was selected as the blade material.
- General guidelines for the design of layered composites have been adopted. For instance, not more than three plies of equal orientation are stacked together and the maximum angle change between between plies is 45°.
- For blade manufacturing reasons a sandwich construction with an easily compressible resin-rich core material was adopted.

In the structural design process of the composite propeller the connection between composite blades and NAB hub was found to be critical. To create enough space for an appropriate connection, the blade area adjacent to the hub was made significantly thicker than in the initial design. A detailed description of the developed connection is omitted in this work as it is irrelevant to the validation study. In general the connection is of a hybrid type, including an adhesive bonding and a mechanical connection. Both were designed to be able to separately sustain the full load. The strength of the designed blade-hub connection was confirmed by static and fatigue tests on specimens and on full-scale. The glass-epoxy blades have been designed for infinite fatigue life according to the guidelines as given in [11]. The ultimate strength of the blades have been assessed for the two critical loadcases of full speed ahead and full bollard pull astern. It has to be noted that the loads for the first loadcase have been obtained with the non-uniform flow BEM-FEM coupling as presented in the previous chapter. However, since the BEM PROCAL is not directly applicable to astern conditions the loads for the second loadcase have been computed with a vortex lattice method, excluding the hydro-elastic effects. From these analyses the full bollard pull astern condition turned out to be the most critical, which is not surprising given the high skew of the blades. Since this loadcase was analysed in a simplified way, the propeller was not designed for backward operation and therefore not for long-term use, but for the period of the full-scale trials only. However, from fatigue analyses and tests both the blade-hub connection and blade material itself seemed to have an infinite fatigue life.

The blades have been produced by a closed mould vacuum assisted resin transfer molding process with a post-cure. For blade manufacturing reasons it was decided to apply a sandwich construction in which a Polymat was used inside. The Polymat core has a variable thickness which is 37.5% of the local blade thickness. Advantages of using the Polymat core is that the mould can be more easily closed due to the compressibility of the core material. Secondly, it has good injection properties and therefore it facilitates the vacuum infusion process. The remaining 31.25% of the blade thickness on both blade sides have the same symmetric but unbalanced laminate. The typical stacking sequence of the uni-directional (UD) 0.5 mm thick glass-fibre plies, according to the ply angle definition as given in Figure 6.12 is, [20/20/-15/-60/-105/-60/-15/20/20]°, but can slightly vary due the local thickness. Essentially, this laminate has fibres in three major orientations: -15°, -60°, -105°. The 20° plies have been added to increase the shear–extension coupling. Since the laminate is symmetric the laminate itself has no bend-twist coupling. However, the shear-extension coupling on laminate level creates a bend-twist coupling on a global level in a sandwich structure were the skin laminates are mirror images around the neutral axis [12].

Where the local thickness requires more layers, first 20° plies have been added to increase the shear-extension coupling, then -15° plies and finally -60° plies have been added. Where the local thickness requires a thinner laminate, plies are dropped from inside.

MATERIAL PROPERTIES

The blades consist of the following materials. For the load carrying parts of the blade construction 0.5 mm thick, 600 g/m^2 E-glass UD plies have been used. A Polymat 140 g/m^2 core material with on each side a fiberglass chopped strand mat (CSM) of 1.5 mm thick has been used for the blade core. To protect the blade surfaces a 0.17 mm thick, 200 g/m^2 E-glass woven-rowing (WR) ply has been added at the outsides of the laminates. In order to improve the resin flow through the product during injection, between every three to five UD plies, a 0.5 mm thick, [0/90]° woven fabric injection weave (IW) has been added. The corresponding material properties are summarized in Table 6.3.

	E_{11} **[GPa]**	E_{22} **[GPa]**	ν_{12} [-]	G_{12} **[GPa]**	ρ **[kg/m^3]**
E-glass UD	34.6	5.00	0.30	3.1	1.8
E-glass WR	21.6	21.6	0.19	3.0	1.8
E-glass IW	10.1	10.1	0.23	2.5	1.4
Polymat	3.50	3.50	0.36	1.4	1.2
CSM	10.4	10.4	0.34	4.0	1.6

Table 6.3: The (in-plane) material properties of the composite propeller constituents.

6.3.4. FEM MODELLING OF THE FULL-SCALE PROPELLER

For FEM modelling and computations Marc/Mentat has been used. The FEM model of the full-scale propeller consists of one propeller blade without the hub part. The hub has not been modelled. The blade has been fully clamped at the blade-hub interface. The models were discretised by quadratic solid elements. A structured FEM mesh has been used with a 29×30×4 element distribution, meaning that 29, 30 and 4 elements are distributed in chord-wise, radial and through-thickness direction, respectively. The element dependent material orientation directions have been established with the approach as described in Chapter 2.

VERIFICATION

The FEM model of the full-scale propeller has been verified by comparing measured and computed natural frequencies and mode shapes for dry conditions only.The dry natural frequencies and mode shapes of the full-scale propeller have been measured during a roving hammer test. A grid on the surface of all the propeller blades was drawn, in each grid point the blades were hit with the hammer and the response was measured at the propeller tip with an accelerometer. Two of the pictures made during the tests are shown in Figure 6.13.

Figure 6.13: Images taken during the natural frequency measurements of the composite blades.

Table 6.4 presents the measured and computed dry natural frequencies for the first four modes. It can be concluded that the computed and measured dry natural frequencies are close together. Furthermore, the weights of the separate blades have been measured and checked with the amount of mass in the FEM calculation. The weight of the blades as measured and in the FEM calculation is approximately 4 kg. Hence, it can be concluded that the FEM model correctly represents the mass and stiffness distribution of the propeller blades.

	mode 1 [Hz]	**mode 2** [Hz]	**mode 3** [Hz]	**mode 4** [Hz]
Measured	119	188	339	430
Computed	114	186	316	435

Table 6.4: Measured and computed natural frequencies.

6.3.5. FULL-SCALE MEASUREMENTS

MEASUREMENT SET-UP

The development of the measurement set-up was a complex process due to the uniqueness of this measurement campaign. In cooperation with MARIN the measurements were conducted, were MARIN took the responsibility to develop the measurement set-up. In an early stage a feasibility study was conducted by them to investigate the possibilities for measuring the propeller deflections on full-scale where several options were studied. It was concluded that under water stereo-photography presented the largest chance of success for this specific case. This approach required several additional tests to assess the feasibility of this measurement technique at the preferred test location and time as the underwater visibility may vary during the year due to algae blooms. The result of the assessment was positive as the water visibility was found excellent. Due to the fast rotational speed of the propeller and the limited amount of natural light available under the ship hull, it was also concluded that a large amount of artificial light was necessary to avoid motion blur. Another challenge was to find the best position for the cameras. It was decided to position the cameras on the rudder, which resulted in an additional challenge for the routing of the cables due to rudder movements.

After performing the pre-study the measurement set-up was further detailed out including: the camera set-up, a custom made remote control of the optics and a custom made underwater strobe illumination system. Since no underwater cameras with the right specifications were available, two high quality machine vision cameras have been used, protected by underwater housings. The cameras were triggered through a hardware pulse synchronized with the propeller shaft. A support structure for the camera housings was developed, consisting of a base plat welded on the rudder and an L-bar mounted to the base plate (Figure 6.14). The L-bars have slot holes for adjustment of the camera views after assembly. The cameras were positioned for an optimal view at the propeller blade in the twelve o'clock position.

A custom made remote control of the optics was developed in order to optimise the lens focus and aperture from on-board. The hardware consisted of small electric engines mounted on 3D printed supports and a micro-controller installed inside the housings for the lens control. Both the hardware and the software were custom made for this project. This development allowed to use high quality wide angle lenses with very low distortion that were not available off the shelf with remote control of the optics.

For the underwater illumination as a first step, off the shelf underwater lights were assessed, but no items, able to provide sufficient light intensity while being reasonably compact, were found. The solution was found by developing small custom made subsea strobe lights triggered by a hardware pulse, synchronized with the propeller shaft and the cameras. Two sets of 4 lights were prepared and mounted respectively on the rudder and on the hull approximately 1 m to portside of the rudder stock (Figure 6.15).

Figure 6.14: Portside rudder with the cameras and the composite propeller with the speckle pattern.

Figure 6.15: Lights on the rudder and hull and routing of the cables.

THE MEASUREMENTS

The measurements were carried out October 31st and November 1st, 2017. The quality of the images that were taken exceeded expectations. An example of two stereo images taken with both cameras for the highest rotation rate is shown in Figure 6.16. During all tests, ship speed, distance and heading, and on both shafts the torque and rotation rate were measured. Tests were conducted at different propeller speeds, sailing on both propellers, but also only on the portside composite propeller. The reason was that for higher speeds a large amount of air bubbles obstructed the view, which was not the case when sailing on one propeller due to turning and drifting of the vessel. For each test a minimum number of 200 images were taken. Bad images due to air bubbles were discarded. From the 40-70 best images an average image was obtained with an image averaging technique. In this way the measurement precision error has been reduced and blade deformations due to transient behaviour were filtered out.

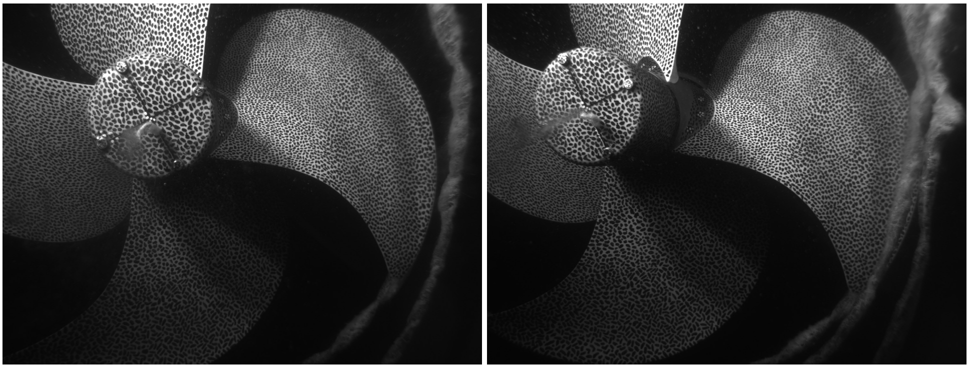

Figure 6.16: Stereo images for the maximum rotation rate (Photos: MARIN).

6.3.6. COMPARISON OF EXPERIMENTAL AND CALCULATION RESULTS

TEST CONDITIONS AND TORQUE RESULTS

Although the measurement data of the highest quality was collected when sailing only on the portside propeller, from a comparison of numerical and experimental results it turned out that the best resemblance between calculation and measurement results has been obtained for the conditions with both propellers in operation. This is not surprising, because due to drifting of the vessel the propeller inflow in the cases of sailing on one propeller will become significantly different from the RANS computed wakefield. Therefore, a fair comparison to the numerical results for these conditions would require a recalculation of the wakefield including the effect of the drift angle. This activity was not carried out as part of this research work. For that reason only results will be presented for the conditions with both propellers in operation. For these conditions measurements have been conducted for the ship speeds and rotation rates of Table 6.5. This table presents also the measured torque of the portside composite propeller and the torque computed for the composite propeller and for the assumed completely rigid starboard propeller. The results show that the flexible properties of the composite propeller reduces the torque by approximately 5%. The results also reveal that the measured torques are more than 15% higher than calculated. This is attributed to using the nominal wakefield for the calculations instead of the effective wakefields.

	Ship speed [kn]	**Rotation rate [rpm]**	**PS measured torque [kNm]**	**Calculated torque PS [kNm]**	**Calculated torque SB [kNm]**
Blade 7, low load, twelve o'clock	7.7	420	2.14	1.84	1.92
Blade 7, high load, twelve o'clock	9.0	473	2.72	2.26	2.38
Blade 8, low load twelve o'clock	7.7	411	2.06	1.73	1.81
Blade 8, high load twelve o'clock	8.7	466	2.61	2.23	2.34
Blade 7, low load, one o'clock	8.1	421	2.11	1.78	1.88
Blade 7, high load, one o'clock	8.8	468	2.74	2.21	2.34
Blade 7, low load, half past two	8.2	419	2.10	1.74	1.84
Blade 7, high load, half past two	8.8	471	2.65	2.25	2.38

Table 6.5: Test conditions, measured torque results portside (PS) composite propeller and calculated torque results for PS composite and starboard (SB) rigid propeller.

UNCERTAINTIES

For uniform flow experiments and calculations on model-scale, an uncertainty estimation has been presented in Chapter 3. From this study it was concluded that the discretisation errors in the BEM-FEM calculations can be assumed negligible compared to modelling uncertainties due to not exactly modelling the properties and conditions as appearing in the experiments. For these class of errors the two most important sources were using the design propeller geometry and the design elastic properties instead of the as-built geometry and actual elastic properties. It is assumed for this work that the error due to differences between design and actual geometry will be negligibly small, because of the improved procedure for the assembly of blades and hub. The results of the natural frequency tests indicate that the FEM model correctly represents the mass and stiffness distribution of the propeller blades, therefore as stiffness modelling error only ±5% has been assumed. The largest modelling error, which is not present in uniform flow experiments, is expected to be in the wakefield. First, the RANS computed nominal wakefield has been used for the calculations instead of the effective wakefield. Secondly, this wakefield has been computed for a ship speed of 10 kn and has been used for other conditions as well. Thirdly, as advance velocity the ship speed has been used, which would be true in laboratory conditions, however in full-scale measurements the advance velocity may be influenced by waves, current and drift angle. It has been considered outside the scope of this work to define how large the wakefield uncertainties are. However, given the differences between measured and computed torque as can be seen in Table 6.5, significant differences between the RANS computed nominal wakefield and actual propeller inflow can be expected. In order to correct for this, the whole pressure distributions calculated with the BEM have been amplified evenly with the ratio between the measured torque and the uncorrected calculated torque as given in Table 6.5 in order to have identical torque in measurements and calculations in the end. The remaining modelling uncertainty (including the ±5% stiffness uncertainty) has been assumed to be ±10% on bend and twist deformations.

For the DIC measurements an uncertainty of ±0.25 mm has been assumed. This value is based on the measurement noise as observed in the data and the consideration that the measured blade response adjacent to the hub should be zero, which is generally not the case. With the calculation rules for uncertainties the twist deformation uncertainty could be obtained from the displacement uncertainty.

COMPARISON OF MEASURED AND CALCULATED BLADE RESPONSE

Figure 6.17 shows the calculated and measured bend and twist deformations at the mid-chord points against the radial position, for the low and high load, for blade 7 and 8 in the twelve o'clock position. Results for both blades have been shown in the same figure in order to compare them. The graphs show that the responses of both blades are very similar. This was already expected from the results of the natural frequency tests. Since the results for blade 7 and 8 are similar, only results for blade 7 will be shown.

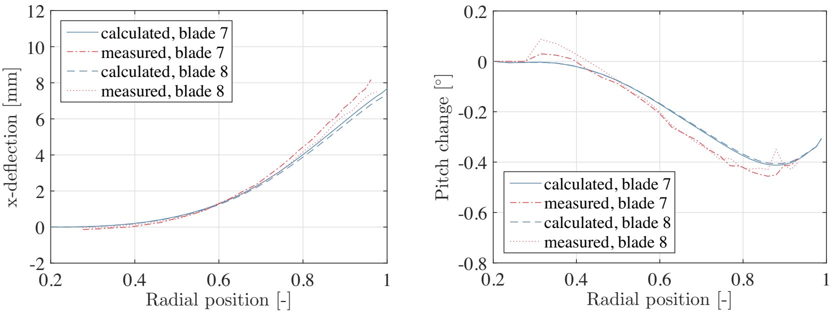

(a) Bend deformation, low load.

(b) Twist deformation, low load.

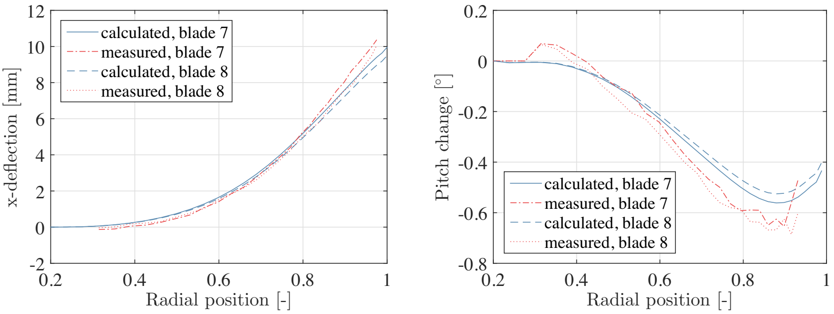

(c) Bend deformation, high load.

(d) Twist deformation, high load.

Figure 6.17: Calculated and measured bend (left) and twist (right) deformations of the mid-chord points against the radial position, for blade 7 and 8 in the twelve o'clock position.

Figures 6.18 to 6.20 show the uncertainty intervals for measured and calculated bend and twist deformations against the radial position, for the low and high load for blade 7 in the twelve o'clock, one o'clock and half past two position. The uncertainty intervals for the numerical results have been obtained from the BEM-FEM calculations with amplified pressures for torque identity and assuming ±10% uncertainty in the obtained bend and twist deformations. The uncertainty interval for the bend deformations is the ±0.25 mm bandwidth around the measured displacements. The uncertainty interval for the measured twist deformations has been computed with the calculation rules for uncertainties from the ±0.25 mm uncertainty in the displacements. Figures 6.18 to 6.20 show a very good resemblance between calculated and measured bend deformations. The BEM-FEM calculation slightly underestimates the bend deformation for the twelve o'clock and half past two position. The opposite is the case for the one o'clock position. A good resemblance between calculated and measured twist response has been obtained for the twelve o'clock position. For the two other blade positions the resemblance is less good, especially for the half past two position. Given its magnitude, the measurement of blade twist is strongly correlated with the measurement uncertainty. The measurement system was optimised for the twelve o'clock position, therefore the light conditions on the blade surface for the one o'clock and two o'clock positions are sub-optimal, especially in the tip area. This may explain why the twist comparison is shown less accurate in the high radii location for these cases. Furthermore, for the half past two position the larger deviation in measured and calculated twist response is also due to difficulties in applying the rigid body motion correction.

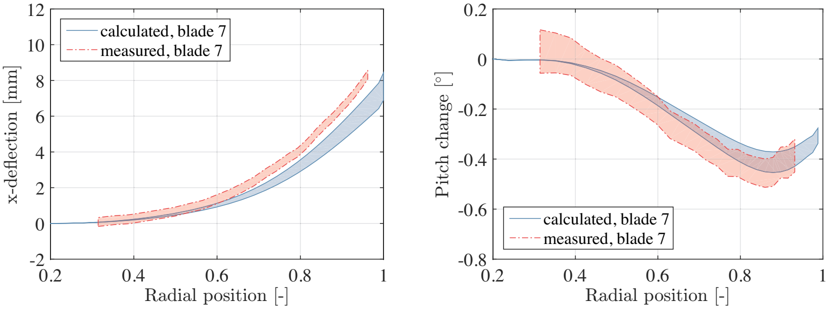

(a) Bend deformation, low load.

(b) Twist deformation, low load.

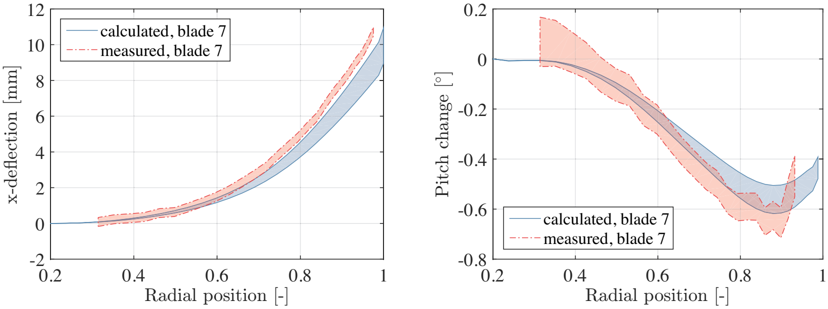

(c) Bend deformation, high load.

(d) Twist deformation, high load.

Figure 6.18: Calculated and measured bend (left) and twist (right) deformations of the mid-chord points against the radial position, for blade 7 in the twelve o'clock position.

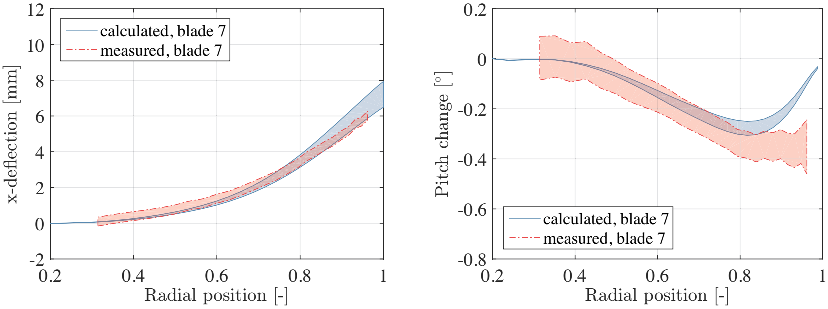

(a) Bend deformation, low load.

(b) Twist deformation, low load.

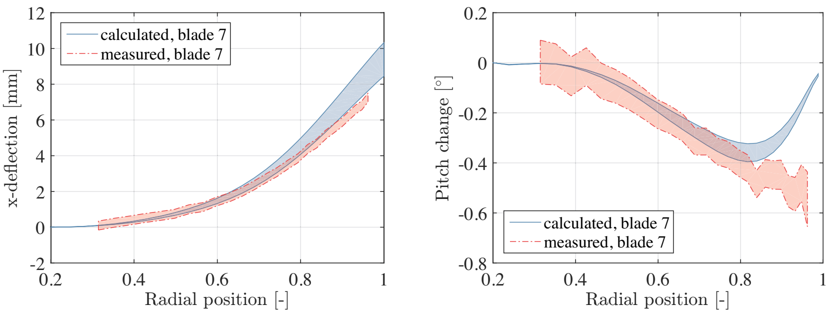

(c) Bend deformation, high load. (d) Twist deformation, high load.

Figure 6.19: Calculated and measured bend (left) and twist (right) deformations of the mid-chord points against the radial position, for blade 7 in the one o'clock position.

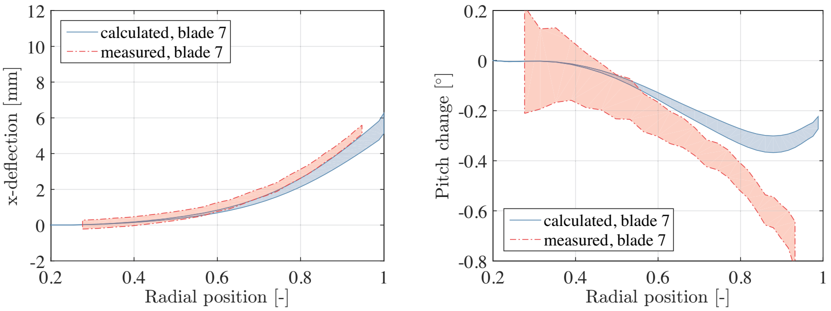

(a) Bend deformation, low load. (b) Twist deformation, low load.

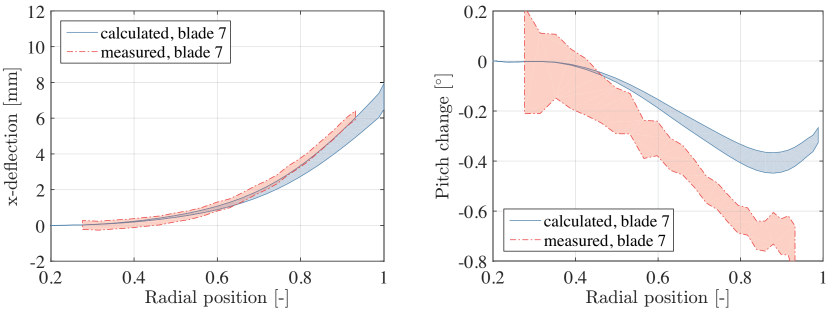

(c) Bend deformation, high load. (d) Twist deformation, high load.

Figure 6.20: Calculated and measured bend (left) and twist (right) deformations of the mid-chord points against the radial position, for blade 7 in the half past two position.

6.4. CONCLUSIONS

Validation studies on model- and full-scale have been presented for the BEM-FEM coupling for non-uniform flows. The model-scale measurements have been conducted in a cavitation tunnel experiment, in which the propeller blade deformations were measured for a full revolution with a stereo camera measurement set-up. The quality of the measurement data was low due to transient blade dynamics as a result of flow separation behind the body and the camera window, and due to unsteady cavitation. Therefore, only a comparison between measured and computed blade deflections have been made. The accuracy of the measured twist deformations was too low to be able to compare them with calculated twist deformations.

The measured and computed blade deflections show many differences. Qualitatively the calculated blade responses compare well with the measurement results, except for the highest radius. For the highest radius the difference between measured and computed deflections is similar to what has been found for uniform flow conditions in Chapter 3. There, those differences have been attributed to flow separation and viscous flows effects.

From the validation study on model-scale the following conclusions can be drawn. First, the study shows that it is possible to measure the unsteady blade deformations for a full revolution. Secondly, qualitatively the blade deflections are well predicted with the non-uniform flow BEM-FEM coupling. Thirdly, the results show that propeller-body interaction effects cannot be neglected. For the calculations the effective wakefields should be used which are case specific. This was not taken into account in this work and that explains partly the differences found between measurements and calculations. For future work it is recommended to perform the BEM-FEM coupling analysis with the correct effective wakefields. Furthermore, it is recommended to repeat the experiments with other propellers and for a non-separating flow.

From the validation study on full-scale the following conclusions can be drawn. The comparison between measured and computed natural frequencies confirms that the FEM modelling is fairly accurate. The measurement of the blade deflections were successfully carried out at full-scale with a stereo-camera system coupled with a DIC technique. The comparison between measured and calculated blade responses shows that the blade response is well predicted with the BEM-FEM coupling for non-uniform flows. The results show that the twist response is relatively small and the uncertainty in the twist response is relatively large. It remains a challenge to obtain accurately the twist response of flexible blades with a stereo camera measurement set-up in combination with a DIC technique, which is a point of attention for the future. Finally, it can be concluded

REFERENCES

[1] Y. Young, “Fluid–structure interaction analysis of flexible composite marine propellers,” *Journal of Fluids and Structures*, vol. 24, no. 6, pp. 799–818, 2008.

[2] B. Chen, S. Neely, T. Michael, S. Gowing, R. Szwerc, D. Buchler, and R. Schult, “Design fabrication and testing of pitch-adapting (flexible) composite propellers,” The SNAME Propeller/Shafting Symposium, Williamsburg, VA, USA, 2006.

[3] H. Lee, M. Song, J. Suh, and B. Chang, “Hydro-elastic analysis of marine propellers

based on a BEM-FEM coupled FSI algorithm," *International Journal of Naval Architecture and Ocean Engineering*, vol. 6, pp. 562–577, 2014.

[4] T. Taketani, K. Kimura, A. S., and K. Yamamoto, "Study on performance of a ship propeller using a composite material," Third International Symposium on Marine Propulsors, Launceston, Australia, 2013.

[5] P. Lv, S. Prothi, F. Mohd-Zawawi, E. Benard, J. Morlier, and J. Moschetta, "Study of a flexible blade for optimized proprotor," ERCOFTAC International Symposium, Mykonos, Greece, 2013.

[6] E. van den Bunt and W. Lafeber, "Optical measurement techniques in model testing," 2nd International conference on advanced model measurement technology for EU maritime industry, Newcastle upon Tyne, UK, 2011.

[7] L. Savio, "Measurements of the deflection of a flexible propeller blade by means of stereo imaging," (Austin, TX, USA), Fourth International Symposium on Marine Propulsors, 2015.

[8] D. Rijpkema, B. Starke, and J. Bosschers, "Numerical simulation of propeller-hull interaction and determination of the effective wake field using a hybrid RANS-BEM approach," Third International Symposium on Marine Propulsors, Launceston, Australia, 2013.

[9] M. Sutton, J. Orteu, and H. Schreier, *Image Correlation for Shape, Motion and Deformation Measurements: Basic Concepts,Theory and Applications.* Springer: New York, NY, USA, 1st ed., 2009.

[10] P. Maljaars, N. Grasso, M. Kaminski, and W. Lafeber, "Validation of a steady BEM-FEM coupled simulation with experiments on flexible small scale propellers," Fifth International Symposium on Marine Propulsors, Espoo, Finland, 2017.

[11] Germanischer Lloyd, *Guideline for the certification of Wind Turbines, Chapter 5.5*, 2010.

[12] W. de Goeij, M. van Tooren, and A. Beukers, "Implementation of bending-torsion coupling in the design of a wind-turbine rotor-blade," *Applied Energy*, vol. 63, no. 3, pp. 191–207, 199.

7

Chapter 7

Review

A partitioned fluid-structure interaction (FSI) coupling method for the hydro-elastic analyses of highly flexible (composite) marine propellers in open water and behind ship conditions has been presented in this work, including validation studies on small- and full-scale in uniform and non-uniform flows. The FSI method has been based on a boundary element method (BEM) and a finite element method (FEM) formulation for fluid and structure, respectively, but the present approach would be suitable for other (in-)viscous flow solvers as well. The scope of this work is limited to non-cavitating propellers, but, because of the full partitioning between the fluid and structural solver, the method can be easily extended to cavitating cases as well.

A separate chapter is dedicated to the FEM modelling of composite propellers. In that chapter the author proposes an easily implementable method for establishing the element dependent material orientations in the FEM models of composite propellers with solid elements. That approach has been used for all the FEM models of the composite propellers presented in this work. From static and natural frequency testing results it can be concluded that the different FEM models represent fairly well the actual structural response by modelling the material orientations in that way.

The hydro-elastic analysis of flexible propellers in uniform flows has been addressed in a separate chapter. In that chapter results of Reynolds-averaged Navier-Stokes (RANS) and RANS-FEM calculations are included together with experimental and BEM-FEM calculated results. Such a comparative study between a lower and a higher fidelity method for propeller hydro-elastic analyses was still lacking. From that work it can be concluded that a BEM-FEM coupling can be effectively used to predict the hydro-elastic response for conditions in which flow separation and viscous effects are not dominating. However, more research is recommended, for instance in the form of a similar comparison between viscous and in-viscous FSI methods for non-uniform flows. These studies are important to investigate the possibilities and limitations of the different methods.

As stated in the first chapter there seems no clear consensus on how to model the FSI of flexible propellers in behind ship conditions, given the assumptions as adopted in the different methods. The validity of these assumption stands or falls on the flexibility of the propeller and how unsteady the flow is. For both a dimensionless number has been defined in Chapter 4. Interesting to note is that both numbers are propeller scale invariant. A study in which different modelling choices have been evaluated has been performed in order to provide insights into the governing aspects in the BEM modelling of flexible propellers for behind ship conditions. It has been shown that, first of all, updating of the hydrodynamic influence coefficients during coupling iterations is of minor importance. Secondly, contributions due to fluid added mass and hydrodynamic damping forces can be included in the analyses by closed form expressions, since the structural response of flexible propellers is dominated by stiffness and therefore the consequences of modelling errors in the fluid added mass and hydrodynamic damping contributions are small. Both simplifications can reduce the CPU time of BEM-FEM coupled analyses significantly. However, this has not been shown in this work, because for a fair comparison of the different methods, additional effort is required to optimise the methods with respect to CPU time, which was considered out of the current scope. This would be interesting to conduct in future research. It is expected that such a study will show that a BEM-FEM coupling in which the two aforementioned simplifications have been adopted, will be well-suited to include in optimisation procedures.

In a separate chapter the BEM-FEM coupling procedure for in behind ship conditions has been treated. The method is basically a full partitioned approach in which coupling iterations between the fluid and structural solver are performed to accomplish the strong coupling between the fluid and structural sub-domain. For this, a new FSI approach for periodic problems has been developed, called the time periodic coupling approach in which coupling iterations are not performed per time step but on a periodic level. This was a necessary development since the BEM method is completely periodical in nature and therefore a time step coupling did not converge. Furthermore, it is also shown in Appendix A that a time periodic coupling can significantly speed-up the convergence to the steady-state FSI solution of periodic problems. Because it allows to solve the structural problem in the frequency domain, meaning that any transients, which slow down the convergence, are not computed. In the BEM-FEM coupling procedure as presented in Chapter 5 the structural sub-problem has been solved in the frequency domain, in modal space, which allows for a model reduction by involving only a limited number of mode shapes. The present FSI framework is not confined to this way of solving the structural equations. For instance, it would be also possible to include in the method a geometrically non-linear FEM calculation, because of the full separation of fluid and structural solver.

The last chapter is dedicated to the validation of the BEM-FEM coupling in non-uniforms flows on model and on full-scale. The model scale experiments have been conducted in a cavitation tunnel, in which the non-uniform wakefield has been obtained by placing a body in front of the propeller. For the first time, the displacement field of propeller blades has been measured for a full revolution. A comparison of these experimental results with the numerical results computed with the BEM-FEM coupling shows that the trend in measurement and calculation results is similar. Validation experiments have been conducted also on full-scale. With cameras mounted on the rudder the blade deformations of a purposely designed 1 m in diameter glass-fibre reinforced composite propeller have been measured. Again a comparison between experimental and numerical results has been made. The results show that the bending response of the blade is accurately predicted with the BEM-FEM coupling. For the twist deformations larger differences have been found, but these differences can be explained from experimental and modelling uncertainties. These uncertainties are relatively large due to the small twist angles.

RECOMMENDATIONS

The following recommendations for future work are proposed:

- Implement adaptations in the BEM method in order to be able to perform hydro-elastic analyses in cavitating conditions with the present BEM-FEM coupling. This is expected to be easily feasible, since this has been kept in mind in the development of the present method.

- Develop an FSI coupling for the hydro-elastic analysis of flexible propellers in astern conditions, since astern loading conditions might be critical in flexible propeller designs [1–3]. The BEM formulation applied in this work can not handle reverse conditions to date.

- Perform more comparative studies between BEM-FEM and RANS-FEM coupled methods in uniform, as well in non-uniform flows. Such studies would provide essential information on the capabilities and limitations of potential flow methods for flexible propeller analyses.

- Include the BEM-FEM coupling procedure in a multi-objective shape and structural optimisation procedure for the design of hydro-elastically tailored flexible propellers. Thus also the possible performance improvements of flexible propellers can be demonstrated by comparing optimised flexible propeller designs to optimal rigid propeller designs.

- Repeat the non-uniform flow BEM-FEM coupled analyses as presented in Chapter 6 with the correct effective wakefields. It is expected that this will result in an even better resemblance to the measurements.

- Execute more validation studies with a focus on accurately measuring the twist deformations. This remains a challenge, because the blade twist is generally small and, since the twist angles are not directly measured but derived from the measured blade displacements, the inaccuracy in the measured twist angles is relatively large.

REFERENCES

[1] P. Chang III, M. Elbert, Y. Young, Z. Liu, K. Mahesh, H. Jang, and M. Shearer, “Propeller forces and structural response due to crashback,” 27th Symposium on Naval Hydrodynamics, Seoul, Korea, 2008.

[2] Z. Liu and Y. Young, “Static divergence of self-twisting marine propellers,” *Journal of Fluids and Structures*, vol. 26, pp. 841–847, 2010.

[3] R. Miller, S. Kim, B. Rhee, and Y. YL., “Unsteady fluid-structure interaction response of a marine propeller in crashback,” 2012 Symposium on Naval Hydrodynamics, Gothenburg, Sweden, 2012.

A

Appendix A

A new approach for fluid-structure interaction analyses of periodic problems

A special type of fluid-structure interaction (FSI) problems are problems with periodic boundary conditions like in turbomachinery. The steady state FSI response of these problems is usually calculated with similar techniques as used for transient FSI analyses. This means that, when the fluid and structure problem are not simultaneously solved with a monolithic approach, the problem is partitioned into a fluid and structural part and that each time step coupling iterations are performed to account for strong interactions between the two sub-domains. This appendix shows that a time-partitioned FSI computation can be very inefficient to compute the steady state FSI response of periodic problems. A new approach is introduced in which coupling iterations are performed on periodic level instead of per time step. The convergence behaviour can be significantly improved by implementing existing partitioned solution methods as used for time step coupling (TSC) algorithms in the time periodic coupling (TPC) framework. The new algorithm has been evaluated by comparing the convergence behaviour to TSC algorithms. It is shown that the number of fluid structure evaluations can be considerably reduced when a TPC algorithm is applied instead of a TSC. One of the most appealing advantages of the TPC approach is that the structural problem can be solved in the frequency domain resulting in a very efficient algorithm for computing steady state FSI responses.

This appendix is based on the journal paper: P. Maljaars, M. Kaminski and J. den Besten, “A new approach for computing the steady state fluid-structure interaction response of periodic problems,” *Journal of Fluids and Structures*, vol. 84, pp. 140–152, 2018.

A.1. INTRODUCTION

Over the past decade many papers have been published on fluid-structure interaction (FSI) for different types of coupled problems. Examples of FSI problems studied in literature are for instance parachute dynamics [1, 2], flutter analysis of wings [3], airbag deployment [4], blood flow in arteries [1, 5] and hydro-elastic analysis of flexible propellers [6, 7].

Monolithic or partitioned approaches can be used to solve the coupled problems. In the monolithic approach the fluid and structure problem are simultaneously solved using a single code. In a partitioned approach the fluid and structure problem are solved in separate codes. In case of strong interaction between fluid and structure, a partitioned approach requires coupling iterations to converge to the monolithic solution, which can be computationally intensive. An important advantage of the partitioned approach is that existing codes can be used.

A straightforward partitioned solution method is the Gauss-Seidel method in which the fluid and structure problem are solved alternately and the last solution is taken as update. The convergence rate of the Gauss-Seidel method is inversely proportional with the ratio between fluid added mass and structural mass. Instability occurs when this ratio exceeds one [8]. It has been shown that the added mass of compressible flows is proportional to the time step, whereas the added mass of an incompressible flow is constant and time step size independent [8, 9] meaning that added mass instabilities in incompressible flows cannot be solved by reducing the time step size.

Several partitioned solution methods have been presented in literature for FSI problems with strong fluid added mass effects, like Aitken under-relaxation [10] and Quasi-Newton inverse least squares (QN-ILS) [11]. Where the first one belongs to the general class of stationary iterative methods and the latter one to the class of Krylov subspace methods. In combination with coupling iterations for each time step, these methods have been used in the past to converge to the solution of the fully coupled problem.

A special class of FSI problems involve periodic boundary conditions like in turbomachinery. A common approach is to solve these problems with similar approaches as used in non-periodic problems, which means with fully time step coupled (TSC) simulations [12]. An important drawback of this approach is that the transient FSI response is calculated as well and any transients in the solution procedure will adversely affect the convergence to the steady state solution.

The aim of this work is to introduce a new approach, called the time periodic coupling (TPC) to get rid of the transient response in order to compute more efficiently the steady state response of periodic FSI problems with strong fluid added mass effects. The conceptual idea of a time periodic FSI coupling approach comes from [13] but has been applied only to a weakly coupled problem so far. The scope of this work is to introduce a TPC approach for strongly coupled FSI problems and to demonstrate the efficiency improvement for some fundamental FSI problems. It will be shown that convergence problems, as appearing in TSC schemes due to strong fluid added mass effects, arise in the TPC as well. In order to stabilize a TPC scheme two partitioned solution methods used in TSC schemes, are applied in the TPC framework. This work is limited to the implementation of the Aitken under-relaxation and the QN-ILS method. The first one because it shows that a TPC approach not automatically performs better than a TSC. The later one because the QN-ILS method is the state of art in advanced under-relaxation methods in FSI calculations [14] and it shows that a TPC in combination with QN-ILS can outperform a TSC. Furthermore, with these two methods both the general class of stationary iterative methods and Krylov subspace methods have been represented. Demonstrating the performance of the TPC approach for other partitioned solution methods, which may belong to the aforementioned general classes, was considered out of the scope of this work.

The contents of this appendix are organized as follows: Section A.2 provides background information about partitioned FSI, Aitken under-relaxation and the QN-ILS method. Section A.2 also presents the concept of the TPC approach. Section A.3 introduces some fundamental FSI problems, which have been analysed in this appendix. Section A.4 compares TSC and TPC solutions for the problems presented in Section A.3. It is shown that both approaches converge to the exact solutions. Furthermore, the TSC and TPC algorithms have been evaluated by investigating the convergence behaviour for different settings. Section A.5 contains the conclusions.

A.2. PARTITIONED SOLUTION METHODS

In this section the time periodic FSI coupling approach is introduced in combination with two methods to keep the coupling iterations stable. First of all, the Aitken under-relaxation which belongs to the general class of stationary iterative methods. Secondly, the QN-ILS method which belongs to the general class of Krylov subspace methods.

A.2.1. FLUID-STRUCTURE INTERACTION

With $\mathscr{F}$ and $\mathscr{S}$ the fluid and structure operators, a partitioned fluid-structure interaction problem can be written as,

$$\begin{aligned} \mathbf{y} &= \mathscr{F}(\mathbf{x}) \\ \mathbf{x} &= \mathscr{S}\left(\mathbf{y}\right) \end{aligned} \tag{A.1}$$

where $\mathbf{x}$ is the structural response of the fluid-structure interface, $\mathbf{y}$ the fluid loading on the interface. The coupled problem can be formulated as solving for $\mathbf{x}$ or $\mathbf{y}$ by satisfying,

$$\mathscr{R}_{\mathbf{x}}(\mathbf{x}) = \mathscr{S} \circ \mathscr{F}(\mathbf{x}) - \mathbf{x} = \mathbf{0} \tag{A.2}$$

$$\mathscr{R}_{\mathbf{y}}\left(\mathbf{y}\right) = \mathscr{F} \circ \mathscr{S}(\mathbf{y}) - \mathbf{y} = \mathbf{0} \tag{A.3}$$

where $\mathscr{R}_{\mathbf{x}}$ and $\mathscr{R}_{\mathbf{y}}$ are the interface residual functions for structural response and fluid loading respectively. It is more convenient to solve for $\mathscr{R}_{\mathbf{y}}$ as will be explained in Section A.2.5. When the Jacobian $\frac{\partial \mathscr{R}}{\partial \mathbf{y}}$ is known, Newton's method can be applied to find the roots of Eq. A.3,

$$\mathbf{y}^{k+1} = \mathbf{y}^{k} - \left(\frac{\partial \mathscr{R}}{\partial \mathbf{y}}\right)^{-1} \mathbf{r}_{y}^{k} \tag{A.4}$$

where k denotes the coupling iteration number and the residual, $\mathbf{r}_{y}^{k}$, is defined as,

$$\mathbf{r}_{\mathbf{y}}^{k} = \mathscr{R}_{\mathbf{y}}\left(\mathbf{y}^{k}\right) \tag{A.5}$$

A.2.2. COUPLING STRATEGIES FOR PARTITIONED FSI PROBLEMS

In case of a black-box coupling the inverse Jacobian is usually not known and time consuming to calculate. Therefore, quasi-Newton methods with approximations of the inverse Jacobian can be employed. In case the non-linearities are relatively small a straightforward approximation of the inverse Jacobian is $-\mathbf{I}$. This approximation is basically a block Gauss-Seidel method in which the fluid and structure subsystem are solved separately and iterations are performed to converge to the fully coupled solution. For FSI problems with strong added mass effects this approach will not converge, (see for instance [15, 16]) and other quasi-Newton methods have to be applied.

A.2.3. AITKEN UNDER-RELAXATION

A method to stabilize coupling iterations is to apply under-relaxation. The inverse Jacobian is approximated as $-\sigma\mathbf{I}$, with σ the relaxation factor in interval $(0,1]$. An optimal relaxation factor has to be found to avoid divergence on the one hand and long computational times on the other hand.

With adaptive Aitken a variable under-relaxation factor σ is computed, which reduces the number of coupling iterations compared to a fixed under-relaxation factor [10]. Two pairs of computed and predicted interface forces ($\mathbf{y}^{k-1}$,$\tilde{\mathbf{y}}^{k-1}$) and ($\mathbf{y}^{k}$,$\tilde{\mathbf{y}}^{k}$) are required to estimate the best prediction of the interface forces for the next coupling iteration ($\tilde{\mathbf{y}}^{k+1}$) based on the secant method. The first step of the secant method reads,

$$\tilde{\mathbf{y}}^{k+1} = \tilde{\mathbf{y}}^{k} + \sigma^{k}\left(\mathbf{y}^{k} - \tilde{\mathbf{y}}^{k}\right) \tag{A.6}$$

where for vector cases the following expression for σ^k has been proposed [10],

$$\sigma^{k} = -\sigma^{k-1}\frac{\mathbf{r}_{\mathbf{y}}^{k-1}\cdot\left(\mathbf{r}_{\mathbf{y}}^{k} - \mathbf{r}_{\mathbf{y}}^{k-1}\right)}{\left\|\mathbf{r}_{\mathbf{y}}^{k} - \mathbf{r}_{\mathbf{y}}^{k-1}\right\|^{2}} \tag{A.7}$$

Hence, with Aitken under-relaxation the relaxation parameter is adjusted based on the inner product of the residuals to control the convergence of the coupling iterations. It has been shown that the convergence behaviour of Aitken's method deteriorates as the fluid-structure mass ratio increases [8] and, therefore, more coupling iterations are required. To reduce the number of coupling iterations more efficient coupling strategies have been developed, like the QN-ILS approach described hereafter.

A.2.4. QUASI-NEWTON INVERSE LEAST SQUARES

With the QN-ILS method [11] an improved approximation of the inverse Jacobian is obtained. In the QN-ILS method the inverse Jacobian is not explicitly determined but implicitly included in the new update of the interface forces $\tilde{\mathbf{y}}^{k+1}$. The QN-ILS method is like Aitken under-relaxation based on known input-output pairs of Eq. A.3, but in the QN-ILS method results of all previous iterates are used. The best candidate for $\tilde{\mathbf{y}}^{k+1}$ is a vector of forces which will minimize $\mathbf{r}_{\mathbf{y}}^{k+1}$. By following [17] an approximation of the new residual vector $\mathscr{R}_{\mathbf{y}}\left(\mathbf{y}^{k+1}\right)$ is written as a linear combination of previous residual vectors,

$$\mathscr{R}_{\mathbf{y}}\left(\mathbf{y}^{k+1}\right) \approx \mathbf{r}_{\mathbf{y}}^{k} + \sum_{i=0}^{k-1}\alpha_{i}^{k}\left(\mathbf{r}_{\mathbf{y}}^{i} - \mathbf{r}_{\mathbf{y}}^{k}\right) \tag{A.8}$$

The coefficients α_i^k are found from a least squares minimization of the approximated residual $\mathscr{R}_{\mathbf{y}}\left(\mathbf{y}^{k+1}\right)$,

$$\boldsymbol{\alpha}^k = \arg \min_{\boldsymbol{\alpha}^k \in \mathbb{R}} ||\mathbf{r}_{\mathbf{y}}^k + \sum_{i=0}^{k-1} \alpha_i^k \left(\mathbf{r}_{\mathbf{y}}^i - \mathbf{r}_{\mathbf{y}}^k\right)|| \tag{A.9}$$

By assuming a linear relation between $\mathbf{r}_{\mathbf{y}}$ and $\mathbf{y}$, the best approximation for $\widetilde{\mathbf{y}}^{k+1}$ is the linear combination of the previous iterates of $\mathbf{y}$,

$$\widetilde{\mathbf{y}}^{k+1} = \mathbf{y}^k + \sum_{i=0}^{k-1} \alpha_i^k \left(\mathbf{y}^i - \mathbf{y}^k\right) \tag{A.10}$$

Eq. A.10 shows that the approximate inverse Jacobian is implicitly included in the expression $\sum_{i=0}^{k-1} \alpha_i^k \left(\mathbf{y}^i - \mathbf{y}^k\right)$. Any linear combination of changes in fluid forces that are obtained from previous iterates are coupled implicitly. The coupling is explicit for the changes in fluid forces that cannot be written as a linear combination of previous iterates. Since the most unstable variations will directly appear in the solution process, they will be included in the approximation of the inverse Jacobian and, therefore, implicitly coupled immediately after performing QN-ILS coupling iterations [18].

A.2.5. TIME STEP COUPLING AND TIME PERIODIC COUPLING

For calculating the steady state response of FSI problems with periodic boundary conditions TSCs are frequently applied. A typical algorithm is shown as Algorithm 1. A certain number of FSI cycles, n_{FSI}, have to be performed until the steady state solution is obtained. To initialize the FSI computation first $\widetilde{\mathbf{y}}_{1..N}^{k=1}$ have to be defined, where N is number of time steps in one period and the superscript 1 refers to the coupling iteration number. This is accomplished by first computing $\mathbf{y}_{1..N}$ from a calculation in which no fluid-structure coupling is involved. Then, $\mathbf{y}_{1..N}$ is taken as the best candidate for $\widetilde{\mathbf{y}}_{1..N}^{k=1}$. Each time step, k coupling iterations are applied until $\|\mathbf{r}\|$ is smaller than a specified tolerance ϵ. The best candidate $\widetilde{\mathbf{y}}_n^{k+1}$ for the next coupling iteration is, for instance, calculated with Aitken under-relaxation or the QN-ILS method. Algorithms for these two methods can be found in [14].

In the TPC algorithm the periodicity in the problem has been utilized to avoid coupling iterations on time step level. An algorithm for a TPC is presented as Algorithm 2. A certain number of FSI cycles have to be performed until the FSI problem is converged. The number of FSI cycles coincides with the number of coupling iterations k. In line 13 of Algorithm 2 the best candidates $\widetilde{\mathbf{y}}_{1..N}^{k+1}$ for the interface forces at all time steps for the next FSI cycle are calculated, for instance with Aitken under-relaxation or the QN-ILS method.

The TPC algorithm shows that the structural and fluid sub-problem comprises the steady state solutions for both sub-problems. For a fast convergence we propose to solve fluid and structural problem, if possible, in the frequency domain. Thus, the steady state solutions for the two sub-problems are immediately obtained and any transients in the solutions, which will slow down the convergence to the steady-state FSI solution, are not computed.

Note, that the algorithms might also start with the fluid evaluations in line 9 and line 8 of Algorithm 1 and 2, respectively. Then, line 11 of Algorithm 1 and line 13 of Algorithm 2 will change in calculating the best candidate for the structural displacements. However, also the structural velocity and acceleration are coupled to the fluid and, therefore, $\dot{\mathbf{x}}^{k+1}$ and $\ddot{\mathbf{x}}^{k+1}$ have to be approximated as well. That would require an additional calculation step, therefore, Algorithms 1 and 2 have been followed for the computations in this work.

Algorithm 1 Algorithm for a time step coupling

```
$n_{FSI} = 0$
Define $\tilde{\mathbf{y}}_{1..N}^{k=1}$
while FSI problem not converged do
    $n_{FSI} = n_{FSI} + 1$
    for $n = 1 : N$ do                          ▷ With $N$ the number of time steps in a period
        $k = 0$
        while $\left\| \mathbf{r}_n^{k-1} \right\| > \epsilon$ do
            $k = k + 1$
            $\mathbf{y}_n^k = \mathscr{F} \circ \mathscr{S} \left( \tilde{\mathbf{y}}_n^k \right)$
            $\mathbf{r}_n^k = \mathbf{y}_n^k - \tilde{\mathbf{y}}_n^k$
            Calculate $\tilde{\mathbf{y}}_n^{k+1}$
        end while
    end for
end while
```

Algorithm 2 Algorithm for a time periodic coupling

```
$n_{FSI} = 0$ $n_s = 0$ $n_f = 0$
$k = 0$
Define $\tilde{\mathbf{y}}_{1..N}^{k=1}$
while FSI problem not converged do
    $n_{FSI} = n_{FSI} + 1$
    $k = n_{FSI}$
    for $n = 1 : N$ do                          ▷ Calculate steady state solution for $\mathbf{x}_{1..N}^k$
        $\mathbf{x}_n^k = \mathscr{S} \left( \tilde{\mathbf{y}}_n^k \right)$
    end for
    for $n = 1 : N$ do                          ▷ Calculate steady state solution for $\mathbf{y}_{1..N}^k$
        $\mathbf{y}_n^k = \mathscr{F} \left( \mathbf{x}_n^k \right)$
    end for
    Calculate $\tilde{\mathbf{y}}_{1..N}^{k+1}$
end while
```

A.3. PROBLEM DESCRIPTION

This section will describe the problems which will be solved. First a two-degree of freedom (2-DoF) model for pitching and plunging motions of a prismatic wing in a fluid will be presented. The FSI response of this problem will be solved with a TSC and TPC approach in which a black-box fluid solver is used. Then, a one-degree of freedom (1-DoF) model for the same wing but for pitching motions only will be presented. This model has been used in another study for comparison of fluid-structure interaction algorithms [19] and will be used in this work to verify the TSC and TPC approach. Finally, this section will present a 1-DoF model, again for the same wing but for plunging motions only. This model will be used for a comparative study between the TSC and TPC approach. The problem involves strong fluid-added mass effects which are known to introduce numerical difficulties, making it a useful problem for demonstrating the benefits of the TPC approach.

A.3.1. 2-DOF MODEL FOR PITCHING AND PLUNGING WING MOTIONS

The problem of interest is the motion of a prismatic wing with a span, s, of 20 m, chord, c, of 1 m and a NACA 0009 cross section profile in an incompressible flow at zero angle of attack and an incoming flow velocity, v_x, of 3 m/s (Figure A.1). The wing is connected with springs to a structure and can rotate around the mid-chord point and move in vertical direction. The wing is subjected to an external harmonic force and moment,

$$\mathbf{f}_0 = \begin{Bmatrix} f_z \\ m_\theta \end{Bmatrix} = \begin{Bmatrix} F_z \\ M_\theta \end{Bmatrix} cos(\omega t) \tag{A.11}$$

where F_z and M_0 are the force and moment amplitudes, 400,000 N and 10,000 Nm, respectively. ω is the radial frequency in rad/s and unless specified otherwise the excitation frequency is 4π rad/s. Due to the external loads the wing oscillates in pitching and plunging motion. The equation of motion with respect to the centre of motion (COM) for this problem reads,

$$\mathbf{M}\ddot{\mathbf{u}} + \mathbf{C}\dot{\mathbf{u}} + \mathbf{K}\mathbf{u} = \mathbf{f}_0 + \mathbf{f}_h(\mathbf{u}, \dot{\mathbf{u}}, \ddot{\mathbf{u}}) \tag{A.12}$$

where the vector $\mathbf{u}$ contains the vertical displacement, z, and rotation of the wing, θ, $\mathbf{f}_h$ is the vector with hydrodynamic loads due to the wing structural response. $\mathbf{M}$, $\mathbf{K}$ and $\mathbf{C}$ denote the mass, stiffness and damping matrices. The mass of the wing is 1,000 kg, the rotational inertia is 100 kg·m^2. The centre of gravity (COG) is 0.05 m in front of the COM. Hence, the mass matrix is given by,

$$\mathbf{M} = \begin{bmatrix} 1,000 & 50 \\ 50 & 100 \end{bmatrix} \tag{A.13}$$

The extensional spring stiffness is 7,500,000 N/m and the stiffness of the torsional spring is 375,000 Nm/rad. Hence, the stiffness matrix is given by,

$$\mathbf{K} = \begin{bmatrix} 7,500,000 & 0 \\ 0 & 375,000 \end{bmatrix} \tag{A.14}$$

Unless specified otherwise, 5% critical damping, ζ, of the individual springs has been used as default for the damping terms in the structural damping matrix. The reason for this high value will be explained in Section A.4.2. Hence, the damping matrix is given by,

$$\mathbf{C} = \begin{bmatrix} 8,660 & 0 \\ 0 & 612 \end{bmatrix} \tag{A.15}$$

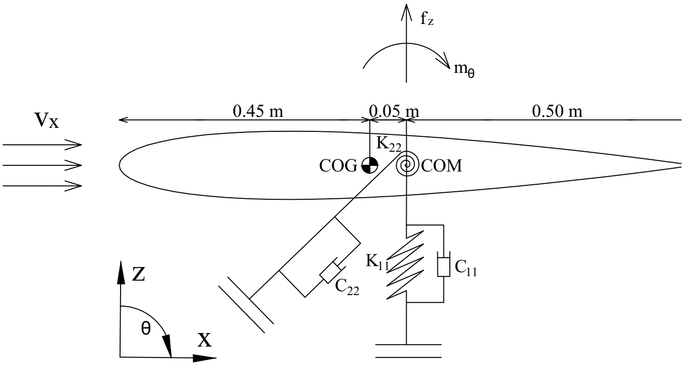

Figure A.1: A two-degree of freedom model for the pitching and plunging motions of a prismatic wing.

A.3.2. 1-DOF MODEL FOR PITCHING WING MOTIONS

To verify the correctness of the TSC and TPC partitioned approaches, calculations have been performed for the specific case of pitching motions only. For that case the 2-DoF model reduces to,

$$M_{22}\ddot{\theta} + C_{22}\dot{\theta} + K_{22}\theta = m_0 - m_h(\theta,\dot{\theta},\ddot{\theta}) \tag{A.16}$$

with θ the pitch angle. For this typical problem approximation formulas for m_h, subdivided in fluid added mass, fluid damping and fluid stiffness loads, have been approximated based on incompressible viscous Reynolds-averaged Navier-Stokes (RANS) computations [20]. The approximation formulas for fluid added mass, m_f, fluid damping, c_f and fluid stiffness, k_f read,

$$\begin{aligned}
m_h &= -m_f\ddot{\theta} - c_f\dot{\theta} - k_f\theta \\
m_f &= \frac{\pi}{128}\rho c^4 s \\
c_f &= \begin{cases} 0.105k^{-0.4}\rho v_x c^3 s & \text{for k≤4,} \\ 0.010k^{0.6}\rho v_x c^3 s & \text{for k≥12,} \end{cases} \\
k_f &= \begin{cases} (0.090k - 0.80)\,\rho v_x^2 c^2 s & \text{for k≤4,} \\ (0.065k - 0.90)\,\rho v_x^2 c^2 s & \text{for k≥12,} \end{cases}
\end{aligned} \tag{A.17}$$

where k is the reduced frequency that describes the unsteadiness of the flow,

$$k = \frac{\omega c}{2v_x} \tag{A.18}$$

With these approximations the equation for the pitching motion is,

$$M_{22}\ddot{\theta} + C_{22}\dot{\theta} + K_{22}\theta = m_0 - m_f\ddot{\theta} - c_f\dot{\theta} - k_f\theta \tag{A.19}$$

A.3.3. 1-DOF MODEL FOR PLUNGING WING MOTIONS

A comparison of the TSC and TPC approach have been performed for the specific case of plunging motions only. In that case the 2-DoF model reduces to,

$$M_{11}\ddot{z} + C_{11}\dot{z} + K_{11}z = f_z - f_h(\dot{z}, \ddot{z}) \tag{A.20}$$

with z the vertical plunge displacement and f_h the hydrodynamic loads due to the vertical plunge motion only. For high reduced frequencies the fluid forces due to the plunging of the wing are dominated by the non-circulatory lift [21, 22]. The non-circulatory lift part can be expressed as a fluid-added mass, m_a, times the acceleration [21, 22], meaning Eq. A.20 can be converted into,

$$M_{11}\ddot{z} + C_{11}\dot{z} + K_{11}z = f_z - m_a\ddot{z} \tag{A.21}$$

In general Eq. A.21 can be written as,

$$(M_{11} + \lambda m_a)\,\ddot{z} + C_{11}\dot{z} + K_{11}z = f_z + (\lambda - 1)\,m_a\ddot{z} \tag{A.22}$$

where λ is called the fluid added mass fraction which controls the amount of fluid added mass in left- and right-hand-side of the equation. For λ a value from the interval $[0,1]$ has to be taken, where for $\lambda = 0$ the problem is fully partitioned and for $\lambda = 1$ the monolithic solution is obtained.

The added mass of the wing has been calculated with the method described in [7, 21] and is approximately 16,000 kg. The advantage of this 1-DoF problem is that the exact Jacobian of the residual function is irrespective of the excitation frequency and can be easily derived. The Jacobian of the residual function is the derivative of the residual function $\mathscr{R}_y$ with respect to the fluid loads on the interface, for the 1-DoF case denoted by y. For the plunging problem for any time step n, Eq. A.3 can be written as,

$$\mathscr{R}_{y_n} = f_{z_n} - m_a\ddot{z}_n - y_n \tag{A.23}$$

A direct relation between $\ddot{z}_n$ and y_n exists and follows from the time integration scheme. In the TSC coupling the average constant acceleration Newmark scheme has been used. This scheme is unconditionally stable without numerical damping. This yields the following relation between $\ddot{z}_n$ and y_n,

$$\ddot{z}_n = S^{-1}\left(y_n - C_{11}\dot{z}_n^* - K_{11}z_n^*\right) \tag{A.24}$$

where $\dot{z}_n^*$ and z_n^* are the velocity and displacement estimates at time step n, respectively. S denotes the Newmark time stepping matrix, which for the 1-DoF problem is equal to,

$$S = M_{11} + \gamma\Delta t C_{11} + \beta\Delta t^2 K_{11} \tag{A.25}$$

with $\gamma = 1/2$ and $\beta = 1/4$ for the Newmark average constant acceleration scheme. Then, the derivative of the residual function to y_n is equal to,

$$\frac{\partial\mathscr{R}_{y_n}}{\partial y_n} = -\left(\frac{m_a}{S} + 1\right) \tag{A.26}$$

A.4. FLUID-STRUCTURE INTERACTION ANALYSES

This section will present the results of the FSI calculations. The different analyses have been structured as follows: first of all, results obtained with the TSC and TPC approach for the 1-DoF pitching problem will be shown together with the analytical solutions in order to verify the correctness of the coupling approaches. Secondly, a comparison of the convergence behaviour of the TSC and TPC approach will be presented from the results obtained for the 1-DoF plunging problem. This section concludes with a TSC and TPC calculation of the 2-DoF problem in order to show the efficiency improvement of the new approach for the more common case that fluid forces are computed with a black-box fluid solver.

A.4.1. VERIFICATION OF TSC AND TPC APPROACH FOR 1-DOF PITCHING PROBLEM

In order to verify the TSC and TPC approach, partitioned solutions for the 1-DoF pitching problem have been compared to the exact monolithic solutions. The monolithic solutions are obtained by moving the fluid forces from the right-hand-side of Eq. A.19 to left-hand-side and then the exact solution for θ can be computed. The partitioned solutions are obtained by keeping the fluid forces in the right-hand-side as unknowns and iterations are required to converge to the monolithic solution. Fig. A.2 shows the exact solution, the TSC solution and the TPC solution for the oscillation frequencies $\{4\pi, 7\pi, 10\pi\}$ rad/s, i.e. stiffness, damping and mass dominated response regimes. For all cases the TSC and TPC procedure converge to the exact solution. The figures also show the number of FSI cycles, n_{FSI}, required for convergence. For convergence the criterion that the root mean square of the relative difference in fluid forces between subsequent FSI cycles should be smaller than 0.1% has been used. The results show that for all the cases the number of FSI cycles is significantly smaller when the TPC has been used. In the next subsection the benefits of the TPC coupling will be further explored for the 1-DoF plunging problem.

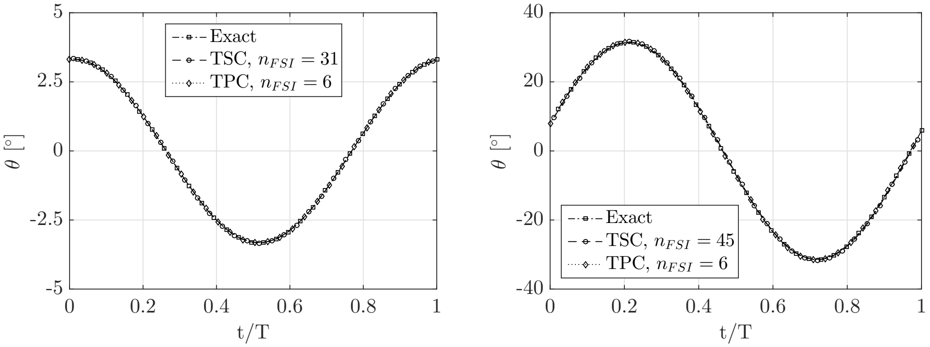

(a) $\omega = 4\pi$

(b) $\omega = 7\pi$

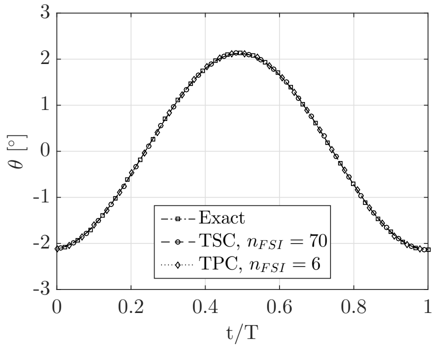

(c) $\omega = 10\pi$

Figure A.2: Exact, TSC and TPC solution for θ as a function of the normalized time, t/T, $T = 2\pi/\omega$, for the 1-DoF pitching problem.

A.4.2. COMPARISON OF TSC AND TPC APPROACH FOR THE 1-DOF PLUNGING PROBLEM

The benefits of the TPC coupling are demonstrated using the 1-DoF plunging problem by comparing the performance of the TSC and TPC algorithms for different settings and using Aitken or the QN-ILS method for the approximation of the best candidate for the fluid interface forces. All the TSC calculations for the 1-DoF plunging problem are performed using the exact Jacobian as derived in Section A.3.3. Therefore, the results obtained with the TPC algorithm are always compared to the most efficient TSC algorithm, since for a TSC framework the fastest convergence of the FSI problem is obtained with the exact inverse Jacobian.

TIME STEP AND AITKEN TIME PERIODIC SOLUTION FOR DIFFERENT FLUID ADDED MASS FRACTIONS

The convergence of the TSC algorithm with the exact (inverse) Jacobian of the residual function and the TPC algorithm with Aitken under-relaxation will be compared for the 1-DoF plunging problem for different fluid added mass fractions. Both algorithms have to run through a number of FSI cycles until a steady state FSI response is obtained. After each FSI cycle the error, ψ, is calculated from,

$$\psi_n = \frac{y_n^k - \tilde{y}_n^k}{y_n^k} \qquad n = 1 \dots N \tag{A.27}$$

$$\psi = rms \begin{Bmatrix} \psi_1 \\ \vdots \\ \psi_N \end{Bmatrix}$$

The error as a function of the number of FSI cycles is depicted in Figure A.3 for various values of λ. For $\lambda = 1$ a monolithic problem is solved and both algorithms are directly converged, since in that case y includes only the non-oscillating wing forces, f_z. For smaller fluid added mass fractions the TSC requires only two coupling iterations per time step; after the first sub-iteration only one corrector step is needed since the exact (inverse) Jacobian of the residual function is known and the residual function, $\mathscr{R}_y$, is linear in the accelerations. Hence, the number of structure and fluid evaluations is $2n_{FSI}N$ in case of the TSC, while this is $n_{FSI}N$ for the TPC. The factor 2 comes from the number of coupling iterations for each time step, which is the minimum number of coupling iterations for the TSC approach.

The results show that the convergence of the TSC is hardly influenced by the fluid added mass fraction. The opposite is the case for the Aitken TPC. When λ becomes too small, the Aitken TPC does not converge. While depending on λ a faster convergence could be obtained with the TPC compared to the TSC.

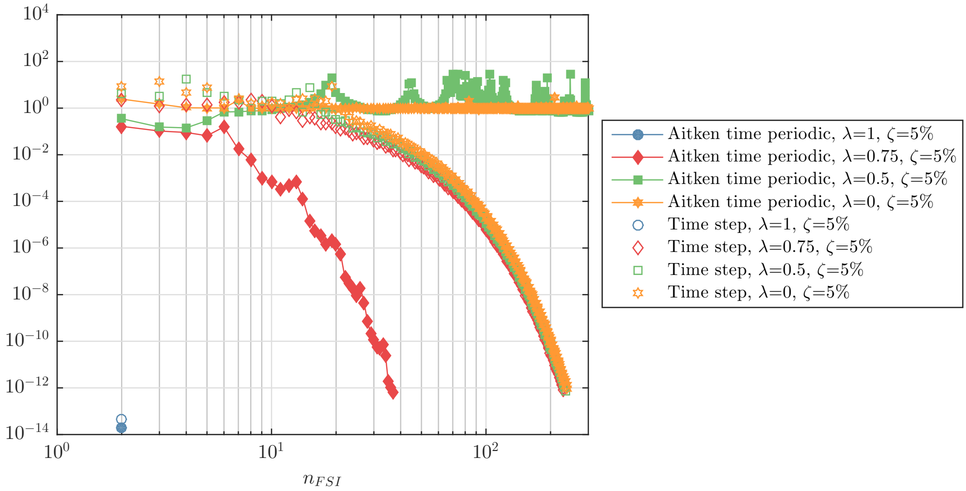

Figure A.3: Convergence behaviour of the time step and Aitken time periodic coupling for the 1-DoF plunging problem for different fluid added mass fractions.

TIME STEP AND QN-ILS TIME PERIODIC SOLUTION FOR DIFFERENT FLUID ADDED MASS FRACTIONS

For the TPC a faster convergence rate can be obtained when a better approximation of the inverse Jacobian of the residual function is included. For that reason the QN-ILS approach has been implemented in the TPC. Results obtained with the TSC and QN-ILS TPC for the 1-DoF plunging problem for different fluid added mass fractions are depicted in Figure A.4. This figure shows that the QN-ILS TPC, in contrast to the Aitken TPC, converges for any λ. For subsequent coupling iterations instabilities in the solution process are included in the approximation of the inverse Jacobian of the residual function and, therefore, implicitly coupled directly after performing QN-ILS coupling iterations [18], keeping the solution process stable even for strong instabilities due to fluid added mass effects. Furthermore, it can be concluded that the number of FSI cycles needed for convergence is smaller for the QN-ILS TPC than for the TSC for any λ. The results also show that the convergence behaviour is more or less independent of λ for the TSC. This is the case for the TPC as well, up to $\psi = 10^{-6}$. For a further convergence the calculation with $\lambda = 0$ requires more FSI cycles. In summary, it can be concluded that the QN-ILS approach stabilizes the solution process of the TPC even for strong fluid added mass effects and fewer FSI cycles are required for convergence than with a TSC algorithm.

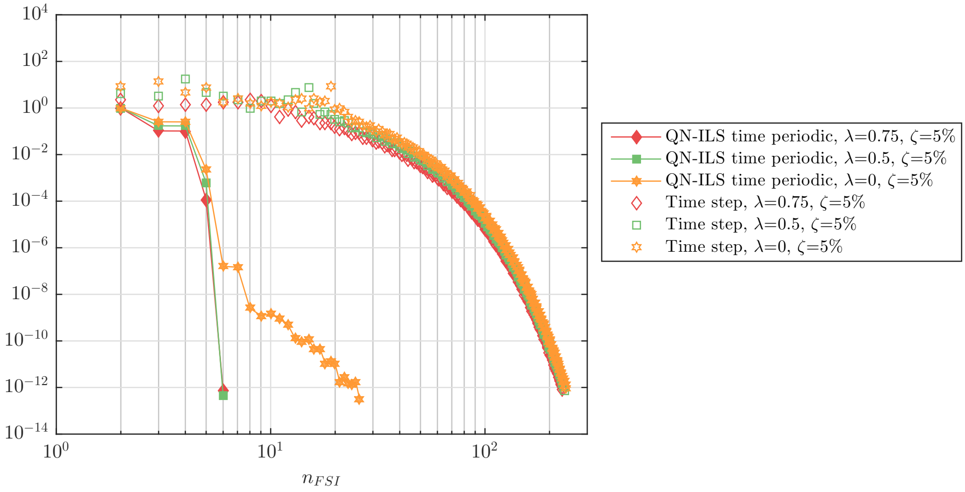

Figure A.4: Convergence behaviour of the time step and QN-ILS time periodic coupling for the 1-DoF plunging problem for different fluid added mass fractions.

TIME STEP AND QN-ILS TIME PERIODIC SOLUTION FOR DIFFERENT DAMPING RATIOS

For periodic FSI problems solved in the time domain the amount of damping in the system determines the number of FSI cycles required to obtain the steady state solution. Therefore, damping has an important influence on the convergence behaviour. In order to damp the transients in the response rapidly, artificial damping could be included, but that will also alter the steady state solution. Figure A.5 shows the influence of damping on the convergence of the TSC with the exact Jacobian of the residual function for the 1-DoF plunging problem. When the damping becomes too small the solution will hardly converge. The number of FSI cycles is inversely proportional to the damping ratio.

In case of the TPC, steady state solutions for the fluid and structural problem are sequentially calculated for each FSI cycle and the structural problem has been solved in the frequency domain. In that way the steady state structural solution for each FSI cycle is immediately obtained and any transients which will adversely affect the convergence to the steady state FSI solution are not computed. Figure A.5 shows also the convergence of the QN-ILS TPC for different damping ratios. It can be concluded that fast damping independent convergence is obtained with the QN-ILS TPC coupling and adopting a frequency domain approach. Figure A.5 explains also why the default damping value is equal to the high value of 5% of the critical damping. This value has been chosen in order to avoid biasing of the results in favour of the new coupling approach. Since for low damping the TPC approach will outperform the TSC even more.

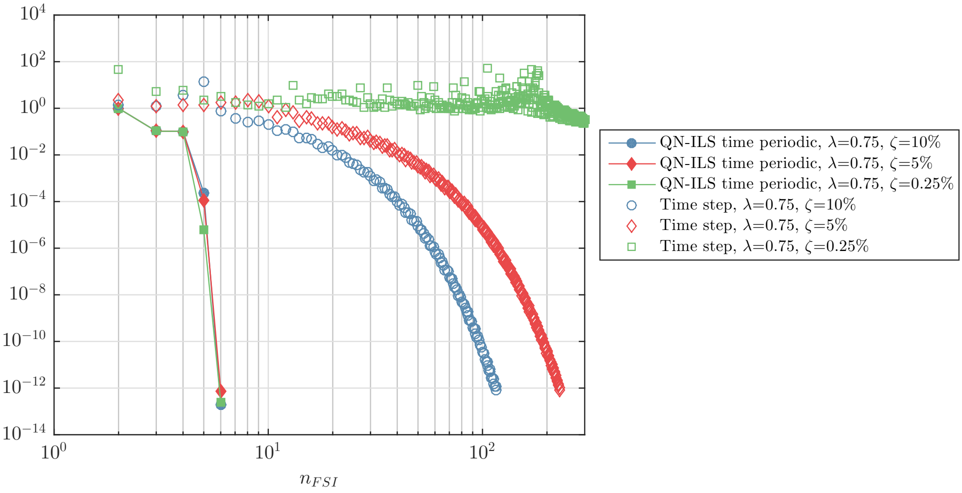

Figure A.5: Convergence behaviour of the time step and QN-ILS time periodic coupling for the 1-DoF plunging problem for different fluid added mass fractions.

TIME STEP AND QN-ILS TIME PERIODIC SOLUTION FOR DIFFERENT OSCILLATION FREQUENCIES

The convergence of the TSC algorithm with the exact (inverse) Jacobian of the residual function and the QN-ILS TPC algorithm will be compared for the 1-DoF plunging problem for the oscillation frequencies $\{4\pi, 7\pi, 10\pi\}$ rad/s. Since, the wet natural frequency (i.e. the natural frequency including the fluid added mass contribution) is 21 rad/s, the three oscillation frequencies cover stiffness, damping and mass dominated response regimes.

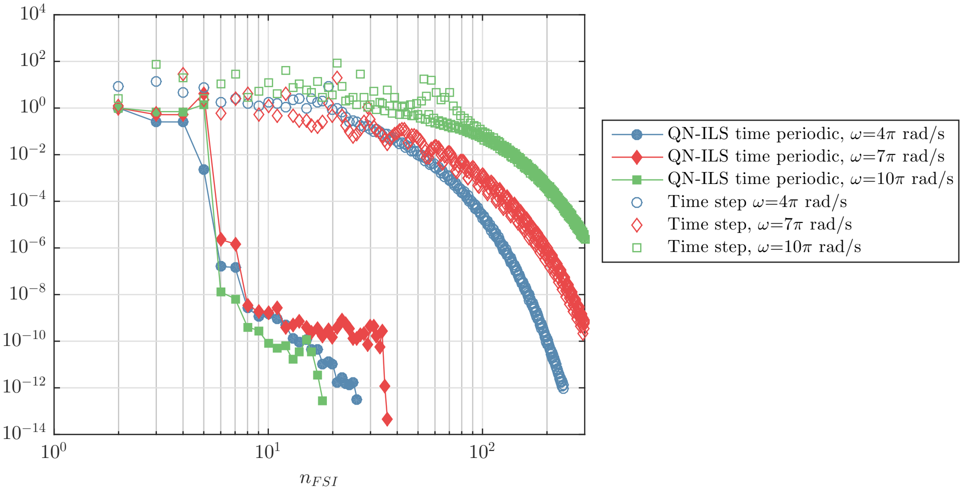

Figure A.6: Convergence behaviour of the time step and QN-ILS time periodic solution for the 1-DoF problem for different oscillation frequencies.

Figure A.6 shows the convergence behaviour of the two algorithms. For any case the convergence rate of the QN-ILS TPC algorithm is much faster than for the TSC algorithm. Up to $\psi = 10^{-6}$ the various TPC calculations converge similarly, for further convergence the number of FSI cycles strongly depends on ω. Over the whole range of errors a frequency dependency can be seen for the TSC approach. The slowest convergence is obtained for $\omega = 10\pi$, which is the case with the mass dominated response.

A.4.3. AITKEN TIME STEP AND QN-ILS TIME PERIODIC SOLUTION FOR THE 2-DOF PROBLEM

In this subsection the convergence behaviour of the TSC and TPC approach will be compared for the 2-DoF problem. In the TPC calculation the structural problem has been solved in the frequency domain, and the QN-ILS method has been used to stabilize the FSI analysis. The fluid forces have been computed with the potential flow solver PROCAL [23, 24], in order to show the efficiency improvement of the new approach for the more common case that fluid forces are computed with a black-box fluid solver. In the TSC calculation Aitken under-relaxation has been used for stabilisation. The fluid forces in the TSC calculation have been obtained from the approximations for the loads as given in Eq. A.17 and Eq. A.21. In that way the TPC calculation has been compared to the fastest TSC calculation. Figure A.7 shows the convergence of the TSC and TPC calculation, for $\omega = 4\pi$. The error has been determined with Eq. A.27 by separately calculating ψ for every degree of freedom and taking the maximum of both errors.

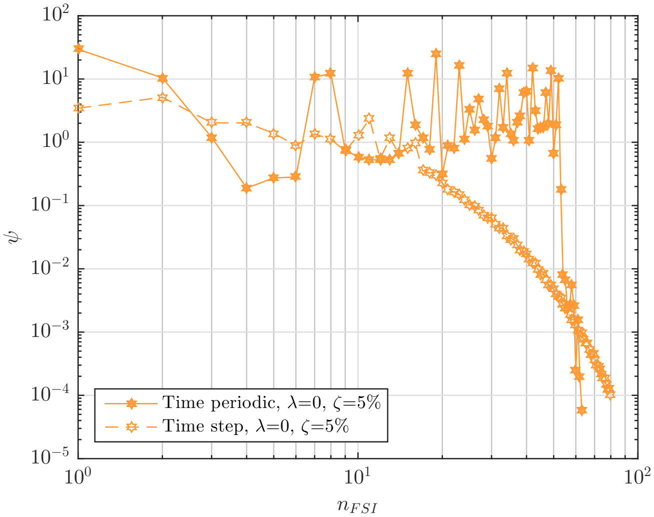

Figure A.7: Convergence behaviour of the Aitken time step and QN-ILS time periodic coupling for the 2-DoF problem, $\omega = 4\pi$.

The number of FSI cycles to reduce ψ to 10^{-4} is for the TPC calculation 63 and for the TSC calculation slightly more: 75 cycles. However, as explained before, in the most optimal case the TSC calculation requires only two structure and fluid evaluations per time step, whereas for the TPC coupling this is one. In the present TSC calculation on average eight structure and fluid evaluations per time step were required, since for this two degrees of freedom problem the exact inverse Jacobian cannot be derived and is approximated with Aitken's method. Hence, it can be concluded that also for this 2-DoF case the TPC approach significantly reduces the computational demand to obtain the steady state FSI solution.

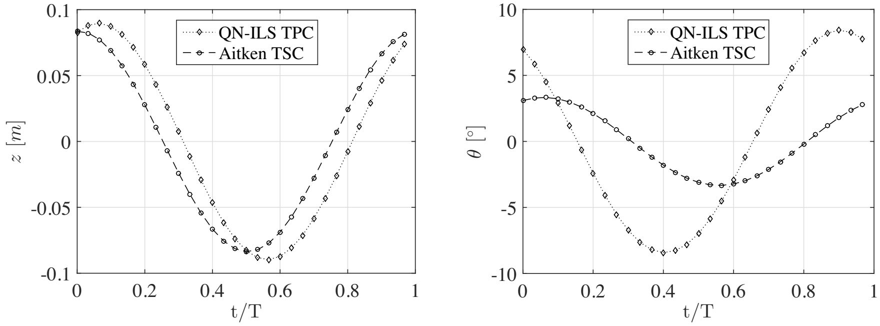

Figure A.8: Aitken time step and QN-ILS time periodic solution for z and θ as a function of the normalized timed, t/T, for the 2-DoF problem, $\omega = 4\pi$.

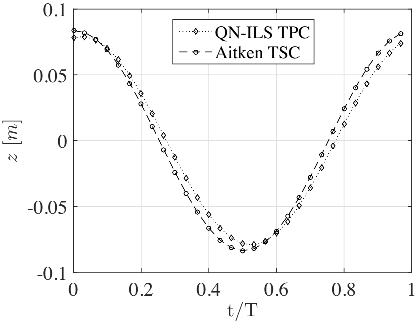

Figure A.9: Aitken time step and QN-ILS time periodic solution as a function of the normalized timed, t/T, for the 1-DoF plunging problem, $\omega = 4\pi$.

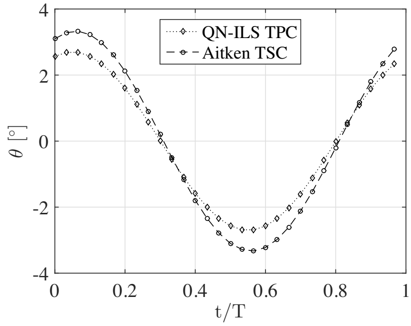

Figure A.10: Aitken time step and QN-ILS time periodic solution as a function of the normalized timed, t/T, for the 1-DoF pitching problem, $\omega = 4\pi$.

Figure A.8 shows the converged solution calculated with the TPC and the black box fluid solver and the solution as obtained from the TSC calculation in which the approximations for the fluid loads have been used. The plunging response as obtained with both approaches are reasonably similar. Larger differences can be seen for the pitching response. These differences can be attributed to the following reasons. First of all, the hydrodynamic loads as obtained with the potential flow solver PROCAL will differ from the approximated loads from RANS calculations as investigated in [19]. Secondly, in the approximation formulas as used in the TSC calculation a constant fluid added rotation inertia has been assumed. Depending on the reduced frequency this might be wrong, since for plunging motions it has been shown that a constant added mass is only valid for sufficiently low or high reduced frequencies [21]. The most important reason is that in the TPC calculation with PROCAL the fluid forces create a coupling between plunging and pitching response. This is not present in the TSC calculation. That can be concluded from the results presented in Figures A.9 and A.10. These graphs present results obtained with the two approaches for the 1-DoF plunging and pitching problem. That means the differences between the TPC and TSC solution in these figures can be only attributed to the first two aforementioned sources. Hence, it can be concluded that the big differences in the right graph of Figure A.8 is mainly due to hydrodynamic coupling between plunging and pitching response which is present in the TPC but not in the TSC calculation.

A.5. CONCLUSIONS

A new approach has been presented for solving more efficiently the FSI response of problems with periodic boundary conditions like in turbomachinery. It has been shown that time step coupled (TSC) simulations arduously converge to the steady state solution due to transients in the response. To get rid of the transient response the new approach is based on coupling the fluid and structural problem on a periodic level rather than per time step. In this time periodic coupling (TPC) the fluid and structural sub-problem can be solved in the frequency domain resulting in a very efficient algorithm for computing steady state FSI responses. To keep the iterative solution process stable, existing partitioned solution methods, like Aitken under-relaxation and Quasi-Newton inverse least squares (QN-ILS) have been used.

The TPC approach has been demonstrated for difficult FSI problems due to strong fluid added mass effects. The convergence rate of the TPC has been compared to a TSC approach. The results show that depending on the ratio between mass in the left- and right-hand-side of the equation of motion and damping in the system, the TPC converges much faster than a TSC. When the amount of fluid added mass in the right-hand-side of the equation of motion became too large, the Aitken TPC did not converge at all. The QN-ILS TPC converged for any case. This work shows that the computational demand to compute the steady state FSI response of periodic problems can be significantly reduced with a TPC approach.

This work has been limited to 1-DoF and 2-DoF problems. Therefore, for future work it is recommended to analyse more extensive cases as well, preferably FSI problems comprising both potential flow and viscous flow calculations. In this work the TPC approach have been presented only in combination with Aitken under-relaxation and the QN-ILS method. In future work the performance of the TPC approach with other partitioned solution methods should be investigated as well.

REFERENCES

[1] Y. Bazilevs, K. Takizawa, and T. Tezduyar, *Computational Fluid-Structure Interaction: Methods and Applications.* John Wiley & Sons Ltd: Chichester, UK, 2013.

[2] K. Takizawa, D. Montes, M. Fritze, S. Mcintyre, J. Boben, and T. Tezduyar, “Methods for FSI modeling of spacecraft parachute dynamics and cover separation,” *Mathematical Models and Methods in Applied Sciences*, vol. 23, no. 2, pp. 307–338, 2013.

[3] F. Liu, J. Cai, Y. Zhu, H. Tsai, and A. Wong, “Calculation of wing flutter by a coupled fluid-structure method,” *Journal of Aircraft*, vol. 38, no. 2, pp. 334–342, 2001.

[4] T. Opstal and E. van Brummelen, “A potential-flow BEM for large-displacement FSI,” tech. rep., Eindhoven University of Technology, Eindhoven, The Netherlands, 2012. CASA-report.

[5] R. Torii, M. Oshima, T. Kobayashi, K. Takagi, and T. Tezduyar, “Fluid-structure interaction modeling of blood flow and cerebral aneurysm: Significance of artery and aneurysm shapes,” *Computer Methods in Applied Mechanics and Engineering*, vol. 45-46, no. 2, pp. 3613–3621, 2009.

[6] P. Maljaars and J. Dekker, “Hydro-elastic analysis of flexible marine propellers,” in *Maritime Technology and Engineering* (C. Guedes Soares and T. Santos, eds.), pp. 705–715, CRC Press-Taylor & Francis Group: London, UK, 2014.

[7] Y. Young, “Time-dependent hydroelastic analysis of cavitating propulsors,” *Journal of Fluids and Structures*, vol. 23, pp. 269–295, 2007.

[8] E. van Brummelen, “Partitioned iterative solution methods for fluid-structure interaction,” *International Journal for Numerical Methods in Fluids*, vol. 65, no. 1-3, pp. 3–27, 2011.

[9] E. van Brummelen, “Added mass effects of compressible and incompressible flows in fluid-structure interaction,” *Journal of Applied Mechanics*, vol. 76, no. 2, p. 021206, 2009.

[10] U. Küttler and W. Wall, “Fixed-point fluid-structure interaction solvers with dynamic relaxation,” *Computational Mechanics*, vol. 43, pp. 61–72, 2008.

[11] J. Degroote, K. Bathe, and J. Vierendeels, “Performance of a new partitioned procedure versus a monolithic procedure in fluid-structure interaction,” *Computers Structures*, vol. 87, no. 11–12, pp. 793–801, 2009.

[12] C. Berthold, “Development of a coupled fluid-structure simulation method in the frequency domain,” Master’s thesis, Delft University of Technology, Delft, The Netherlands, 2016.

[13] B. Beulen, M. Rutten, and F. vandeVosse, “A time-periodic approach for fluid-structure interaction in distensible vessels,” *Journal of Fluids and Structures*, vol. 25, no. 5, pp. 954–966, 2009.

[14] J. Degroote, R. Haelterman, S. Annerel, P. Bruggeman, and J. Vierendeels, “Performance of partitioned procedures in fluid-structure interaction,” *Computers Structures*, vol. 88, no. 7–8, pp. 446–457, 2010.

[15] P. Causin, J. Gerbeau, and F. Nobile, "Added-mass effect in the design of partitioned algorithms for fluid-structure problems," *Computer Methods in Applied Mechanics and Engineering*, vol. 194, no. 42–44, pp. 4506–4527, 2005.

[16] C. Förster, W. Wall, and E. Ramm, "The artificial added mass effect in sequential staggered fluid-structure interaction algorithms," *European conference on computational fluid dynamics, ECCOMAS*, pp. 1–20, 2006.

[17] T. Scholcz, *Multi-fidelity methods for fluid-structure interaction and uncertainty quantification.* PhD thesis, Delft University of Technology, Delft, The Netherlands, 2015.

[18] J. Degroote, P. Bruggeman, R. Haelterman, and J. Vierendeels, "Stability of a coupling technique for partitioned solvers in FSI applications," *Computers Structures*, vol. 86, no. 23–24, pp. 2224–2234, 2008.

[19] Y. Young, E. Chae, and D. Akcabay, "Hybrid algorithm for modeling of fluid-structure interaction in incompressible, viscous flows," *Acta Mechanica Sinica*, vol. 28, no. 4, p. 1030–1041, 2012.

[20] C. Münch, P. Ausoni, O. Braun, M. Farhat, and F. Avellan, "Fluid-structure coupling for an oscillating hydrofoil," *Journal of Fluids and Structures*, vol. 26, p. 1018–1033, 2010.

[21] P. Maljaars, M. Kaminski, and J. den Besten, "Boundary element modelling aspects for the hydro-elastic analysis of flexible marine propellers," *Journal of Marine Science and Engineering*, vol. 6, no. 2, p. 67, 2018.

[22] J. Katz and A. Plotkin, *Low-speed aerodynamics.* Camebridge University Press: New York, NY, USA, 2001.

[23] G. Vaz, *Modelling of sheet cavitation on hydrofoils and marine propellers using boundary element methods.* PhD thesis, Instituto Superior Técnico, Lisbon, Portugal, 2005.

[24] G. Vaz and J. Bosschers, "Modelling of three dimensional sheet cavitation on marine propellers using a boundary element method," Sixth International Symposium on Cavitation, Wageningen, The Netherlands, 2006.

DANKWOORD

Veel dank ben ik verschuldigd aan een ieder die mij afgelopen jaren geholpen en ondersteund heeft om mijn promotieonderzoek te kunnen doen. Als eerste wil ik de bedrijven en organisaties bedanken, die het GreenProp project financieel hebben ondersteund. Dat betreffen: NWO, DMO, MARIN, Wärtsilä en Solico. Het project is een succes geworden, mede dankzij jullie bijdrage die veel verder ging dan alleen financiering. Ik heb maximale inzet van een ieder ervaren, en dat heeft mij weer gestimuleerd en gemotiveerd. Het MARIN zou ik expliciet willen bedanken voor het mogen gebruiken van de PROPART-routines. De CRS wil ik bedanken voor het gebruik van de panelenmethode PROCAL en voor het gezamenlijk doen van metingen bij het MARIN. Damen Shipyards zou ik willen bedanken voor hun input gedurende het hele onderzoekstraject. Ook het belangeloos meten van de eigenfrequenties en trilvormen van de ware grootte schroef wil ik expliciet noemen.

Achter de eerder genoemde organisaties en bedrijven zitten tal van mensen die op één of andere manier betrokken zijn geweest bij mijn promotiestudie. Het is ondoenlijk om een ieder bij name te noemen en te bedanken. Enkele personen wil ik toch expliciet noemen. Dat zijn als eerste mijn promotoren Mirek Kaminski en Tom van Terwisga. Mirek, het was me een genoegen om onder jouw hoede en in jouw vakgroep werkzaam te zijn. Je stimulans, gecombineerd met een hoge dosis enthousiasme en je vertrouwen in mij heeft me gemotiveerd om deze promotiestudie te doen. Tom, bedankt dat je vanaf het begin ook mijn promotor wilde zijn en op die manier het hele traject door je bijdrage hebt geleverd. Mirek en Tom, met alle verschillen tussen jullie beiden, heb ik erg veel waardering voor jullie als persoon en hoogleraar. Ik noem het in die volgorde, want zo hebben jullie mij ook altijd benaderd. Eerst als persoon en daarna als promovendus. Hartelijk dank daarvoor!

Al mijn collega's bij de TU Delft zou ik ook hartelijk willen bedanken voor de collegialiteit en de fijne sfeer. In het bijzonder wil ik Henk den Besten noemen. De promotiestudie heb ik soms ervaren als een eenzaam traject. De tijd die jij voor me vrijmaakte om met mij te sparren heeft veel voor me betekend. Bedankt daarvoor.

Bij het MARIN zijn ook veel personen aan wie ik dank verschuldigd ben. Het aantal MARIN-mensen dat in de lopen der jaren bij mijn project betrokken is geweest, is niet op twee handen te tellen. Enkele personen wil ik expliciet bedanken. Dat zijn Johan Bosschers, Evert-Jan Foeth, Nicola Grasso en Erik van Wijngaarden. Johan, met name voor het wegwijs maken in PROCAL en de ondersteuning bij het programmeren van de aanpassingen in PROCAL. Evert-Jan, bedankt voor je hulp bij het gebruiken van de PROPART-routines. Nicola, jou wil ik ook graag expliciet noemen. Jouw inzet om de metingen tot een succes te maken ging verder dan ik had mogen verwachten. Erik, ik wil jou met name bedanken voor de feedback die je hebt gegeven op al mijn artikelen en proefschrift. Dit heeft de kwaliteit aanzienlijk verbeterd.

Mariska, ik wil jou bedanken voor alles wat je de achterliggende jaren voor me hebt betekend. Werk en privé waren de laatste jaren niet altijd duidelijk gescheiden. Zelfs op vakanties ging de laptop mee om nog wat berekeningen te kunnen doen. In ieder geval heb jij ervoor gezorgd dat de balans niet naar de verkeerde kant oversloeg en anders hebben de achterliggende twee jaren onbewust onze jongens, Jesse en Marijn, daar wel voor gezorgd.

Wanneer ik dit dankwoord zo zou eindigen zou ik het belangrijkste vergeten. Want wat heb ik dat ik niet heb ontvangen? (1 Korinthe 4:7). De gezondheid, kracht en wijsheid om deze promotiestudie te doen heb ik daarom te danken aan Hem die allen het leven en de adem, en alle dingen geeft. Soli Deo Gloria.

Curriculum Vitæ

Pieter Johannes Maljaars

Education

2007–2010	B.Sc. in Marine Engineering (cum laude) Delft University of Technology, The Netherlands
2010–2013	M.Sc. in Marine Engineering (cum laude) Delft University of Technology, The Netherlands *Specialisation:* Ship and Offshore Structures
2014–2018	Ph.D. Delft University of Technology, The Netherlands *Thesis:* Hydro-Elastic Analysis of Flexible Marine Propellers *Promotors:* Prof. dr. ir. M.L. Kaminski and Prof. dr. ir. T.J.C van Terwisga

Employment record

2013–2016	Project engineer and naval architect D.W. den Herder/HAL Maritiem B.V., Sliedrecht, The Netherlands
2014–2018	Researcher Delft University of Technology, The Netherlands
2018	Noise and vibration engineer JVS B.V., Hendrik-Ido-Ambacht, The Netherlands

Awards

2008	Young Talent Encouragement Award
2013	KNVTS Maritime Student Award

LIST OF PUBLICATIONS

JOURNAL ARTICLES

- P. Maljaars, M. Kaminski and J. den Besten, "Finite element modelling and model updating of composite propellers," *Composite Structures*, vol. 176, pp. 154–163, 2017.

- P. Maljaars, L. Bronswijk, J. Windt, N. Grasso and M, Kaminski, "Experimental validation of fluid-structure interaction computations of flexible composite propellers in open water conditions using BEM-FEM and RANS-FEM methods," *Journal of Marine Science and Engineering*, vol. 6, no. 4, 51, 2018.

- P. Maljaars, M. Kaminski and H. den Besten, "Boundary element modelling aspects for the hydro-elastic analysis of flexible marine propellers," *Journal of Marine Science and Engineering*, vol. 6, no. 2, 67, 2018.

- P. Maljaars, M, Kaminski and J. den Besten, "A new approach for computing the steady state fluid-structure interaction response of periodic problems," *Journal of Fluids and Structures*, vol. 84, pp. 140–152, 2018.

- P. Maljaars, N, Grasso, J. den Besten and M. Kaminski, "BEM-FEM coupling for the analysis of flexible propellers in non-uniform flows and validation with full-scale measurements," submitted to *Journal of Fluids and Structures*.

CONFERENCE PAPERS

- P. Maljaars and J. Dekker, "Hydro-elastic analysis of flexible marine propellers," in *Maritime Technology and Engineering* (C. Guedes Soares and T. Santos, eds.), pp. 705–715, CRC Press-Taylor & Francis Group: London, UK, 2014.

- P. Maljaars, "Hydro-elastic analysis of flexible propellers: An overview," Fourth International Symposium on Marine Propulsors, Austin, TX, USA, 2015.

- P. Maljaars, N. Grasso, M. Kaminski, and W. Lafeber, "Validation of a steady BEM-FEM coupled simulation with experiments on flexible small scale propellers," Fifth International Symposium on Marine Propulsors, Espoo, Finland, 2017.

ISBN 978-94-6375-233-6